Université de Montréal

An In-Depth Study of High Energy Oxygen Implantation into Ion-Damaged Silicon

par

Sandy Bultena

Département de physique
Faculté des arts et sciences

Thèse présentée à la Faculté des études supérieures
en vue de l'obtention du grade de
Philosphiæ Doctor (Ph.D.)
en Physique

décembre, 1995

Abstract

To produce high quality SIMOX (separation by implantation of oxygen) wafers, it is necessary to reduce the damage that remains in the silicon film after it has been annealed. The current method of achieving this is to create BOX (buried oxide) wafers, which are essentially low-dose SIMOX wafers.

To create BOX structures, it is necessary to understand and manipulate the three precipitation processes (homogenous (HO), heterogenous (HE) and etherogeneous (ET) precipitation) that occur in the silicon wafer during the implantation. The interaction between oxygen and pre-existing damage in a silicon wafer during the oxygen implantation and annealing is studied in an effort to understand how the presence, or absence, of damage changes the HE precipitation process.

Oxygen is implanted into pre-damaged silicon, as well as undamaged silicon. The energy of the oxygen implants is fixed at 2.50 MeV. The oxygen doses that are studied are $\phi = 0.3 \times 10^{17}$, 1.0×10^{17} and 3.0×10^{17} O/cm^2. The implant temperature is 570°C.

Three different types of pre-damage are used. The first two types are produced by a silicon implant at room temperature, followed by a 1 h, 900°C anneal. When $\phi(Si) = 5 \times 10^{14}$ Si/cm^2, the resulting pre-damage is composed almost entirely of dislocation loops, and when $\phi(Si) = 1 \times 10^{15}$ Si/cm^2, it is composed almost entirely of dislocation dipoles. The depth of the pre-damage is varied by adjusting the implant energy. The silicon energies are $E = 2.00$, 2.25, 2.50 and 2.75 MeV. The third type of pre-damage is created by a 2.5 MeV oxygen implant (2×10^{15} O/cm^2) around 300°C, *not* followed by an anneal. This pre-damage consists of small defect clusters and micro-precipitates.

The distribution of oxygen as a function of depth was determined by Elastic Recoil Detection (ERD) and Secondary Ion Mass Spectrometry (SIMS). The damage profiles were characterized by Cross-sectional Electron Microscopy (XTEM) and Rutherford Backscattering Spectrometry & Channeling (RBS/C). The location and sizes of the oxide precipitates were characterized by XTEM.

First, the properties of oxygen implantation into un-damaged silicon are studied. The range and straggling of the oxygen ions are determined. The oxygen concentration profiles as a function

of dose (as-implanted and annealed), and the damage type and distribution as a function of dose (as-implanted and annealed), are also studied.

An empirical model is presented which describes the experimental results. It is demonstrated that the minimum dose needed to form a BOX layer in an undamaged silicon wafer is $\phi \sim 1-2 \times 10^{18}$ O/cm^2 when $E = 2.5$ MeV.

With the exception of the $\phi = 3.0 \times 10^{17}$ O/cm^2 sample, the silicon film is free of damage, up to a depth of 2.33 μm. In the $\phi = 3.0 \times 10^{17}$ O/cm^2 sample there is damage located in a narrow (0.4 μm) depth region around 1.2 μm. After discussing the properties of strain, and possible strain relief mechanisms, it was concluded that the strain in the silicon film exceeded the elastic limit, which resulted in the formation of small dislocations and oxide precipitates.

Next, the properties of oxygen implantation into pre-damaged silicon are studied. The oxygen concentration profiles and the damage profiles, as a function of (1) oxygen dose, (2) pre-damage type and (3) distance separating the pre-damage region from the oxygen implant, are studied.

The following results are presented. The remaining quantity of damage and precipitates at the pre-damage depth (d_{Si}) is an inverse function of the oxygen dose. When d_{Si} is less than the depth of the maximum damage production (d_O), the concentration of oxygen at d_O is reduced in the annealed samples. When $d_{Si} = d_O$ the concentration of oxygen in this region is increased. The number of threading dislocations between d_{Si} and d_O is related to the stability of the pre-damage during the oxygen implantation. It is shown that the relevant properties of the pre-damage are (1) the rate that interstitials can be absorbed by the pre-damage, (2) the number of nucleation sites for oxide precipitation and (3) the relative stability of the pre-damage during the oxygen implantation.

Empirical models are developed which discuss the interactions between the pre-damage, silicon interstitials and oxide precipitation. We demonstrate that the oxide precipitation at d_O, and the subsequent oxygen concentration profile after annealing, is a result of oxygen and silicon interstitial diffusion from d_O to d_{Si} in the early stages of the implantation. We also demonstrate that the damage in the silicon film is a result of excess silicon interstitials, and can be reduced by providing a diffusion barrier between the oxygen implant region and the silicon film.

Résumé

Afin de produire des couches SIMOX (Séparation par IMplantation d'OXygène) de bonne qualité, il est nécessaire de réduire le dommage résiduel dans la couche de silicium après l'avoir recuite. Un échantillon SIMOX est en fait une couche d'oxyde de 0,1–1 μm d'épaisseur enfouie sous une épaisseur de 0,1 à 5 μm de silicium cristallin que l'on forme sur une pastille de silicium monocristallin. La performance de plusieurs dispositifs électroniques se trouve améliorée lorsqu'ils sont frabriqués sur des gaufres SIMOX. On forme une couche SIMOX en implantant une forte dose d'oxygène ($\phi > 1 - 2 \times 10^{18}$ O/cm^2) à haute énergie (150 keV – 5 MeV) dans une gaufre de silicium suivi d'un recuit à haute température. On tente actuellement de produire des couches SIMOX en utilisant des doses plus faibles d'oxygène ($\phi \sim 2 - 5 \times 10^{17}$ O/cm^2) dans le but de former des couches d'oxyde enfouies, communément appelées BOX (*Buried OXide*). Les principaux avantages sont: (1) une réduction du dommage dans la couche de silicium puisque l'on implante une dose plus faible d'oxygène et (2) une production d'un plus grand nombre d'échantillons à un moindre coût.

Afin de créer des structures BOX, il est nécessaire de comprendre et de contrôler les trois processus de nucléation qui se produisent dans la gaufre de silicium durant l'implantation. La nucléation hétérogène (HE) est le principal processus de nucléation qui se produit aux sites cristallins endommagés. Ce processus survient principalement dans la région où se produit le maximum de dommage (d_O). La nucléation homogène (HO) se produit à la profondeur du maximum de la concentration d'oxygène (R_p) où cette concentration dépasse la limite de solubilité de l'oxygène dans le silicium. Le troisième processus de nucléation (nucléation étherogène (ET)) résulte de l'interaction de l'oxygène avec la cascade ionique dense et chaude et se produit à des profondeurs plus grandes que R_p. La différence entre les propriétés des nucléations HO, HE et ET constitue le processus fondamental régissant la formation des couches d'oxyde enfouies BOX.

Il est important de bien comprendre comment le processus de nucléation HE se produisant dans le silicium durant l'implantion est influencé par la présence ou l'absence de dommage et également en quoi cela affecte l'échantillon durant le recuit. Pour répondre à ces questions, nous avons décidé d'étudier l'interaction entre l'oxygène et le dommage préexistant dans une gaufre de silicium durant l'implantation et durant le recuit.

On a déterminé la distribution d'oxygène en fonction de la profondeur par la méthode de détection du recul élastique (ERD) et par spectrométrie de masse des ions secondaires (SIMS). Les profils de dommage furent caractérisés par microscopie électronique à transmission (XTEM) et par spectrométrie de rétrodiffusion Rutherford en mode canalisation (RBS/C). La position et la taille des précipités d'oxyde ont été déterminées par XTEM.

On a implanté l'oxygène dans des échantillons de silicium pré-endommagés et non endommagés. L'énergie d'implantation des atomes d'oxygène était de 2,50 MeV. Ce choix de l'énergie d'implantation se voulait un compromis entre une énergie élevée, où la séparation des régions hétérogènes (2,3 μm) et homogènes (2,55 μm) est bien définie, et une énergie faible, où les résultats pourraient être plus facilement reliés aux structures BOX. Les doses d'oxygène étudiées furent $\phi = 0,3 \times 10^{17}$, $1,0 \times 10^{17}$ et $3,0 \times 10^{17}$ O/cm^2. La température de l'échantillon était maintenue à 570°C lors de l'implantation.

On a étudié les propriétés de l'implantation d'oxygène dans le silicium non endomagé en premier lieu. La couche de silicium demeure cristalline jusqu'à une profondeur de 2,33 μm, sauf pour la dose $\phi = 3,0 \times 10^{17}$ O/cm^2. À cette dose, on retrouve une région étroite (0,4 μm) de dommage à la profondeur de 1,2 μm. La formation des petites dislocations et des précipités d'oxyde résultent du fait que la déformation du silicium excédait la limite élastique.

La forme des profils de concentration d'oxygène dans les échantillons recuits dépend de la dose d'oxygène. Cet effet est décrit à partir d'un modèle empirique. Ce modèle nécessite l'existence d'au moins deux maxima locaux de la taille des precipités, situés respectivement à la profondeur du maximum de dommage (précipités HE) et à la profondeur du maximum de concentration des ions oxygène (précipités HO). Le nombre de précipités et leurs tailles augmentent avec la dose. Aux doses étudiées dans ces expériences, les précipités HO sont plus gros que les précipités HE. La nucléation ET n'affecte pas la nucléation HE. Les précipités qui sont plus petits qu'une certaine taille critique (~50 nm à la température du recuit) vont se dissoudre au tout début du recuit.

En utilisant le modèle empirique mentionné ci-haut, on peut expliquer les profils d'oxygène après un recuit de 12 h comme étant dus au processus standard d'Ostwald (*Ostwald ripening*) appliqué aux précipités résiduels de l'échantillon. A la température de recuit utilisée, la majorité des précipités d'un échantillon implanté à une dose de 3×10^{16} O/cm^2 sont plus petits que le rayon critique et, par conséquent, se dissolvent au début du recuit. La distribution finale de l'oxygène a la forme d'une boîte.

Dans le cas d'échantillons implantés à une dose de 1×10^{17} O/cm^2, seuls les précipités HO sont plus larges que le rayon critique. Finalement, dans un échantillon implanté à une dose de 3×10^{17} O/cm^2, les précipités HE et HO sont tous plus larges que le rayon critique. Ces précipités croissent durant le recuit et le profil final de la concentration d'oxygène est formé de deux pics distincts. Pour ce dernier échantillon, il n'y a pas de diffusion d'oxygène entre les régions HO et HE durant le recuit. Pour cette raison, toute couche d'oxyde fabriquée à des doses $\phi = 3 \times 10^{17}$ O/cm^2 ou plus élevées doit être au moins aussi épaisse que la distance qui sépare les régions de nucléations HE et HO. On en conclut que la dose minimale pour former une couche d'oxyde est d'environ $1 - 2 \times 10^{18}$ O/cm^2.

Dans un deuxième temps, la compréhension de l'interaction entre la dommage et le comportement de l'oxygène dans le silicium s'est poursuivie par une étude de l'oxygène implanté dans des échantillons de silicium pré-endommagés suivi d'une comparaison de ceux-ci avec les échantillons préparés sur des substrats non endommagés. On a étudié trois types de pré-endommagement. Les deux premiers types furent produits par l'implantation de silicium à la température de la pièce suivie d'un recuit à 900°C pendant 1 h. Pour une dose $\phi(Si) = 5 \times 10^{14}$ Si/cm^2, le prédommage se compose presque entièrement de boucles de dislocations. Pour une dose $\phi(Si) = 1 \times 10^{15}$ Si/cm^2, le prédommage se compose presque exclusivement de dipôles de dislocations. La profondeur de création de ce prédommage (d_{Si}) change avec l'énergie d'implantation du silicium. Les énergies chosies furent $E = 2{,}00$, 2,25, 2,50 et 2,75 MeV. Le troisième type de pré-endommagement fut créé par l'implantation d'oxygène (2×10^{15} O/cm^2) d'une énergie de 2,5 MeV à une température $\sim$ 300°C; aucun recuit ne fut fait dans ce cas. Le prédommage consiste en de petits amas de défauts et de micro-précipités.

Bien que la distribution des atomes d'oxygène dans les échantillons tels qu'implantés n'est généralement pas affectée par les différences entre les processus de nucléation HE, HO et ET, la distribution des précipités d'oxyde l'est. Cela résulte en une mosaïque de résultats pour les échantillons recuits. Les profils de concentration d'oxygène et du dommage furent analysés en fonction (1) de la dose d'oxygène, (2) de la distance de la région pré-endommagée de celle où l'oxygène a été implanté et (3) du type de prédommage. La distribution des précipités d'oxyde dans les échantillons tels qu'implantés est déduite de l'état des échantillons recuits.

La quantité de dommage et de précipités qui restent à la profondeur d_{Si} est inversement proportionelle à la dose d'oxygène, en accord avec les résultats des profils de concentration d'oxygène.

En conséquence, la présence du prédommage dans les échantillons avant l'implantation est moins apparente pour des doses plus élevées d'oxygène.

Si la profondeur du prédommage (d_{Si}) est plus faible que la profondeur du maximum de production de dommage (d_O), la concentration d'oxygène à d_O est réduite dans les échantillon recuits. Quand $d_{Si} = d_O$, la concentration d'oxygène dans cette région augmente.

Le profil final de la concentration d'oxygène dépend du type de prédommage. Le nombre de dislocations entre d_{Si} et d_O est relié à la stabilité du prédommage lors de l'implantation d'oxygène, ce qui, par la suite, change la quantité de précipités dans la région entre d_O et d_{Si}. Les propriétés pertinentes du prédommage sont (1) le taux d'absorption des interstitiels par le prédommage, (2) le nombre de sites de nucléation pour la formation de précipités d'oxyde et (3) la stabilité relative du prédommage lors de l'implantation d'oxygène.

Un modèle a également été développé pour expliquer les différences entre les profils de concentration d'oxygène des échantillons recuits. Au début de l'implantation, il y a précipitation dans trois régions distinctes: (1) dans la région du prédommage (d_{Si}), (2) dans la région du maximum de dommage (d_O) et (3) dans la région du maximum de pénétration de l'oxygène dans le silicium (R_p). Au tout début de l'implantation, la majorité des sites de nucléation pour l'oxydation se situent à la profondeur d_{Si}. Les atomes d'oxygène et les silicium interstitiels diffusent vers d_{Si}, ce qui réduit le taux de croissance du dommage et des précipités d'oxyde à d_O. Il y a cependant plus d'ions d'oxygène déposés dans cette région par unité de temps qu'il y en a autour de d_{Si}. En conséquence, les précipités y croissent plus rapidement que dans la région d_{Si}. Les interstitiels de silicium en excès qu'on retrouve dans cette dernière région ne sont pas libres de migrer vers la surface. Ils interagissent plutôt avec le prédommage ou avec le dommage causé par l'oxygène, résultant en la formation de dislocations entre ces deux couches. Une nouvelle région d'oxydation préférentielle qui s'étale entre d_{Si} et d_O est formée. Après le recuit de l'échantillon, les régions qui contiennent de gros précipités forment des pics de concentration d'oxygène.

En résumé, nous avons démontré que la précipitation d'oxyde à d_O peut être contrôlée par un endommagement préalable de la gaufre de silicium avant l'implantation. Si le prédommage se situe à d_O, la nucléation HE est augmentée. Dans l'avenir, il serait possible de créer des structures BOX à des énergies élevées d'implantation d'oxygène en contrôlant la nucléation HO de la même façon.

Table of Contents

List of Tables

List of Figures

Nomenclature

γ	ratio of stopping power for aligned and non-aligned ions in a crystal
θ_B	Bragg scattering angle
ϕ	total dose (or fluence) of the oxygen implanted into silicon
ϕ_{Si}	total dose (or fluence) of the silicon implanted into silicon
ϕ_{HE}	the oxygen dose where the size of the precipitates at d_O are the same as the precipitates at d_{Si}
σ	integrated Rutherford scattering cross section
σ_D	integrated scattering cross section off of a crystal defect
$\psi_{\frac{1}{2}}$	critical angle for channeling
χ	ratio of aligned yield to random yield (RBS/C analysis)
χ_R	random fraction of beam during RBS/C analysis
χ_V	random fraction of beam during RBS/C analysis for a virgin sample
$\vec{b}$	Burger's vector of a dislocation.
$\vec{B}$	upward drawn incident beam direction in an electron microscope, opposite to the direction of the electron beam
BF	bright field (electron microscope image)
BOX	buried oxide (typically refers to low dose SIMOX structures
BPM	beam profile monitor
Cz	Czochralski (type of silicon wafer)
$d\sigma/d\Omega$	differential Rutherford scattering cross section
$d\sigma_D/d\Omega$	differential scattering cross section off of a crystal defect
d_O	depth of the maximum damage production when oxygen is implanted into silicon
d_{Si}	depth of the maximum damage production when silicon is implanted into silicon *or* depth of the pre-damage
dE/dx	total stopping power of an ion in an amorphous target
DF	dark field (electron microscope image)
$dP(\psi_{\frac{1}{2}}, dx)$	probability that a channeled probing ion, passing through a thickness dx, will scatter with an angle greater than $\psi_{\frac{1}{2}}$
EOR	end of range (refers to a depth region in a sample beyond the range where the majority of the implanted ions come to rest)

ERD	elastic recoil detection
ET	etherogeneous (refers to precipitation which occurs well past the EOR region)
f_σ	$(d\sigma_D/d\Omega)\,/\,(d\sigma/d\Omega)$
FFT	fast Fourier transform
FWHM	full width at half maximum
$\vec{g}$	a vector normal to the reflecting plane (hkl), with magnitude $1/d_{hkl}$, *or*, the vector corresponding to the diffracting planes in an electron microscope DF or BF image
HE	heterogeneous (refers to precipitation which occurs on damage sites)
HF	hydrofluoric acid
HINIS	high intensity negative ion source
HO	homogeneous (refers to precipitation which occurs when there is a supersaturation of oxygen
IBL	Ion beam laboratory (at the Université de Montréal)
IDC	intermediate defect cluster (for example: row vacancies)
KOH	potassium hydroxide
LN	liquid nitrogen (temperature)
n	atomic density (atoms/cm^3)
n_D	density of defects (atoms/cm^3)
$P(\psi_{\frac{1}{2}}, x)$	probability that a channeled probing ion, passing through a thickness x, will scatter with an angle greater than $\psi_{\frac{1}{2}}$
pre-damage	damage that is created before implanting oxygen into silicon
r_c	the critical radius of an oxide precipitate, defined such that if $r < r_c$ the oxide precipitate will dissolve
R_p	the range, or depth, of the peak concentration of oxygen in silicon
ΔR_p	the sigmoidal width (Gaussian) of the concentration profile
RIE	reactive ion etch
RBS	Rutherford backscattering spectrometry
RBS/C	Rutherford backscattering spectrometry with channeling
$\vec{s}$	the deviation from the Bragg reflection position, defined by $\vec{s}+\vec{g}=\vec{g}'$ where $\vec{g}'$ defines the exact Bragg condition. $\vec{s}>0$ when $\theta > \theta_B$.
SAD	selected area diffraction
SBD	surface barrier detector
SIMOX	separation by implantation of oxygen

SIMS	secondary ion mass spectrometry
SOI	silicon on insulator
standard	a sample that was not pre-damaged before implanting oxygen
T_i	implant temperature
TCE	trichloroethylene
TEM	transmission electron microscopy
TOF	time-of-flight
TRIM	transport of ions in matter (computer simulation)
XTEM	cross-sectional transmission electron microscopy
Y	yield (refers to number of detected recoils or scattered ions)

Acknowledgements

I would like to gratefully acknowledge all the help, guidance and patience that I received from my two co-directors, Drs. Arthur Yelon and John Brebner. In addition I would also like to thank Dr. Sjoerd Roorda for many interesting discussions.

My work would not have been possible without the help and guidance from Drs. Subhash Gujrathi and Kenneth Oxorn, who not only taught me everything there is to know about ERD, but also spent many hours providing insights to science in general, and my work in particular.

In recognition of all the nitty gritty little details about the Tandem accelerator and the RBS/channeling chamber that were passed along to me, I would like to thank Dr. George Kajrys and his invaluable store of knowledge. When times were tough (often), and a reasonable interpretation of my data seemingly impossible, my fellow students and lunch-mates would rally around and, through many brainstorming attempts, aid me in the overall understanding of my data. Many thanks to Yves Trudeau, Gilles Gagnon and George Kajrys.

I would like to extend my thanks to Drs. J. Jackman and G. McMahon from CANMET, who provided me with the SIMS analysis presented in this thesis. I would also like to thank Dr. G. Carpenter from CANMET who determined that those funny spots in my XTEM samples were voids.

I would very much like to express my gratitude and appreciation to Michael LeBlanc, who was my dark room assistant. Many many hours were spent in the dark room, processing prints. The entire process proceeded faster and with greater ease with his help.

And finally I would like to thank my husband, Kenneth Oxorn, and my son, Michael LeBlanc, for supporting me throughout this work. Their loving support and understanding has been invaluable.

The financial support of the Université de Montréal, Natural Sciences and Engineering Research Council of Canada and Fonds Quèbècois pour la Formation des Chercheurs et l'Aide à la Recherche, is gratefully acknowledged.

Chapter 1
Introduction

In recent years, the electronics industry has shown a resurgent interest in SOI technology [1-3]. SOI (Silicon on Insulator) structures consist of a silicon wafer with a thin film of crystalline silicon separated from the bulk by a thin insulator. The basic advantage of SOI structures is that a dielectric isolation under a mono-crystalline silicon layer can be used to improve the performance of many electronic devices. These include ULSI-CMOS (ultra large scale integration – complementary metal oxide semi-conductor) logic, radiation hard RAM (random access memory) bipolar CMOS and wave guides, to name just a few. The two main characteristics of the SOI device, silicon film thickness and insulator thickness, can be adjusted to suit the needs of each electronic application.

As an added bonus to improved performances in many electronic devices, it is also projected that the cost of producing SOI devices will be less than that of producing their standard counterparts [1]. This is because the fabrication of an SOI device requires 20% fewer processing steps, which offsets the additional cost of an SOI wafer.

The most promising technique for the production of SOI material is the formation of a buried SiO_2 insulating layer in a single crystal by high-energy (150 keV – 5 MeV) oxygen implantation [4,5]. This is referred to as SIMOX (Separation by IMplantation of Oxygen). The ideal SIMOX wafer has a pure silicon crystal film with no oxygen, no dislocations, no defects and an atomically sharp Si/SiO_2 interface. The goal of SIMOX fabrication is to create a wafer as close to the ideal as possible.

When SIMOX was first being studied, the standard production technique [6] was to implant silicon with low energy (keV), high current oxygen beams with doses greater than 10^{18} O/cm^2. The high beam current heats the target to a temperature in excess of 300°C. After annealing for 2 to 6 h at elevated temperatures (>1150°C) a continuous stoichiometric silicon-oxide layer is formed. When a SIMOX sample is created in this fashion, it typically has many defects and excess oxide precipitates in the silicon film. It is also common to have regions of crystalline silicon in the SiO_2 layer. These degrade the quality of any electronic device built on this wafer.

Over the years, the procedures for making SIMOX samples gradually changed. It was found that the quality of the final product improves as the annealing temperature increases. Annealing temperatures as high as 1405°C (7°C less than the melting point of silicon) were studied [7,8]. The duration of the annealing was increased in an effort to give more time for the oxygen to form a continuous oxide layer [9]. It was also found that the final form (after annealing) of the SIMOX layer is very much a factor of the sample implant temperature, and so the sample is now heated externally. There exists an ideal temperature (~600°C) at which the damage in the as-implanted and annealed samples is at minimum [10,11]. Away from this ideal temperature, there are two processes which compromise the quality of the final product. First, as the temperature of the wafer is reduced there is an increase in the number of defects. These defects getter oxygen during the annealing process. Second, if the implant temperature is increased, larger oxide precipitates are formed which do not dissolve. These precipitates prevent dislocations from annealing.

It was also found that the ideal parameters for making SIMOX samples are different for high energy (MeV) and low energy (keV) implantations. For MeV implants, low implant temperatures, which are not attainable with the high current low energy ion implanters, result in better SIMOX samples [12-15]. When the implant temperature is low, the oxide precipitates are very small, and they dissolve quite readily during the anneal. Therefore these precipitates do not pin dislocations, and thus the annealing of the implantation induced damage is more effective.

The next major advance in SIMOX production was the discovery that, at lower oxygen doses ($< 10^{18}$ O/cm^2), there is a range of oxygen doses that will result in a thin continuous Buried OXide (BOX) layer after annealing at high temperatures [16]. If the dose is too low, the oxygen forms a network of oxide precipitates. If the dose is too high, the oxide layer is broader, not necessarily continuous, the silicon/oxide layer is not smooth and there are silicon islands in the oxide layer. BOX formation has two major advantages over SIMOX: (1) lower oxygen doses means there is less damage in the silicon film and (2) lower doses mean a higher throughput of samples and a reduced cost to the manufacturer.

The range of doses that will result in a BOX layer is a direct consequence of the distribution and size of the oxide precipitates in the as-implanted sample, as a function of dose. In the as-implanted sample there is preferential precipitation (HE precipitation) at the peak concentration of damage (d_O). There is also precipitation at the peak concentration of oxygen (R_p) which is the result of having a

supersaturated solution of oxygen in silicon (HO precipitation). A third region of precipitation was noted much deeper in the sample, and this precipitation process (ET precipitation) is thought to be a result of the interaction of the oxygen with the dense hot ion cascades which occur at the EOR (end-of-range) [17]. At lower oxygen doses and elevated implant temperatures, HE precipitation dominates over HO precipitation. At higher oxygen doses, HO precipitation dominates. Thus BOX layers are formed by finding the delicate balance between having enough oxygen for a stoichiometric oxide layer to form at d_O, and yet a low enough dose such that HE precipitation still dominates. For a given dose, the interplay between HO and HE precipitation is a function of the implant temperature, which affects the implantation-induced defects, and the ion energy, which determines the distance separating the region of maximum damage production and the region of maximum oxygen concentration. The difference in the properties of HO, HE and ET precipitation is the fundamental process governing BOX formation.

The latest efforts on BOX fabrication take advantage of the HE and ET preferential oxidation sites to create regions of large precipitates that will be the focus of the precipitate growth when the sample is annealed [18]. To use the HE precipitation effectively a clear understanding is needed of how the presence, or absence, of damage changes the oxidation in the silicon sample during the implantation, and how this affects the sample during the anneal.

The purpose of this thesis is to study the interaction of oxygen and crystalline damage within a silicon crystal so that the processes involved in making BOX devices can be better understood.

To study the interaction between damage and oxygen in silicon, damage is needed in the silicon crystal which is not a function of oxygen dose. It is for this reason that we choose to damage the silicon *before* implanting the oxygen. Thus it is easier to separate out the effects of the oxygen implanted damage and the pre-existing damage. The damage, or pre-damage, has to be stable at the implant temperature. The depth of the pre-damage must be adjustable, and it is preferable to have more than one type of defect to study. Standard samples are also studied to provide a basis for comparison. The standard samples are made by implanting oxygen into un-damaged silicon. With these conditions met, we can analyze and interpret the oxygen concentration profiles and the damage profiles as a function of (1) oxygen dose, (2) pre-damage type and (3) distance separating the pre-damage region from the oxygen implant. The distribution of the oxide precipitates in the as-implanted samples are inferred from the status of the annealed samples.

In an effort to more readily observe the differences in HO, HE and ET precipitation, we choose to implant oxygen at high energies (2.5 MeV). At higher energies there is a larger separation between the depth of the peak oxygen concentration and the depth of the peak oxygen damage concentration. Oxygen doses are chosen between 0.3×10^{17} to 3.0×10^{17} O/cm^2. This is lower than standard SIMOX. However, studying the samples as a function of dose reveals how a sample evolves during larger dose implants.

The pre-damage in the sample is created by implanting high energy ions. Silicon was chosen to produce the damage so that there would be no additional chemical interactions between the silicon, damaging ion and the implanted oxygen. To ensure that the damage is relatively stable during the oxygen implants, which are carried out at a sample temperature of 570°C, the defects in the implanted silicon were first annealed at 900°C for 1 h. At this time the remaining damage is mostly extended defects which are stable at temperatures less than 1000°C [19]. The depth of the pre-damage is chosen to be shallower than the peak oxygen concentration and is varied (by adjusting the energy of the silicon implant) between $0.8R_p$ to $0.95R_p$. Two kinds of silicon pre-damage are used, which is achieved by varying the silicon dose used to make the damage.

Cross-sectional Transmission Electron Microscopy (XTEM) and Rutherford Backscattering Spectrometry with Channeling (RBS/C) are used to study the damage. XTEM, Rutherford Backscattering Spectrometry (RBS), Elastic Recoil Detection (ERD) and Secondary Ion Mass Spectrometry (SIMS) are used to study the oxygen concentration profiles. The distribution of oxide precipitates and their relative sizes is inferred from these results.

The organization of the thesis is presented as follows: Chapter 1 is this introduction. Chapter 2 gives a review of the physical phenomena and theories which have been explored by others, but are necessary for the reader to know in order to follow the thesis herein. Chapter 3 gives a description of the experimental apparatus and analysis techniques as they pertain to this thesis, with the emphasis on the reliability and accuracy of the measured quantities. Chapter 4 is divided into three sections to make the understanding of the thesis easier. The first is a presentation of the experimental results and brief discussion of the damage produced by silicon in silicon, the second is a presentation of the experimental results and detailed discussions of range, damage and oxygen profiles for oxygen implanted into silicon, and the third is a presentation of the experimental results and detailed discussions of damage and oxygen profiles for oxygen implanted into pre-damaged silicon, which are compared with results from

section 2. Chapter 5 summarizes the models and conclusions, and discusses possible directions for further work. Chapter 6 presents the conclusions.

In this thesis, we hope to demonstrate many things. We will show that although the distribution of oxygen in an as-implanted sample is typically not affected by the differences in HE, HO and ET precipitation, the distribution of the oxide precipitates *is*, and these differences can result in a myriad of different results after the samples have been annealed. We will demonstrate that the damage in the silicon film is a result of excess silicon interstitials, and can be reduced by providing a diffusion barrier between the oxygen implant region and the silicon film. We will demonstrate that for BOX formation to be effective, the size of the precipitates at d_O must be large enough so that they will not dissolve during the early stages of the annealing. Models to describe the interaction between the oxygen, pre-damage and implantation induced damage will be presented. The proposed interaction of interstitials, vacancies and oxygen in the silicon film [14,20] during high energy oxygen implantations has been independently verified by our work.

Chapter 2
Review

In this chapter we will review the basic principles of crystal defects, ion implantation, ion implantation induced damage, annealing, oxygen in silicon, and finally the formation of SIMOX (Separation by IMplanted OXygen) and BOX (Buried OXide) structures, as they pertain to the work presented in this thesis. In most cases, only the general principles of each section will be discussed, and if further information is desired we refer the reader to the references quoted within the text or at the beginning of each section.

2-1 CRYSTAL DEFECTS [21,22]

Before we can describe the damage created by ion implantation, it is necessary to review some of the basic types of defects found in silicon crystals. In the following sections, only a few of the many types of crystal defects will be described.

2-1-1 Dislocations

The first group of defects to be discussed are dislocations. Dislocations are described as a region of crystal where there is a row or plane of atoms that are displaced from their perfect crystal positions. Outside of this region, the crystal is only negligibly different from a perfect crystal lattice. A general dislocation is described by a non-vanishing Burgers vector ($\vec{b}$), which is defined as follows (see figure 2-1). Consider a closed curve in a perfect crystal passing through a succession of lattice sites, defined by the addition of a series of Bravais lattice vectors. If there is a dislocation in the area within this curve, then the same addition of Bravais lattice vectors may not define a closed loop. The Burgers vector $\vec{b}$ is defined as the vector joining the starting and stopping position of the curve, and is independent of the initial path chosen.

Figure 2-2a illustrates one of the two simplest kinds of dislocations, the edge dislocation. An edge dislocation can be thought of as the termination line of an extra vertical half-plane of atoms crowded into the upper half of the crystal (as shown in the figure). The simple edge dislocation

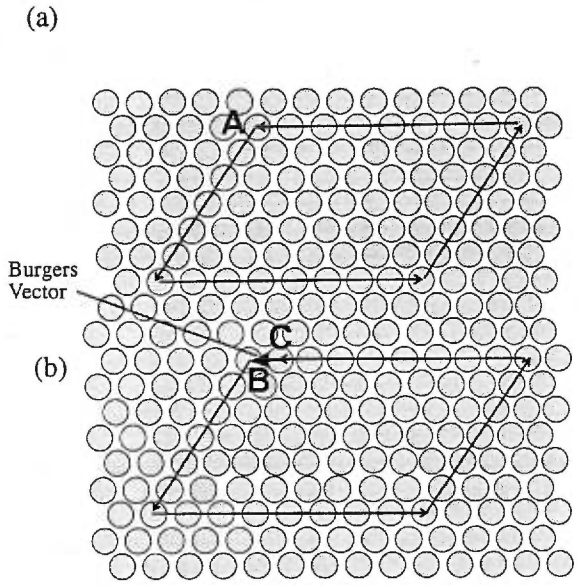

Figure 2-1. (a) A closed curve in a perfect crystal formed by the addition of Bravais lattice vectors (6 down, 8 right, 6 up, 8 left). (b) The same addition of Bravais lattice vectors as described in (a) (from 'B' to 'C') do not form a closed loop since there is a defect within. The Burgers vector is defined as the sum of these vectors. The dislocation that the second path surrounds is seen most readily by viewing the page at a very low angle.

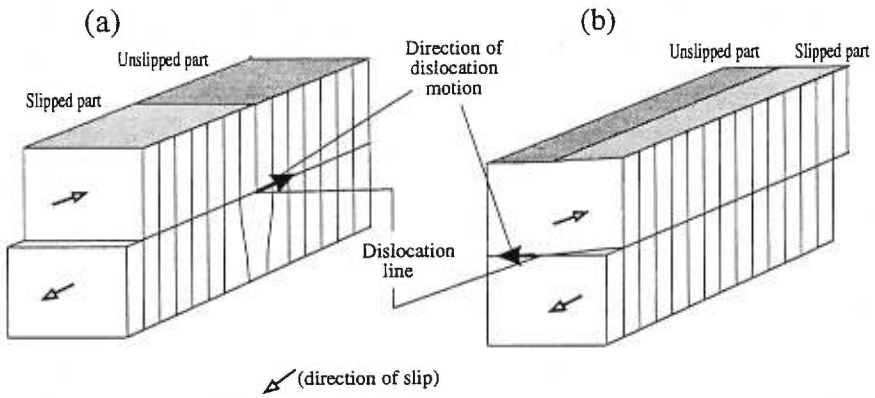

Figure 2-2. (a) Slip in a crystal via the motion of an *edge* dislocation. (b) Slip in a crystal via the motion of a *screw* dislocation.

extends indefinitely in the slip plane in a direction normal to the slip direction. The Burgers vector for an edge dislocation is perpendicular to the dislocation line.

Figure 2-2b illustrates the other one of the two simplest kinds of dislocations, the screw dislocation. A screw dislocation can be thought of as a crystal which has been cut partway through, to the dislocation line, where one half of the crystal has been displaced exactly one atomic spacing with respect to the other. A screw dislocation marks the boundary between slipped and unslipped parts of the crystal. The boundary parallels the slip direction, instead of lying perpendicular to it as it is for the edge dislocation. The Burgers vector for a screw dislocation is parallel to the dislocation line.

Another common dislocation in crystals is the stacking fault. A stacking fault, by definition, is a disorder in the stacking arrangement of the successive planes in a crystal. Consider the order in which successive {111} planes in a face centered cubic (*fcc*) crystal are stacked and let each of the three planes be uniquely defined by the letters `a`, `b` and `c`. The stacking order in a perfect *fcc* crystal, along the <111> axis, is:

....abcabcabc....

One example of a stacking fault occurs when one plane (`c`) is missing, *e.g.*:

....abcababcabc...

The Burgers vector for this dislocation is $\vec{b} = 1/3 <111>$. Another specific example of stacking faults, referred to as twinning, occurs when one section of the crystal becomes the mirror image of the other, for example:

....abcabcbacbabcabc.... .

Stacking faults are mediated by dislocations, in which the applied stress causes the coherent formation of dislocations in successive crystal planes. As each dislocation moves through the crystal, it leaves in its wake a lattice plane displaced by a non-Bravais lattice vector. Because the Burgers vector of a stacking fault is not an integer multiple of a Bravais lattice vector, stacking faults are sometimes referred to as partial dislocations.

Stacking faults, edge dislocations, screw dislocations, and other dislocations can merge together to form more complicated structures with a large variety of types and sizes. These defect structures are often referred to as simply 'extended' defects. Two simple examples of these are the dislocation

loop and the dislocation dipole, illustrated in figure 2-3. An extrinsic dislocation loop consists of an extra, bounded, plane of atoms in the crystal. The plane is typically described as being bounded by a loop of edge dislocations. An intrinsic dislocation loop is defined by the absence of a bounded section of a crystal plane. A dislocation dipole consists of two parallel edge dislocations whose Burgers vectors are the same magnitude, but anti-parallel.

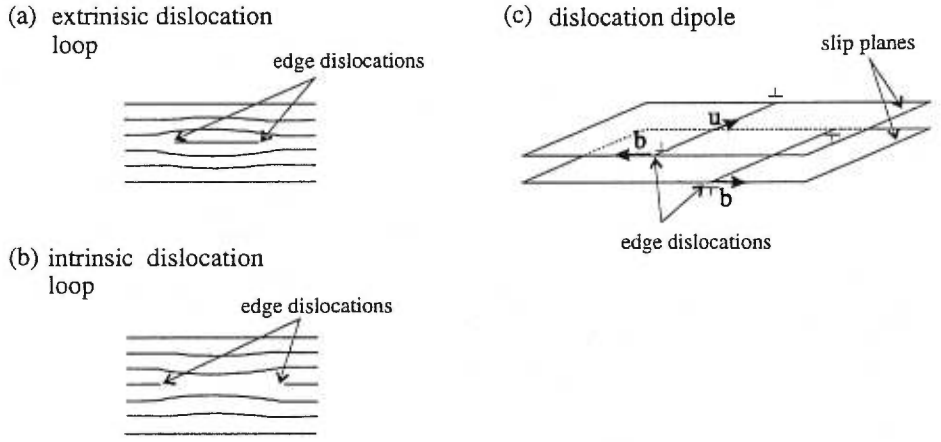

Figure 2-3. A schematic representation of (a) an extrinsic dislocation loop, (b) an intrinsic dislocation loop, and (c) a dislocation dipole. The Burgers vector is represented by $\vec{b}$. The vector along which the extra row of atoms terminates is indicated by $\vec{u}$. $\perp$ represents an extra row of atoms above the slip plane, and $\top$ represents an extra row of atoms below the slip plane.

2-1-2 Point Defects and Intermediate Defect Clusters

In addition to dislocations or twists in the crystalline planes, defects can also be attributed to individual atoms. A point defect occurs when one of the atoms in the crystal is missing (vacancy) or when there is an additional atom occupying a non-crystal position (interstitial). At room temperature, there will always exist both types of defects within the crystal. The equilibrium density of the defects is found by minimizing the Gibbs free energy which gives the result

$$n_j = N_j \exp\left(\frac{\epsilon_j}{k_B T}\right) \tag{2-1}$$

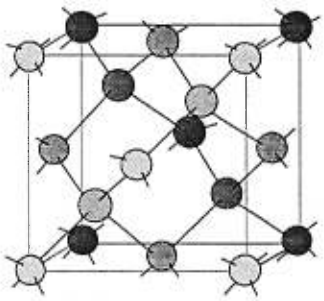

Figure 2-4. A diagram of a perfect silicon crystal.

where ϵ_j is the energy required to either remove an atom from the crystal lattice or add an atom to the crystal lattice and j indicates the type of defect. ϵ_j is usually of the order of several eV.

Some theoretical calculations predict that the most stable self-interstitial in silicon at room temperature is a split <100> interstitial [23], so called because the defect occurs in the <100> direction. A model of a perfect silicon crystal is shown in figure 2-4. The most common point defects are illustrated in figure 2-5.

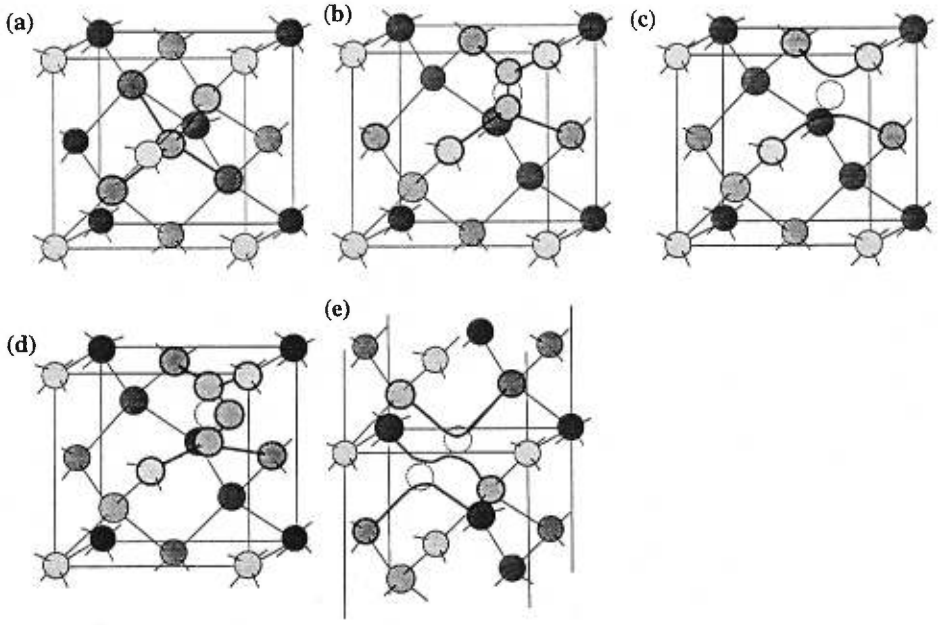

Figure 2-5. An illustration of (a) T_d interstitial (b) split <110> interstitial, (c) vacancy, (d) di-interstitial, and (e) di-vacancy, in the silicon crystal structure. The open circles represent the exact crystal positions of the displaced or missing atoms.

These simple defects are mobile, and during implantation and high temperature annealing, they aggregate to form more complex defect structures. It has been theorized that, if the dominant factor in the organization of point defects is the number of dangling or stretched bonds per defect absorbed, point defects will first condense into a row configuration elongated in <110>, as shown in figure 2-6 [23]. Note that the vacancy row configuration has extended or stretched bonds and the interstitial row configuration has dangling bonds.

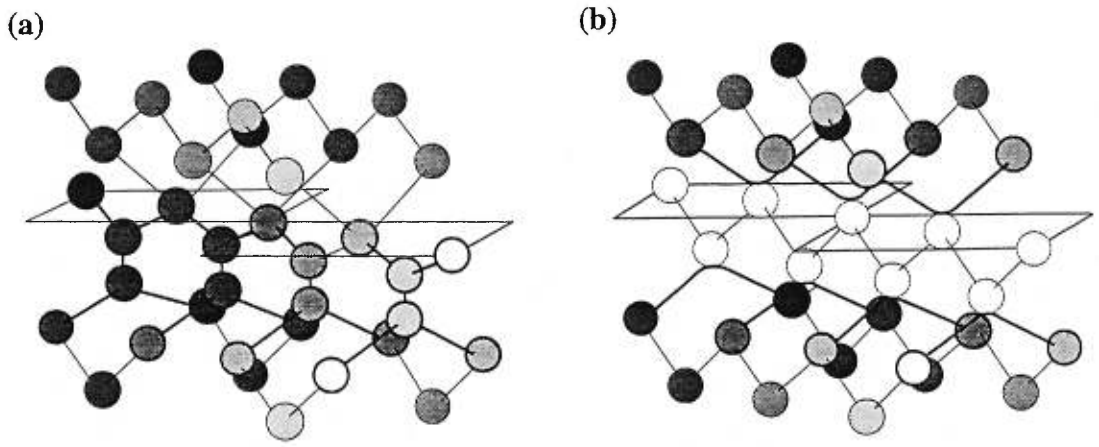

Figure 2-6. Row (a) interstitial and (b) vacancy defects elongated along the {110} chain. The open circles represent the positions of the missing atoms.

These row configurations are part of a class of defects called intermediate defect complexes (IDCs), so called because they subsequently evolve into dislocation and extended defects. Row configurations evolve into <100> elongated dislocation dipoles. This evolution is driven by the realignment of the atoms to reduce the number of dangling and extended bonds. Figure 2-7a illustrates the arrangement of atoms in a row multi-vacancy (projected onto the (110) plane). The missing rows are shown in the figure as Xs. After a shear stress in the $(\overline{1}11)$ plane in the <112> direction (figure 2-7b), the resulting configuration has no dangling bonds. This could easily be the precursor to a dislocation dipole. Figure 2-7c similarly illustrates two row split-interstitials projected onto the (110) plane. After the atoms re-arrange themselves to reduce the number of dangling bonds (figure 2-7d), the result is also a precursor to a dislocation dipole.

Simple defects can also aggregate together to form other kinds of dislocations. For example interstitials can condense into a single plane between two atomic planes, thus forming an extrinsic

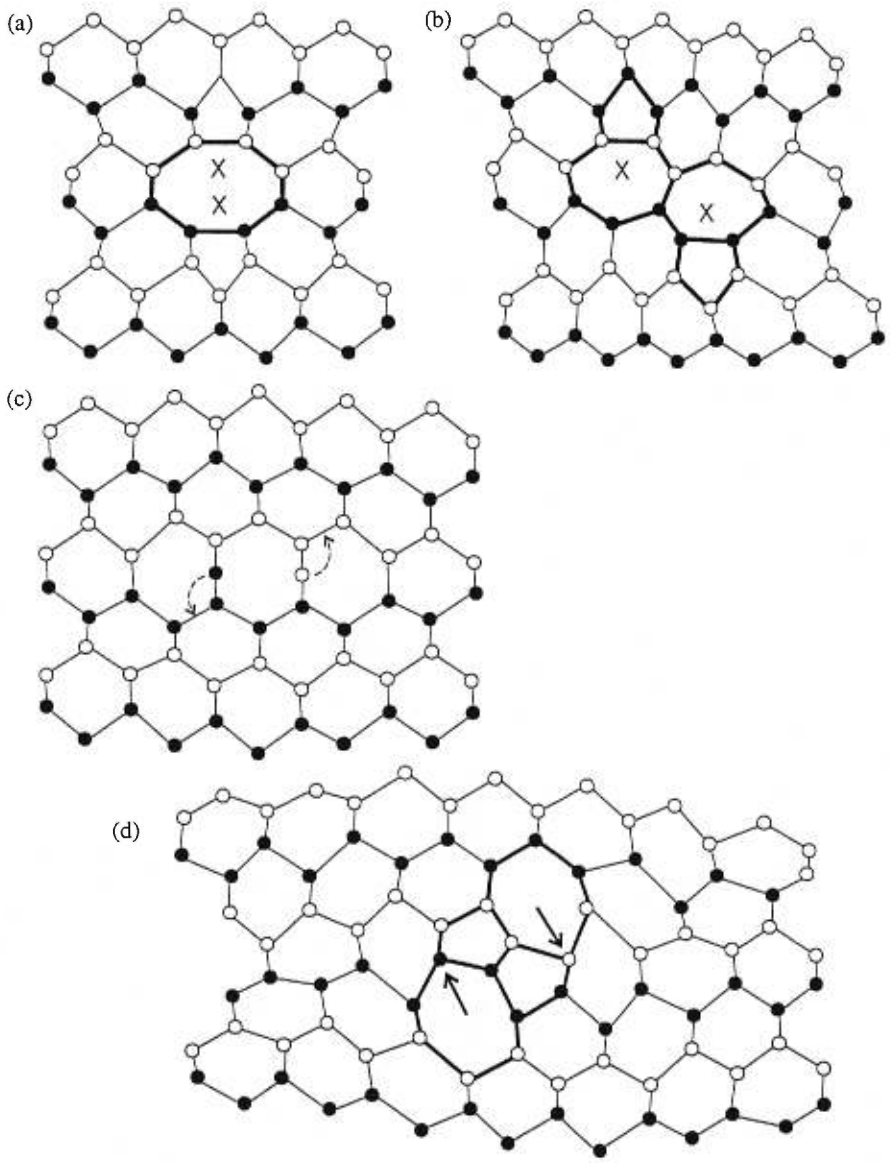

Figure 2-7. (a) The bonding (projected onto the (110) plane) surrounding a planar multi-vacancy [110] chain and (b) its resulting configuration following a shear. The positions of the missing rows are indicated by **X**s. (c) The bonding (projected onto the (110) plane) surrounding two chains of split-<110> interstitials and (d) the subsequent rebonding of the structure. The dotted arrows indicate the movements of the two extra rows of atoms, and the solid arrows indicate their subsequent positions.

dislocation loop. They can also aid in the growth or shrinkage of a dislocation, such as edge dislocations, which grow or shrink as they absorb or emit point defects at the point where the extra plane ends. In most instances, these interactions between point defects and dislocations occur during heat treatments.

2-2 ION IMPLANTATION

This section describes some of the basic properties of ion implantation, such as the transfer of energy from the ion to the target, the range of the ion in the target, and damage in the target resulting from the ion implantation. There is also a section which describes the specific properties of high energy (MeV) implantation, which can be significantly different than low energy implantation (keV).

2-2-1 Stopping Power [24]

As an energetic ion travels through a solid, as long as its energy is less than the nuclear coulomb barrier, it will lose energy by transferring some of its kinetic energy to the target nucleus via elastic collisions and to the target electrons by inelastic collisions. This energy loss continues until such time as the ion comes to rest. The total cross-section for energy loss is divided into two parts, nuclear and electronic stopping. This separation of the stopping mechanisms ignores possible correlations between the two processes, which is considered negligible when averaged over many collisions.

2-2-1-1 Nuclear Stopping

To study nuclear stopping (or nuclear energy loss), we assume that the target nucleus is not physically bound to its lattice position during the passage of the ion, and that the elastic recoil energy transferred to it may be treated by analyzing the kinetic scattering between two electronically screened charged particles.

Given two point particles, with masses and charges (M_1, M_2) and (Z_1, Z_2), in an elastic collision (where kinetic energy and momentum are conserved), the transfer of energy to the target nucleus can be calculated. It is

$$T = \frac{4E_0 M_1 M_2}{(M_1 + M_2)^2} \sin^2\left(\frac{\Theta}{2}\right) \tag{2-2}$$

where E_0 is the initial energy, and Θ is the scattering angle in the center-of-mass coordinates.

The nuclear stopping cross-section $S_n(E)$ is defined as the energy transferred to the target ion, integrated over all possible impact parameters p.

$$S_n(E) = 2\pi\gamma E_0 \int_0^{p_{max}} \sin^2 \tfrac{\Theta}{2}\, p\, dp \qquad (2\text{–}3)$$

$$\gamma \equiv 4M_1M_2/(M_1 + M_2)^2$$

where p_{max} is the sum of the two atomic radii, beyond which the interatomic potential, $V(r)$, and the kinetic energy, T, are zero.

The energy lost via nuclear collisions by the ion per unit path length (dE/dx) is related to the nuclear stopping cross-section $S_n(E)$ by the relation

$$\frac{dE}{dx} = NS_n(E) \qquad (2\text{–}4)$$

where N is the atomic density of the target.

2-2-1-2 Electronic Stopping

The electronic cross-section is difficult to define in absolute terms since there are many possible ways that the ion can lose energy to the electrons, namely:

1) Direct kinetic energy transfers to target electrons, mainly due to electron-electron collisions.
2) Excitation or ionization of target atoms.
3) Excitation of band- or conduction-electrons, i.e. weakly bound or non-localized target electrons.
4) Excitation, ionization or electron-capture of the projectile itself.

For light ions the stopping power (or energy loss) is a function of the electron density ρ_e of the target. The stopping power is relatively constant when the projectile is much faster than the target electrons. It then falls sharply when the ion velocity becomes equal to the Fermi velocity (v_F) of a free electron gas with density ρ_e.

In the case of low-velocity heavy ions, the majority of the target electrons are travelling faster than the projectile, and the collisions with the ion are mostly without direct energy loss to electron-electron collisions. The energy lost by the projectile is caused by the ionization of the target atom. The stopping power for these ions is proportional to v in metals and $v^{0.7}$ in semiconductors. For high-velocity ions, the stopping power is calculated by scaling the appropriate proton stopping powers.

The stopping powers (nuclear and electronic) used in this work are the theoretical values as calculated by Ziegler [24] and are considered to be accurate within 10% of experimental values.

2-2-2 Range and Straggling of Ions

As an ion travels through a solid, it loses momentum via the energy losses described above. However, with each binary collision between the ion and the target nucleus, the direction of motion of the ion is altered, and hence the final depth of the ion cannot be predetermined. The probability curve of the ion stopping at a given depth is usually represented by a Gaussian curve, with the peak position defining the range of the projectile (R_p), and sigma (σ) defining the range straggle (ΔR_p).

Typically, the implanted profile is simulated by TRIM (TRansport of Ions in Matter), a Monte Carlo program which follows the trajectory of each ion as it traverses through the target material. The ion is assumed to change direction and lose energy in discrete amounts as a result of binary nuclear collisions, and to move in straight free flight paths while losing energy continuously from electronic interactions between collisions. It is assumed that the target material is amorphous. TRIM calculations do not include diffusion of the implanted ions within the target, changes in the dE/dx due to the inclusion of the implanted species, removal of the surface due to sputtered material, and changes in the density due to phase changes, such as amorphization, during the implantation. In spite of these inherent difficulties, TRIM typically gives reasonable results for the range and straggling of ions in solids.

Many researchers have studied the range of oxygen in silicon, as well as it's longitudinal and lateral spread, and compared them to TRIM and other Monte Carlo simulations. At oxygen energies of less than 2 MeV, the simulations agree fairly well with the experimental results. However, at higher energies, TRIM typically underestimates the range (see Table 2-I).

Kappert *et al.* [27] investigated the range and damage profiles for 2–20 MeV oxygen ions in a silicon target, with doses up to 10^{18} O/cm^2. The comparison between the experimental results and the computer calculations were consistent within experimental limits for the measurement of the range and damage peaks. However, the experimental results for the FWHM of the oxygen distribution are systematically larger, up to 13% larger than the calculated values. Fahrner *et al.* [28] investigated boron and oxygen depth and damage ranges with implantation energies of 58 MeV and 65 MeV. They

TABLE 2-I

Experimental and theoretical range and straggling depths for oxygen into silicon. The depth of the peak concentration is denoted by R_p. ΔR_p is the sigma of a Gaussian fit of the depth distribution. Because the concentrations are often skewed Gaussians, the results can be fitted to two Gaussians for each side of the peak, resulting in two σ's, ΔR_1 and ΔR_2. The FWHM is denoted by $R_{1/2}$. $\Delta R_\perp$ is the transverse straggling of the implanted ions. The damage depth range d_O is also shown.

E (MeV)	R_p (μm)	ΔR_p (μm)	$R_{1/2}$ (μm)	ΔR_1 (μm)	ΔR_2 (μm)	$\Delta R_\perp$ (μm)	d_O (μm)	Δd_O (μm)	
0.6	1.00±.02	0.11±.01	—	0.12	0.10	0.21±.01	—	—	exp†
1.0	1.40±.02	0.16±.01	—	0.17	0.14	0.23±.01	—	—	exp†
	1.52±.05	0.17	—	—	—	—	—	—	exp[1]
	1.39	—	—	—	—	—	—	—	TR[1]
1.5	1.77±.02	0.16±.01	—	0.18	0.14	0.26±.01	—	—	exp†
2.0	2.10±.02	0.17±.01	—	0.19	0.15	0.27±.01	—	—	exp†
	2.16	—	0.32	—	—	—	2.05	0.43	exp‡
	2.17	—	0.34	—	—	—	2.05	0.52	MC‡
	2.16±0.1	—	0.32±.04	0.18	0.14	—	2.05	—	exp*
	2.17	0.20	0.34	0.21	0.13	—	2.05	—	MC*
2.5	2.55±.05	0.13	—	—	—	—	2.33	—	exp[2]
	2.38	0.10	—	—	—	—	2.25	—	TR[2]
3.0	2.90±0.1	—	0.36±.04	0.21	0.15	—	2.75	—	exp*
	2.78	0.21	0.32	0.18	0.14	—	2.66	—	MC*
4.0	3.41±0.1	—	0.39±.04	—	—	—	3.30	—	exp*
	3.47	0.21	0.35	0.22	0.13	—	3.35	—	MC*
5.0	3.97±0.1	—	0.39±.04	0.22	0.17	—	3.90	—	exp*
6.0	4.46±0.1	—	0.40±.04	0.22	0.18	—	4.40	—	exp*
	4.60	0.22	0.36	0.22	0.14	—	4.52	—	MC*
	4.51±0.1	0.24	—	—	—	—	—	—	exp[1]
	4.26	—	—	—	—	—	—	—	TR[1]
8.0	—	—	—	—	—	—	5.75	—	exp*
	5.88	0.22	0.35	0.23	0.12	—	5.76	—	MC*
12.0	—	—	—	—	—	—	8.10	—	exp*
	8.30	0.22	0.38	0.22	0.16	—	8.17	—	MC*
20.0	13.17±0.1	—	0.46±.04	0.23	0.23	—	13.20	—	exp*
	13.22	0.22	0.40	0.22	0.18	—	13.12	—	MC*
65.0	—	—	—	—	—	—	49.8	1.50	exp‡
	49.9	—	0.40	—	—	—	49.8	0.65	MC‡

†Grob *et al.*[25,26]
*Kappert *et al.* [27]
‡Fahrner *et al.* [28]
[1]Touhouche *et al.* [29]

exp – experimental results
MC – Monte Carlo
TR – TRIM
[2] Bultena [this work]

found that the theoretical values for straggling of ion damage (ΔR_d) in the 100 MeV range is about two thirds too small compared to the experimental value. Their results for oxygen implants are given in Table 2-I.

Grob *et al.* [26] studied the lateral spread of oxygen ions implanted in silicon with energies ranging from 0.6 to 2.0 MeV. For each energy, two samples were implanted, the first at normal incidence ($\theta = 0$) and the second at an angle $\theta = 60°$ relative to the surface normal. The first implant gave the value of the mean projected range R_p and the longitudinal straggling ΔR_p. The second implant at 60° is used to calculate the transverse straggling from the standard deviation (σ^2) of the oxygen distribution using the following formula,

$$\sigma^2 = \Delta R_p^2 \cos^2 60 + \Delta R_\perp^2 \sin^2 60. \qquad (2\text{–}5)$$

The results are summarized in Table 2-I The experimentally measured projected range (R_p) is slightly higher than those calculated with TRIM over the range of energies studied. The longitudinal straggling results (ΔR_p) agrees well with TRIM and saturates at high energies. In a first approximation, the ratio $\Delta R_\perp / \Delta R_p$ is a constant (~ 1.6) within the energy range studied, indicating a trend to saturation of ion spread in both directions.

2-2-3 Implantation Damage [30,31]

As the projectile ion slows down during implantation, the crystal atoms gain energy from the nuclear collisions. If the energy transferred is greater than the displacement energy ϵ_d (15 eV for a silicon target [32,33]) the target atom will be knocked out of the crystal position creating a Frenkel pair (interstitial plus vacancy). Each recoiled target atom will in turn act as a projectile, losing energy via electronic and nuclear collisions, causing even more atoms to be knocked out of their crystal sites. Each projectile can create many new "projectiles" via nuclear collisions. The growing avalanche of dynamic recoils is known as a linear cascade. As the recoils slow down, such that they can no longer generate defect pairs, they behave similarly to very low energy incident projectiles and dissipate their residual energy to their neighbours via phonon excitation and lattice vibrations. This results in a large thermal spike with a time scale in the order of $10^{-14} - 10^{-13}$ s.

In the linear cascade region, where collisions are spatially isolated and of low density (with respect to the atomic density), the total number of point defect pairs (N_d^*) generated by each projectile of energy E_0, averaged over many events, can by approximated by the modified Kinchin Pease formula [30].

$$N_d^* = \frac{0.42 E_0 \nu(E_0)}{\epsilon_d} \tag{2-6}$$

where $\nu(E_0)$ is the fraction of the projectile energy dissipated in nuclear collisions, and ϵ_d is the displacement energy.

In the cascade volume, the incident ion and subsequent recoil atoms impart momentum to the scattered atoms, but not to the vacancies left behind. Hence the vacancies are concentrated near the centre of the cascade while the interstitials are concentrated towards the periphery of the core in all three coordinates (x, y, z). Sputtering of the target material can be described as the backward flux of dynamic recoil interstitials.

If the nuclear energy losses of a heavy ion is greater than ϵ_d/d (d is the inter-atomic spacing), then displacement events occur at every inter-atomic spacing. This creates a dynamic displacement spike with a very rich vacancy core (depleted zone) surrounded by a thin mantle of interstitial rich substrate, i.e., a pressurized shell surrounding a cavity. Cascades which satisfy these conditions are called displacement cascades. When silicon is implanted in silicon, displacement cascades occur only when the ion energy $\sim$ 1 keV.

Whatever the target material, each projectile creates a highly damaged region, with vacancies and interstitials unevenly distributed, which is thermodynamically hot due to the phonon and lattice excitations, as described previously. The mobility of both defect species (vacancies and interstitials) will be high while the cascade temperature is large. The damage created in the crystal is determined by the distribution of defect pairs, and their ability to move together to recombine.

The damage, defined as the total number of point defect pairs, is typically interpreted in terms of the cascade damage density (F_D) which is defined as $F_D = 0.35 N_d^*/N_v$, where N_d^* is the total number of generated defect pairs, and $N_v/0.35$ is the number of atoms in the cascade volume [34]. The damage cascade volume is approximated as an ellipse of revolution having transverse and longitudinal straggle ($\Delta R_\perp$, ΔR_p) as the minor and major axes, respectively. The factor 0.35 is obtained since, if a Gaussian distribution is assumed, about 35% of the damage will be contained in this ellipsoid.

For low temperature (50K) low dose ($\sim 10^{13}/\text{cm}^2$) implantations into silicon, the damage density shows a positive correlation with the deposited energy density, in the form of $F_D \propto \overline{E}^{1.6}$ [34]. At room temperature there is more dynamic annealing (Frenkel pair recombination) due to the increase in temperature. Consequently F_D is dramatically reduced.

Immediately after the cascade has been created, the defects in the cascade begin to re-form (quench) into either amorphous regions, defect structures, or even re-grown crystal structures. The relaxation process is influenced by the substrate material (metal vs semi-conductor for example), crystal structure, temperature of the implant, orientation of the crystal surface, the impurity levels (if any), and the energy of the incident ion.

During the quenching process, as described in a review article by Carter and Grant [30], the interstitial distribution will tend to drive interstitials both inwards along the concentration gradient to the vacancy rich core, and outwards into the surrounding crystal. They may then recombine with vacancies, interact with dopants, or combine to form more stable complexes such as dislocation loops. Even at low substrate temperatures, interstitial mobility is generally high. The vacancy loss process may occur both by the recombination with free interstitials in the overall cascade volume or via vacancy escape into the surrounding crystal. In silicon, vacancies become mobile around 100K, and can be trapped by oxygen impurities (A-centres), by dopant atoms (E-centres), or combine to form di-vacancies. These point defects then condense to form IDCs, which is the first step of amorphization. If vacancy loss cannot occur, recrystallization cannot occur.

There are two models to describe the formation of amorphous regions. The first is the heterogeneous model, which assumes that the amorphous zone is generated directly by the incident ions. At low temperatures, each incident ion in silicon creates one amorphous zone. The difference in density between the amorphous zones and the surrounding crystal gives rise to a strain within the crystal that is linearly dependent upon the total volume of amorphous material. Cellini *et al.* [35] studied the relation between the strain and the total number of defects in silicon and found that the proportionality constant between the two was consistent with the heterogeneous model. As the number of amorphous zones increases with increasing ion dose, these regions gradually overlap until a completely amorphous layer is formed. If the temperature is too high, the amorphous zones are expected to shrink, and may anneal prior to the zone overlap if the flux is too low. Amorphous zones in silicon formed by ion implantation are unstable at room temperature, which suggests that their formation is controlled by

the existence of a temperature dependent critical size, which has an equal opportunity of shrinking or growing. Below this critical size, the phase is unstable. However, if the radiation flux is high enough, amorphous zones will merge and then grow.

In the homogenous model, it is the change in the average defect density which increases, until the damaged crystal becomes metastable. Since amorphous semiconductors are typically less dense than their crystalline counterparts, a large accumulation of vacancies, which changes the density, will result in an amorphous phase. In silicon, the ratio of the amorphous to crystalline density is 0.983 [36]. Once a critical vacancy density is accumulated locally an amorphous phase forms, which then grows at the expense of the crystalline phase. The free energy of the amorphous phase is 0.1 eV/atom higher than the crystalline phase. This suggests that a point defect concentration of 2% is sufficient for amorphization, if one assumes a defect energy formation of $\sim$ 5 eV. In this model, the defect concentration during irradiation will also depend on a balance between defect creation and annihilation rates. The increasing difficulty of amorphizing semiconductors with increasing ambient temperature can be understood because the vacancies flow out of the center of the cascade region with greater ease as the substrate temperature increases. Thus, at higher implant temperatures, the defect density is reduced and the interstitials and vacancies cluster to form extended defects.

In general, amorphization is expected to result from a combination of heterogeneous and homogeneous processes, with the dominant process depending on ion species and energy.

2-2-4 High Energy Implantation Damage

The damage profiles for high energy implantation are different from the damage profiles for low energy implantation, mostly due to the fact that MeV implanted ions lose most of their kinetic energy via electronic interactions within the target. The electronic energy loss does not necessarily create damage. However, it can affect the mobility of point defects as well as enhance the cross section for nuclear collisions. Figure 2-8 shows the nuclear and electronic energy losses, as a function of energy and depth, of oxygen ions through a silicon target. As the ion slows down, the energy loss to the target electrons diminishes, while the energy loss to the target nuclei increases, until at very low energies, the energy loss is dominated by nuclear interactions. It is primarily these nuclear interactions that cause crystal damage, since most of the energy transferred is to the target atoms rather than the electrons. The ion implantation damage occurs near the final resting place of the ion, and is generally referred to as the

peak damage. The damage that occurs past this point is called the end-of-range (EOR) damage. For medium and heavy atomic mass projectiles ($M > 20$ amu), nuclear energy loss dominates for energies in the range from zero to tens or hundreds of keV, whilst for lighter ions, nuclear collisions dominates only in the low keV regime.

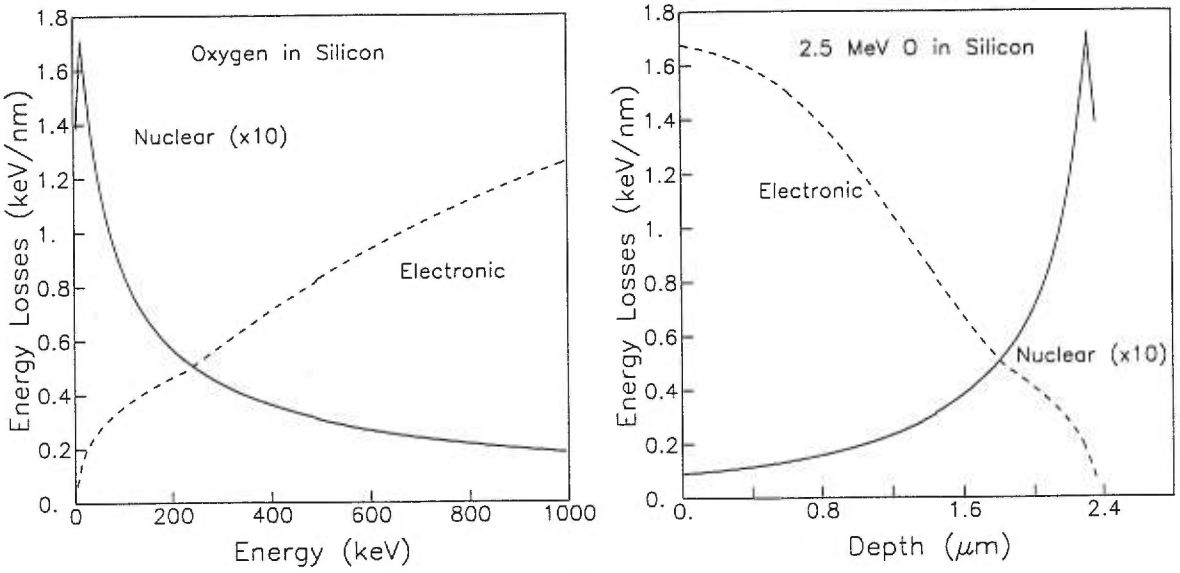

Figure 2-8. (a) A plot of the Electronic and Nuclear Stopping powers for oxygen ions projected into a silicon target. (b) Nuclear and electronic energy losses as a function of depth for 2.5 MeV O^+in silicon.

During high energy implantations, more energy is transferred to the knock-on atoms via nuclear collisions than in keV implantation. These knock-on atoms can travel large distances before they, too, lose energy via nuclear collisions. Hence high energy cascades are expected to be strongly inhomogeneous since they are composed of spatially separated sub-cascades. Consequently, the defect formation will be a heterogeneous process. This high transfer of energy to the knock-on collisions in a preferred direction (the ion beam direction), creates a large separation of the vacancies and interstitials. The correlation between damage and excess defect production, which is defined as the difference between interstitials and vacancies as a function of depth, strongly supports the hypothesis that damage growth and its morphology are to a large extent controlled by the mechanism of Frenkel-pair separation [37]. Vacancy-type defects are found at depth just prior to the EOR, and interstitial-type defects just after the EOR.

In addition to the above, the lateral and transverse straggle for MeV ions is much larger than for keV ions, and hence the density of the total number of defects created per unit dose is significantly reduced. For example, although an increase in the ion energy from 150 keV to 2 MeV oxygen involves an increase in the energy E_ν deposited in nuclear collisions by a factor of 1.9 [25] the average density (E_d) of the energy deposited by a single projectile is considerably lower for 2 MeV implants. The decrease in E_d (E_ν / unit volume) is given by [26]

$$\frac{E_d\,(2\text{ MeV})}{E_d\,(150\text{ keV})} = 0.18. \qquad (2-7)$$

At room temperature the recombination of Frenkel pairs and clustering rates of point defects depend on the ion species used, which suggests that the nucleation of stable defect clusters during high energy implantation is related to the primary defect density E_d [38].

All these factors, (large electronic energy losses, increased depth of maximum damage, large spatial separation of sub-cascades, large separation of vacancies and interstitials, and decreased density of Frenkel pairs created per unit volume per ion), contribute to the effective differences in the ion induced damage morphology between MeV and keV implantation.

2-2-4-1 Damage as a Function of Depth

The damage density, as well as the defect types, of MeV ion-implanted silicon varies as a function of depth, and is significantly different in character between the sub-surface and the EOR region.

Traditional linear cascade theory predicts very little damage to the crystal in the near surface region for MeV implanted silicon. This is not always consistent with experimental results. It has been suggested that the defects formed in the subsurface region of the crystal are due to their radiation-stimulated migration from the bulk to the surface [39]. It has also been postulated that in the subsurface region, the relaxation of the electronic excitations of the silicon atoms located off lattice sites (interstitials, grain boundaries, etc) proceeds much more effectively than on atoms occupying regular positions. This leads to selective heating of the defects, giving them a greater mobility. Thus, the greater the ion energy, the greater the mobility of defect forming atoms in the subsurface region, and hence, the probability that defects recombine during the process of migration is increased. During high energy implantation we observe two competing processes, a) defect formation in the subsurface

region due to the migration of defects from the bulk outwards and, b) effective annealing of defects due to the increased mobility of defect forming atoms near the surface.

For a liquid nitrogen (LN) temperature implant of 1.25 MeV Si, discrete amorphous regions are observed throughout the silicon matrix [40]. The density of these amorphous pockets increases with increasing depth, although the average sizes are constant throughout the sample. This suggests that the cluster size is determined primarily by the kinetics of cluster growth during the LN implantation. These results are not entirely inconsistent with the linear cascade model. However, when high energy ions are implanted into silicon at room temperature, the damage near the surface region saturates, with respect to the ion dose, at a relatively low level [37,39,41,42]. At this temperature, and in this depth region, the relaxation of the cascade volume is sufficiently rapid to allow out-diffusion of defects from the cascade or sub-cascade volume on a time scale similar to the quench rate. As a consequence, knock-on cascades are ineffectual at room temperature in nucleating damage during their quench. Extended defect nucleation and growth are suppressed and no amorphous clusters occur before the EOR. The damage in the surface region anneals out at 200°C, which is the temperature where di-vacancies become mobile. Therefore, it is believed that the defects that do exist in the surface region consist of small isolated defect complexes, such as di-vacancy and di-interstitial defects. Di-vacancies are thought to be the predominate defect within the near surface region of 1.25 MeV Si implanted samples [38]. Under near-room temperature conditions, these defects have an extremely long half-life ($\approx 10^5$ s) [43].

Holland *et al.* [37] proposed a homogenous damage growth model to explain the saturation of damage in the near surface region. It assumes that the point defects created along the tracks of different ions are sufficiently long lived to become uniformly distributed within the irradiated volume. It also assumes only small defect clusters form, as mentioned above. Thus,

$$\begin{aligned}
\frac{dn_i}{dt} &= G - k_1 n_i n_v - k_2 n_i n_0^v - 2k_4 n_i^2 + k_5 n_v n_0^i \\
\frac{dn_v}{dt} &= G - k_1 n_i n_v + k_2 n_i n_0^v - 2k_3 n_v - k_5 n_v n_0^i \\
\frac{dn_0^v}{dt} &= k_3 n_v^2 - k_2 n_i n_0^v \\
\frac{dn_0^i}{dt} &= k_4 n_i^2 - k_5 n_v n_0^i
\end{aligned} \tag{2-8}$$

where G is the generation rate of the Frenkel pairs, n_i, n_v are the number of interstitials and vacancies respectively, n_0^i, n_0^v are the number of di-interstitials and di-vacancies, and k is the recombination rate. If one assumes a steady state ($dn/dt = 0$), then the defect saturation level would be a function of the generation rate ($\sim \sqrt{G}$). The experimental results show a $1/3$ power dependence on the dose rate rather than the predicted $1/2$ power dependence. This model is rather simplistic in that there is no depth dependence for the defect generation rate nor any beam heating effects due to increased beam intensity. Therefore this level of agreement between the experiment and the model indicates the basic validity of the theory behind the model.

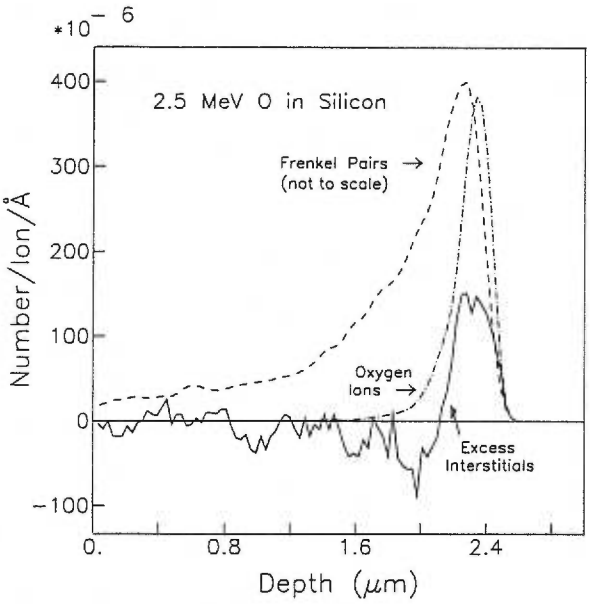

Figure 2-9. TRIM calculation of ion distribution, Frenkel pair distribution (not to scale) and the excess interstitial distribution (not to scale).

The damage at the EOR behaves differently from that created in the surface region because: a) there is the addition of mass from the implanted ion itself, b) there is a much higher density of defects created in this region, and c) there is a large separation between the interstitials and vacancies. Figure 2-9 is a graph of the ion distribution, the Frenkel pair distribution, and the excess interstitial distribution, defined as $I(x)-V(x)$ where $I(x)$ and $V(x)$ are the interstitial and vacancy concentrations at depth x, respectively, for 2.5 MeV oxygen implanted silicon. As can be seen from this figure, the interstitials and vacancies are well separated, with the excess interstitials located after the EOR, and the excess vacancies immediately before the EOR. The damage morphology in the EOR is believed to be

controlled by the competition between the recombination of Frenkel pairs, and the clustering of point defects from different cascades. As the cascades overlap, large defect complexes form, with the ability to remain stable, or to grow, during room temperature implantation [38]. The excess interstitials form extended defects, such as dislocation loops, which can be a biased sink for more interstitials, leaving an excess of vacancies. These vacancies then cluster and eventually form amorphous regions. The final EOR structure of a room temperature implant is typified by an amorphous layer followed by a region with a high density of extrinsic dislocations.

2-2-4-2 Damage as a Function of Temperature

Since the temperature of the sample during implantation affects the diffusivity of vacancies and interstitials, and the since the defect morphology is based upon the ability, or lack thereof, of Frenkel pairs to recombine, it can be easily seen that the final defect structure is dependent upon the implant temperature. For example, the fraction of primary defects that recombine during a 1 MeV oxygen implantation into silicon, at room temperature, is 98% when compared to an equivalent implantation at LN temperature [38,44].

When silicon is implanted at LN temperature, the damage structure for O and Si increases monotonically as a function of depth, until the maximum is reached at the EOR. The damage profiles are consistent with the linear cascade theory, where the damage is produced solely by nuclear collisions [38]. Similarly, the EOR damage (s) measured by optical reflectivity, for 2 MeV silicon into -150°C silicon at low doses, is directly proportional to the total dose ϕ [41], which again is as expected from simple collision theory.

The decreasing ratio s/ϕ with increasing target temperature T_i is caused by an enhanced recombination of vacancies and interstitials within each individual damage zone, due in part to a higher defect mobility. The probability of the point defects forming stable clusters is expected to decrease progressively with increasing T_i. The decrease of damage efficiency with increasing temperature, T, can be described by [45]

$$\frac{s}{\phi} = A - B \exp \frac{E}{k_B T} \tag{2-9}$$

where A and B are constants, E is the energy deposited into the cascade, and k_B is the Boltzmann constant.

Schultz [46] studied the effect of temperature (LN to 127°C) and dose rate (10nA to 1μA) of 1 MeV implantation of silicon into silicon, with a total dose of $1 \times 10^{15}/\text{cm}^2$. As was expected, there was a decrease in the amount of damage created as the implantation temperature was increased. Below a certain implant temperature T_l, an amorphous layer is formed at the EOR. At temperatures above T_l, the level of damage at the EOR decreases as T increases until, at a temperature T_h, a minimum damage level is attained. With the lowest dose rate studied (10 nA/cm^2) the critical temperature for amorphization was 17°C and the critical temperature for the minimum damage production was 47°C, a temperature range of only 30°C. For different dose rates the results are similar, with the exception that both T_l and T_h are offset by a fixed amount. The maximum change in damage as a function of temperature occurs around room temperature. From this, it was concluded that the temperature and dose rate during the implantation are *very* important experimental parameters.

2-2-4-3 Damage as a Function of Dose

As one would expect, the final damage in the silicon crystal is dependent on the dose of the implanted ion. However, in spite of the fact that the total number of Frenkel pairs created is a linear function of dose, certainly the final number of displaced ions is not. At very low doses ($\sim 10^{12}/\text{cm}^2$), the individual ion tracks are well separated, and the recombination of Frenkel pairs is confined to each individual cascade volume. At higher doses ($\sim 10^{13}$ /cm^2 for 2 MeV Si in silicon) the mean distance between different ion tracks is less than 2 nm, and thus the recombination of point defects is more efficient because defects recombine from different cascades.

A dramatic illustration of this effect is the behaviour of 16 MeV nitrogen in silicon implanted at room temperature [39]. The damage increases throughout the depth (excluding the surface region which has no measurable damage) as the dose is increased from 5×10^{14} to $5 \times 10^{15}/\text{cm}^2$, but subsequently, at higher doses (up to 1×10^{16}) the damage decreases rapidly. In other words, large irradiation doses result in annealing rather than defect production.

At low doses ($3 - 8 \times 10^{14}$ cm^2) of 1 MeV silicon, the total damage increases sublinearly with increasing dose, while at higher doses ($0.8 - 2 \times 10^{15}$ /cm^2) the damage shows a linear relation between the dose and damage [47]. The damage morphologies are different in these two dose regimes. Point defects (primarily planar tetra-vacancies and silicon di-interstitials [48]), are formed for the low dose implants, while complex defects dominate in the higher dose regimes. Below the amorphization

level, the width of the heavily damaged region increases as the implant dose increases, and both small amorphous pockets as well as small defect clusters are generated [47]. The critical dose for transition from crystalline to amorphous can be estimated to be $2 \times 10^{15}/\text{cm}^2$ for 1 MeV silicon at room temperature [41].

2-2-4-4 Defect Engineering

Because the defect production is very much a function of the implant conditions (temperature, dose, dose rate, etc.), it is sometimes possible to 'design' the final defect structure. In addition to controlling the implant temperature and dose, it is also possible to anneal the damage within the sample by further ion implantation. Battaglia *et al.* [49] calculated the annealing properties of doped damaged silicon, where the damage was created with 150 keV Au, and the annealing was done with 600 keV Kr. With an implantation temperature of 125°C, which is insufficient to provide thermal annealing, a total dose of 3×10^{15} Kr/cm^2 was sufficient to completely remove all the damage created by the Au implant in the p-doped silicon. At lower temperatures, the damage in the region of the Au implant increased with increasing Kr dose. It was postulated that the regrowth of the pre-existing damage is related to the selective heating of the displaced atoms via the electronic energy losses from the Kr atoms.

2-3 ANNEALING

A crystal with dislocation loops, stacking faults, or Frenkel pairs is not an equilibrium structure because the defects carry with them strain energy, core energy, and stacking fault energy. Thermal annealing speeds up the process of crystal repair to reduce the total energy. Dislocations move with relative ease in a perfect crystal. However if they encounter interstitials, impurities, or other dislocations crossing their paths, the work required to move them can increase considerably [50]. This is referred to as "pinning" a dislocation. On the other hand, if the defect and impurity density is low then nearly all the vacancies formed during the implantation will recombine with a foreign or a silicon interstitial during annealing, if $T > 800°$ [51].

Calcagno *et al.* [52] studied damage removal in silicon (implanted with 4×10^{15} Ge/cm^2 at 600 keV, room temperature) using rapid thermal annealing with various temperature and times. The data indicate an exponential dependence of the damage removal on the annealing time:

$$n(t) = n_0 \exp(-t/\tau) \tag{2-10}$$

where τ is the defect lifetime. A plot of the defect lifetime versus $1/k_BT$ (T = temperature of the anneal) gives the activation energy of the defect removal as 4.3 ± 0.2 eV. The activation energy is near the activation energy of self-diffusion. Thus the annealing of extended defects suggests the formation and migration of silicon self-interstitials.

Thermal annealing does not guarantee a perfect crystal because the possible aggregation of defects may form some sort of extended defect. For example, the precipitation of lattice vacancies into penny-shaped vacancy plates may be followed by collapse of the plates and the formation of dislocation rings that grow with further vacancy precipitation. In thermally-recrystallized, ion-implantation induced amorphous silicon, there exists a peculiar class of defects not found in metals: the so called rod-like defects, which are possibly dislocations in the early nucleating stage or defects with structures closely associated with the dislocation nucleation process [53]. The type of secondary defects found is also sensitive to the orientation of the implanted surface [51] particularly if the ion dose and implantation temperature are such that an an amorphous layer is formed. For example, twinning occurs during the regrowth of an amorphous layer in the {111} direction [54].

During the initial stages of annealing, XTEM pictures often indicate the presence of small defects which have the appearance of thin rods, as well as small {113} stacking faults. These defects may be either point defect rows and/or narrowly spaced dislocation dipoles. Rod-like defects and {113} stacking faults are metastable and typically transform into dislocations upon heat treatment.

The process of crystal regrowth through thermal furnace annealing is a complicated procedure due to the interaction of various defects with dopants and with themselves. The final damage structure can be defined by 5 categories, as described by Jones *et al.* [55]. Category I defects are those that are left behind after annealing a silicon sample that has been damaged, but not amorphized. Category II is the EOR damage beyond the amorphous region created during implantation. Category III defects result from the imperfect regrowth of an amorphous layer, category IV defects are the result of the intersection of the regrowth of two amorphous zones, and finally, category V defects are formed if the solid solubility of the implanted species at the annealing temperature is exceeded.

If the sample is not amorphous (category I) before annealing, the damage typically consists of extended dislocation loops and point defect structures. Annealing at T~600°C will recrystallize amorphous zones but not defect clusters. Annealing at a higher temperature causes the defect clusters

to agglomerate and form extended defects that are of an interstitial nature. Annealing at temperatures of 900°C or higher is necessary to eliminate secondary defects which form when the primary damage is annealed. Initially, the point defects will form IDCs (rod-like defects, {113} stacking faults ~ 20Å) in order to minimize the number of dangling bonds. However rod-like defects are unstable above 700°C, and consequently they will dissolve during the growth of the extended dislocations, which form on the {111} habit planes, elongated in the {110} direction. The extrinsic dislocation loops are the most energetically favourable way of accommodating the increase in lattice density, due to the increase in mass from the implanted ions.

As was noted in the previous section, under most implantation conditions that result in an amorphous layer, there is a region beyond the amorphous zone which is saturated with interstitials. This region is where category II defects are formed. These defects are typically extrinsic dislocations and stacking faults. If there is no amorphous layer, then these defects do not form here since the category I defects act as sinks for the excess interstitials. Due to the difference in the inherent density of amorphous silicon and interstitially saturated silicon, the amorphous region is negatively strained while the EOR region is positively strained. This enhances the formation of extrinsic dislocation loops at the EOR. The EOR defects can be reduced by using low temperature implantations (77K) because the amorphous zone will be wider, and consequently absorb a larger proportion of the excess interstitial region [56,57].

Category III defects are a result of imperfect regrowth of an amorphous layer and consist mainly of segregation defects, micro-twins, and hairpin dislocations. Amorphous silicon recrystallizes during thermal annealing when individual atoms attach themselves to the original crystal structure at the amorphous/crystalline interface. The measured interface velocity V is described by

$$V = V_0 \exp(-2.70\,\mathrm{eV}/k_B T) \qquad (2-11)$$

where V_0 is dependent upon the direction of growth and the type of doping. Regrowth rates of amorphous silicon are strongly dependent on the type of dopants found in the amorphous layer. Phosphorus, arsenic, and especially boron enhance the growth rate, while oxygen, carbon and the noble gases retard it [58].

The relative growth rate of amorphous silicon is also a function of the substrate orientation [58]. In the <111>, <110>, and <100> directions, the relative growth rate ratio is 1:6.5:15 [51]. This

difference in growth rates can be accounted for if one assumes that an atom is part of the crystal, rather than the adjacent amorphous material, if it has formed at least 2 regular bonds to the lattice. On the {100} interface, a single atom can be added to the face anywhere, whereas on the {110} interface, two atoms must first nucleate a growth step by attaching to the crystal simultaneously, and on the {111} interface, three adjacent atoms must attach simultaneously, which can lead to the formation of microtwins.

During the growth of the crystal, the implanted ion stays in the amorphous layer as long as thermodynamically possible. However if the solubility of the implanted species is low then at some maximum concentration a precipitate forms. The growing crystal must then grow around the opposite sides of the precipitate island, inhibiting defect-free growth. The result is segregation type defects, and an uneven distribution of the implanted ion.

Hairpin dislocations are created when the regrowing amorphous/crystalline (a/c) interface encounters small micro-crystalline regions that have become slightly misorientated with respect to the bulk crystalline material. As the micro-crystalline pocket is incorporated into the single crystal bulk, a hairpin dislocation is nucleated. This dislocation propagates with the advancing a/c interface, becoming 'V' in shape, until it intersects with the surface. Hairpin dislocations can be avoided by keeping the sample cool during implantation, which prevents the formation of micro-crystalline regions.

During high-energy implantation it is typical to form two a/c interfaces (on either side of the amorphous layer). Each a/c interface advances independently, and if there is a slight mismatch of the surface crystalline material with respect to the bulk silicon, defects, such as grain boundaries, will form. These defects (category IV) will lie at the point where the two a/c interfaces meet. From this, the relative velocities of the two interfaces can be measured.

Finally, category V defects are the result of the implanted species forming precipitates in the sample during the anneal. The precipitation of oxygen in silicon is described in detail in the next section.

2-4 OXYGEN IN SILICON

2-4-1 Precipitation

The solubility of oxygen in silicon at the melting point of silicon is $\sim 3 \times 10^{18}/\text{cm}^3$, which is of the same order of magnitude as the interstitial oxygen concentration normally found in a commercially grown Czochralski (CZ) wafer [59]. Consequently, CZ wafers contain a supersaturated concentration of oxygen, and upon annealing, the oxygen will interact with the silicon to form SiO_2 precipitates. The nucleation sites for precipitation are typically point defects or defect clusters [17,60-63]. Oxygen is trapped at silicon vacancies, which is guaranteed by the relief of the stress associated with the undecorated vacancy, as illustrated in figure 2-10. In a silicon vacancy, the atoms A,B,C,D have been pulled out of their exact crystal positions in an effort to reduce the length of their respective bonds (see figure). The covalent bonding of oxygen with silicon relieves the stress of the stretched bonds since the Si-O-Si length is 0.366 nm, very close to the Si-Si distance of 0.383 nm. The double decorated oxygen/vacancy complex is the most stable [17]. As these oxygen decorated vacancies cluster, SiO_2 precipitation occurs [63]. Another preferential site for oxygen precipitation [17] is thought to be the dumbbell interstitial (similar to a <100> split interstitial, but has a double bond rather than a dangling bond), and is shown in figure 2-11. There is an addition of four oxygen atoms and the migration of the silicon interstitial to one of its next nearest neighbours which allows the process to repeat itself. In the early stages, no net interstitials are created. However, once the associated stress from the volume increase is above the threshold for the formation of a silicon interstitial, interstitials are created by the following mechanism,

$$2y\text{O}^i + x\text{Si} \rightarrow y\text{SiO}_2 + (x-y)\text{Si}^i \qquad (2-12)$$

where strain-free precipitation requires that the volume of SiO_2 is equal to the displaced Si atoms, (ie. $x/y = 2.25$).

This process of strain relief is inefficient at low temperatures (<700°C) and oxygen/vacancy complexes [17] (200-400°C), thermal donors [17] (400-500°C), and needle shaped precipitates which induce strains in the silicon matrix [64] (450-700°C) are formed. At intermediate temperatures (650-1050°C) plate-like precipitates form, inducing stress in the silicon as well as creating dislocation loops from the expelled interstitials. At higher temperatures (above 1050°C) amorphous precipitates are formed whose volume can be easily accommodated by the ejection of silicon interstitials. Hence the

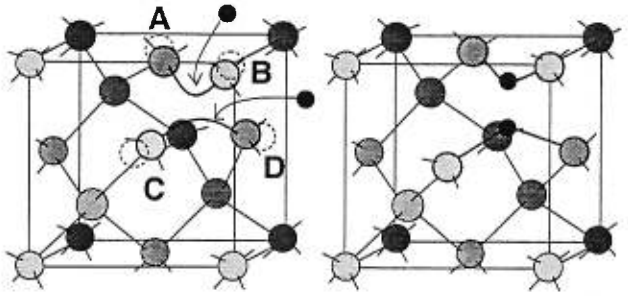

Figure 2-10. The formation of a doubly decorated oxygen/vacancy complex. Oxygen atoms are represented by black circles. The open circles represent the exact crystal position of the displaced or missing atoms.

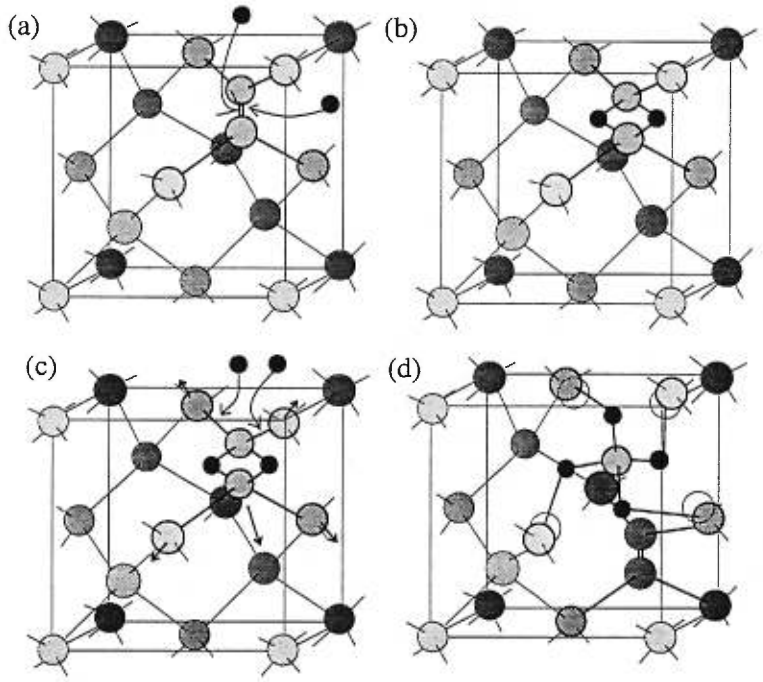

Figure 2-11. The formation of a coherent oxide precipitate on a <100> split-interstitial by the insertion of 4 oxygen atoms (black circles), and the migration of the interstitial. The open circles represent the exact crystal positions of the displaced or missing atoms.

morphology and shape of the precipitates are no longer determined by stresses. These precipitates do not induce strain in the silicon matrix [40,63,64]. Nuclei of precipitates formed on dislocations are initially elongated along the lines of the dislocation [21]. Since the (111) silicon planes have the highest oxidation rate [12], larger precipitates are octahedral in shape, exposing the most (111) planes. To reduce the curvature of the octahedron tips, which reduces the surface energy, the tips are cut

off by the (100) planes. Substoichiometric oxygen concentrations are thought to be SiO_x ($x < 2$) by Maeyama *et al.* [65], but Reeson *et al.* [66] suggest that SiO_x is actually SiO_2 interwoven with crystalline silicon. The interstitials that are created in the above process migrate through the crystal via diffusion coefficients that are dependant on temperature [6]. The surface acts as an infinite sink for these defects. Dislocations and IDCs are formed in the near surface region as a result of this migration [67].

Intrinsic oxygen also getters on extended defects and defect clusters created during ion implantation [60-63]. By using different ion species and doses, Tamura *et al.* [61] demonstrated that the gettering efficiency of oxygen (annealed at 1000°C for 1 h) is not dependent on the type of defect structure. However, given that oxygen is not gettered at the EOR damage by Si or Ge implants (there is virtually no mismatch stress for Si or Ge in silicon), Tamura also concluded that it is necessary to have a strain field in order to getter oxygen. There is also another region (at a depth of $\sim 1/2$ the distance from the surface to the EOR) in MeV implanted silicon which getters oxygen, which is not so readily understood. XTEM and RBS/C analysis does not indicate any damage in this region. The gettering of oxygen in this region does not occur for B or C implants. However, for even slightly heavier elements (Fl, Si, P), the total gettered oxygen concentration is a function of the mass of the implanted ion, saturating with As and Ge implantations. This phenomenon is attributed to a vacancy-rich surface region (as derived by the homogenous model from Holland *et al.* as described in §2-2-4). However, this does not explain why the oxygen should getter preferentially at one particular depth position, rather than the entire surface region. This phenomenon has also been observed for 200 keV oxygen implanted silicon annealed at 1150°C for 2 hours [63], for 6 MeV oxygen as-implanted samples [29], and 2.5 MeV oxygen as-implanted and annealed (12 h, 1300°C) samples, as seen in this thesis.

Once an oxide precipitate has formed, it retards the movement of silicon interstitials, since the diffusion of silicon in SiO_2 is very low ($\sim 10^{-20}$ cm^2/s at 600°C [68], as compared to oxygen in SiO_2 ($\sim 10^{-15}$ cm^2/s at 600°C [69]). Since extended defects grow and shrink by the absorption or expulsion of point defects, oxide precipitates effectively pin the dislocation and prevent it from annealing. For example, in CZ wafers ($\sim 10^{17}$–10^{18} O/cm^3) ion implanted damage cannot be removed as effectively by annealing as the same amount of damage in a float-zone (FZ) wafer ($\sim 10^{15}$ O/cm^3) [62].

2-4-2 Ostwald Ripening

The Gibbs free energy of a system composed of a silicon matrix, an SiO_2 precipitate with radius r, a concentration of oxygen C_o and a corresponding concentration of interstitials C_i, can be expressed by the following [70]

$$\Delta G = -N_o k_B T \ln\left[\frac{C_o}{C_o^s(T)}\right] - N_i k_B T \ln\left[\frac{C_i}{C_i^s(T)}\right] + 4\pi r^2\sigma + G_\epsilon \qquad (2-13)$$

where N_o and N_i are the number of oxygen atoms and self-interstitials respectively, $C_o^s(T)$ and $C_i^s(T)$ are the solubility limits of the oxygen and silicon interstitials in the bulk silicon at a temperature T, $4\pi r^2\sigma$ is the SiO_2 /Si surface tension contribution, and finally G_ϵ is the strain energy, which is relieved by the production of interstitials. When modelling the behaviour of the oxide precipitate during a high temperature anneal, the stress term G_ϵ can be neglected.

For a given temperature, there exists a critical radius, r_c, such that the energy of the SiO_2 /Si surface tension balances the energy of the oxygen and interstitial supersaturations,

$$r_c \approx \frac{2\sigma\Omega}{k_B T \ln\left[(C_o/C_o^s(T))(C_i^s(T)/C_i)^{1/2}\right]} \qquad (2-14)$$

where Ω is the molecular volume of SiO_2 . The critical radius is not only temperature dependent, but is also dependent on the level of supersaturation $(C_o/C_o^s(T))$ of oxygen in the silicon. If $r < r_c$, it is energetically more favourable for the oxide precipitate to dissolve, reducing r and increasing C_o, until an equilibrium is reached. Likewise, if $r > r_c$, the precipitate will grow by absorbing oxygen from the matrix, thus increasing r while decreasing C_o. The equilibrium concentration of oxygen $C_o^{eq}(r)$ at the surface of the precipitate of size r is given by

$$C_o^{eq}(r) = C_o^s(T)\left(\frac{C_i}{C_i^s}\right)^{\frac{1}{2}} \exp\left[\frac{1}{r}\left(\frac{\sigma\Omega}{k_B T}\right)\right] \qquad (2-15)$$

Note that more oxygen can remain in solution surrounding a precipitate if the interstitial concentration is higher. The concentration of oxygen surrounding the precipitate only shows spatial variation close to the individual precipitates [71].

If there are two precipitates of different sizes, each in equilibrium with the oxygen concentration at the interface, close enough that there also exists a gradient of oxygen concentration separating the two precipitates, a process called Ostwald ripening will occur. The oxygen surrounding the smaller precipitate will diffuse towards the larger precipitate, which has a lower equilibrium concentration.

As the oxygen diffuses away from the smaller precipitate, the critical radius is increased, thus making the smaller precipitate unstable, which in turn causes the precipitate to start dissolving, again increasing the concentration in the immediate area. If the oxygen can diffuse away faster than it can be re-absorbed by the precipitate, the precipitate continues to shrink. Similarly the oxygen that has migrated to the larger precipitate will be absorbed, and continue to be absorbed as long as the concentration of oxygen is higher than $C_o^{eq}(r)$. Over time, the smaller precipitate will dissolve, and the subsequently released oxygen will be absorbed by the larger precipitate. This process is called Ostwald ripening, and is, if one ignores the interstitial saturation and stress effects, a purely diffusion limited process.

During annealing, the oxygen solubility concentration $C_o^s(T)$ increases as the temperature increases, effecting a subsequent increase in the critical radius. Precipitates with $r < r_c$ immediately start to dissolve. This, coupled with a much higher diffusion rate of oxygen in silicon, greatly enhances the Ostwald ripening process.

Up until this point we have effectively ignored the contribution of the silicon interstitial supersaturation. Because of the coupling between the oxygen diffusion flux arriving at the precipitate and the diffusion flux of self-interstitials leaving the precipitate, the precipitate growth is governed by the slower one of these two processes, which is the oxygen diffusion [72]. This is expressed by the following:

$$D_i C_i^s > D_o C_o^s \times \frac{C_o^s}{C_o + C_o^s} \qquad (2-16)$$

where D_i and D_o are the diffusion coefficients for silicon and oxygen interstitials, respectively. Taylor, Tan and Gösele [70] studied this mathematically, and they concluded that the supersaturation of interstitials is not as important as it initially appears, although the growth rate of the precipitates is reduced in regions of high interstitial supersaturation.

2-4-3 A Model of Annealing

In larger systems, with many oxide precipitates, the results of Ostwald ripening are not always obvious. Reiss & Heinig *et al.* [73,74] modeled the evolution of precipitates via the Ostwald process. The strain associated with precipitation and the effect of defect production on the process was not included in the model. The precipitates were assumed to be spherical, located at points r_k, with radii of R_k. The

reaction rate Q_k is proportional to the difference between the concentration of the solute around the precipitate, and the equilibrium concentration as calculated by equation 2-15. Thus, the change in the oxygen concentration (∂C) at $\vec{r}$ and time t is

$$\partial C(\vec{r},t) = D\vec{\nabla}^2 C(\vec{r},t) + \sum_{k=1}^{K} \delta(\vec{r}-\vec{r}_k)\, Q_k \qquad (2-17)$$

These equations are solved numerically by assuming that the process is adiabatic ($\partial C/\partial t = 0$ for small time steps). From Q_k, the radius of each precipitate k is adjusted accordingly. The system is strongly nonlinear with respect to the time evolution of the radii of the precipitates. The evolution of the system is strongly dependent on the intial conditions, such as the spatial and size distribution of precipitates at the beginning of the simulation.

In one simulation, the initial distribution of precipitates was homogeneous, but randomly distributed throughout a sphere. Outside of this sphere, the concentration of the solute was kept at the solubility limit. Consequently, the precipitates at the outer regions dissolved while the inner precipitates grew, with a general trend of solute moving towards the centre of the sphere. In a similar simulation, where the volume density (ν) of precipitates was increased by a factor of 125, the final structure had three distinct bands of precipitates, separated by a nearly constant distance λ, with the centre of the sphere denuded of precipitates. Further simulations showed that the number of bands increased, while the distance between these bands decreased, as a linear function of the mean initial distance between each precipitate ($\sim 1/\sqrt[3]{\nu}$).

To explain the mechanism which results in the banding of the precipitates, as a function of the precipitate density, consider the following argument. Start with evenly sized precipitates homogeneously scattered throughout a sphere, where, outside the sphere, the bulk material is an infinite sink for diffusing solute. Initially, the concentration of solute in the sphere is in equilibrium with respect to the precipitates (figure 2-12a). Now, at the edges of the sphere the solute will diffuse out because of the difference in concentrations. This increases the critical radii of the precipitates in this region, and consequently they begin to dissolve (figure 2-12b). This of course increases the oxygen solute concentration (figure 2-12c). If the nearest precipitate is close enough, the solute concentration will increase sufficiently to cause this precipitate to grow, which will then subsequently reduce the solute concentration below the initial value (figure 2-12d). Again, the solute from its nearest inner neighbours will diffuse outward, increasing the size of the precipitates on either side of it. This process will

continue on inward to the centre of the sphere. However, if the precipitates are spaced too far apart, the solute will diffuse into the matrix before increasing the concentration around the next nearest precipitate, and it will then, too, start to dissolve.

From these simulations, it can be readily seen that even a simple distribution of precipitates can lead to quite complicated structures upon annealing. The segregation of oxygen into distinct bands has been seen in high energy as-implanted samples [16] with high T_i, suggesting that Ostwald ripening occurs even during the oxygen implantation.

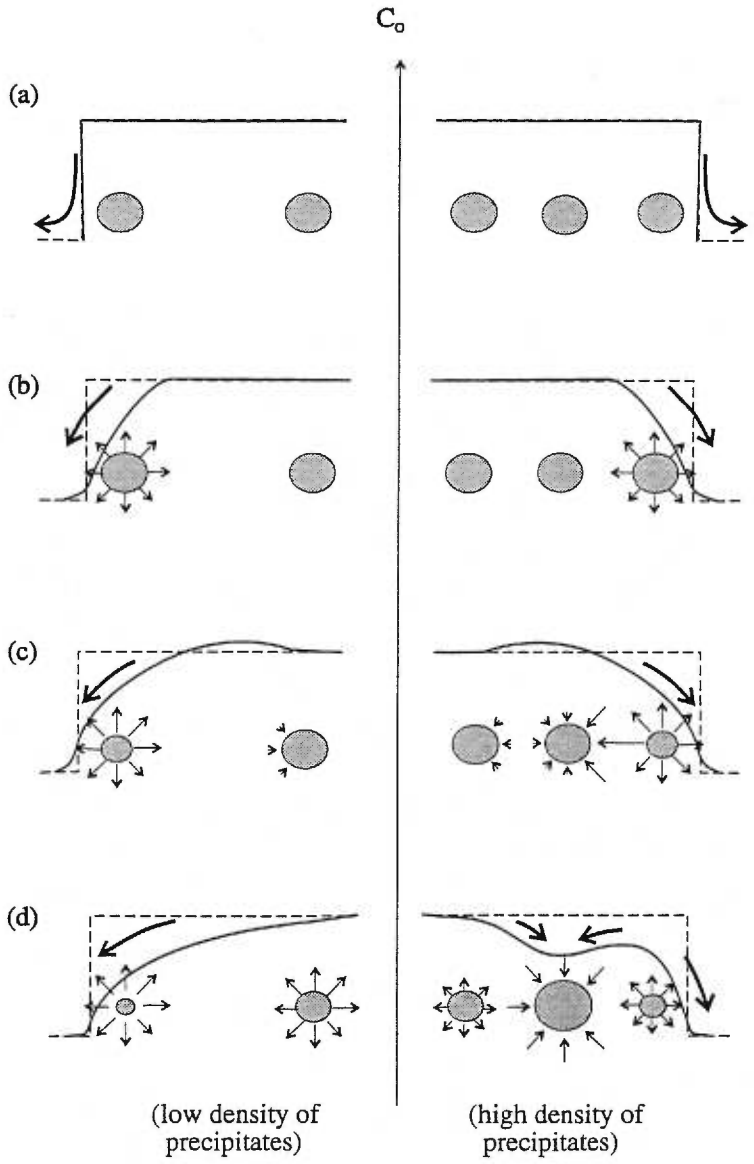

Figure 2-12. A figure demonstrating Heinig's computer simulation of Ostwald ripening. (a) Initial conditions. (b)–(d) Subsequent steps in the evolution of the precipitates and oxygen solute concentrations. The solid line indicates the relative concentration of oxygen in solute only. The thick arrows indicate the diffusion direction of the oxygen solute. The thin arrows surrounding the precipitates (grey circles) indicate whether the precipitate are growing or shrinking.

2-5 FORMATION OF SIMOX

The ideal SIMOX (Separation by IMplantation of OXygen) wafer has the following structure, 1) a perfect silicon crystalline film with no oxygen or oxide precipitates, 2) a flat, stoichiometric SiO_2 layer with no silicon inclusions, and 3) a defect free silicon substrate. Unfortunately, commercial SIMOX has not yet reached this goal. However, with continued experiments, and the knowledge gained therein, success seems likely. However, to achieve this, the interplay between the oxygen, oxide precipitation, defects, and strain must be understood in order to find the 'ideal' conditions for implantation and annealing.

The silicon film is defined as the silicon which remains between the SiO_2 layer and the surface. The substrate is defined as the silicon which forms the bulk of the wafer, and is deeper than the SiO_2 layer.

2-5-1 As Implanted

Given the interplay between damage, strain, oxygen concentration and precipitates during the anneal process of oxygen implanted silicon, it is generally understood that the final product is very much dependent upon the state of the as-implanted sample.

2-5-1-1 Defects [14,15,17,20,63,75-80]

There are many interstitials formed during the implantation of oxygen into silicon, some via nuclear collisions, and others from the result of the oxygen precipitation. These interstitials then migrate towards the surface. However, wherever there are SiO_2 precipitates, the interstitials will become trapped, and extrinsic dislocation loops and stacking faults form. The typical defects in oxygen implanted silicon are {113} and {111} stacking faults, pure edge dislocation loops, half loops, and multiple fault defects. In the region of maximum damage production, d_O, all the dislocations are pinned by SiO_2 precipitates [63]. At higher doses of oxygen, this region becomes amorphous.

In the silicon film, the damage arises from the excess interstitials migrating to the surface. If the flux is high, the resulting epitaxial growth on the surface cannot accomodate all the interstitials. As a result, extrinsic dislocations and stacking faults form near the surface, aided by the high concentration

of oxygen. It is believed that it is this defect zone that is the source of the threading dislocations in the annealed SIMOX samples [20,63].

2-5-1-2 Oxide Precipitation and Growth [4,17,65,66,81-89]

There are three characteristic precipitation processes occurring in the wafer during implantation, as described by Cerofolini *et al.* [88], and each process dominates over the others depending on the implantation conditions. At high current densities (J), high implantation temperature (T_i), and high dose (ϕ), homogeneous (HO) precipitation dominates. HO precipitation occurs at R_p, the region of maximum concentration of oxygen, and consequently the precipitates in this region continue to grow as more oxygen is implanted.

At low J, high T_i and low ϕ, heterogeneous (HE) precipitation dominates. This precipitation occurs at d_O, the region of maximum damage production. In this highly defective, oxygen-rich area, the oxidation takes place preferentially along the defects. They then grow by the diffusion of oxygen from the region of R_p. However, if the flux J is too high, the HO precipitation will occur before there is enough time for the oxygen to diffuse from R_p to d_O. Similarly, at low J, there is a critical dose above which the supersaturation of oxygen around R_p is sufficient for HO precipitation to occur. Once this occurs, there will be a competition between the HO and the HE processes.

Etherogeneous (ET) precipitation, described in detail in reference [17], is the process which results in the formation of SiO_2 precipitates past the region of maximum oxygen concentration.

In the final stages of certain cascades, there is a very hot region which effectively accomplishes three things; all the existing oxide precipitates in this region dissolve due to the high temperature, the released oxygen atoms and the pre-existing interstial oxygen form one large oxide precipitate, and the remaining silicon in the cascade volume recrystallizes. And so at low T_i, when the oxygen and interstitial diffusivity is low, large precipitates will preferentially form in these dense hot regions. In this region, precipitates are typically larger and less dense than those formed by HO. These preferential oxidation regions result in the multiple band structures typically observed in annealed samples.

In direct contrast to the above model, Reiss *et al.* [74] claim that the multi-band structures observed after annealing result only from the Ostwald ripening process as described previously in §2-4-3.

At doses lower than that required to form stoichiometric SiO_2, the oxygen profiles in the as-implanted state are skewed Gaussians with the sharper interface located at the lower (deeper) SiO_2/Si interface. As the oxygen concentration increases, the SiO_2 precipitates coalesce to form a continuous buried layer. The silicon interstitials formed during the oxidation process can no longer reach the surface to annihilate, and hence the saturation of interstitials prevents further growth into the substrate because there is no longer a mechanism for stress release [6,90]. Once the silicon interstitials supersaturate, they cluster to form the additional atomic planes which comprise the stacking faults and dislocation loops typically found in SIMOX structures, aided by the excess strain of the silicon crystal [4,67]. Once formed, the oxide layer then grows preferentially at the upper surface interface. This process is enhanced by the following effects, oxygen has a reduced depth range once the oxide layer is formed due to the differences between the energy losses in silicon and silicon dioxide, and O_2 molecules diffuse rapidly (the diffusion coefficient is $\sim 8 \times 10^{-16}$ cm^2/s in SiO_2 at 850°C [84]) with extensive diffusion and atomic exchange with the SiO_2 network [82,84]. Therefore, once a layer has been formed, continued oxygen implantation results in a rapid diffusion of the excess oxygen to the upper SiO_2/Si interface.

2-5-1-3 Temperature of Implant [5,10-13,15,25,66,85-87,91-97]

One of the predominant implant conditions which affects the post-annealed wafer is the implantation temperature, T_i. It is important to note that T_i controls precipitation both thermodynamically, through the over-saturation concentration $C_o^s(T)$, and kinetically, because the concentration remaining at depth R_p results from the total implant dose minus that which has diffused out into the heterogeneous or etherogeneous sites.

At low T_i (250–400°C), the diffusion of oxygen and interstitials is low, and the critical radius r_c is small, and so oxide precipitation on defects will be enhanced, thus inhibiting the already low migration of the silicon interstitials. This results in a high density of defects within the silicon film, and at these temperatures, amorphous regions on either side of the SiO_2 layer are always present [86]. At high T_i (500–700°C), the point defect clustering is retarded; however, the larger critical radius of oxide precipitates and the higher diffusion rate of oxygen will result in large SiO_2 precipitates being formed. If the final radius of an oxide precipitate is larger than r_c at the anneal temperature, the precipitate may not be dissolved during the anneal. When these precipitates are near the oxide layer, the result is an SiO_2 layer with undulating interfaces. The higher temperatures reduce the defects

to such an extent that there are no amorphous silicon regions on either side of the oxide layer; these regions are polycrystalline [86,87].

For high dose SIMOX ($> 10^{18}/cm^2$), there is an ideal temperature in which the number of defects, and hence nucleation sites for precipitation, are reduced, and yet the sizes of the precipitates are small enough that they can be dissolved upon annealing. This critical temperature for low energy (keV) SIMOX production is ~600°C. For MeV SIMOX production, the 'ideal' temperature is not so clear. In the as-implanted state, the damage at the EOR goes down with increasing temperature, but the damage at the surface increases [13,15]. At low T_i, polysilicon or twinned regions result after annealing, albeit with a good quality SiO_2 layer, and high T_i results in less damage but larger oxygen precipitates in the film. It should be noted that all MeV implants retain a crystalline surface region even in the as-implanted state, which improves the chances for a better recovery after annealing.

2-5-1-4 Strain [14,20,34,80,98-100]

It has been shown that there are two distinct regions of strain in an oxygen implanted sample. These strain regions are due an excess of vacancies in the near surface region and the formation of SiO_2 precipitates at the EOR. At very low doses, as studied by Venables and Jones [20] ($1 \times 10^{16}/cm^2$, 160 keV, T_i=500°C, $10\mu A/cm^2$), there exists only a compressive strain in the region of the implanted oxygen (R_p). At higher doses (1×10^{17} and 3×10^{17}) there are two distinct strained layers, with the surface layer being under high tensile stress and the implant region still under compressive strain. As the dose increases, the strain in the surface layer increases until there is an abrupt occurrence of a tangled network of dislocations located in the film, with a defect-free region on either side. At the same dose that this defected band occurs, there is also a subsequent reduction in the tensile stress in the surface film. The dose ϕ_{st} at which this network of dislocations form is a function of energy as well as the implant temperature, as can be seen from Table 2-II.

From the results from Ellingboe *et al.* [13] it appears that the location of the dislocations is closer to the surface as the implant temperature increases. Holland & Zhou *et al.* [15,14] found that at lower implant temperatures, it was the critical dose that changed rather than the position of the dislocation network. However, at high T_i (650 and 800°C) and doses above ϕ_{st}, the damage started at the surface. At doses below ϕ_{st} Harbeke *et al.* [98] noted that the stress is reduced as T_i increases.

TABLE 2-II

The dose (ϕ_{st}), energy, and implant temperature dependence of the formation of a dislocation network in the silicon film. The dose ϕ_{st} is in given in $\times 10^{18}$ O/cm^2, the location of the dislocation band is given as an approximate percentage of the implant depth R_p, and finally, the lattice strain is in percentage.

T_i	1.0 MeV (a)	450-500 keV (b)	200 keV (c)
100°C		$0.4 < \phi_{st} < 0.7$ $r \sim 1/3R_p$	
150°C	$0.73 < \phi_{st} < 1.45$ $r \sim 0.7R_p$		
300°C	$0.73 < \phi_{st} < 1.45$ $r \sim 0.85R_p$		
450°C	$0.73 < \phi_{st} < 1.45$ $r \sim$ surface	$0.8 < \phi_{st} < 1.1$ $r \sim 1/3R_p$ strain $= -0.32$	
500°C			$0.3 < \phi_{st} < 0.6$ $r \sim$ surface strain $= -0.26$

(a) Ellingboe *et al.* [13], (b) Holland & Zhou *et al.* [14,15], (c) Venables and Jones [20]

There has also been some other unusual results in oxygen implanted silicon. A network of voids or O_2 gas filled bubbles [81,101,102] in the as-implanted state, or a superlattice of oxygen precipitates [103,104], have been found under very stringent implant conditions. In all of these cases, the researchers claim that the presence of these features significantly reduces the number of defects and strain within the silicon film.

2-5-2 Annealed [4,7-9,68,74,83,89,105]

Through the years, it has been well established that the higher the annealing temperature, the better the final results. Typically, the anneal temperature is above 1300°C, with the highest anneal temperature 1405°C [7], 7° below the melting point of silicon.

During annealing, if the sample is still under tensile stress, the stress is released by the formation of voids at the boundary of the negatively strained layer. The volume density of voids is proportional to the stress released [20]. These voids are believed to be filled with O_2 gas. In the samples that already

have a dislocation network, annealing results in threading dislocations and oxygen precipitates in the surface layer, and very few, if any, voids or cavities. From these results, Venables and Jones [20] concluded that in the low dose regime, the oxygen is bound in vacancy clusters ($\sim$ 10Å), and hence during the anneal, the clusters agglomerate to form the O_2 filled voids. However, once the stress is released by the formation of dislocations, the vacancy concentration goes down [14], thus releasing the oxygen to form oxide precipitates. During the subsequent anneal, these precipitates retard the mobilities of the point defects, with the result being a higher density of threading dislocations.

During the annealing process, the oxide precipitates that have a radius less than the critical radius ($\sim$5 nm at 1050°C and $\sim$50 nm @1300°C [12]) dissolve, and the oxygen then migrates to the most stable precipitate, or to the surface. This progressively decreases the oxide precipitate density within the Si surface. The larger precipitates become more rounded to minimize the interface free energy and as they coalesce, they migrate towards the larger precipitates. In the upper oxide interface, the precipitates melt into the layer, making the interface sharper, which reduces the interfacial energy. Initially, the top silicon layer is denuded of oxygen near the surface by the migration of the oxides. However, depending on the length of annealing, the oxygen atoms released by the dissolution of the oxide precipitates migrate towards the surface. In highly defective regions, the diffusion constant decreases [87], hence oxygen may become trapped and form new oxide precipitates, in addition to the HE precipitates already formed during the implantation. At low doses ($\sim$ 10^{17} /cm^2), HE precipitation prevails over HO and, in some instances, a single buried SiO_2 layer can be formed upon annealing [16,63,76]. At higher doses, two regions of precipitates form upon annealing [16,4,8,82,106], and finally, at very high doses, these two regions overlap.

As the oxides dissolve, migrate, and grow, the crystal defects also change. The silicon film recrystallizes from the relatively undamaged top surface layer towards the buried oxide layer by solid phase epitaxial growth and by homogeneous nucleation [107]. However, the presence of micro-precipitates in low concentrations disturbs the solid phase epitaxial growth. The oxide precipitates inhibit the migration of point defects, effectively pinning the dislocations. Microtwins are typical defects formed during the epitaxial growth of amorphous silicon which has a high concentration of oxygen [12]. As well, the oxygen precipitates act as nucleation sites for polysilicon and can also inhibit grain growth.

The annealed samples often contain a high density of threading dislocations. These threading dislocations are made by half-loops (partial dislocation loops) extending progressively deeper into the oxygen-denuded silicon film, effectively following the migration of oxygen towards the buried layer. Once these semi-loops reach the buried oxide layer, they are unable to extend any further and are observed as threading dislocations [83]. After annealing the {113} defects have generally evolved into {111} and {100} stacking faults and the dislocation loops have grown, becoming pinned by the oxide precipitates, which results in more threading dislocations. It is extremely rare to find dislocation loops in SIMOX wafers after annealing [81].

The overall effect of annealing is the sharpening of the SiO_2 layer and the reduction of the silicon defects formed during the implantation process. The density of dislocations in the silicon film in commercially grown SIMOX is typically $10^5-10^7/cm^2$ [77].

2-5-3 Final Product [64,68,78,86,108,109]

Although not all of these regions exist in every SIMOX wafer, the layer structure of the annealed SIMOX wafer can be described by the following:

(1) In the top surface layer, the oxygen has either diffused out of the sample or has diffused towards the SiO_2 interface which results in an good quality oxygen-denuded silicon crystal. This region has few defects, since the surface acts as a sink for point defects and since the sample recrystallizes from the top downward.

(2) Immediately below the surface region, the recrystallization of the silicon is affected by the oxygen concentration, and thus forms a large density of oxygen rich dislocations. Zhou *et al.* [14] attributed this to the release of stress.

(3) Deeper in the sample, the oxygen diffuses into region 4, resulting in a an oxygen-free zone.

(4) The interfacial region, near the peak of the radiation damage, is the location of heterogeneous precipitation created during the implantation.

(5) Because the regrowth of the silicon crystal is inhibited by region 4, the region between the heterogeneous precipitation and homogeneous precipitation regions forms a polycrystalline lattice with a high concentration of oxygen.

(6) This layer is amorphous SiO_2 which may have broadened during the anneal. Depending on the implant conditions, crystalline silicon inclusions with the same orientation as the substrate [109] may be present near the upper and lower Si/SiO_2 interface. Cerofolini *et al.* [88] hypothesize

that these inclusions are a result of silicon becoming trapped during the merging of the HO and HE precipitate zones, and the merging of the HO and ET precipitate zones. Since silicon has a low diffusivity in SiO_2 , (as described earlier) it is extremely difficult for these inclusions to be annealed out [64].

(7) The large density of silicon interstitials after the SiO_2/Si interface gives rise to a polysilicon region and highly damaged zone.

Since low dose implantations have less damage and smaller precipitates, one of the many methods of improving the overall quality of the final product is to anneal the sample at various stages during the implantation [14,20,68,95,99,110-112]. Another method under current study is the removal of the residual defects by 'ion-beam-defect engineering', where the defects in the silicon film are reduced via post-implantations of silicon [77,113].

2-5-4 Low Dose SIMOX (BOX)

The advantages of using low doses to make SIMOX, or BOX (Buried OXide), samples are 1) lower cost (less time needed for the implantations) 2) less damage in the silicon film (since the dose is lower, the subsequent damage is also lower) and 3) a thin SiO_2 layer has a higher capacitance than an thick SiO_2 layer, which therefore reduces the power consumption in the resulting electronic devices [114].

One method of BOX formation is to adjust the dose and implant temperature such that there are enough HE oxide precipitates in the damaged zone to form a continuous layer upon anneal, but not enough oxygen to generate HO precipitation [18,76,115]. For example [76], at 90 keV, T_i=680°C, a low dose of 2.2×10^{17} O/cm^2 is insufficient to produce a continuous oxide layer, while 4×10^{17} /cm^2 gives an oxide layer with embedded silicon islands. These islands are probably the result of the HO and HE precipitates merging during the anneal. However, there is an ideal dose, 2.8×10^{17} /cm^2, which gives a thin, uniform SiO_2 layer, with very few defects in the silicon film ($\sim 10^6$ /cm^2). Similarly, at 70 keV, the optimum dose is 5.2×10^{17} /cm^2 (T_i=680°C) while 5.5×10^{17} /cm^2 increases the threading dislocation in the silicon film by a factor of at least two [115]. This method of creating SIMOX is restricted to low energy oxygen in order to minimize the straggling effects, and hence the depth of the final oxide layer is restricted.

Another method of making low dose SIMOX [18] is to take advantage of ET precipitation by first implanting at very low fluences and low temperatures (100 keV, 1×10^{15} /cm^2, 250μA/cm^2, no external heating), which creates a band of precipitates at a depth $R_\ddagger$ (after annealing) which is beyond the maximum range of oxygen concentration R_p. The HO precipitation of a subsequent implant (140 keV, 5×10^{17} /cm^2, 450μA/cm^2, R_p(140 keV) = $R_\ddagger$ (100 keV)) is aided by the initial oxygen precipitates, and subsequently the straggling effect of oxygen is reduced. This experiment was successful in obtaining a continuous buried oxide with no silicon inclusions. The defect concentration in the silicon film was not reported. One major advantage of this method over the previous one described is that the depth of the SiO_2 layer is not as severely restricted, as long as $R_p(E_2) = R_\ddagger(E_1)$.

It is our goal, in this work, to expand the knowledge about the interactions between oxygen, precipitates, and damage so that it might be possible to create BOX samples using high energy oxygen implantation.

Chapter 3
Experimental Techniques

3-1 IMPLANTATION SYSTEM

3-1-1 Accelerator

All the high energy (MeV) silicon and oxygen implanted samples used in this study were prepared at the Ion Beam Laboratory (IBL) at the Université de Montréal. High-energy ion beams are generated using a High Intensity Negative Ion Source (HINIS), a 90 kV injection system, a 6 MV Van de Graaff Tandem accelerator and a series of analyzing, steering and focussing magnets.

The ion source produces silicon ions from a powdered SiO_2 cathode and oxygen ions from a powdered Al_2O_3 cathode. The ions are accelerated to 18 keV, after which a 90° analyzing magnet is used to select the mass of the ion pre-accellerated at 90 keV and injected into the Tandem accelerator. After being accelerated by the Tandem, the now positively charged ion beam passes through another 90° analyzing magnet. Only those ions with a given mass and charge state pass through the analyzing slits, resulting in a non-contaminated (only one ion species) ion beam.

After passing through the analyzing magnet the beam passes through a switching magnet ($+60°$ to $-30°$) which directs the beam to a specific experimental chamber. Because we have different requirements for the silicon and oxygen implantations, we use two different implantation chambers.

3-1-2 Silicon Implantation Chamber

The silicon implantation chamber is comprised of a set of standard vacuum pumps and gauges, a removable aperture (used to define the implant area), a large movable copper target holder and a Faraday cup located behind the target holder. The vacuum in the chamber during an implantation is better than 10^{-7} torr. The ion beam is swept over a tantalum aperture using electro-static beam sweepers. The position of the beam is determined by the current on the aperture and the current on the sample holder.

Many samples can be mounted simultaneously on the samples holder, thus decreasing the time needed to change targets. During the implantation, the sample holder is kept at a +200 V potential which prevents the escape of secondary electrons. Consequently the total charge deposited on the sample (and hence the dose) can be measured with a standard current integrator. To prevent accidental channeling of the ion beam, the target holder is rotated 7° from the beam axis, and the sample is rotated $\sim 10°$ about the normal before mounting on the sample holder. The temperature of the target holder is not controlled during our implantations. Given the large mass of the sample holder, low beam currents (200 nA) and short implantation times (less than 15 min), the temperature of the sample holder (measured by a K-type thermocouple) never rises above the ambient room temperature (typically 23°C). The silicon samples are clamped to the sample holder, but no effort is made to ensure a proper heat sink. Consequently the actual temperature of the silicon sample during the implantation is unkown.

3-1-3 Oxygen Implantation Chamber

The oxygen implantation chamber is comprised of a set of standard vacuum pumps and gauges, a removable aperture (used to define the implant area), a small temperature controlled (-150° to 600°C) target holder mounted on a precision specimen translator with 4-degrees of motion, x, y, z and θ, and a Faraday cup located behind the target holder. The vacuum in the chamber during an implantation is better than 10^{-8} torr.

The ion beam is rastered using magnetic steering magnets coupled to a WAVETEK function generator. The triangular waveforms used to power the magnets are set at frequencies of 15 Hz for the x-direction and 1 Hz in the y-direction. The steering magnets are 8 m from the target, and since the implantation size is never larger than 1 cm (x and y), the total angular displacement during the sweeping is less than 0.1°. The implant region is defined by sweeping the beam over a 1×1 cm^2 tantalum aperture, located 30 cm in front of the target holder. The position of the beam is determined by the current on the aperture.

The target holder is composed of a 90 W resistive tungsten heater, complete with a K-type thermocouple used in the temperature control system, a thin, electrically isolated, molybdenum cover. In the normal operating mode the target holder is also connected to a small reservoir (used for LN cooling) via a 6 cm copper braid. This braid is disconnected during our experiments. To prevent

accidental channeling of the ion beam, the target holder is rotated 7° from the beam axis (using the specimen translator), and the sample is rotated $\sim 10°$ about the normal before mounting on the sample holder. During long experiments (> 2 h) it is necessary to move the target out of the beam path so that the dose measurement system can be calibrated with the Faraday cup, which is located behind the sample holder. The accuracy of the specimen translator allows the placement of the target into its previous position to within 0.05 cm.

3-1-3-1 Dose Measurement

It is not possible to measure the current, or the integrated dose, on the target holder if it is also used to heat the sample. Hot electrons coming from the heating system neutralize the positive charge from the incoming ions. Therefore a less direct approach to dose measurement is needed. Before the steering magnets there is a rotating finger which passes through the ion beam. The secondary electrons resulting from collisions of the ion beam with the rotating finger are collected on an electrically isolated cylinder. The entire unit is a beam profile monitor (BPM) without a current amplifier. The electrons generated by the BPM are collected and counted in a standard current integrator.

The current from the BPM is calibrated to the beam current, as measured by a Faraday cup located just behind the regular position of the sample holder, before and after each and every experiment. It has been determined that for any given experimental set-up (beam sweeping, beam focussing, *etc.*) the BPM current is a linear function of the beam current over a range of 200 nA to 1.2 μA. Since the BPM is located before the tantalum aperture, the calibration is dependent on the exact parameters of the beam rastering system. Therefore the BPM must be calibrated for every experiment. During long implantations the BPM is calibrated every 2 hours to ensure that there has been no excessive beam drift. The calibration never varied more than 5% during a given implantation, and in most cases the variation was less than 2%. The implant dose is calculated using the average of the calibrations taken immediately before and after each two hour period. The estimated accuracy of the dose measurement is 5 to 10%, which is consistent with the RBS and ERD analysis of the implanted samples.

3-1-3-2 Temperature Control

To compensate for sample heating due to the ion beam, the thermocouple used by the temperature control unit is clamped to the *surface* of the sample (just adjacent to the implant region) rather than the sample holder. The temperature is controlled by a variable current power supply which is regulated by the difference between the pre-set temperature and the measured temperature. The current is slowly adjusted until the temperature difference is negligible ($\pm 1°$). Starting at room temperature, an equilibrium temperature of 570 ± 1°C is achieved after 20 min. The implantation begins only after the sample has reached the equilibrium temperature. The additional $\sim$ 2.5 W (2.5 MeV O^+, 1 μA) of power from the ion beam is compensated for by a reduction in the heater current. Consequently the temperature of the sample surface remains constant, independent of the beam current.

3-2 ANNEALING

To anneal the samples after implantation, a Thermco Ranger 3000 conventional furnace is used. It consists of resistive heaters wrapped around a long quartz tube. The theoretical temperature range is 400 to $1400 \pm 25°C$, but because the furnace is old it is recommended that the annealing temperature be limited to 1300°C and under. The temperature is measured and controlled by thermocouples. Neutral gas is circulated through the quartz tube during the entire annealing procedure.

The samples are placed in a quartz 'boat' and pushed slowly into the centre of the furnace. To reduce the chance of thermal shock this procedure is prolonged over 30 minutes when the anneal temperature is 1300°C and 20 min when the anneal temperature is 900°C. The sample is removed from the furnace in the same fashion.

The annealing temperature for silicon implanted samples is 900°C and the gas flow is N_2. The samples implanted with oxygen are annealed at 1300°C. The gas flow for some of the earlier samples was N_2, but it was discovered that N_2 diffuses into the samples during the anneal (see Appendix A). Now, the oxygen implanted samples are annealed with an Ar (mixed with 5% O_2) gas. This results in a 0.3 to 0.35 μm oxide layer forming on the surface of the sample. It is removed, when necessary, by immersing the sample in an HF (hydrofluoric acid) solution.

3-3 ETCHING

One of the analytical techniques (ERD) used to study the samples is not capable of probing further than 1 μm under the surface of the sample. Since the area of interest is more than 2 μm under the surface, it is sometimes necessary to etch samples. Before etching, the sample is thoroughly cleaned first with tetrachloraethalene (TCE), then with acetone and finally in propanol. Any SiO_2 on the surface of the sample is then removed in a 10% solution of HF. Two etching techniques were used.

3-3-1 Caustic Etch using KOH

The etch rate of silicon in a KOH solution is a function of the temperature of the solution, the orientation of the crystal surface, the density of dopants and defects in the crystal and the *ph* level of the solution. Different concentrations of KOH solutions and different temperatures were investigated. In order to prevent the deposition of silicon hydrides on the surface of the sample and reduce the etch rate [116], propanol was added to the KOH solution. The final mixture was:

1 liter H_2O, 312 g KOH and 250 ml iso-propyl alcohol.

The alcohol does not participate in the etching process.

One end of the clean sample is wrapped with teflon tape in an effort to prevent the etching solution from attacking the material underneath. The sample is then immersed in the 22°C etching solution. Because the alcohol does not mix well with the KOH solution, the entire mixture must be vigorously stirred during the etch. Unfortunately, the alcohol in the etching solution softens the teflon tape, which sometimes allows the solution to etch the supposed un-etched region. Consequently no accurate measure of the etch could be obtained. Many other methods for providing an un-etched region on the sample were tried, but none proved to be reliable.

3-3-2 Reactive Ion Etch

A more reliable etching method is the Reactive Ion Etch (RIE). A 100 W *rf* plasma made from a gas mixture of 95% CF_4 and 5% O_2 at 20 mT with a flow rate of 8 sccm gives an etch rate of 250 ± 50 Å/min.

When using the RIE technique, the non-etched regions are obtained by covering a portion of the sample with a small piece of silicon. The amount of silicon etched from the sample was

measured using a profilometer to determine the step height between the un-etched region and the etched region. However, the measurement of the etch was dependent on where the step height was measured, sometimes differing by as much as 0.2 μm. This is likely due to an uneven etch rate near the border between the un-etched and etched regions of the sample. The surface roughness of the sample in the centre of the etched regions was typically less than 100Å.

The only analysis performed on the etched samples was ERD. The measured depth resolution is given in §3-4-2-3 and figure 3-2.

3-4 ANALYTICAL TECHNIQUES

3-4-1 Ion Beam Analysis

The three primary ion-beam analysis techniques used in this study are ERD (Elastic Recoil Detection), RBS (Rutherford Backscattering Spectrometry) and RBS/C (Rutherford Backscattering Spectrometry with Channeling).

When high energy ions with energy less than the nuclear Coulomb barrier strike a target, the nuclear collisions will cause a large number of incident ions to backscatter out of the target (RBS), and in glancing angle target geometry some of the target atoms will also be recoiled out (ERD). The energy of the backscattered and recoiled atoms depends on the energy-loss parameters, the scattering angle, the masses of the projectile and target atoms, and the depth of the nuclear collision. The resulting energy spectra of the recoiled and scattered atoms can be used to determine the relative abundance of atomic elements in the target. In the case of RBS/C analysis, the target is oriented such that the ion beam direction is along a major crystallographic axis. This reduces the number of nuclear collisions, and hence the number of scattered ions. The reduced number of scattered ions is a function of the quality of the crystal, and thus the energy profile of the scattered ions can be used to obtain information about the damage structure, as a function of depth.

3-4-1-1 Depth Measurement

To calculate the depth of the nuclear collision which corresponds to a given energy of a scattered or recoiled atom, the following analytical procedure is used. The target is initially divided into small sections of equal width (Δx). The width is chosen (2 μg/cm^2 for a 2-3 MeV ^{4}He probing beam (RBS/C) and 1 μg/cm^2 for a 30 MeV ^{35}Cl probing beam (ERD)) such that the energy loss per unit depth (dE/dx) is almost constant over the depth region x to $x + \Delta x$. The change in energy as the ion passes through the target is calculated one section at a time until it reaches the depth $n\Delta x$. The energy loss of the scattered ion or recoiled target atom is then calculated in the same manner, one section at a time, as it passes through the target towards the detector. This is illustrated in figure 3-1 where: E^n is either (a) the detected energy of the projectile (mass m_1) scattered from a target atom (mass m_2) at depth $n\Delta x$ or (b) the detected energy of the recoiled target atom; E_0 is the initial energy of the probing ion; dE/dx is the stopping power of an ion with energy E (Ziegler [24]); and k is the kinematic factor. This is the technique we use to construct a table relating the measured energy of the atom to the the scattering depth.

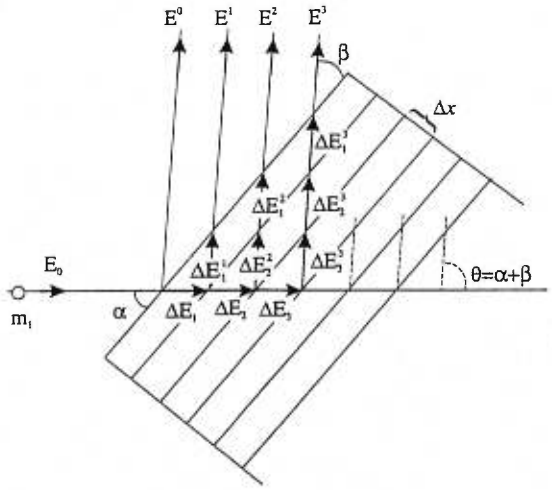

$$E^n = k \cdot \left(E_0 - \sum_{i=1}^{n} \Delta E_i \right) - \sum_{i=1}^{n} \Delta E_i^n$$

$$\Delta E_i = \frac{dE_i}{dx} \frac{\Delta x}{\sin \alpha}, \quad \Delta E_i^n = \frac{dE_i^n}{dx} \frac{\Delta x}{\sin \beta}$$

$$\text{ERD: } k = \frac{4 m_1 m_2}{(m_1 + m_2)^2} \cos^2 \theta$$

$$\text{RBS: } k = \left[\frac{\sqrt{{m_2}^2 - {m_1}^2 \sin^2 \theta} + m_1 \cos \theta}{m_1 + m_2} \right]^2$$

Figure 3-1. An illustration of the method used to construct a conversion table relating the depth of the scattering centre to the measured energy of the recoiled or scattered ion. m_1 is the mass of the projectile, m_2 is the mass of the target atom.

3-4-2 Elastic Recoil Detection

At IBL, ERD is typically done with a 30 MeV ^{35}Cl probing beam, with an entrance angle α and exit angle β of 15° with respect to the sample surface. A time-of-flight (TOF) method is used to separate the masses and the energies of the recoiled elements as well as the Rutherford Backscattering incident ions. The energy of the ions is measured with a standard Surface Barrier Detector (SBD). For a detailed description of the experimental hardware and analysis procedures at IBL, we refer the reader to the following publications [117- 119]. It is worthwhile to note that (1) any elements above the detection level are revealed during the mass analysis and so no *a priori* knowledge of the sample's composition is needed, and (2) the concentration profiles are determined directly from the energy spectra; they are not a 'best-fit' simulation.

3-4-2-1 Mass Resolution

The mass resolution is a function of the energy and time resolution. The time resolution is independant of the mass of the measured particle, however, the energy resolution is not. The energy resolution of an SBD detector is approximated by $\delta E = A + BE^{\frac{1}{3}}$ where A and B are mass related constants [120]. The energy resolution is degraded for heavier elements. Consequently, the mass resolution is also degraded for heavier elements. At IBL, we have a mass resolution better than 1 amu for light elements (< 24 amu). Although it would be difficult to separate them, we can differentiate between the isotopic mass peaks of silicon recoils, but for more massive elements (> 40 amu) this is no longer possible.

3-4-2-2 Depth Resolution

Because the analysis is based upon a direct conversion from energy to depth, it stands to reason that the depth resolution is a function of the detected energy spread. The measured energy spread is a function of (a) the detector resolution, (b) the probing beam spot size (the scattering angle is no longer precise, and thus the calculated path length and kinematic factor is not correct), (c) the detector size (solid angle), which changes the angular acceptance of the recoiled atoms, (d) the energy straggling within the target and (e) multiple scattering within the target. The depth resolution (based upon the theory expressed in references [121,122]) for oxygen in silicon (30 MeV Cl probing beam) was calculated for various geometric configurations, and the results are shown in figure 3-2b. It can be seen that $\alpha = \beta = 15°$ gives the best overall depth resolution throughout the probing depth.

The theoretical depth resolution calculations assume that the surface of the sample is perfectly flat. However, on real samples, imperfections of the sample surface can and do degrade the depth resolution. Figure 3-2a, taken from reference [123], compares the experimentally measured depth resolution to the theoretical calculation. As expected, the measured depth resolution is not as good as the theory predicts. However, it is still less than 50 nm at a probing depth of 800 nm.

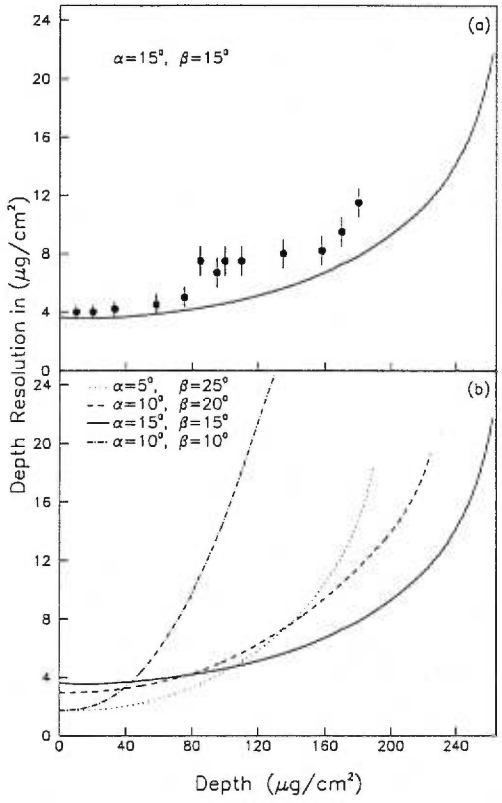

Figure 3-2. (a) Theoretical total depth resolution for O recoils in Si for $\theta = 30°$ and $\alpha = \beta = 15°$ as a function of depth compared with the experimental values from several SiO_2 targets. (b) Calculated depth resolutions for different scattering geometries. ($1\ \mu g/cm^2 \approx 43$Å for silicon)

3-4-2-3 Detection Limit

The number of detected recoiled atoms for a given element is a function of the scattering cross-section ($d\sigma/d\Omega$), the geometry of the experimental set-up (solid-angle, etc.), the efficiency of the detection system (better than 95% for all elements with masses greater than 4 amu [119]) and the total number of probing ions hitting the target, usually referred to as the total charge Q. In principle,

using a reasonable beam current, any concentration of a doping element is detectable given a large enough Q. However a semi-infinite dose of a high energy Cl probing beam is not practical because of (a) time limitations and (b) a possible alteration in the the target composition, as a function of depth, due to knock-on collisions. In practice, the limiting factor for detecting low concentrations of a particular element is the background noise. If the production rate of the noise signals is higher than the production rate of scattered recoils, it is impossible to detect this element, irrespective of Q.

In our experiments the background noise is predominantly a result of 'tailing' in the energy signal of other, more abundant, recoils or scattered ions. A low energy signal coupled with an accurate TOF measurement results in an incorrect mass calculation. Thus the detection limit is more a function of the probing beam and the target composition than it is of the total deposited charge Q. The majority of the noise signal comes from the scattered Cl ions, and although it is possible to reduce the noise by using a ^{63}Cu probing beam, which cannot kinematically scatter from silicon at a 30° angle, the reduction in depth resolution due to an increase in multiple scattering precludes this choice.

So for silicon targets, using a 1-2 nA 30 MeV Cl probing beam for approximately 2 h with a 30° total scattering angle, the detection limit for elements less than 24 amu is approximately 3×10^{14} at/cm^2 over a probing depth of 1 μm.

3-4-2-4 Concentration Accuracy

In the ERD analysis the depth scale and stopping powers (dE/dx) are in naturalized units, i.e. μg/cm^2 and MeV/(mg/cm^2) respectively, which is independent of the density of the material being probed. After analysis, the concentration of the elements are either given *relative to* a pre-determined element in a particular layer of the sample, or as a percentage in that particular depth region δx. If the density of the material is unknown, it is not possible to give an absolute concentration in atoms/cm^3. However, in the samples studied in this thesis, the density is known for the *pure* silicon regions (5×10^{22} at/cm^2), and it is assumed that the density does not change significantly in the oxygen rich region. This is not an unreasonable approximation since the concentration of SiO_2 was never more than 23% of the total volume at any given depth, and the difference in density between Si and SiO_2 (2.2 vs 2.32 g/cm^2) is small. This gives less than a 1.5% error in the density approximation. When the density of the material is known and constant throughout the depth of the probing region, it is

a simple matter to convert the relative concentration profiles to absolute concentrations, and so for simplicity's sake, the data was presented in this form.

In the figures which show the calculated ERD results, there are error bars on each data point. These error bars were calculated based solely on statistical analysis. For each depth channel there is a fixed width ($dx_i = x_{i+1} - x_i$) and its associated concentration of oxygen C_i. The total number of oxygen atoms detected (Y_i) within the energy region $E(x_{i+1}) - E(x_i)$ is counted. The uncertainty in the concentration is then given by

$$\delta C_i = C_i \frac{\sqrt{Y_i}}{Y_i}. \tag{3-1}$$

The curves representing the ERD analysis were obtained by using a Fast Fourier Transform (FFT) filter to the calculated data.

3-4-3 Rutherford Backscattering Spectrometry

In our RBS experiments, there are two SBD detectors at angles of 157.5° and 112.5°. Since it is kinematically impossible for target atoms to recoil at angles greater than 90°, only the scattered probing ions will be detected, and therefore no mass analysis is needed. The probing beam used for these experiments was a 3 MeV ^{4}He beam, which gives a probing depth in silicon of approximately 3 μm. It is not practical to increase the probing depth by increasing the He energy because, at higher energies, there are resonance peaks for He scattered from oxygen. A complete description of the principles of RBS analysis can be found in reference [124].

3-4-3-1 Energy/Depth Resolution

As mentioned previously, the energy resolution is a function of (a) the detector resolution, (b) the probing beam spot size, (c) the detector size (solid angle), (d) the energy straggling and (e) multiple scattering. The primary energy loss of a light ion is due to electron interactions rather than nuclear scattering and consequently the multiple scattering term may be neglected. The energy spread (δE_g) due to the geometric contribution [(b) and (c)] has been calculated for 3 MeV He in a silicon sample (using the theories described in [122]) and is approximately 10 keV at the surface and 15 keV at a depth of 3 μm. If we use the Bohr approximation to the energy straggling of He in silicon [124], the energy straggle (δE_s) is 35 keV at 3 μm. Adding in the detector resolution (δE_d typically 15 to 20 keV) [125], we have a total energy resolution of 22 keV at the surface and 43 keV at 3μm. This

corresponds to a depth resolution $\delta x = \delta E/(\partial E_d/\partial x)$ of 0.04 μm at the surface and 0.07 μm at 3 μm. The experimental energy resolution is not available. However, it can be assumed to be more than the theoretical estimates.

3-4-3-2 Detection Limit

The energy of the backscattered ion is a function of the mass of the target element from which it scattered, where heavier target atoms result in more energetically scattered He ions. Thus the signal from an element whose mass is larger than the bulk material is separate from the bulk signal (at least in the near surface region). The detection limit for heavy impurities is approximated by [124]

$$\frac{N_{imp}}{N_{sub}} = \left(\frac{Z_{sub}}{Z_{imp}}\right)^2 \times 10^{-3}. \tag{3-2}$$

As an example, the detection limit for arsenic in silicon is $\sim 10^{19}$ at/cm^3.

The signal from an element whose mass is lower than the bulk material is much more difficult to detect, for two reasons. First, the signal from the low mass element is added to the signal from the bulk material, and will be masked by the statistical fluctuations in the bulk signal. Second, the signal for low mass elements is reduced because the scattering cross-section $d\sigma/d\Omega$ is reduced ($\propto Z^2$). An approximate detection limit was calculated using only statistical considerations. If the number of counts per energy channel (yield) of the bulk material is Y, the detection limit is

$$\frac{N_{imp}}{N_{sub}} \sim 3.33 \left(\frac{Z_{sub}}{Z_{imp}}\right)^2 \frac{\sqrt{Y}}{Y}. \tag{3-3}$$

The yield Y is of course a function of the total charge Q. For Y between 1,000 and 12,000 counts, the detection limit of oxygen in silicon is between 1.6×10^{22} and 4.6×10^{21} at/cm^3. However, if the presence of SiO_2 is inferred by the reduction in the silicon yield (1 silicon atom is displaced by approximately 2 oxygen atoms) the ratio of the atomic numbers is not relevant, and the detection limit then comes between 1×10^{22} and 3×10^{21} at/cm^3.

3-4-4 Channeling

Channeling of energetic ions occurs when the incident beam is carefully aligned with a symmetry direction of a crystal. Looking at an aligned crystal (figure 3-3) it is easy to see that the majority of ions that are not immediately scattered off the surface of the target will pass relatively unhindered between the axial rows or planes of the crystal. This is referred to as channeling. Since well-channeled particles do not get close enough to the atomic nuclei to undergo large angle Rutherford scattering, the backscattering yield is reduced by a factor of $\sim$ 30-50 for most crystals. The resulting energy spectrum from the recoiled atoms can be used to determine the nature and depth of crystal imperfections as well as the presence of impurity atoms. Many books [32,124,126] and papers [127,128] have been written which describe channeling, its application to defect studies and experimental procedure, and should be referred to for more information. Only a very brief review will be presented here.

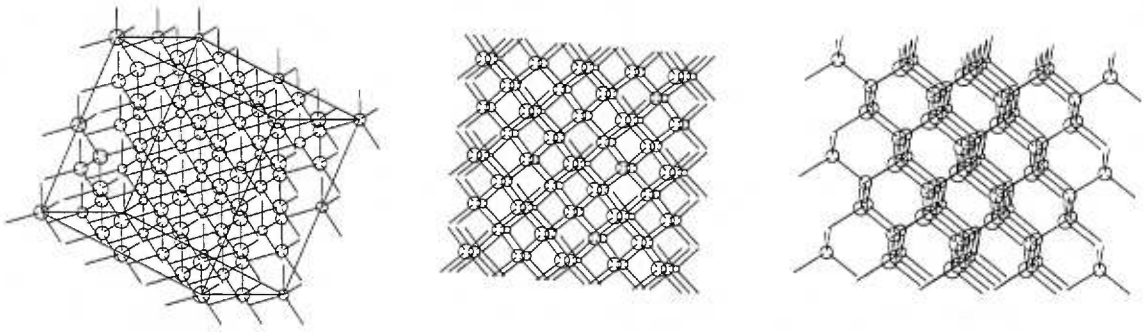

Figure 3-3. A model of a silicon crystal aligned in a (a) random, (b) <100> and (c) <110> direction.

3-4-4-1 Depth Resolution

For any channeling analysis, it is necessary to be able to relate a detected energy $(E_d)_i$ to a depth x_i of the scattering centre. The analytical procedure is identical to the one outlined in §3-4-1-1. However, the standard Ziegler [24] energy loss parameters (dE/dx) are no longer appropriate. The range of channeled ions is much larger than the range of non-channeled ions. The ratio of the energy loss between a channeled and a non-channeled He ion, γ, is a non-linear function of energy [129], and is strongly dependent on the accuracy of the alignment where a 0.5° deviation from the crystal axis can change γ from 0.5 to 1.0 [130]. However, in spite of its inherent inaccuracies, the energy loss of the

channeled ion (ΔE_i in figure 3-1) is calculated by multiplying the standard Ziegler stopping powers dE/dx by a constant ($\gamma \sim 0.5$–0.6). If we use $\gamma = 0.5$, the calculated depth scale (and probing depth) increases by approximately 25%. Because of the uncertainties in γ, any depth scale calculated from channeled ions is always assumed to be a reasonable, but not necessarily accurate, approximation.

3-4-4-2 Defect Analysis

For an ion to be channeled in a crystalline target, the deviation from the crystalline axis direction must be less than the critical angle $\psi_{\frac{1}{2}}$, which is a function of the interatomic spacing, the energy of the channeled ion, the atomic number of the ion and substrate atoms. For a <110> channeled 2 MeV He ion in silicon, $\psi_{\frac{1}{2}} \sim 0.75°$. If the direction of an ion deviates more than $\psi_{\frac{1}{2}}$ from the aligned direction, it is said to be 'de-channeled'. The percentage of the ion beam that is not channeled is referred to as the random fraction, and is denoted by χ_R.

At a depth x, the random fraction in a crystal with defects is the random fraction that would normally occur in a virgin crystal, χ_V, plus the fraction of the remaining channeled beam $(1 - \chi_V)$ that scatters, with angles greater than $\psi_{\frac{1}{2}}$, off of $n_d\, x$ defects. Thus the random fraction is:

$$\begin{aligned} \chi_R(x) &= \chi_V(x) + \big(1 - \chi_V(x)\big) \cdot P(\psi_{\frac{1}{2}}, x) \\ P(\psi_{\frac{1}{2}}, x) &= 1 - \exp\Big[-\int_0^x dP(\psi_{\frac{1}{2}}, dx)\Big] \\ dP(\psi_{\frac{1}{2}}, dx) &= \sigma_D\, n_D(x)\, dx \end{aligned} \tag{3–4}$$

where

$P(\psi_{\frac{1}{2}}, x)$: is the probability that an ion passing through the target of width x will be de-channeled,

$dP(\psi_{\frac{1}{2}}, dx)$: is the differential probability over a distance dx, and

σ_D : is the integrated scattering cross-section for scattering angles greater than $\psi_{\frac{1}{2}}$.

The interaction between the random fraction of the beam and the target is the same as if the target were randomly oriented, and thus the yield from this part of the beam is χ_R times the normal random yield. The remaining fraction of the beam $(1 - \chi_R)$ can scatter off of n_D randomly distributed defects. If the cross-section for scattering directly off of the defect is $d\sigma_D/d\Omega$ and the standard Rutherford scattering cross-section is $d\sigma/d\Omega$, then the ratio (χ) of the channeled yield to the random yield, at a given depth x, is:

$$\begin{aligned} \chi(x) &= \chi_R(x) + \big(1 - \chi_R(x)\big) f_\sigma \frac{n_D(x)}{n} \\ f_\sigma &= \frac{d\sigma_D/d\Omega}{d\sigma/d\Omega}. \end{aligned} \tag{3–5}$$

If the defects in the crystal are randomly distributed point defects (neither specifically substitutional nor specifically interstitial), small amorphous pockets, or even thin amorphous regions, then the cross-section $d\sigma_D/d\Omega$ is the standard Rutherford cross-section (i.e. $f_\sigma = 1$). In the analysis used in this thesis, we use an approximation for $\psi_{\frac{1}{2}}$ from reference [32] to calculate σ_D.

$$\sigma_D = \int_{\psi_{\frac{1}{2}}}^{\infty} \frac{d\sigma_D}{d\Omega}\, d\Omega = 2.3 \times 10^{-21}\, \frac{Z_1 Z_2 d}{E}\ \text{cm}^2, \tag{3–6}$$

where

d : is the atomic spacing along the axial direction in Å, and

E : is the energy of the channeled particle (MeV) just prior to scattering.

The number of defects is then calculated iteratively by using the following equations.

$$\begin{aligned} n_D(x_i) &= n\left(\frac{\chi(E_i) - \chi_R(E_i)}{1 - \chi_R(E_i)}\right) \\ \chi_R(E_i) &= \chi_V(E_i) + \big(1 - \chi_V(E_i)\big)\left(1 - \exp\left[-\sum_{j=0}^{i-1} \sigma_D\, n_D(x_j)\, dx_j\right]\right) \end{aligned} \tag{3–7}$$

where

i : is the energy channel number,

x_i : is the depth of the scattering centre corresponding to a measured energy E_i,

$\chi(E_i)$: is the measured yield, expressed as a fraction of the random yield, at an energy E_i (depth x_i),

$\chi_R(E_i)$: is the random fraction of the beam at an energy E_i (depth x_i),

$\chi_V(E_i)$: is the random fraction of the beam at an energy E_i (depth x_i) in a virgin sample,

$n_D(x_i)$: is the number of point defects per cm^3 at depth x_i,

n : is the atomic density of the probed material.

For the specific case of extended defects, dislocation loops, twins and stacking faults, the differential scattering cross section $d\sigma_D/d\Omega$ for large scattering angles is negligible (i.e. $f_\sigma \approx 0$). However, the integrated cross-section σ_D is not. Because the scattering-cross section is a function of the Burgers vector and the size of the defect, it is difficult to quantify without further analysis. However it is known that the cross-section is not a strongly varying function of E and so, assuming that the type of damage in the sample does not vary widely with depth, a depth profile of the relative

damage in the sample can be obtained. Again, we use the iterative approach to solve for the differential probability of dechanneling $dP(\psi_{\frac{1}{2}}, dx)$:

$$\begin{aligned} dP(\psi_{\frac{1}{2}}, dx_i) &= \ln\left[\frac{1-\chi_V(E_i)}{1-\chi_R(E_i)}\right] - \sum_{j=i}^{i-1} dP(\psi_{\frac{1}{2}}, dx_j) \\ &= n_D(x_i)\,\sigma_D\,dx_i \end{aligned} \tag{3-8}$$

where

$dP(\psi_{\frac{1}{2}}, dx_i)$: is the differential de-channeling probability over a depth x_{i-1} to x_i,

$n_D(x_i)$: is the number of extended defects per cm^2 at depth x_i, and

σ_D : is the integral cross-section (cm) for scattering with angles greater than $\psi_{\frac{1}{2}}$ off of extended defects.

The above analysis is based upon many assumptions and approximations, some of which are: (1) the critical angle $\psi_{\frac{1}{2}}$ is not a function of the crystal damage, (2) the flux of channeled particles is uniformly distributed throughout the channel, (3) de-channeled particles are not scattered into aligned directions, and (4) the defects are either *all* point defects or amorphous material, or *all* extended defects. Although there is no quantitative error analysis, it is generally accepted that the overall distribution of the damage is representative of the 'real' damage distribution, and that the number of defects, when compared from sample to sample, is reasonably accurate.

The real difficulty in defect analysis arises from the differences in the stopping powers for channeled and non-channeled ions. It is assumed that the conversion from an energy scale to a depth scale is the same for both the random spectrum and the aligned spectrum, but as was discussed in the previous section, this is not the case. So in effect, $\chi(E_i)$ is the ratio of aligned and random yields from two different regions in the sample. If the sample's composition is uniform as a function of depth, this does not affect the defect analysis. However if the sample is not uniform, $\chi(E_i)$ is the ratio of the yields between two depth regions which could have completely different elemental compositions. In this instance, the calculated damage profile is distorted and must be interpreted accordingly.

3-4-5 Secondary Ion Mass Spectrometry

SIMS (Secondary Ion Mass Spectrometry) is used as a complementary technique to ERD for profiling the oxygen concentration in our samples. SIMS measures and counts the number of charged recoil ions from a target as it is being sputtered by, at least in our case, a Cs^+ ion beam. During the SIMS analysis, the beam is electronically scanned over a 150 μm spot on the surface of the sample, but only the sputtered atoms from the center region of the scanned area (8 μm) are used in the analysis. To obtain a depth profile of specific elements in a target, a e/m spectrometer is used to isolate and count a particular charged ion or molecule during a fixed time period. The spectrometer is then adjusted for a new e/m ratio which corresponds to the next element being profiled. All the specified elements are sampled, and the cycle then repeats itself. The resulting data is the number of counts of each specific ion/molecule as a function of sputter time.

3-4-5-1 Depth

After measuring the depth of the sputtered crater with a profilometer, the depth scale is calculated by assuming that the sputter rate is constant. The accuracy of this method is difficult to quantify since it is dependent on the target and the experimental conditions. For our particular case, the calculated sputter rates varied by more than 5% for different experiments on the same sample. Clearly the sputter rate is not always constant. On one sample the calculated depth of the maximum oxygen concentration ($\sim$ 2.4 μm) varied by more than 0.17 μm between successive profiles. Another factor degrading the depth resolution is the fact that nuclear collisions between the ion beam and the sample can induce an intermixing of elements between two regions. This ion mixing leads to an artificial broadening of the concentration profiles.

3-4-5-2 Concentration Measurement

The sputtered material is emitted as individual atoms or as molecules in various neutral and charged states. The relative abundances of the various charge states are dependent upon the ion or molecular species, and on the target composition. For example, in the presence of oxygen, the relative production of both positively and negatively charged ions for many elements is greatly enhanced [131]. Thus it is difficult to obtain an accurate measure of the ratio of one element to another without first calibrating the system with a standard target which is as close, chemically speaking, as can be to the target

sample. Because the total concentration of oxygen was known in our samples (equal to the implant dose), it was simpler to normalize the SIMS results to the implant dose. In addition to errors in the calculated depths, it should be noted that differences in the sputter rate as a function of depth will alter the apparent concentration profile.

The detection limit of oxygen in silicon is of the order of 10^{18} at/cm^3, which is two orders of magnitude more sensitive than ERD. This sensitivity is limited by the natural affinity between silicon and oxygen. The detection limit is improved as the sputter rate increases since there is less time for the oxygen within the system to react with the silicon sample. However, this degrades the depth resolution.

3-4-6 Transmission Electron Microscopy

Transmission Electron Microscopy (TEM) operates by passing a high-energy electron beam through a very thin target and recording the image on a photographic plate. The electron beam is focussed through a series of magnetic lenses, and either the diffraction pattern or the sample image is formed on the photographic plate. This is illustrated schematically in figure 3-4. Different target materials have different electron absorbtion coefficients, and so by using the image contrast it is possible to differentiate between regions in the sample that have different chemical compositions. In addition, extended defects, twins, stacking faults and other defects also have their own characteristic contrast, and so the types of defects, as well as their qualitative distribution, are visible. For more detailed information about TEM how-to's and analysis procedures refer to the books by Edington [132] and Glauert [133].

Before continuing further, it is necessary to define certain symbols and vectors used when discussing TEM.

- BF : Bright field (image).
- DF : Dark field (image).
- SAD : Selected Area Diffraction.
- θ_B : Bragg scattering angle.
- $\vec{B}$: Upward drawn incident beam direction in the specimen that is opposite to the direction of the electron beam.
- $\vec{b}$: The Burgers vector of a dislocation.

$\vec{g}$: (= <hkl>) A vector normal to the reflecting plane (hkl), with magnitude $1/d_{hkl}$.

$\vec{s}$: The deviation from the Bragg reflection position, defined by $\vec{s}+\vec{g}=\vec{g}'$ where $\vec{g}'$ defines the exact Bragg condition. $\vec{s}>0$ when $\theta > \theta_B$.

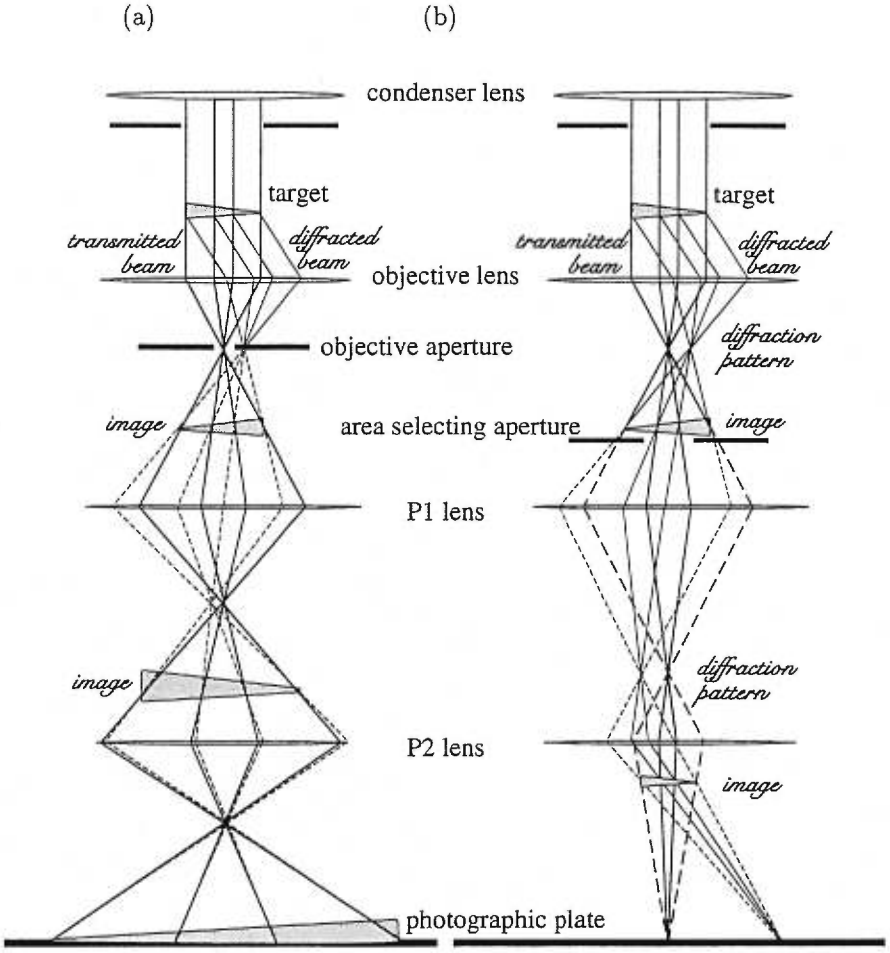

Figure 3-4. A diagram illustrating the (a) BF imaging and (b) SAD mode of the electron microscope. After an electron beam is intercepted by an aperture, the continuation of its path is indicated by a dashed line.

3-4-6-1 Imaging

In the standard diffraction mode used for discerning objects > 15 Å, the diffracted beams are intercepted by the objective aperture and do not contribute to the image (BF) (see figure 3-4a) or conversely, only one strongly diffracted beam contributes to the image (DF). Typically the best images are formed when the sample is tilted such that there is only one strongly diffracted beam.

The transmitted and diffracted beams interact with each other as they pass through the sample, and this interaction leads to certain characteristic contrasts in the sample image, such as thickness fringes and bend contours. As part of the transmitted beam is diffracted, its intensity (ϕ_o) is decreased while the intensity of the diffracted beam (ϕ_g) increases. However, some of the diffracted electrons can be diffracted back into the transmitted beam, thus increasing ϕ_o while decreasing ϕ_g. If there is no absorption of the electron beam then the intensities of the diffracted beam and the transmitted beam are sinusoidal as a function of sample thickness z. Thus, in a typical wedge-shaped crystalline sample, where only one of the beams (transmitted or diffracted) contribute to the image, there are alternating dark and bright regions near the thin edge of the sample. These are referred to as thickness fringes.

As the thickness of the sample increases, the oscillating intensities of the transmitted and diffracted beams are damped due to the absorption effects on the electron beam, and the general intensity becomes uniform. In addition to normal absorbtion, there is also anomalous absorbtion, which is characterized by the fact that the intensity distribution of the transmitted beam is not symmetric about $\vec{s} = 0$ ($\vec{s}$ is the deviation from the exact Bragg condition). The maximum intensity of the transmitted beam occurs when $\vec{s}$ is small and positive. When $\vec{s}$ is less than zero, the overall transmitted intensity is low. The maximum intensity of the diffracted beam occurs when $\vec{s} \approx 0$. If the sample is bent or twisted, $\vec{s}$ is not constant over the sample area and consequently, for BF images, there can be dark lines or bands (bend contours) which correspond to regions in the sample where $\vec{s} < 0$.

Any defect or strain region which distorts the reflecting plane (hkl) also changes the Bragg condition, and hence $\vec{s}$ also changes. In a typical BF image ($\vec{s} > 0$), defects are seen when the distortion in the (hkl) planes reduces the value of $\vec{s}$ to zero or below. When $\vec{s} = 0$ there is enhanced diffraction, and thus the intensity of the transmitted beam is reduced. If $\vec{s} < 0$ the anomalous absorbtion effect greatly reduces the intensity of the transmitted beam, although a similar increase in the diffracted beam is not seen. Thus defects appear as dark regions in a BF image and as bright regions in a DF image. Because the distortion in the (hkl) crystal planes is related to the product $\vec{g} \cdot \vec{b}$ ($\vec{g} = <hkl>$ and $\vec{b}$ is the Burgers vector), not all defects can be seen. Figure 3-5 illustrates this effect using a simple edge dislocation.

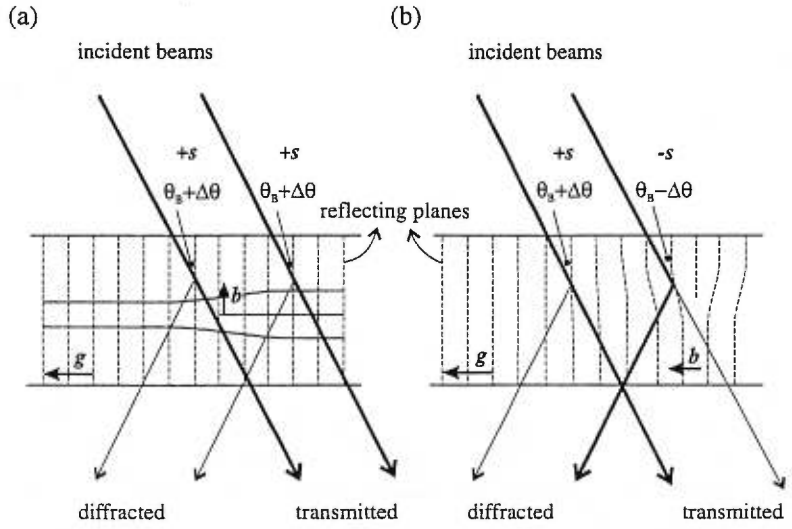

Figure 3-5. An edge dislocation with a Burgers vector $\vec{b}$ (a) perpendicular to $\vec{g}$ and (b) parallel to $\vec{g}$.

If the sample is oriented such that $\vec{B}$ (the anti-direction of the electron beam) is perpendicular to the sample surface, then the depths of various defects or layers can be measured to within 5% on an uncalibrated TEM photograph [134].

3-4-6-2 Sample Preparation

Before any sample can be viewed in a TEM picture, it must first be thinned ($\sim$ $1/2$ μm) so that the electrons can pass through the sample. We will briefly describe the method we use to prepare samples for cross-sectional TEM (XTEM) pictures. For a more detailed description of standard sample preparation techniques, refer to reference [135]. First, two samples are glued together, surface to surface, with silver epoxy. Other silicon wafers are then glued to the back of the samples to provide physical support (figure 3-6a). The targets are gently pressed together in a vise, and the epoxy is cured in a 100°C oven for 1 h. Since the samples are implanted at temperatures of 570°C, it is assumed that the 1 h, 100°C treatment for curing the epoxy does not change the sample significantly.

These targets are then cut cross-sectionally into 1 mm slices (figure 3-6b). The slices, and possibly other slices from other samples, are mounted on a flat hand held mount using strong wax. They are then gently ground down to 200 μm using Al_2O_3 abrasives and a glass plate. One side is polished using diamond paste, a polishing cloth and a glass plate. A 3 mm diameter copper ring is

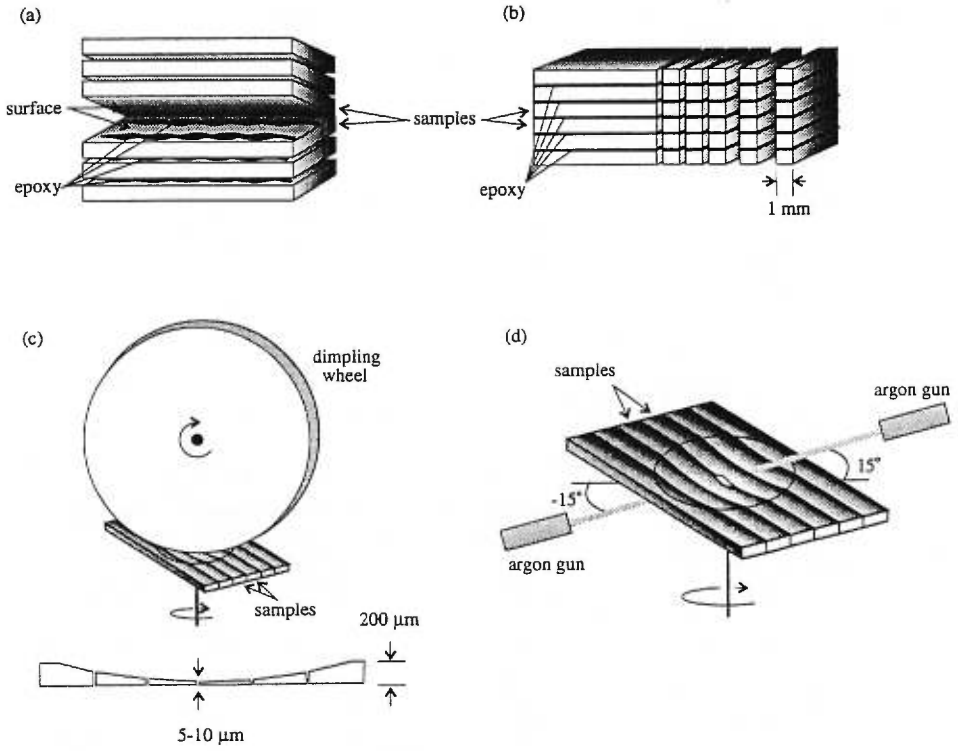

Figure 3-6. XTEM sample preparation: (a) glueing, (b) slicing, thinning (not shown), (c) dimpling, and (d) ion milling. Note that the drawing of the sample slice in part *d* is greatly magnified with respect to the argon guns.

glued on with epoxy to provide additional mechanical support for the now fragile slices. Any excess silicon is removed. Each slice is then dimpled and polished using a spinning 15 mm rotary wheel on a slowly rotating slice (figure 3-6c) until the thinnest region is about 5 to 10 μm thick.

Finally, the sample is ion milled using two, 4 kV 1 mA, argon guns at $\pm 15°$ from the top and bottom of the thinned sample (figure 3-6d). The sample slice slowly rotates. Thinning continues (10 to 15 h) until a small hole appears in the centre of the slice. The two wedged-shaped samples can now be viewed in the electron microscope, where naturally the thinnest regions of the sample surrounds the hole.

Chapter 4
Experimental Results and Discussion

4-1 EXPERIMENTAL PARAMETERS

The purpose of this thesis is to study the interaction between oxygen and pre-existing damage in a silicon wafer during oxygen implantation and annealing. To create the damage, silicon was implanted with high energy Si ions, and then annealed. This creates a band of dislocations that is stable at the oxygen implantation temperature of 570°C. Oxygen was then implanted into these pre-damaged samples, as well as virgin silicon, and studied using the analytical techniques described in chapter 3. The experimental parameters are listed table 4-I.

TABLE 4-I
Experimental Parameters

initial wafer:	CZ n-type undoped [100] silicon
silicon implants:	
energy:	2.00 $\rightarrow$ 2.75 MeV
dose:	$5 \times 10^{13} \rightarrow 1 \times 10^{15}$ Si/cm^2
dose rate:	150 $\rightarrow$ 200 nA/cm^2 (Si^{1+})
implant temp:	room temperature
implant angle:	7° from beam, 10° tilt
implant size:	1 cm^2
anneal:	furnace, 900°C, 1 h in N_2 flow
	ramp up/down: 45°C/min
oxygen implants:	
energy:	2.50 MeV
dose:	$3 \times 10^{16} \rightarrow 3 \times 10^{17}$ O/cm^2
dose rate:	0.8 $\rightarrow$ 1.0 μA/cm^2 (O^{1+})
implant temp:	570°C, as measured by a thermocouple
	clamped to the surface of the sample
implant size:	1 cm^2
implant angle:	7° from beam, 10° tilt
anneal:	furnace, 1300°C, 12 h in N_2 or Ar/O_2 flow
	ramp up/down: 50°C/min

4-1-1 Oxygen

The energy of the oxygen implants was fixed at 2.50 MeV. This energy was chosen as a compromise between high energy, where the separation of the homogeneous and heterogeneous regions are well defined, and low energy, where the results would be more closely related to SIMOX work. Another consideration was that, at 2.5 MeV, it is not necessary to etch the samples prior to RBS/C analysis, although it is necessary to etch the sample prior to ERD analysis. The oxygen doses, ϕ, were chosen so that the dose was high enough to obtain an oxygen concentration profile with ERD and RBS/C ($\phi > 10^{16}$ O/cm^2), and yet low enough that heterogeneous precipitation would still be observable ($\phi \sim 10^{17}$ O/cm^2 [16]). Three doses were chosen, 0.3×10^{17}, 1.0×10^{17}, and 3.0×10^{17} O/cm^2. At low implant temperatures the sample will amorphize the EOR region, which would then cancel the effect of having a pre-damaged region. To prevent this, the sample was pre-heated and maintained at a constant temperature of 570 ± 10°C (as measured by a thermocouple clamped to the surface of the sample) during the implantation. The annealing was done in a conventional furnace in either an Ar/O_2 or N_2 gas flow. The anneal temperature was 1300°C (the maximum temperature of our furnace), and the anneal time was 12 h.

4-1-2 Silicon

The energies of the silicon implants were chosen, using TRIM calculations, so that the maximum damage region would be approximately at the same depth as the damage region produced by a 2.5 MeV oxygen implantation. The TRIM calculations are shown in figure 4-1. The implant energies were varied so that the effect of the proximity of the damage region to the oxygen implanted region could be studied. Thus, the silicon implant energies used in this study are 2.00, 2.25, 2.50 and 2.75 MeV. The silicon doses were chosen so that the dose would not be high enough to cause the sample to amorphize during a room temperature implant, and yet not so low that there would be no damage left in the sample after the anneal. To ensure the relative stability of the defects during the 570°C oxygen implantation, a 1 h 900°C furnace anneal was chosen.

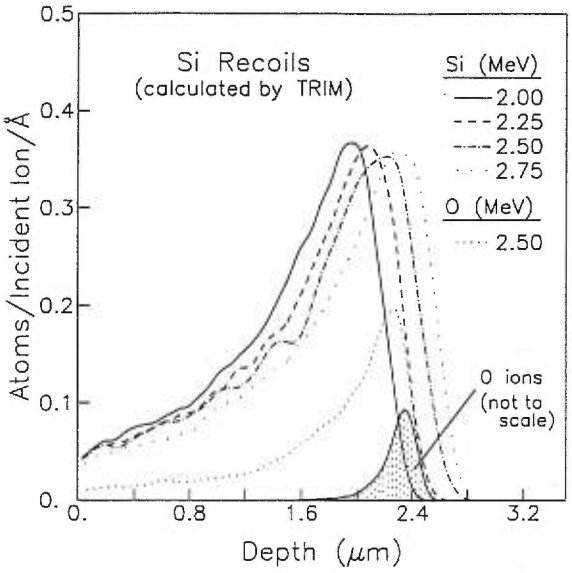

Figure 4-1. TRIM predictions for the depth profile of recoiled atoms for 2.0-2.75 MeV Si and 2.5 MeV O implanted silicon, as well as the predicted oxygen distribution.

4-1-3 Analysis

The implant parameters and subsequent analysis are summarized in Table 4-II. The distribution of oxygen as a function of depth was determined by Elastic Recoil Detection (ERD) and Secondary Ion Mass Spectrometry (SIMS), the damage profiles were characterized by Cross-sectional Electron Microscopy (XTEM) and Rutherford Backscattering Spectrometry & Channeling (RBS/C), and finally the location and sizes of the oxide precipitates were characterized by XTEM.

The ERD analysis was done at the Ion Beam Laboratory at the University of Montreal with the assistance of Dr. S.C. Gujrathi. The probing beam was typically 30 MeV ^{35}Cl, although a few of the analyses were done with a 42 MeV ^{65}Cu beam. The entrance and exit angles were both 15°. The beam current was $\sim$ 1–2 nA, with a total spot size $\sim$ 1 mm^2.

The RBS/C analysis was also done at the Ion Beam Laboratory at the University of Montreal. The probing beam was 3.0 MeV ^{4}He, unless otherwise specified, with a beam current $\sim$ 2nA. There were two detectors at angles of 22.5° and 67.5° to the beam direction. The sample surface was at 90° to the beam when probing the <100> channel, and 45° when probing the <110> channel. The random spectral analysis was typically taken at $\varphi \sim 10°$ and $\theta \sim 5°$ from the aligned direction.

TABLE 4-II

A summary of the implanted samples and the techniques used to analyse them.

	No Oxygen Implant	2.5 MeV 3×10^{16} O/cm^2	2.5 MeV 1×10^{17} O/cm^2	2.5 MeV 3×10^{17} O/cm^2
No Silicon Implant		ERD XTEM	RBS/C ERD XTEM	RBS/C ERD XTEM SIMS
2.00 MeV 5×10^{14} Si/cm^2	RBS/C XTEM	RBS/C XTEM	RBS/C ERD XTEM SIMS	RBS/C ERD XTEM
2.25 MeV 5×10^{14} Si/cm^2	RBS/C	RBS/C ERD	RBS/C ERD	
2.50 MeV 5×10^{14} Si/cm^2	RBS/C	RBS/C	RBS/C ERD	RBS/C ERD
2.75 MeV 5×10^{14} Si/cm^2			ERD	
2.00 MeV 1×10^{15} Si/cm^2	RBS/C XTEM		RBS/C ERD	
2.25 MeV 1×10^{15} Si/cm^2			ERD	

RBS/C: Rutherford Backscattering & Channeling
ERD: Elastic Recoil Detection
XTEM: Cross-sectional Transmission Electron Spectroscopy
SIMS: Secondary Ion Mass Spectrometry

The SIMS analysis was done in Ottawa at the Metals and Materials Technology Laboratories CANMET with Dr. G. McMahon and Dr. J. Jackman using a CAMECA 4f system. The sputtering beam was Cs^+, and the currents used were between 300 nA and 400 nA. An electron gun was used to prevent charge build-up on the surface of the sample.

The XTEM samples were prepared at the University of Montreal, but the majority of the photos were taken with the Philips 200 kV CM20 Electron Microscope at McGill University in Montreal. There were a few difficult samples that were analyzed in Ottawa at CANMET with the aid of Dr. G.J.C. Carpenter.

4-2 SILICON IN SILICON

In an effort to find the sets of experimental parameters that yield stable pre-damage in silicon, several samples were studied. These samples were implanted with silicon at various doses ($\phi = 5 \times 10^{13}$, 1×10^{14}, 5×10^{14}, 1×10^{15} Si/cm^2) and at various energies (E = 2.00, 2.25, 2.50, and 2.75 MeV). The as-implanted samples were analyzed by RBS/C using a 3 MeV He beam. After the samples were annealed at 900°C for 1 h, they were again analyzed with RBS/C. The 2.00 MeV silicon implants ($\phi = 5 \times 10^{14}$ and 1×10^{15} Si/cm^2) were also analyzed with XTEM.

In this section we will present two sets of experimental parameters that satisfy the pre-damage conditions. They are (1) 5×10^{14} Si/cm^2, 2.00–2.75 MeV and (2) 1×10^{14} Si/cm^2, 2.00–2.50 MeV, followed by a 1 h, 900°C anneal. When $\phi(Si) = 5 \times 10^{14}$ Si/cm^2, the resulting pre-damage is composed almost entirely of dislocation loops, and when $\phi(Si) = 1 \times 10^{15}$ Si/cm^2, it is composed almost entirely of dislocation dipoles.

4-2-1 Range

To change the depth of the pre-damage, the energy of the silicon implant must be adjusted. The depth of the peak of the damage profile was calculated from the RBS/C spectra, using the method described in §3-4-1, for 2.00, 2.25, and 2.50 MeV, $\phi = 5 \times 10^{14}$ Si/cm^2, as-implanted samples and compared to TRIM calculations and XTEM photographs. The results are tabulated in Table 4-III.

TABLE 4-III
Location of damage peak in silicon damaged silicon.

		2.00 MeV	2.25 MeV	2.50 MeV	2.75 MeV
XTEM	(±0.15 μm) :	2.0 μm			
RBS/C†	(±0.1 μm) :	1.91 μm	2.11 μm	2.25 μm	
TRIM	(±0.1 μm) :	1.96 μm	2.10 μm	2.22 μm	2.33 μm

†The depth was calculated assuming that the stopping power in an aligned direction was 0.5 that of a random direction.

To calculate the depth scale from RBS/C, it was necessary to approximate the He stopping power in the aligned direction. The stopping power in a channel is very sensitive to experimental conditions, such as the beam energy and the beam phase space, and the damage within the sample. Consequently, the depth scale in the aligned direction cannot be accurately determined. However, if we approximate the stopping power for a channeled particle to be a factor of 2 smaller than the stopping power in an amorphous sample (see §3-4-4), then the calculated depth of the damage peak gives a value reasonably close to that given by TRIM (Table 4-III), and XTEM measurements.

4-2-2 Damage

4-2-2-1 As-Implanted

The damage profile as a function of dose was measured using RBS/C analysis. Figure 4-2 shows the RBS/C results for 2.0 MeV silicon-implanted silicon ($\phi = 5 \times 10^{13}$, 1×10^{14}, 5×10^{14}, and 1×10^{15} Si/cm^2) in the as-implanted state. The RBS/C spectra from a virgin sample in the aligned direction and in a random direction are shown by solid lines. Even at the lowest dose, there is damage near the surface of the sample. At the highest dose, the sample is not amorphous at the EOR. The general shapes of the RBS/C spectra for the samples with $5 \times 10^{13} \leq \phi \leq 5 \times 10^{14}$ Si/cm^2 are all similar. The dechanneling increases gradually from the surface to the EOR ($\sim$2 μm), indicating a steady rise in the number of defects from the surface to the EOR. At a dose of 1×10^{15} Si/cm^2 however, the shape of the spectrum is quite different. The majority of the dechanneling occurs at the EOR region. The dechanneling in the near-surface region is not significantly more than that in the $\phi = 5 \times 10^{14}$ Si/cm^2 sample, indicating a saturation of defects in this region. At the EOR the damage rises sharply, indicating that the damage production in this region has not saturated as a function of dose. This large increase in the dechanneling at the EOR is most likely due to the creation of stable point defect complexes, or small amorphous zones, or both.

The two samples chosen for further study are the the $\phi = 5 \times 10^{14}$ and 1×10^{15} Si/cm^2 samples. Since the shape of their RBS/C spectra are not similar, it is quite probable that their defect characteristics are also dissimilar. To gain a better understanding of the damage within the sample, the profile of defects as a function of depth was calculated using the theory described in §3-4-4, with the assumption that all the defects in the as-implanted samples are point defects or amorphous clusters. The results of these calculations are shown in figure 4-3a and figure 4-3c. The shaded area

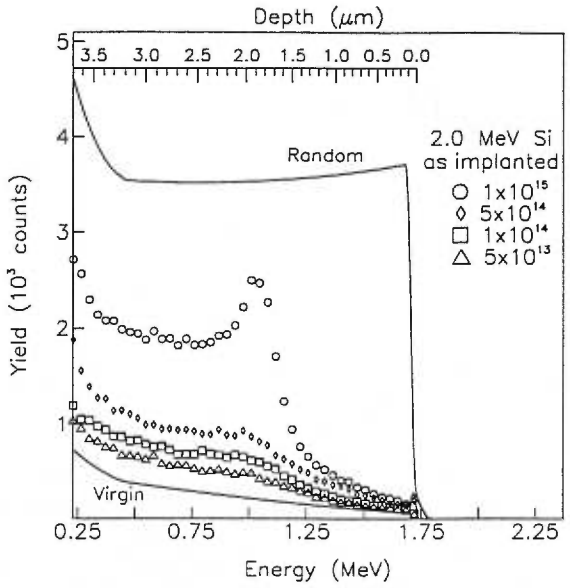

Figure 4-2. RBS/C results of silicon implanted into silicon at room temperature. The aligned spectra were taken in the <100> channel. The virgin and random spectra are given as solid lines. The depth scale was calculated assuming that the stopping in the channeled direction is $^1/_2$ of the stopping in a random direction. (3 MeV He, $\theta = 22.5°$, <100>)

between χ and χ_R is proportional to the number of point defects in the sample. The number of point defects, as a function of depth, is shown in figure 4-3b and figure 4-3d. The damage profile calculated by TRIM is also shown.

The TRIM calculation for the number of point defects is based solely on the linear cascade model, with no recombination between vacancies and interstitials, and with each point defect immobile. When the implant dose is low, the recombination of interstitials and vacancies occurs primarily within individual ion cascades, and consequently the shape of the damage profile is similar to the damage profiles calculated by TRIM. For the 5×10^{14} Si/cm^2 sample, it can be seen that the damage profile is similar in shape to the TRIM profile. However, the TRIM results had to be reduced to fit the experimental results. From the scaling factor needed to adjust the TRIM profile to fit the experimental data, we calculated that $\sim 65\%$ of the Frenkel pairs recombined during the implantation.

As the dose increases, the defect density increases and vacancy/interstitial pairs from different ion cascades begin to interact. At this stage, the TRIM predictions can no longer be applied, as for the $\phi = 1 \times 10^{15}$ Si/cm^2 sample (figure 4-3d). According to the theory of homogeneous damage production

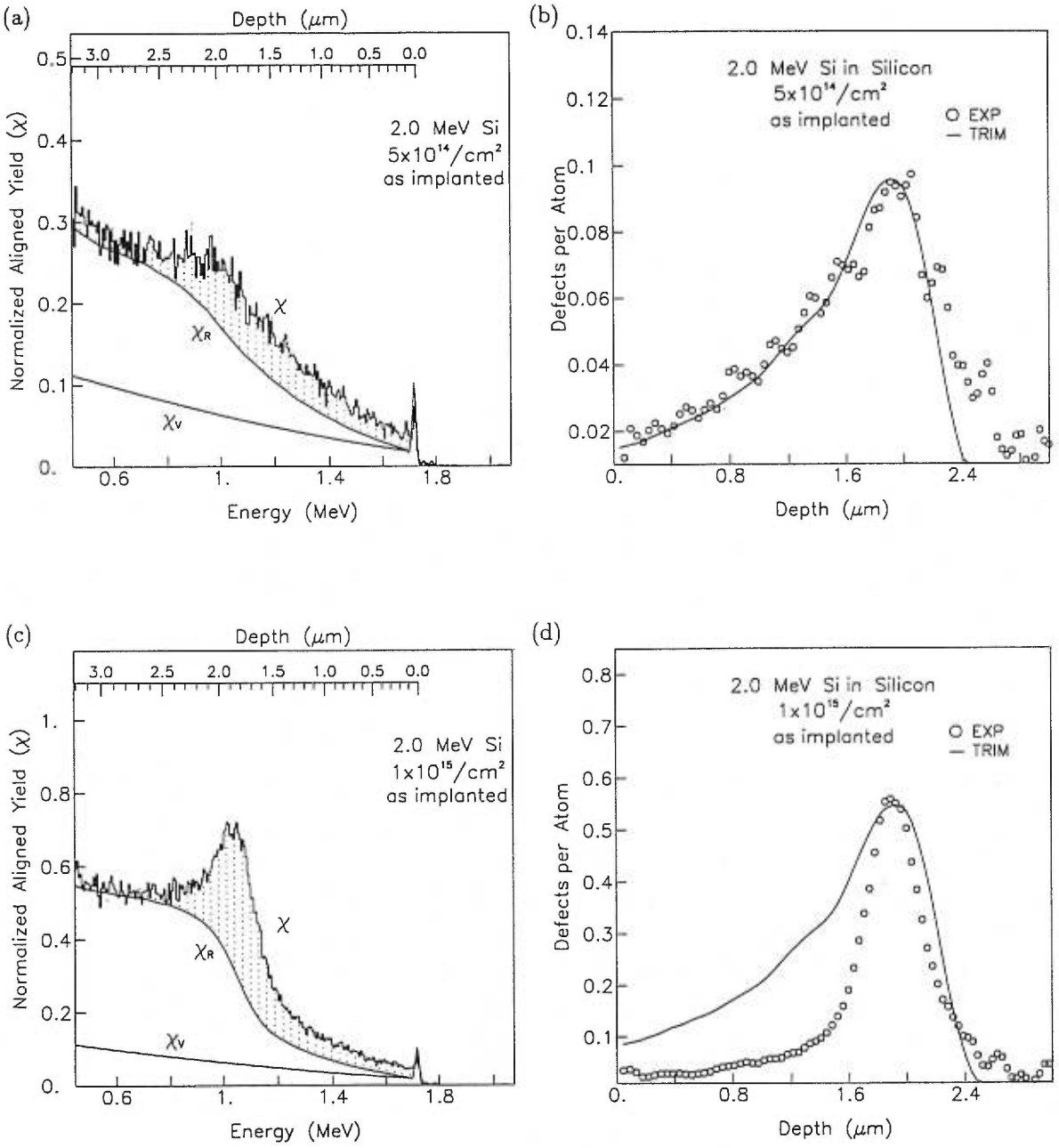

Figure 4-3. The normalized aligned yield (χ) for (a) 5×10^{14} and (c) 1×10^{15} Si/cm^2 as-implanted samples, for a virgin sample (χ_V), and for the calculated random fraction (χ_R). The calculated damage profiles (circles) for (b) 5×10^{14} and (c) 1×10^{15} Si/cm^2 samples, and the TRIM (not to scale) calculation of displaced atoms (lines). The depth scale was calculated assuming that the stopping in the channeled direction is $1/2$ of the stopping in a random direction. (3 MeV He, $\theta = 22.5°$, <100>)

(described in detail in §2-2-4), the defects in the silicon film are limited to vacancies, interstitials, di-vacancies and di-interstitials and they are uniformly distributed throughout this region. As a result, the defects from different ion cascades can recombine. The recombination rate of the point defects in the surface region increases as the density of damage increases, and hence the number of defects in this region is not a linear function of the dose. At some critical dose, $\phi_c \sim 10^{15}$ Si/cm^2 [61], the production rate of point defects is equal to the recombination rate. Consequently, at doses higher than ϕ_c, the damage concentration saturates. This explains why the concentration of damage for the $\phi = 1 \times 10^{15}$ Si/cm^2 sample in the surface region is significantly lower than what is predicted by the linear cascade model.

In the EOR region the production rate of Frenkel pairs is much higher than in the near surface region. The density of defects at any given time is also much higher. Consequently there is a higher probability that defects in this region will agglomerate into defects more complex than the di-vacancies and di-interstitials that are produced in the silicon film. In the EOR region, vacancies will agglomerate to form stable defect complexes, or small regions of amorphous material, and the interstitials will form small defect complexes, or, if the density is high, they may form intermediate defect configurations (IDCs) such as row defects, or even extrinsic dislocations. Hence the damage in this region does not saturate with the implant dose.

4-2-2-2 Annealed

After the silicon samples were implanted, they were annealed at 900°C in a furnace with a N_2 gas flow. Figure 4-4 shows the annealed and as-implanted back-scattering yields from the 5×10^{14} Si/cm^2 sample. The dechanneling from the annealed sample is the same as the yield from the virgin sample in the surface region, and this indicates that this region is now relatively defect-free.

To obtain a depth profile of the damage for the annealed sample we assumed that the dechanneling was only a result of lattice distortions due to extended defects (see §3-4-4). Because the scattering cross-section, σ_D, is unknown (it is a function of the size and Burgers vector of the dislocation loop), only the probability of dechanneling for the 5×10^{14} Si/cm^2 sample is shown in figure 4-4b. However, in this energy range of He, the cross-section σ_D is only weakly dependent on the He energy. Therefore dP/dz can be considered to be proportional to the number of defects. The FWHM (full-width at half maximum) of the damage peak is 0.25 μm.

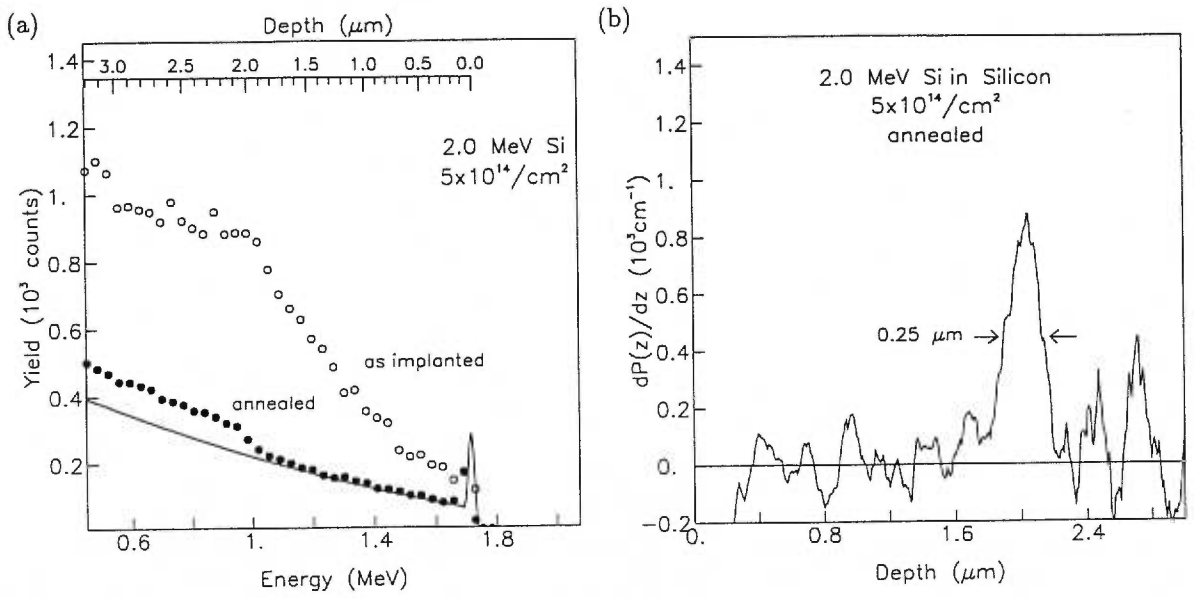

Figure 4-4. (a) RBS/C <100> aligned backscattering yields from Si implanted silicon. The solid line is the aligned yield from a virgin sample. (3 MeV He, $\theta = 22.5°$, <100>) (b) The product of the number of defects and the cross-section for dechanneling as a function of depth for the annealed silicon sample. The depth scale was calculated assuming that the stopping in the channeled direction is $1/2$ of the stopping in a random direction. (3 MeV He, $\theta = 22.5°$, <100>)

The annealed samples were prepared for XTEM using the techniques described in §3-4-6. Figure 4-5 shows XTEM pictures from samples implanted with a dose of 5×10^{14} Si/cm^2, and annealed at 900°C for 1 h. In figure 4-5a, the damage profile as predicted by TRIM is overlaid on the XTEM picture. It can be seen that the majority of defects in the silicon occur at the maximum damage peak predicted by TRIM. The width of the damage layer is approximately 0.30 μm wide, which is similar to the results obtained from the RBS/C analysis. There are two distinct defects that lie past the main defect band (A and B). These two defects were only two found in this XTEM sample, which gives an approximate defect density (of these defect types) as $\sim 10^7$ defects/cm^2. The oscillating contrast of defect B is indicative of a steeply inclined dislocation. The dark band on the surface of the sample is an oxide layer formed during the anneal due to the residual oxygen in the furnace. Figure 4-5b is a similar sample, with the magnification set at larger scale. From this photo it can be seen that the majority of the defects are dislocation loops with sizes between 30–75 nm. The smaller dislocation loops are closer to the surface of the sample. There is a large defect (300 nm) extending into the silicon substrate (located in the upper right hand corner of the photo, labelled A) that has a significantly

(a)

(b)

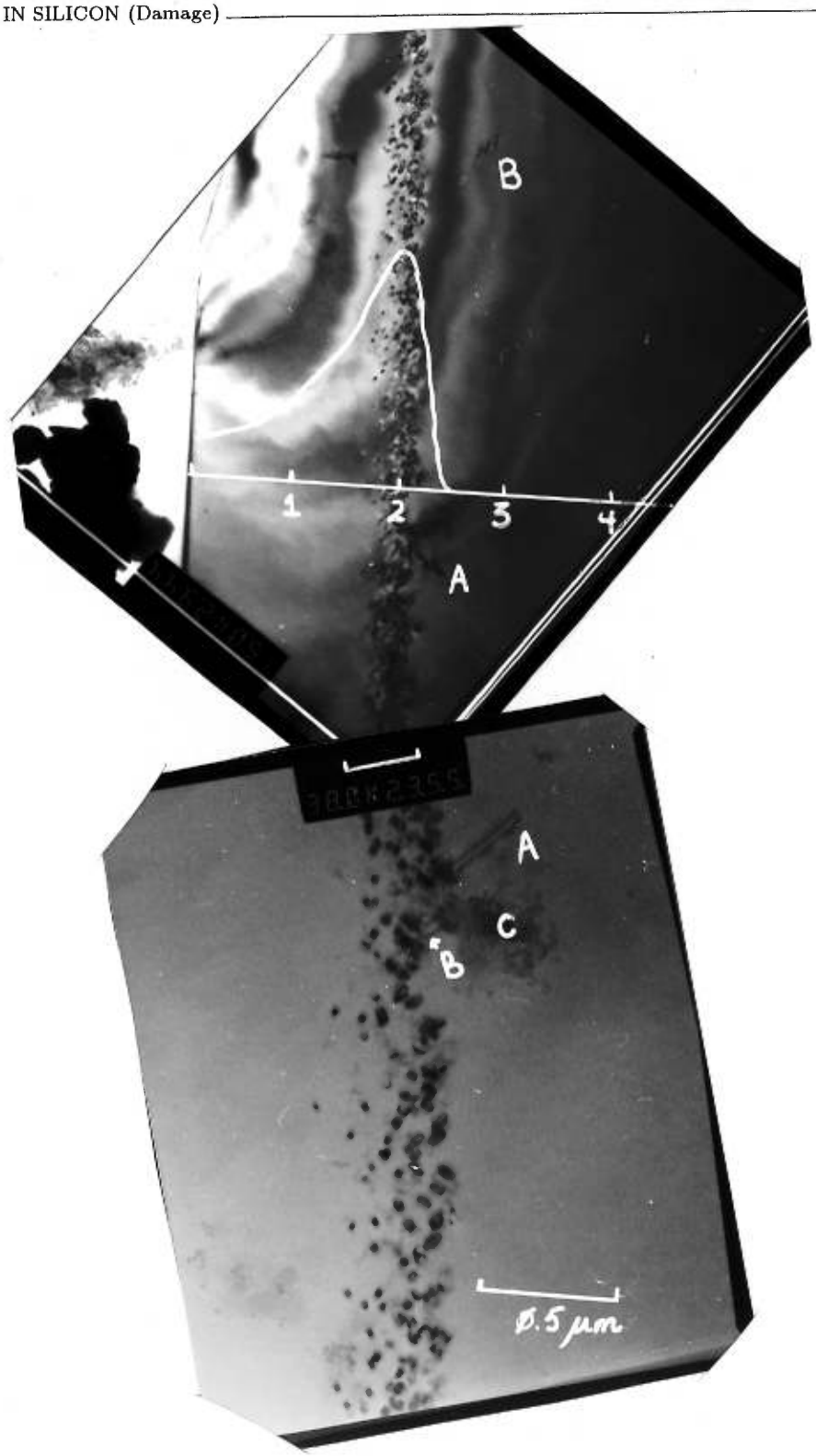

Figure 4-5. XTEM photos of samples implanted with $\phi = 5 \times 10^{14}$ Si/cm^2 and annealed at 900°C for 1 h. (a) $\vec{g}$ = <111>, M=15,000x. The damage profile, as calculated by TRIM, is also shown on the photo. (b) $\vec{g}$ = <220>, M=38,000x. $\vec{B}$ = [110]. The scale units are given in μm .

different characteristic contrast. It is most likely a dislocation dipole (see figure 2-4). A similar dipole, although smaller (labelled B), can be seen as well. The dark hazy spot (C) on the photo is glue that had not been properly cleaned after preparing the sample.

The sample implanted with 1×10^{15} Si/cm^2 was also studied by XTEM after being annealed for 1 h at 900°C. This is shown in figure 4-6a and figure 4-6b. In figure 4-6a, the damage profile, as calculated by TRIM, is also shown. The damage in this sample is predominantly dislocation dipoles, similar to the one seen in figure 4-5. The longest defects are typically parallel to the surface, located at a depth that is equivalent to the maximum damage peak as calculated by TRIM. In figure 4-6a there is a defect that extends from the main defect band to the surface†. In figure 4-6b, there is one defect, parallel to the surface, that is more than 5 μm long. There are also defects that lie in the {111} plane that cross the previous mentioned defect, as well as dislocation dipoles deeper in the substrate. We hypothesize that the presence of long dislocation dipoles is due to the higher density of point defects in the as-implanted sample, which then condense into row defects (see §2-1-2). Row defects are the precursors to dislocation dipoles.

Since extended defects, including dislocation dipoles and dislocation loops, are stable up to a temperature of 1000°C [19], these two samples satisfy the necessary prerequisites for pre-damaged samples. The pre-damage is stable, the depth of damage is adjustable, and the type of damage in one sample is different than the type of damage in the other.

† Although it is not visible on the photo, the surface of the sample is visible on the film negative

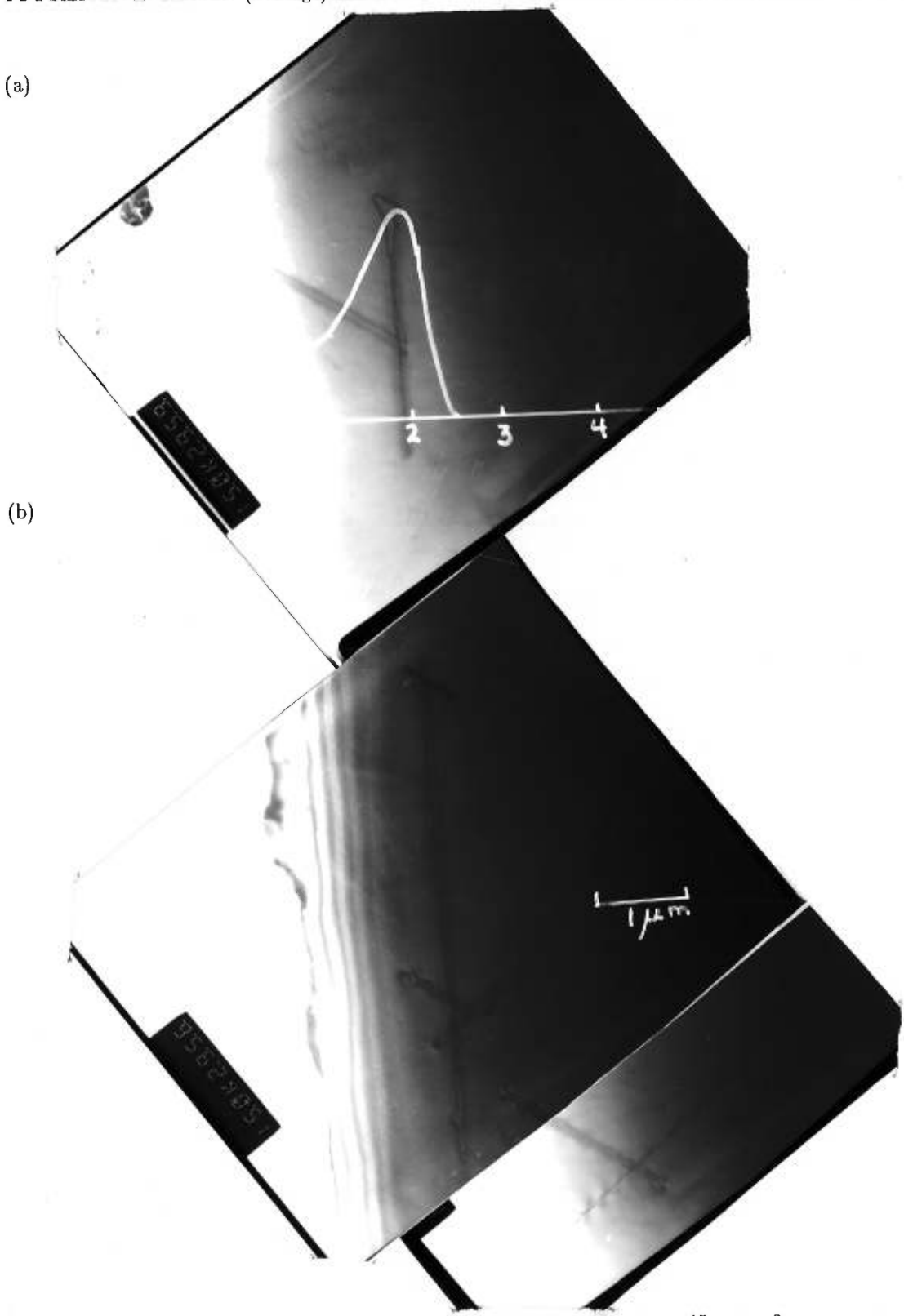

Figure 4-6. XTEM photos of samples implanted with $\phi = 1 \times 10^{15}$ Si/cm^2 and annealed at 900°C for 1 h. (a) $\vec{g}$ = <111>, M=15,000x. The damage profile, as calculated by TRIM, is also shown on the photo. (b) $\vec{g}$ = <111>, M=15,000x. $\vec{B}$ = [110]. The scale units are given in μm .

4-3 OXYGEN IN SILICON

To understand the effects of oxygen implantation into pre-damaged silicon, the properties of high temperature (570°C) oxygen implantation into un-damaged silicon must first be studied.

The three doses used in this study are $\phi = 0.3 \times 10^{17}$, 1.0×10^{17} and 3.0×10^{17} O/cm^2. Each sample was cut into two pieces and then analyzed separately. Typically, one half of the sample was annealed while the other half was left in the as-implanted state. These samples provide the standards with which to compare the results from the pre-damaged samples.

The range and straggling of the oxygen ions are determined.

The oxygen concentration profiles as a function of dose (as-implanted and annealed) are studied. A model is presented which describes the experimental results in terms of HO and HE preciptation. It is demonstrated that if the precipitates at d_O do not anneal in the early stages of the anneal, they act as an oxygen diffusion barrier. This limits the minimum dose that can be used to fabricate a SIMOX or BOX sample.

The damage type and distribution as a function of dose (as-implanted and annealed) are also studied. At the EOR, the damage is similar for all three samples. There is a thin layer of small defect clusters in the silicon film of the 3×10^{17} O/cm^2 sample. These defects are attributed to the relaxation of the strain, caused by excess vacancies, in the silicon film. This relaxation releases the oxygen atoms which were bound to the vacancies, and allows them to form precipitates. After the sample is annealed, there are three oxygen concentration peaks in the silicon film of this sample.

4-3-1 Range and Straggling

The measurement of the depth profiles of oxygen implanted silicon was obtained by RBS, ERD, and SIMS. Although the oxygen concentration profile cannot be obtained by XTEM, the depth range, rather than the depth of the maximum oxygen concentration, of the oxide precipitates in the annealed samples can be determined.

4-3-1-1 RBS/C

The oxygen profile cannot be determined directly from the He energy spectrum because a helium ion that has scattered off an oxygen atom at a depth of 2.5 μm has an energy which is too low to be detected in our experiment. However, the density of silicon in SiO_2 is less than it is in silicon ($2.2 \times 10^{22}/cm^3$ in SiO_2 and $5.0 \times 10^{22}/cm^3$ in Si) and thus a dip in the RBS spectrum indicates the presence of SiO_2. The oxygen concentration and profile can be calculated directly from the difference in counts from a pure silicon sample and an oxygen implanted sample, where a 56% reduction in the backscattered yield would indicate a region of pure SiO_2. Figure 4-7 shows the RBS spectra for two samples ($\phi = 3.0 \times 10^{17}$ and 1.0×10^{17} O/cm^2) and the calculated oxygen concentration profiles as a function of He energy. The oxygen profile, as a function of energy, is converted to a profile of oxygen concentration versus depth by using the Ziegler stopping powers of He in silicon [24]. The depth scale is calculated without adjusting the stopping powers for the presence of SiO_2 in the sample. For the oxygen doses used in this study, the above approximation introduces, in the region of maximum oxygen concentration, less than a 2% error in the stopping powers. The width of the surface oxides formed during the anneal were measured with RBS and ERD for each set of samples. The samples were then etched in HF (hydrofluoric acid) to remove the surface oxide. The depth scales shown in figure 4-7, and in all subsequent figures, have been adjusted to compensate for the volume of Si removed during the HF etch.

The depth resolution of a 3 MeV He scattered off the surface of a silicon sample was measured, and is 0.04 μm, which is consistent with the theoretical depth resolution estimated in §3-4-3. Similarly, the theoretical depth resolution at the oxygen peak is estimated to be 0.07 μm. However, it is known that the theory underestimates the observed resolution [123], and so to err on the side of caution, we quote a depth resolution of 0.1 μm. It is difficult to measure the oxygen profiles with $\phi = 1.0 \times 10^{17}$ O/cm^2 because the dip in the RBS spectrum is not much larger than the statistical fluctuations (see figure 4-7). With a dose of 3.0×10^{17} O/cm^2, the dip exceeds the statistical fluctuations. Using the same logic, one can see that the oxygen profiles for the annealed samples have a better statistical significance than the as-implanted samples because the oxygen dip narrows and deepens upon annealing. In spite of the estimated depth resolution of RBS at 2.5 μm being $\sim$0.1 μm, the statistical variance of the measured peaks was less than 0.06 μm for the as-implanted samples

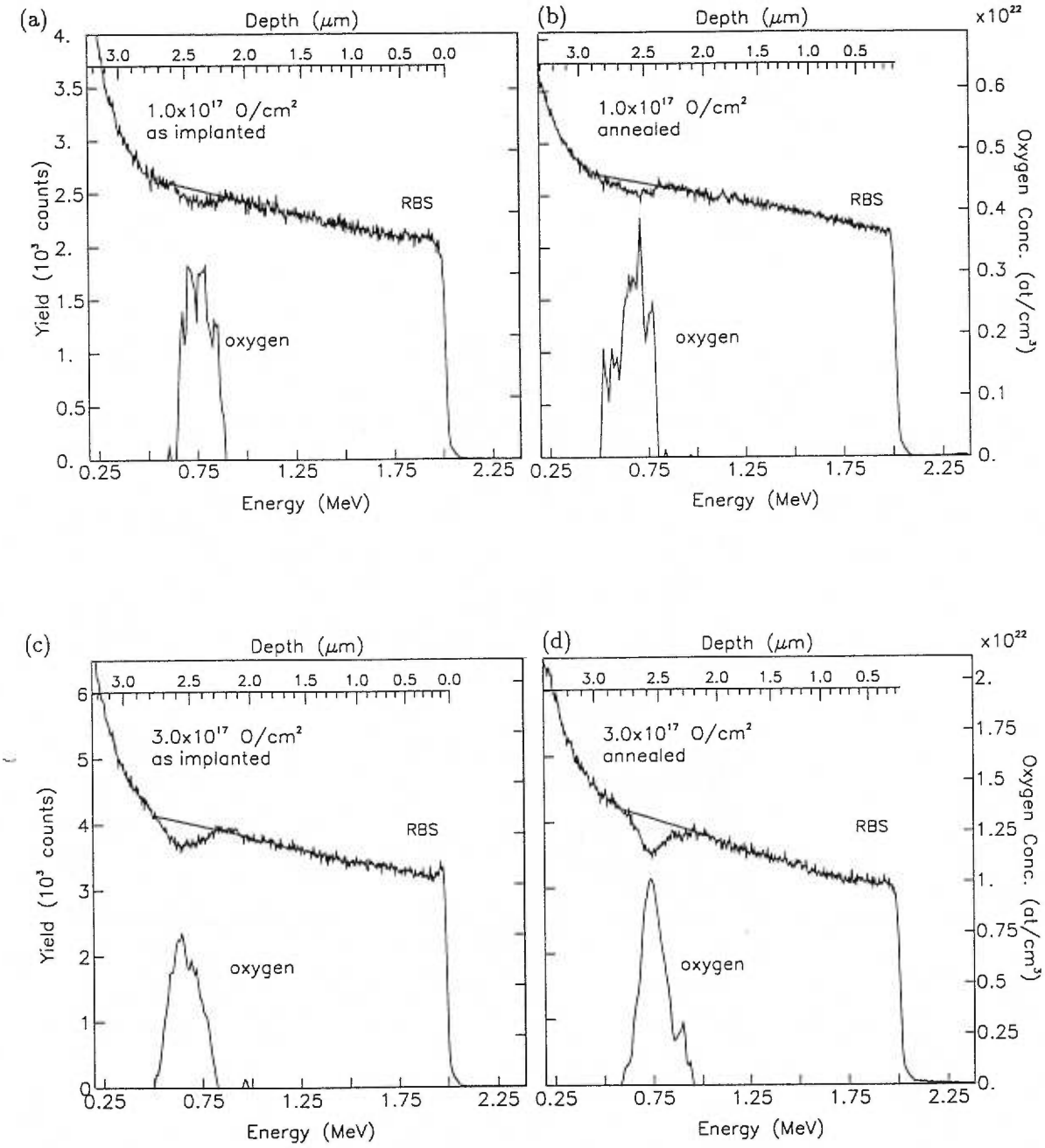

Figure 4-7. RBS spectra for $\phi = 1 \times 10^{17}$ O/cm^2 (a) as-implanted, (b) annealed, $\phi = 3 \times 10^{17}$ O/cm^2 (c) as-implanted, and (d) annealed samples, and the respective calculated oxygen concentration. The straight lines approximate the random spectra for non-implanted silicon. (3 MeV He, $\theta = 67.5°$, <110>)

(9 separate samples were measured) and less than 0.04 μm for the annealed samples (7 measured samples). The peak of the oxygen concentration, as calculated by RBS, is located at 2.54±0.05 μm.

4-3-1-2 ERD

The absolute depth of the oxygen profile cannot be obtained from ERD measurements, for the following reason. The probing depth of ERD in silicon is approximately 0.9 μm, and therefore the samples have to be etched prior to the analysis. Two etching techniques were used, a wet etch in a KOH/propanol mixture, and a reactive ion etch (RIE) using CF_4 and O_2. The details of these etching techniques are described in §3-3. It is not possible to obtain a measure of the depth of etching when using KOH. The measurement of the RIE etch depth was only accurate to within 0.2 μm. Therefore, the absolute depth of the ERD profiles are adjusted to the depths deduced from RBS/C and XTEM, as these measurements are more precise.

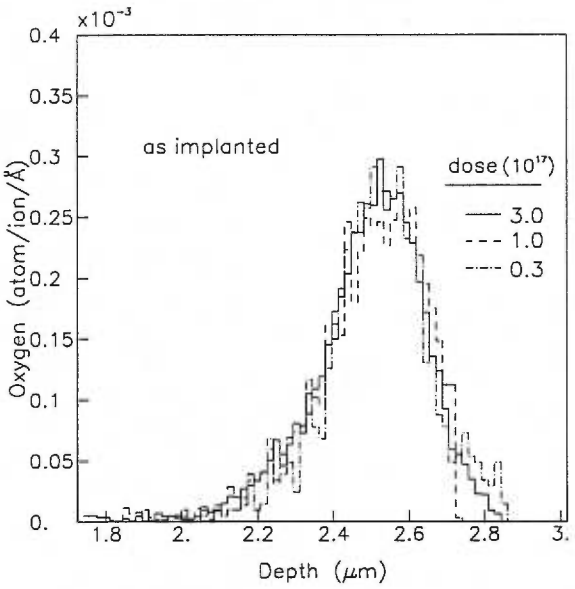

Figure 4-8. The as-implanted oxygen concentration profiles (atoms/ion/Å) for ϕ = 0.3, 1.0 and 3.0 x 10^{17} O/cm^2 samples. The profiles were measured using ERD.

Although the absolute depth is not well measured, the relative depths within each sample have depth resolutions of 0.01 μm at the surface of the etched sample (typically at 1.8 μm) and better than 0.05 μm at the peak position of the oxygen (§3-4-2). It is for this reason that the straggling

calculations were done with the ERD measurements rather than the RBS measurements. The data for seven samples were fitted to a Gaussian profile, and the straggling was defined as σ. In all cases, the shape of the as-implanted oxygen profiles were the same, independent of dose, within the limits of statistical error (see figure 4-8). The straggling of 2.5 MeV oxygen in silicon was measured by ERD to be 0.13 ± 0.01 μm.

4-3-1-3 SIMS

To convert SIMS data into a depth profile, the sputter rate of the target must be calculated. If one assumes that the sputter rate is constant throughout the experiment, then the sputter rate is calculated by dividing the depth of the sputtered crater by the total sputter time. The depth of the crater is measured with a profilometer. Using this technique, the depth of the oxygen peak for 3.0×10^{17} O/cm^2 was measured, and the results were 2.45, 2.41, and 2.43 μm (one sample, multiple measurements). For the sample with a dose of 1.0×10^{17} O/cm^2, the oxygen peak was measured at 2.7 μm. These results are within 6% of the positions of the oxygen peaks as measured by RBS, and hence are considered reasonable. The straggling measured by SIMS is 0.16 μm, and is larger than that measured by ERD.

4-3-1-4 Discussion

The depth of the oxygen peak for as-implanted samples is summarized in Table 4-IV. As can be seen from the data, the oxygen peak, as measured by RBS and SIMS is approximately 6% deeper than what is predicted by TRIM. This is not remarkable in and of itself, since others have also reported a discrepancy between TRIM and experimental results, where TRIM typically underestimates the range of oxygen in silicon for MeV implantations [25,26,29]. The volume increase of the sample due to the implantation and formation of SiO_2 ($\phi = 3.0 \times 10^{17}$ O/cm^2) is less than 70 nm-cm^2, and is not sufficient to explain the discrepancy between TRIM and the experimental results.

The straggling, as calculated from ERD and SIMS measurements is also larger than that predicted by TRIM. The samples studied in this thesis were all implanted at high temperatures and low current densities, and consequently the oxygen can migrate over large distances during the implantation since the diffusion rate is high and the implant times are long (24 h for $\phi = 3.0 \times 10^{17}$ O/cm^2). We also know that oxygen can accumulate preferentially on damage sites (HE precipitation), at the

TABLE 4-IV

A summary of the measured and estimated projected range and straggling of 2.5 Mev O in silicon. The measured concentrations were fitted to a Gaussian shape with the peak denoted by R_p and σ denoted by ΔR_p. Each measurement listed in the table was obtained from a separate sample. The error in the average calculation was determined by the statistical variations in the measurements, and did not include the inherent depth resolution of the measuring technique. The TRIM estimate was based on the full collision cascade calculations, and the the peak, not the mean, depth was listed.

	1×10^{17} O/cm^2		3×10^{17} O/cm^2		average	
	R_p	ΔR_p	R_p	ΔR_p	R_p	ΔR_p
RBS	2.6, 2.5, 2.55, 2.5, 2.55, 2.4		2.57, 2.52, 2.56		2.53±.06	
ERD		0.13, 0.13, 0.13, 0.14, 0.12[†]		0.13, 0.13, 0.12		0.13±0.01
SIMS	2.7	0.17	2.43±0.02	0.16	2.56±0.2	0.16±0.01
TRIM					2.38	0.10

[†] 0.3×10^{17} O/cm^2

peak projected range (HO precipitation), and even past the maximum projected range (ET precipitation) during implantation, depending on the implant conditions (§2-4-1). Hence, the fact that the straggling in the oxygen concentration profile is larger than that predicted by TRIM is not surprising.

In conclusion, the depth range for oxygen in silicon, independent of dose, was measured to be 2.55 ± 0.10 μm, with a straggle of ~ 0.15 μm.

4-3-2 Damage

The damage in our samples was probed by two complementary techniques, RBS/C and XTEM. Channeling is sensitive to small defect clusters, point defects, interstitial atoms, and amorphous pockets, and can be used to obtain a qualitative profile of the damage in the sample, as a function of depth (although the depth scale itself is only an approximation). It is difficult with RBS/C to determine the nature of the defects within the sample, except in pure amorphous or nearly perfect crystalline material. If the de-channeling is caused by a multitude of different defect types, as it is in this case, it is also difficult to obtain a quantitative measure of the damage. By using XTEM to profile the damage in the samples, the predominant defect nature (amorphous, polycrystalline, twins, extended defects) can be readily observed either directly, or with diffraction analysis. However, measuring the

relative amounts of damage can be difficult and time consuming, and we did not do this in our study. Unlike RBS/C, point defects are virtually invisible when imaging samples with XTEM, unless very high magnifications are used. It is possible with XTEM to obtain a reasonably accurate measure of the depth scale.

4-3-2-1 As-Implanted

Figure 4-9 shows the aligned <110> and non-aligned energy spectra for backscattered He ions from as-implanted samples implanted with $\phi = 0.3 \times 10^{17}$, 1.0×10^{17} and 3.0×10^{17} O/cm^2. It should be immediately pointed out that the sample implanted with $\phi = 0.3 \times 10^{17}$ O/cm^2 was initially implanted with 2 MeV silicon and then annealed for 1 h at 900°C. This does not appear to affect the RBS/C spectrum (as will be discussed in §4-4-1) and is thus used to illustrate the differences in the damage levels at different oxygen doses. The depth scales shown in the figure are calculated using the stopping powers for amorphous targets, and consequently are not valid for the aligned spectra.

The most immediate and obvious characteristic of all the aligned spectra is that the yield in the near surface region of the samples is the same as the yield in a virgin sample, indicating that the sample has very few defects in the crystalline film. The second most obvious feature is that none of the samples show any indication of an amorphous region, even at the EOR. The aligned backscattered yields of these samples all have a similar shape, with the lowest yield from the lowest dose sample. Contrary to intuition, the highest dose sample (ϕ =3.0×10^{17} O/cm^2) does not have the highest backscattered yield. The change from undamaged crystal to the region of maximum damage occurs over a depth range ~0.3 μm.

It is much more difficult to interpret the channeling results from these samples than it was for the silicon in silicon samples because the de-channeling comes from more than one source, namely, amorphous SiO_2, interstitial oxygen, interstitial silicon, and various types of dislocations. If the He ion is scattered off of an interstitial oxygen, it will not have the same energy as He scattered from a silicon interstitial, and consequently there will not be direct backscatter from oxygen interstitials observed in this data (the energy would be too low to be detected at the depths at which the oxygen is located). Multiple scattering will occur (He scatters from an oxygen ion, so it is no longer channeled, and then backscatters from a silicon atom). However, this is difficult to analyze analytically when the target contains an uneven distribution of scattering centers (oxides in this case). In addition, when

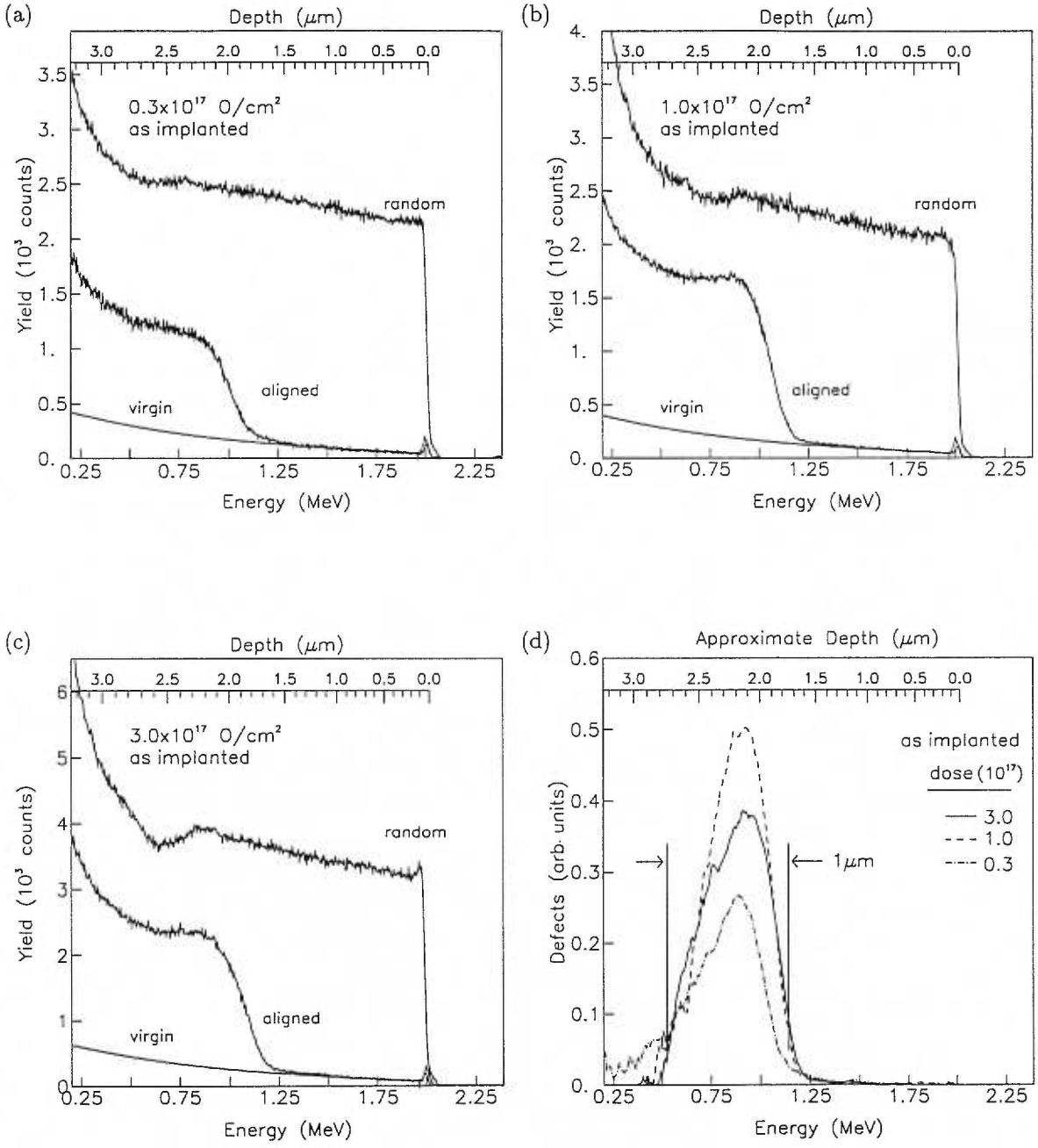

Figure 4-9. RBS/C spectra of as-implanted ϕ = (a) 0.3, (b) 1.0 and (c) 3.0×10^{17} O/cm^2 samples. (3 MeV He, $\theta = 67.5°$, <110>) (d) Damage profiles calculated, assuming that only point defects are present. All depth scales were calculated assuming that the targets were amorphous.

there is more oxygen in the sample, there are more dechanneling centers present, which increases the backscatter yield, but there is less silicon per cm^3, which decreases the backscatter yield. Each de-channeling center has a different probability of scattering the He ion, and unless the exact ratios of the respective de-channeling effects are known, the results of the damage calculations should not be considered absolute. However, we do know that there is a larger cross-section for de-channeling from point defects and interstitials than there is for dislocations [124], and therefore, if the predominant defects are interstitials, then the defect analysis will give a reasonable approximation of the damage distribution.

Bearing the above in mind, if we assume that the predominant cause of de-channeling in the samples is not point defects but small amorphous pockets of SiO_2 or Si, which may be treated like clusters of point defects, then the damage profiles of the samples are represented by the curves shown in figure 4-9d. The data was analyzed assuming that the average scattering cross-section for the defects is equivalent to the Rutherford cross section (*i.e.* $f_\sigma = 1$, eq'n 3-5). The assumption that the predominant defects are point defects is not unreasonable, for the following reason. Firstly, the majority of the Frenkel pairs are created in the EOR region (> 1000 Frenkel pairs per oxygen ion). The concentration of oxygen in the EOR region is $\sim 10^{21}$ O/cm^3 for the lowest dose (0.3×10^{17}) sample, which is more than a factor of 3 larger than the solubility limit of oxygen in silicon at 1400°C ($\sim 10^{18}$ at/cm^3). Therefore the oxygen has most probably formed oxide precipitates which prevent the silicon interstitials from migrating out of this region (the diffusion of Si in SiO_2 is 10^{-20} cm^2/s at 600°C). Consequently one would expect a large fraction of the de-channeling to be a result of direct scattering off silicon interstitials or from the silicon in the SiO_2 pockets.

The shape of the damage distribution is a skewed Gaussian, with the interface between the silicon film and the EOR sharper than the interface between the EOR and the substrate. Although the depth of the damage cannot be calculated accurately from RBS/C, the relative width of the damage can be measured. This is because the He ions lose energy in this damaged region at the same rate as if it were an amorphous sample. The width of the damage region is approximately 1 μm.

The damage profile for the high dose sample ($\phi = 3.0 \times 10^{17}$ O/cm^2) is lower than the medium dose sample ($\phi = 1.0 \times 10^{17}$ O/cm^2). However, the damage profile was calculated assuming that only point defects or small amorphous pockets were present. The lower damage profile for the high dose

sample indicates that the defects have aglomerated together to form intermediate defect clusters or extended defects.

Figure 4-10 shows the XTEM photos of the ϕ =0.3 $\times$ 10^{17} O/cm^2 as-implanted sample at 15k and 38k magnification. There are no observable defects in the silicon film (the region between the surface of the sample and the highly defected oxygen-rich region. See figure 4-10a. The damage starts abruptly at 2.3 μm. The dark bands crossing the picture are contour lines and are related only to the fact that the silicon sample is slightly bent within the microscope. There are also no observable defects in the silicon substrate. Figure 4-10b shows an expanded view of the defect layer. There appear to be two distinct regions of damage. The main band of damage is approximately 0.5 μm wide, located at a depth of 2.3 μm to 2.8 μm. In this region, one can see small straight black lines intermixed in the damage region, indicating the presence of extended defects or IDCs. The other region of damage extends much deeper into the substrate, with some damage apparent even at a depth of 3.3 μm (indicated by 'A' in figure 4-10b). This damage region does not exhibit the same characteristic contrast as the previously mentioned region, but instead appears as small points of contrast, which could be small amorphous pockets, point defect clusters, or even strained SiO_2 precipitates. A further increase in magnification did not clarify the nature of these spots. The maximum oxygen concentration (using the estimate of 2.55 μm as determined in the previous section) falls in the middle of the dark defect band, and is indicated by an arrow. The sample is not amorphous in this region. There is not a great deal of observable stress, typically indicated by a light band on either side of the defect region.

For the medium dose sample, ϕ = 1.0 $\times$ 10^{17} O/cm^2, there are also no detectable defects in the silicon film (figure 4-11a). Figure 4-11b is the same sample, with the magnification increased, giving a better picture of the damaged region. The transition from the crystalline film to the damage region is abrupt, and starts at 2.3 μm, but the interface between the damage layer and the substrate is not abrupt at all, rather the quantity of damage slowly decreases as it extends into the substrate, as was the case with the low dose sample. The range of damage in the sample is, if one includes all visible evidence of damage, 2.3 μm to 3.2 μm. A Selected Area Diffraction (SAD) pattern was taken of the damaged region, and is shown in figure 4-11c. There is no evidence of amorphous material, twins, or polycrystalline silicon in this region.

Figure 4-12 shows the XTEM photos for the high dose sample (ϕ = 3.0 $\times$ 10^{17}). Although the damage region appears to be amorphous (figure 4-12a), this is only an illusion due to the fact that the

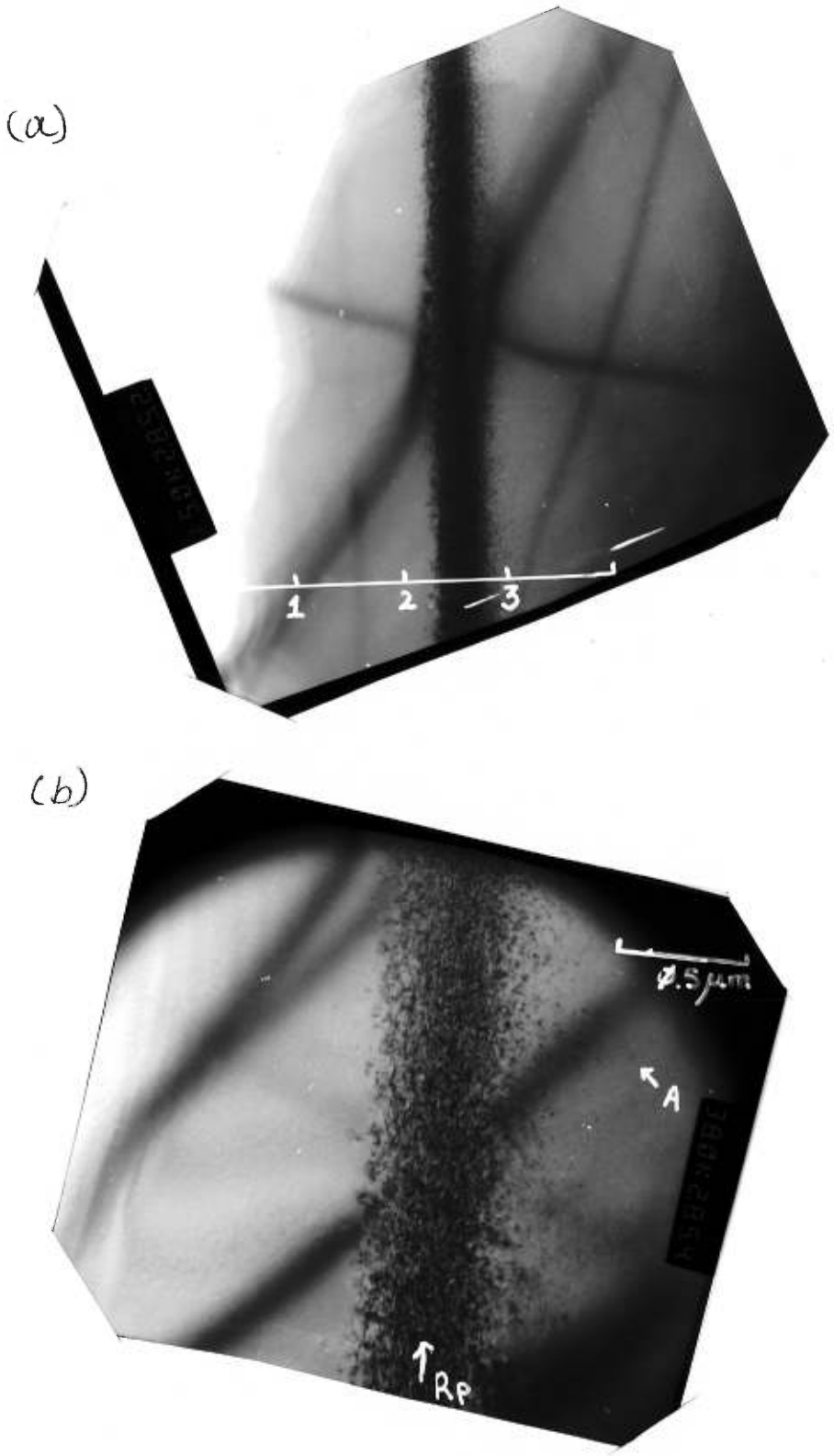

Figure 4-10. XTEM photos of as-implanted $\phi = 0.3 \times 10^{17}$ O/cm^2 sample. (a) M=15,000x, $\vec{g}$ = <111> and (b) M=38,000x, $\vec{g}$ = <111>. $\vec{B}$ = [110]. The scale units are given in μm .

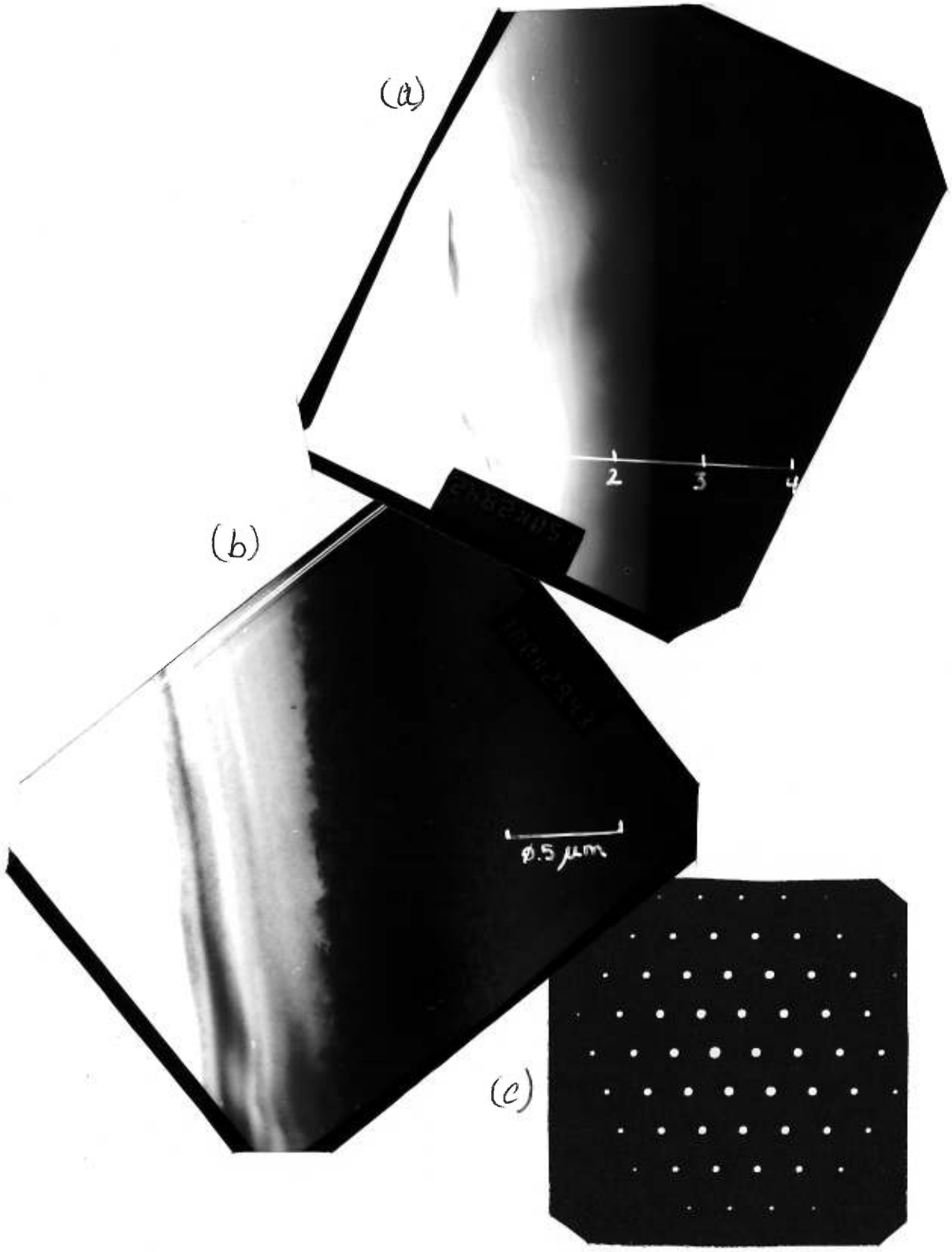

Figure 4-11. XTEM photos of as-implanted $\phi = 1.0 \times 10^{17}$ O/cm^2 sample. (a) M=15,000x, $\vec{g}$ = <111> and (b) M=38,000x, $\vec{g}$ = <111>. $\vec{B}$ = [110]. The scale units are given in μm . (c) Selected Area Diffraction Pattern (SADP) of damaged region, $L = 1.1$ m.

sample has not been well thinned. When inspecting the sample at the edges of the thinned regions, it was observed to be similar to the damage in the low dose sample. SAD patterns were also taken, and confirmed that this region is not amorphous. What is noticeable about this sample though, is that the silicon film is no longer defect free. There appears to be a band of small defects located at ~1 μm. The silicon on either side of this band remains defect free. Figure 4-12b is an expanded view of these defects. The defect in the center of figure 4-12b (A) has a large strain field surrounding it, indicated by a dark region slowly fading to the background contrast. It could be an oxide precipitate with an associated strain field, although this hypothesis has not been experimentally confirmed. One of the smaller defects (B) is characterized by a straight dark line, surrounded by a strain field, possibly indicating a dislocation. High resolution XTEM would be needed to confirm this.

4-3-2-2 Annealed

After the samples were annealed at 1300°C for 12 h, they were again analyzed with RBS/C. The results are shown in figure 4-13a-c. In all cases the dechanneled yield is reduced. Figure 4-13d shows the RBS/C spectra of the $\phi = 1.0 \times 10^{17}$ O/cm^2 sample, before and after annealing, after the sample was etched approximately 1 μm in KOH. As can be seen from the figures, not only is the channeling yield reduced, but the shape of the spectrum has also changed. The peak damage region (indicated by a dashed line in figure 4-13d) is not as pronounced, and there is no subsequent decrease in the yield immediately after this region. It can also be seen from figure 4-13d that there is a slight increase in the depth of the crystalline film. The slight rise in the spectra in figure 4-13d (indicated by arrows) is due to the He ion scattered off the oxygen in the sample.

XTEM analysis indicates that most of the damage in the samples has changed into extended defects which are pinned by the oxide precipitates. This formation and growth of the oxide precipitates, and the change in the damage type, is illustrated very effectively with the low dose, $\phi = 0.3 \times 10^{17}$ O/cm^2, sample, as shown in figure 4-14a and figure 4-14b. The silicon film is still effectively defect free. The surface of the sample has a thick SiO_2 layer (3000 Å) that grew during the anneal in an Ar/O_2 atmosphere. Even at the low magnification, the oxide precipitates in the EOR are visible (small dark polygons). At the higher magnification it can be seen that the remaining defects are predominantly dislocations (straight dark lines) extending between the oxide precipitates. In addition to the dislocations, the photo also shows signs of strain surrounding the dislocations and some of the oxide precipitates. These photos were taken under high contrast conditions (dynamical),

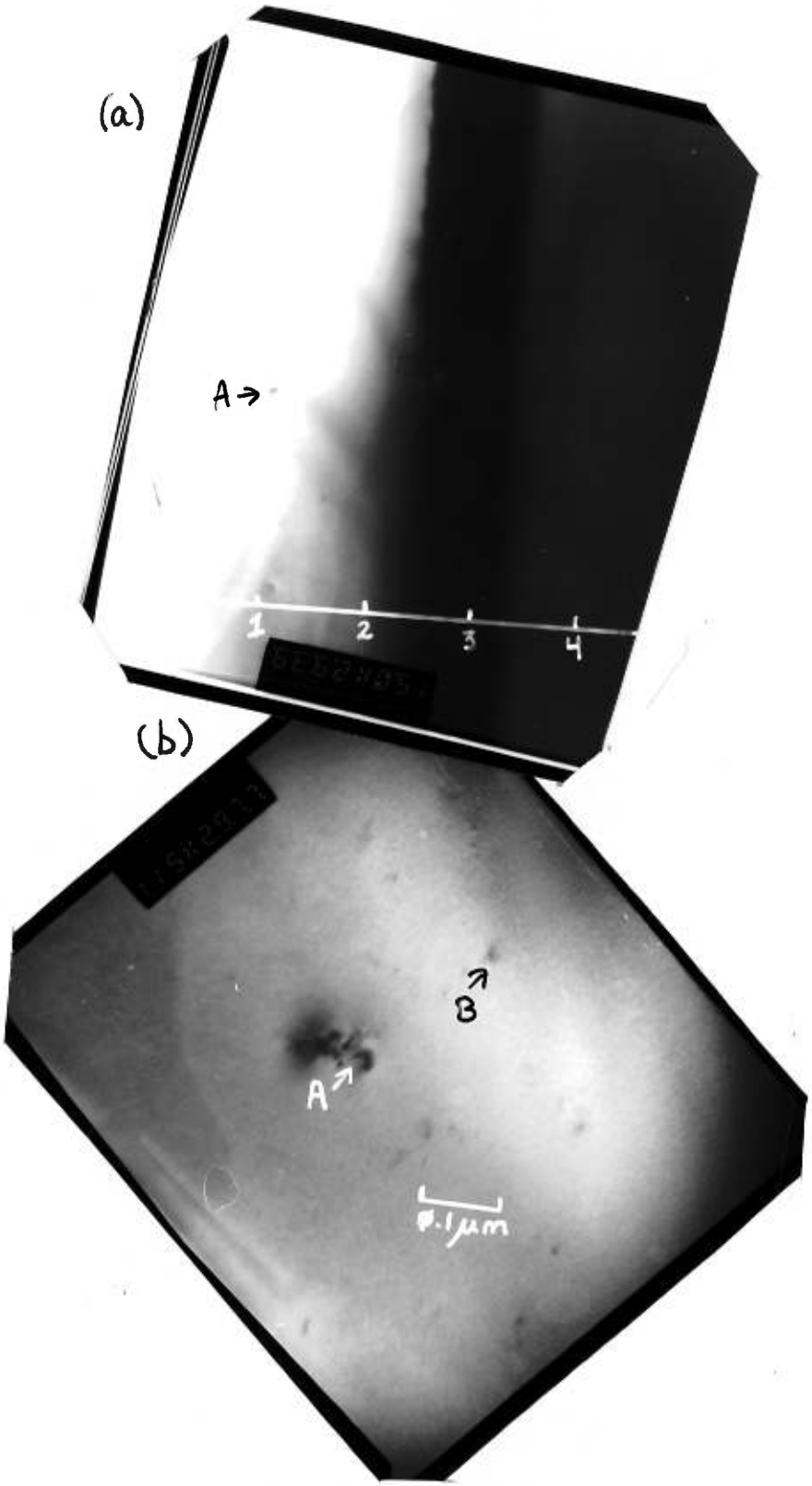

Figure 4-12. XTEM photos of as-implanted $\phi = 3.0 \times 10^{17}$ O/cm^2 sample. (a) M=15,000x, $\vec{g}$ = <111>. (b) Defects found at ~1 μm. M=115,000x, $\vec{g}$ = <111>. $\vec{B}$ = [110]. The scale units are given in μm . For discussion of labelled defects, see text.

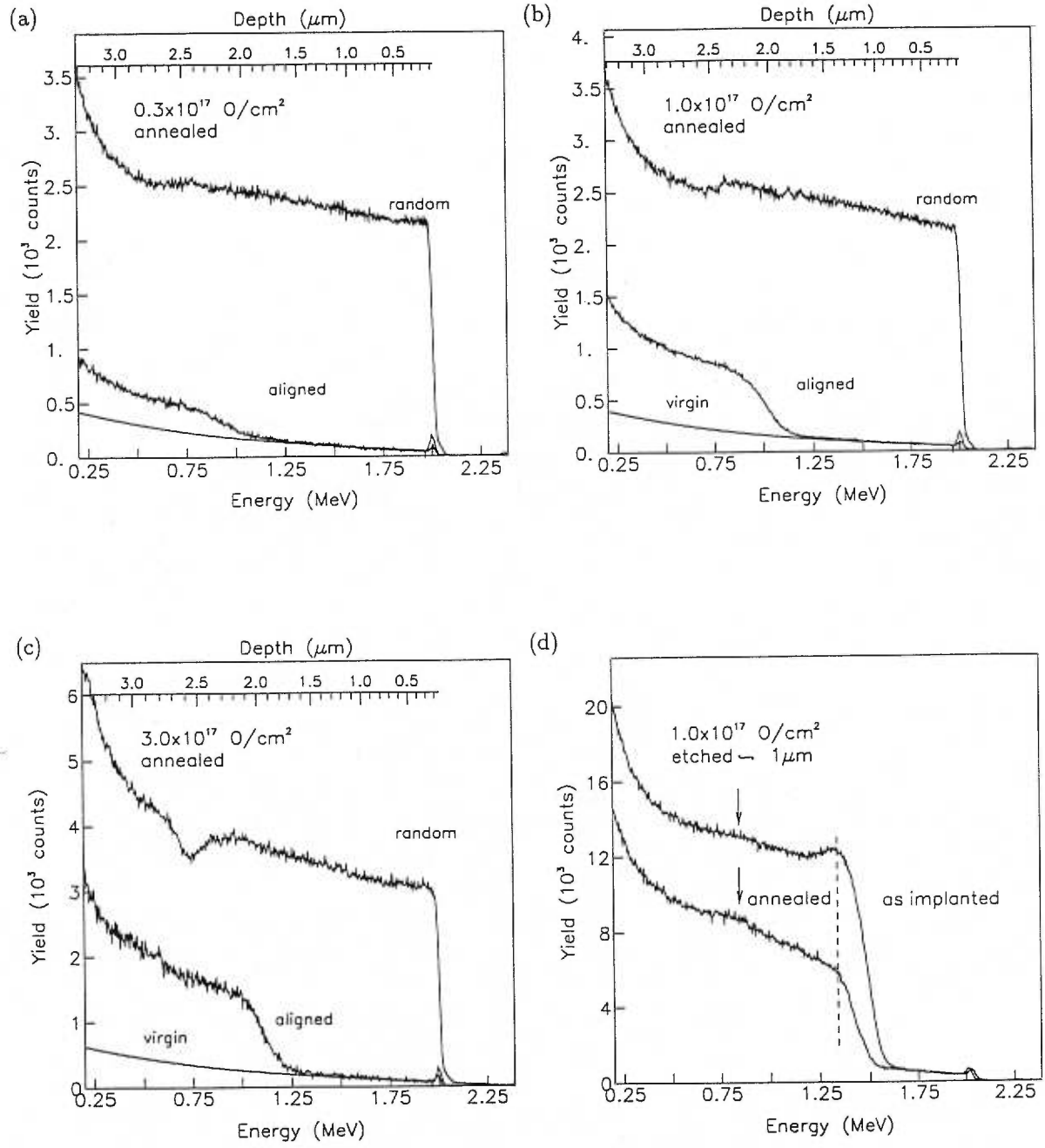

Figure 4-13. RBS/C spectra of annealed ϕ = (a) 0.3, (b) 1.0 and (c) 3.0×10^{17} O/cm^2 samples. The depth scale was calculated assuming that the target was amorphous. (3 MeV He, $\theta = 67.5°$, <110>) (d) Aligned backscattering yield of as-implanted and annealed samples implanted with 1.0×10^{17} O/cm^2. Arrows indicate direct backscatter from oxygen atoms in the sample. Both samples have been etched in KOH prior to the analysis.

with the diffraction beam $\vec{g}$ = <111>. In a low contrast, multi-beam condition, a photo of a high dose, $\phi = 3.0 \times 10^{17}$ O/cm^2 sample also shows the stressed silicon between the oxides (figure 4-15a). This is seen most dramatically in the upper left corner of the photo. No strain is observed in the oxide precipitates themselves. A micro-diffraction pattern was obtained† from the oxide precipitate indicated by the arrow, and is shown in figure 4-15b. This pattern is indicative of amorphous material. The diffraction spots come from the silicon that lies either above or below the oxide precipitate.

In all three samples, the damage at the EOR was composed of dislocations extending between oxide precipitates. There is strain around the precipitates and dislocations, although the precipitates themselves show no sign of internal strain. The only significant difference between the EOR regions as a function of dose was the size and number of oxides, and the total number of dislocations connecting them. However, there is a very big difference in the quality of the silicon film in the high dose ($\phi = 3.0 \times 10^{17}$ O/cm^2) sample. Whereas the lower dose samples have no visible signs of defects or oxide precipitates in the silicon film, this sample has many defects in the silicon film, shown in figure 4-16. At about a depth of 1 μm, there is a large rectangular dark region on the photo. Upon further magnification, the nature of this defect, or precipitate, did not become any more apparent. It was the only defect of this kind that was observed. There are other small defects that can also be discerned, if one looks closely at the photo, but beware of tiny white spots – they are most probably just dust specs on the negative. The defects can be seen as very small black dots scattered throughout the silicon film. These small defect clusters were only noticed after the photo had been developed. The nature of these defects are unknown. They do not form a distinct layer or band, nor can they be described as following the same pattern as the defects noticed in the as-implanted silicon film of the same dose.

† Courtesy of G. Carpenter of CANMET.

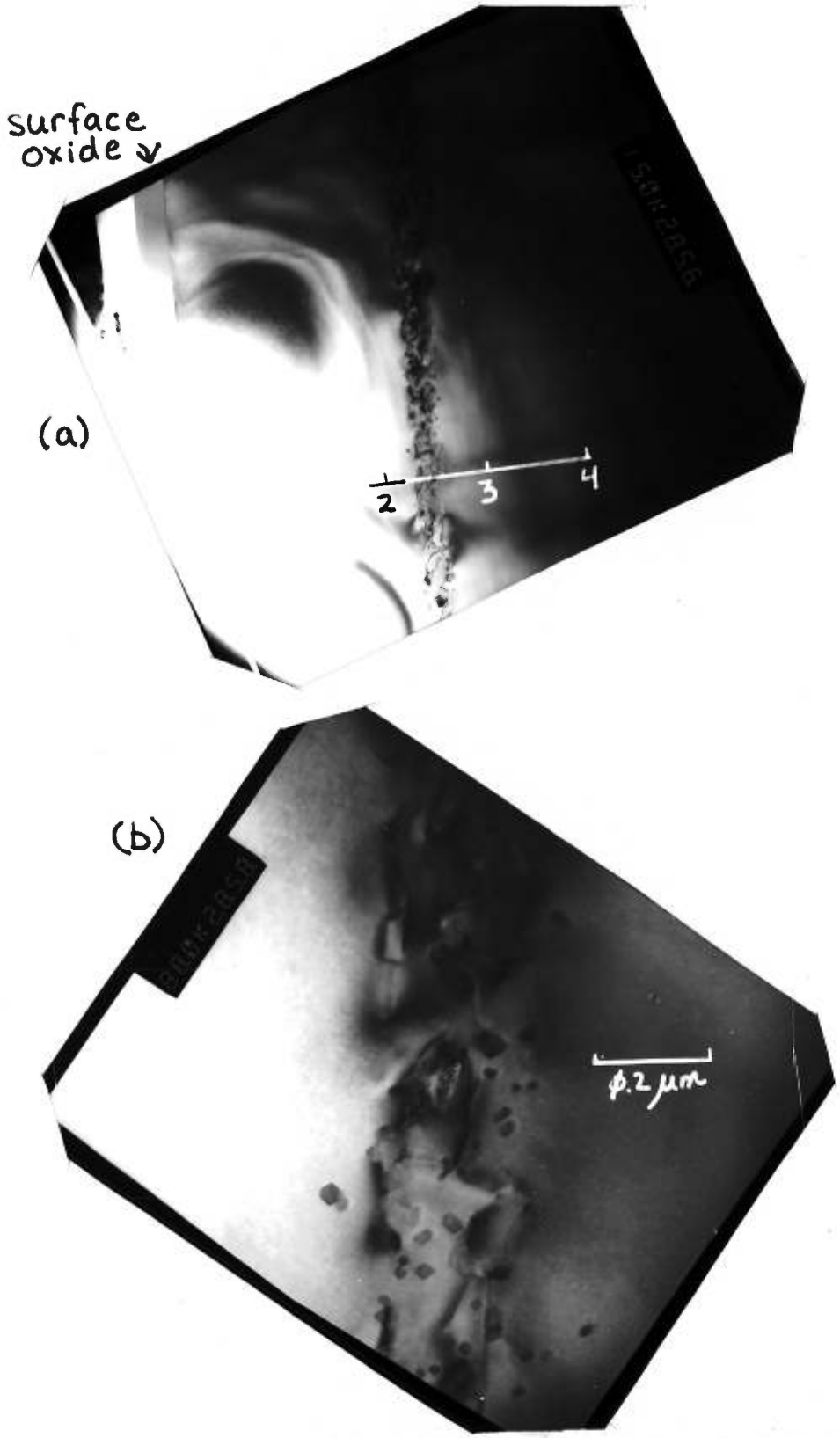

Figure 4-14. XTEM photos of annealed $\phi = 0.3 \times 10^{17}$ O/cm^2 sample. (a) M=15,000x, $\vec{g}$ = <111> and (b) M=38,000x $\vec{g}$ = <111>. $\vec{B}$ = [110]. The scale units are given in μm .

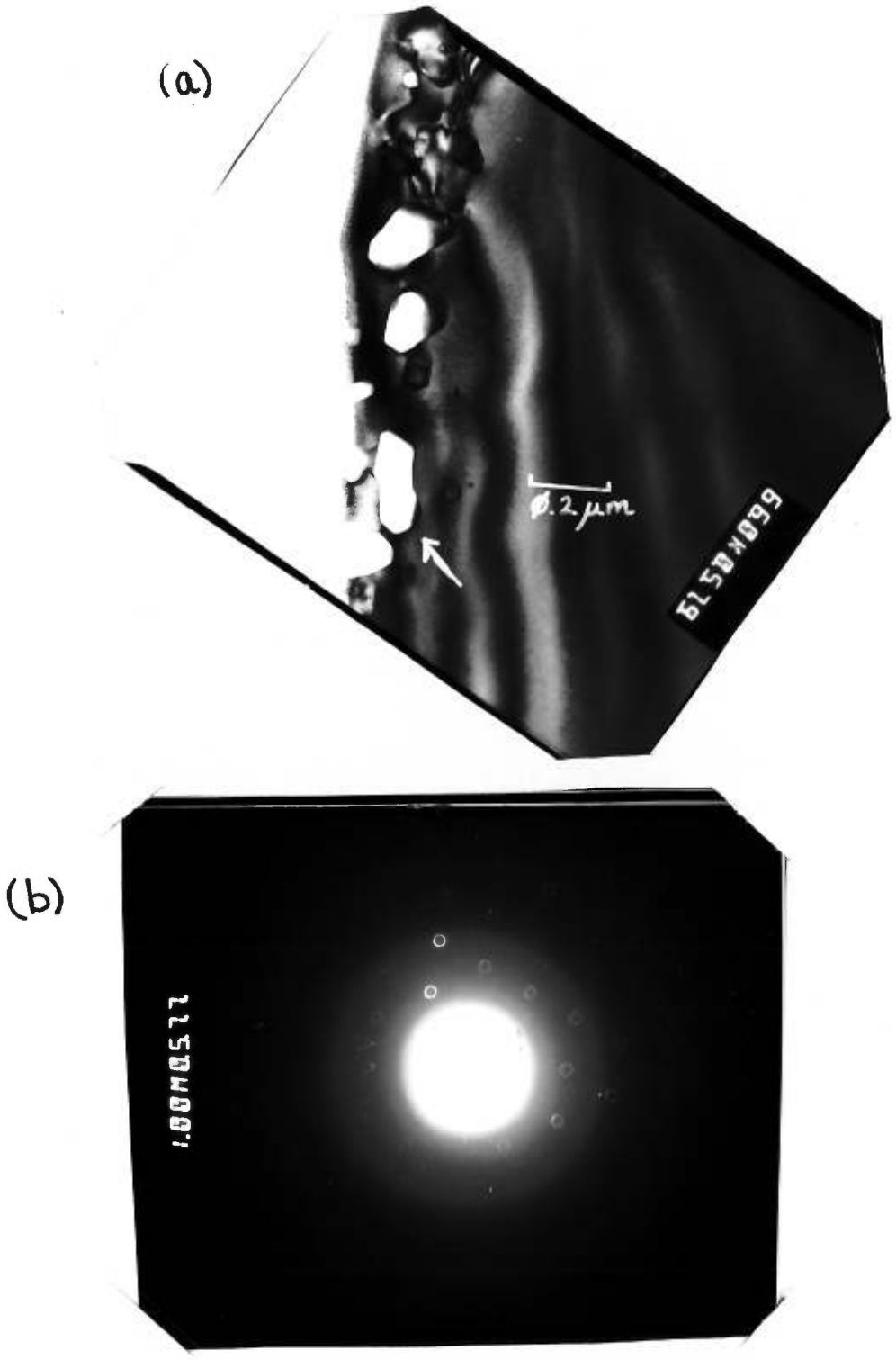

Figure 4-15. (a) XTEM photo of annealed $\phi = 3.0 \times 10^{17}$ O/cm^2 sample. M=66,000x, $\vec{g}$ = multi-beam. (b) A micro-diffraction pattern, $L = 1.00$ m, taken from the oxide precipitate indicated by the arrow in (a). $\vec{B} = [110]$. The scale units are given in μm .

Figure 4-16. XTEM photo of annealed $\phi = 3.0 \times 10^{17}$ O/cm^2 sample. M=15,000x, $\vec{g} = <111>$. $\vec{B} = [110]$. The scale units are given in μm .

4-3-2-3 Discussion

One would expect, at the high implant temperatures used in these experiments (T_i = 570°C), that most of the Frenkel pairs would recombine during the implantation, thus preserving the crystalline nature of the target. For the most part, this expectation has been borne out by our RBS/C and XTEM studies. Even in the as-implanted state, the RBS/C analysis indicates that there is little or no damage in the silicon film. Similarly, the damage in the EOR was not sufficient to produce an amorphous layer, even at the highest dose of 3.0×10^{17} O/cm^2. In contrast, Touhouche *et al.* [136] found that the damage at the EOR was sufficient to produce an amorphous layer when $\phi = 0.3 \times 10^{17}$ O/cm^2 and $T_i < 100$°C.

The general shape of the damage distribution is the same for all the oxygen doses studied. There is little or no damage in the silicon film. At approximately 2.3 μm, the damage concentration changes from a nearly perfect crystal to a highly damaged crystal over a depth region of 0.3 μm. The damage in the region 2.3–2.6 μm is predominantly stacking faults and small dislocations. After 2.6 μm the defect structure changes into what appears to be small amorphous pockets, oxide precipitates or point defect complexes. This damage extends into the substrate to depths of 3.2 μm. Each of these depth regions will be discussed separately.

The XTEM results indicate that there is some damage in the silicon film of the $\phi = 3.0 \times 10^{17}$ O/cm^2 sample. This damage is located in a narrow (0.4 μm) depth region around 1.2 μm. Other researchers [13-15] studying MeV oxygen implantation into silicon have found that at higher oxygen doses ($\phi > 1.0 \times 10^{18}$ O/cm^2) and high implant temperatures, a dense band of tangled dislocations will form in the silicon film, somewhere between the surface and R_p. Different researchers have found this dislocation band at different locations within the silicon film (see Table 2-II). The dislocation network (which only appears when $T_i > 400$°C) occurs at a depth where the strain is balanced between the negative strain at the surface (excess vacancies) and the positive strain at R_p (excess interstitials and SiO_2). The formation of the dislocations is the method by which the excess strain in the sample is released† [14,20,34,80,98-100]. The silicon on either side of this band is typically defect free. Comparing our results to the ones described above, we conclude that the thin band of small (~20 nm) and thinly dispersed defect clusters in the $\phi = 3.0 \times 10^{17}$ O/cm^2 sample is the initial defects which are formed in an effort to reduce strain in the silicon film.

† For a more detailed analysis of strain reduction through the process of defect formation, see §2-5-1-4

Our analysis has shown that the depth (d_O) up to which the silicon film retains a high crystalline quality is not a function of oxygen dose. For any one sample there is only a slight gradient in the oxygen and oxide concentration profiles in the depth region surrounding d_O (to be demonstrated in §4-3-4). Thus the sudden onset of damage at 2.33 μm is not related to a critical concentration of oxygen or oxide precipitates. According to the standard defect production models [37], the high crystalline quality of the silicon film is a result of a rapid recombination of defects in the silicon film. However, at the EOR the defects cannot recombine fast enough and thus complex defects form at depths greater than d_O. Thus we conclude that the depth d_O is a function of the generation rate of defects (which is proportional to the ion flux) and the recombination rate of these same defects (which is dependent upon T_i).

The maximum scattering yields in the RBS/C spectra occur at approximately 0.3 μm after the onset of damage. Since it is known from the XTEM photos that the damage starts at 2.3 μm, and since it is also known from RBS studies that the depth of the peak oxygen concentration, R_p, is 2.55 μm, it is concluded that the maximum yield in the aligned RBS/C spectra is a result of direct scattering from silicon, or from the silicon in the oxide precipitates, in the region of maximum oxygen concentration.

The maximum range of the damage (3.2 μm) extends well beyond the peak range of the oxygen ions (2.55 μm). There are a few possible explanations for this. The first is that the excess silicon interstitials created by oxide precipitation diffuse outwards, away from R_p, and then cluster to form small defect centers. This diffusion can be enhanced by the strain gradient produced by the formation of oxide precipitates. It is also possible that the oxygen ions had been unintentionally channeled during the implantation. However, all seven samples analyzed by XTEM show the same defect structure, and it is unlikely that oxygen was accidently channeled seven times in a row.

There is yet a third possible explanation for the extended range of damage seen in the XTEM results. There could be a few, but nonetheless large, oxide precipitates in this region. Cerofolini *et al.* [17] have hypothesized (see §2-4-1) a region beyond the ion range where hot collisional cascades cause the oxygen ions, within the volume of the cascade, to coalesce into a single oxide precipitate (ET precipitation). The depth at which the largest oxides are present changes with the dose, increasing as the dose increases. Their studies were done with 100 keV oxygen ions, and thus it was difficult to visually separate the different regions within the as-implanted samples. At 2.5 MeV it is possible that, because the physical separation of EOR damage and the ET precipitation region is larger, it is

easier to visibly differentiate these two regions. The ET precipitation hypothesis is consistent with the difference in appearance of the two defect regions visible in the XTEM photographs (figure 4-10b). If this hypothesis is valid, then one would also expect that a 6 MeV oxygen implantation would show an extended damaged region. In the work of Touhouche *et al.* [136], silicon was implanted with 3.0×10^{17} O/cm^2 at 6 MeV. The implant was done with a sample temperature of less than 100°C and consequently the EOR was amorphous, with a large strained layer beyond the amorphous layer. The width of the amorphous region is ≈ 0.5 μm, and the strained region beyond the amorphous band goes 0.4 μm deeper into the substrate. Whether this is, or is not, indicative of ET precipitation is not clear.

After the samples are annealed, there is a coarsening of the oxide precipitates, which is expected. The damage in the EOR is now predominantly dislocations, extending from one precipitate to another. In addition to the dislocations, the regions between the precipitates are strained. The location and size of the oxide precipitates after annealing will be discussed in detail in the next section. There continues to be small defect clusters present in the silicon film of the $\phi = 3.0 \times 10^{17}$ O/cm^2 sample. However they no longer appear to be confined to a fixed depth region.

4-3-3 Oxygen Distribution

The distribution of oxygen ions and oxide precipitates were characterized by ERD, SIMS and XTEM, before and after annealing. The annealing was done in a conventional furnace for 12 h at 1300°C. No distinction is made here between samples that have been annealed in an Ar/O_2 flow or N_2 flow as the oxygen profiles remain the same. This is discussed in Appendix A. The reader is reminded that the ERD spectra have been shifted so that the depth is consistent with the RBS/C results, as described in §4-3-1.

4-3-3-1 As-Implanted

Figure 4-17 shows the results of the ERD analysis of three samples implanted with doses of $\phi = 0.3 \times 10^{17}$, 1.0×10^{17} and 3.0×10^{17} O/cm^2. The dots are the original data points and the error bars indicate the statistical uncertainty. The solid line is the same data after being smoothed using a Fast Fourier Transformation (FFT) algorithm. Unlike the higher dose sample (figure 4-17c)

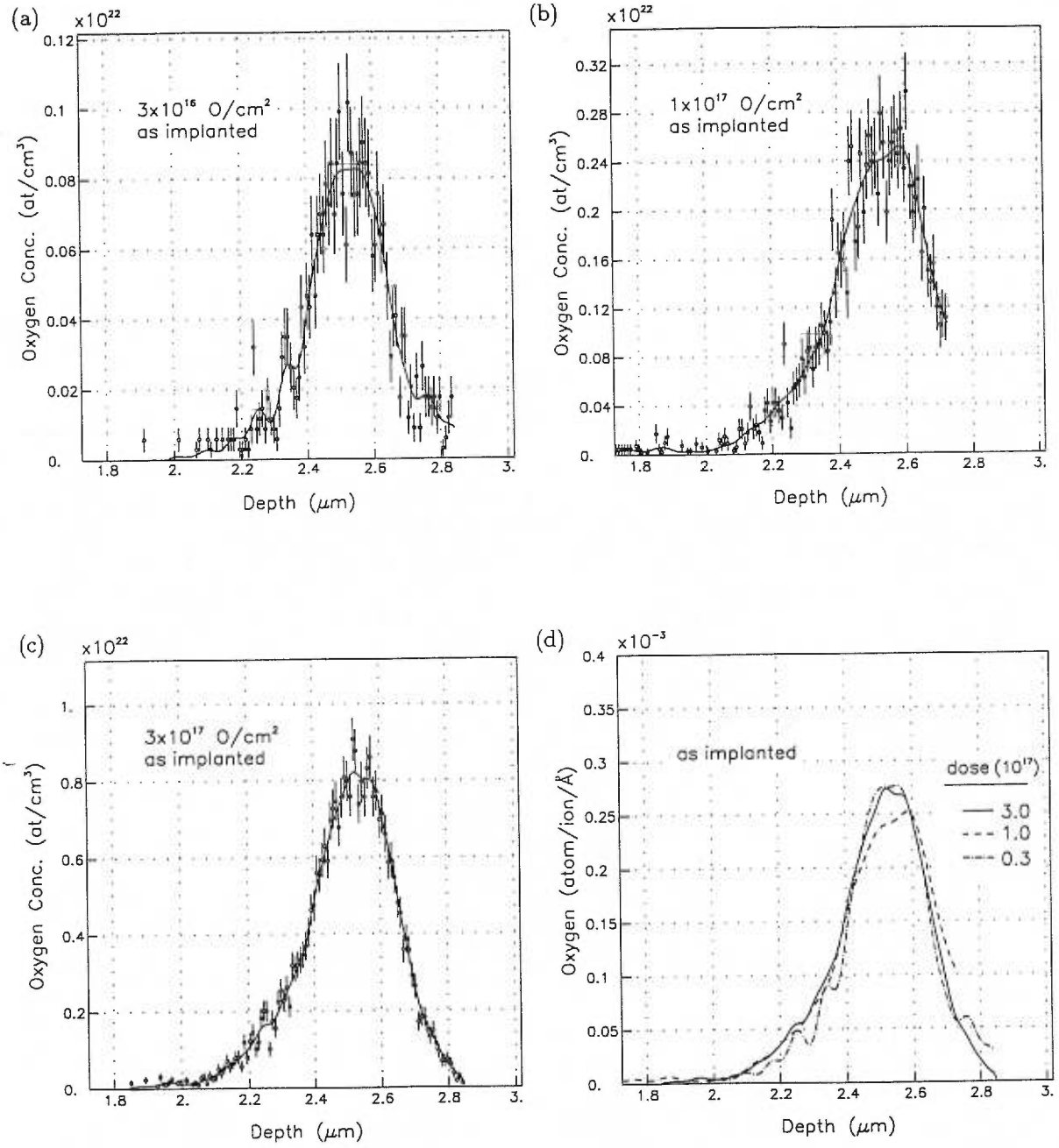

Figure 4-17. Oxygen concentration profiles (at/cm^3) of as-implanted ϕ = (a) 0.3, (b) 1.0, and (c) 3.0 × 10^{17} O/cm^2 samples. The dots are calculated from ERD data, and the solid lines are the results after smoothing. (d) Oxygen profiles of (a), (b), and (c) after converting to at/ion/Å.

the two lower dose samples (figure 4-17a and 4-b) had not been etched sufficiently to obtain a profile which extends past the last remnants of oxygen. The respective peak oxygen concentrations for these three samples are 0.8×10^{21}, 2.5×10^{21} and 8.0×10^{21} O/cm^3. The concentration of oxygen in amorphous SiO_2 is 4.4×10^{22} O/cm^3, which means that, if all the oxygen is in an oxide phase, the SiO_2 to Si ratio varies between 2 and 20%. Within the limits of statistical uncertainty, the normalized (at/ion/Å) oxygen profiles are equivalent for all three doses, as shown in figure 4-17d. This result is not surprising since, at these doses, the phase change due to the oxygen implantation (formation of SiO_2) is limited to small SiO_2 precipitates, and does not create stoichiometric oxide layers. The oxygen profiles are nearly gaussian. The standard deviation,σ, of the fitted gaussian distribution is 0.13 μm.

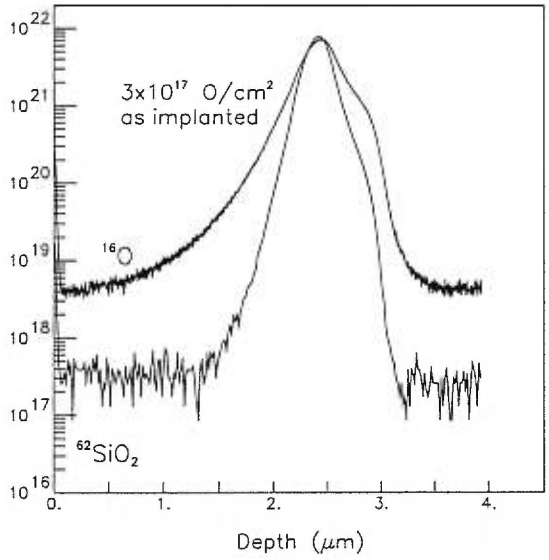

Figure 4-18. Oxygen concentration profile of as-implanted $\phi = 3.0 \times 10^{17}$ O/cm^2 sample using SIMS analysis of ^{16}O and $^{62}(SiO_2)$ signal. The ^{16}O spectrum has been normalized to the total dose. The ordinate axis represents the oxygen concentration per cm^3. The $^{62}(SiO_2)$ spectrum has been scaled so that the peak concentration matches the ^{16}O peak concentration.

Another high dose sample (3.0×10^{17} O/cm^2) was studied by SIMS and the results are shown in figure 4-18. The oxygen content was profiled by using the ^{16}O, $^{44}(SiO)$ and $^{62}(SiO_2)$ signal. The ^{16}O spectrum has been normalized to the implanted dose. The $^{62}(SiO_2)$ has not been normalized, although the scale was chosen so that the peak concentration of the $^{62}(SiO_2)$ signal would be the

same as the peak concentration of the ^{16}O signal. The profile of the $^{44}(SiO)$ molecule is not shown because it is virtually indistinguishable from the ^{16}O profile. The $^{62}(SiO_2)$ profile however, shows a marked difference from the ^{16}O profile, and is thought to be an indicator of the oxide phase within the silicon. The rise in SiO_2 molecules occurs after the oxygen concentration exceeds 3×10^{19} O/cm^3, which indicates that the surface region, at least, is supersaturated with non-precipitated oxygen.

The oxygen concentration in the silicon film rises smoothly, starting from less than 5×10^{18} O/cm^3 at the surface, to a peak concentration of 0.8×10^{22} O/cm^3. There is no indication that excess oxygen has clustered at 1.1 μm, the depth of the anomalous defect band found in this sample. Similarly, there is no indication that the oxygen concentration is affected by the onset of the highly defected region (roughly 2.3 μm to 2.8 μm) at the EOR. The decrease in the oxygen concentration from R_p into the substrate is not smooth. There is a kink in both spectra (^{16}O and $^{62}(SiO_2)$) at approximately 3 μm deep, after which the concentration of oxygen drops rapidly to, or below, the detection limit of the apparatus.

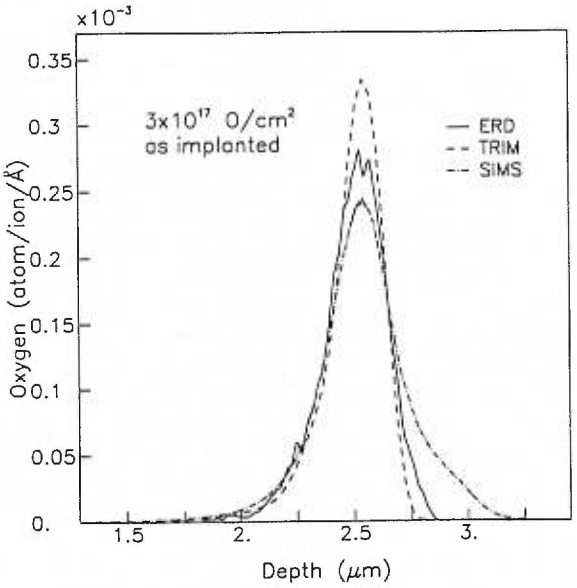

Figure 4-19. A comparison of the as-implanted oxygen profile (ERD and SIMS) with the oxygen profile predicted by TRIM calculations, for $\phi = 3 \times 10^{17}$ O/cm^2. The TRIM and SIMS data have been shifted along the depth scale such that the peak concentrations are at 2.55 μm.

In figure 4-19, the ERD, TRIM and SIMS oxygen profiles for $\phi = 3.0 \times 10^{17}$ O/cm^2 are shown. The TRIM profile was shifted by 0.2 μm and the SIMS by 0.08 μm so that the shapes of the profiles could be compared more easily. The leading edge of the oxygen profile, from both the ERD and SIMS analysis, is consistent with the TRIM calculations, but the trailing edge is not. It appears that oxygen from the EOR diffused into the substrate during the implantation. This tailing of the oxygen concentration is more pronounced in the sample analyzed by SIMS than in the sample analyzed by ERD. This difference will be discussed in §4-3-3-3.

All in all, it is not unreasonable to conclude that the as-implanted oxygen profile is independent of the doses used in this experiment, and that the damaged silicon film in the 3.0×10^{17} O/cm^2 sample does not affect the oxygen distribution. It is also reasonable to conclude that not all of the implanted oxygen has precipitated, but is bound in oxygen/vacancy complexes instead.

4-3-3-2 Annealed

During annealing, the oxide precipitates that have a radius less than the critical radius r_c will dissolve. The subsequently released oxygen solute will then diffuse to the larger, and more stable, oxide precipitates. These precipitates will continue to grow via the Ostwald process, and should two precipitates come in contact with each other, they will merge in order to reduce the Si/SiO_2 surface tension. It has been well established that the hotter and longer the anneal temperature and times, the better the quality of the SIMOX structure. For the low doses used here, there is not enough oxygen to form a complete SiO_2 layer. However, even with a 12 h anneal time (1300°C), oxides have not yet finished coalescing. This is dramatically illustrated in figure 4-20, an XTEM photo of a 3.0×10^{17} O/cm^2 sample. The large precipitate in the center of the photo has a diameter of approximately 125 nm. A smaller precipitate can be seen to be merging with this larger one (upper left), and given a longer anneal time, they would have melded together to form one, even larger, precipitate. Because of the crystalline nature of the target the precipitates are not spherical (minimum surface area), but rather they are facetted, with the edges lying along the {100}, {110} and {111} planes. The smallest precipitate seen in this photo is ~30 nm. Dislocations which extend between precipitates are also visible.

The XTEM results for the annealed samples are shown in figure 4-21. The sizes of the precipitates in the low dose sample ($\phi = 0.3 \times 10^{16}$ O/cm^2) are rather uniform, relatively speaking, with a diameter of approximately 50 nm. The largest precipitate seen (not shown) for this dose had

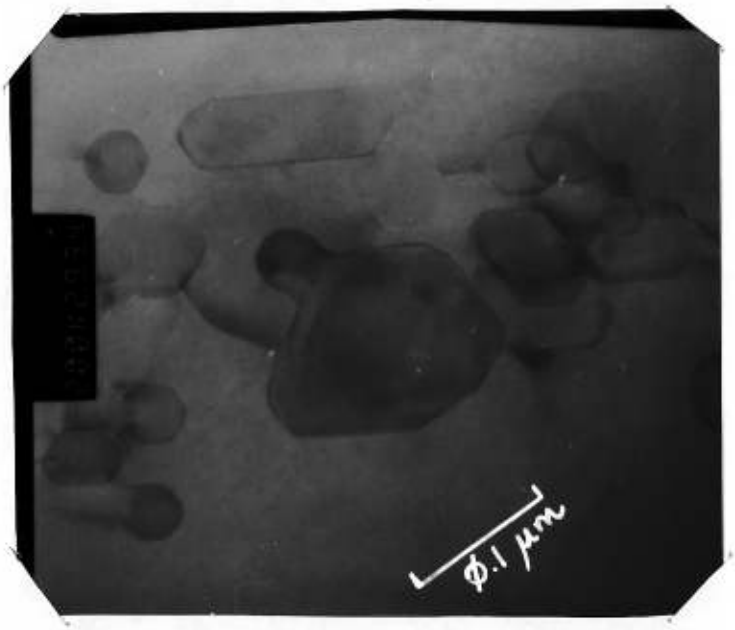

Figure 4-20. XTEM photo of annealed $\phi = 3.0 \times 10^{17}$ O/cm^2 sample. M=200,000x, $\vec{g} = <111>$. $\vec{B} = [110]$.

a diameter of 100 nm, while the smallest seen was 25 nm in diameter. The medium dose sample ($\phi = 1.0 \times 10^{17}$ O/cm^2) was not well thinned, and it is difficult to measure the size of the precipitates. One was measured however, and it had a diameter of 80 nm. In the substrate region, there are a few precipitates, mostly noticeable by the long dislocations joining them to the main oxygen band at the EOR. These have a diameter of ~25 nm. The precipitates in the high dose sample ($\phi = 3.0 \times 10^{17}$ O/cm^2) ranged between 55 nm and 105 nm in the shallower region of the EOR. The largest precipitate seen (figure 4-15) for this dose had a diameter of 200 nm. There are also a significant number of oxide precipitates deeper in the substrate ($\gg R_p$) with an average size of ~25 nm.

The oxygen distribution after annealing for all three doses is shown in figure figure 4-22. The dots represent the original ERD data with the error bars indicating the statistical uncertainty of each point, and the solid lines are the results of smoothing with a FFT. The as-implanted profiles are shown as dotted lines. Unlike the as-implanted profiles, the annealed profiles have unique characteristics. For the $\phi = 0.3 \times 10^{17}$ O/cm^2 sample, the width (FWHM) of the oxygen profile remains unchanged, although the oxygen from the outlaying regions have diffused to the EOR to give a more boxlike profile.

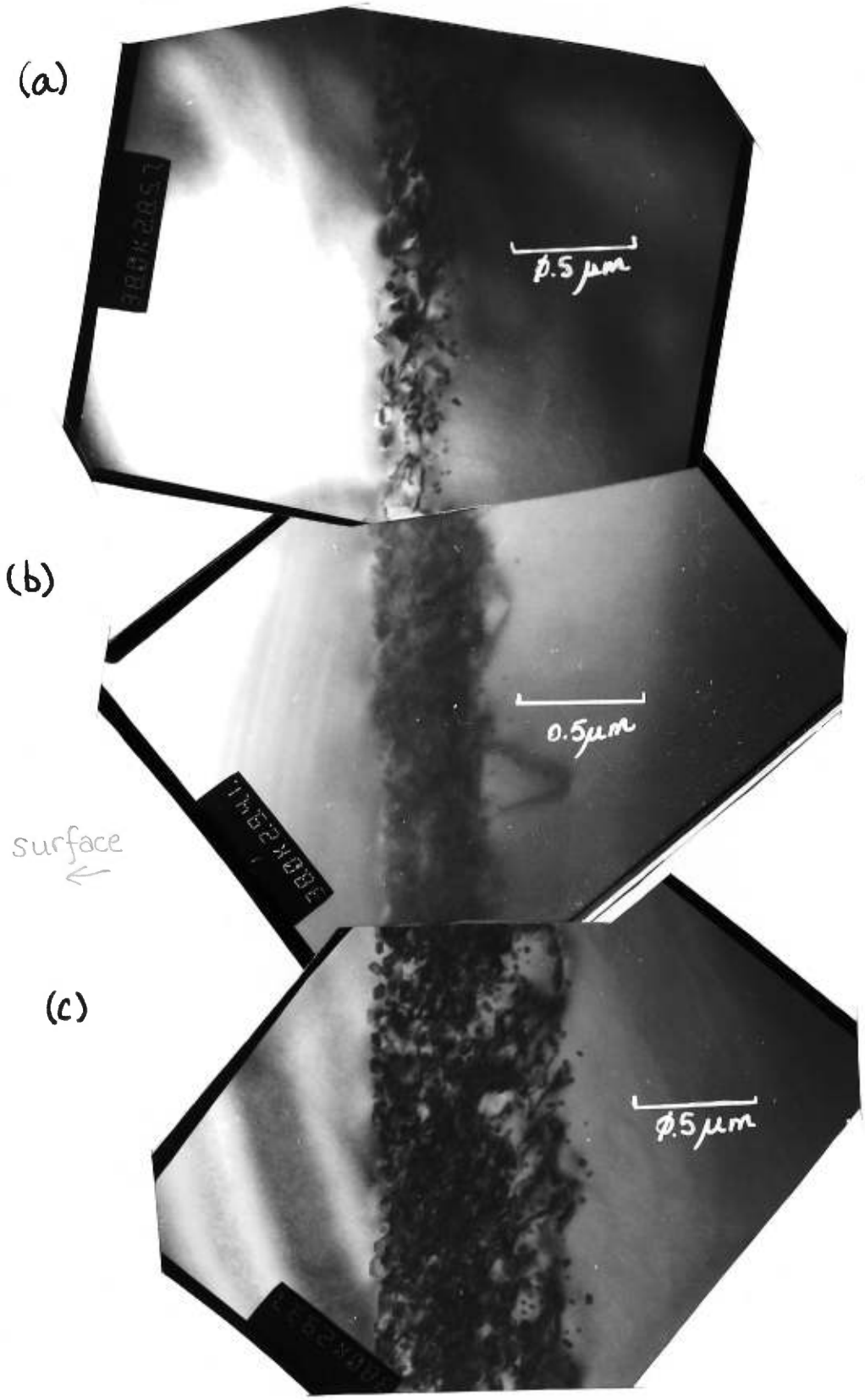

Figure 4-21. XTEM photos of annealed ϕ = (a) 0.3, (b) 1.0 and (c) 3.0×10^{17} O/cm^2 samples. M=15,000x, $\vec{g}$ = <111>, $\vec{B}$ = [110]. The scale units are given in μms.

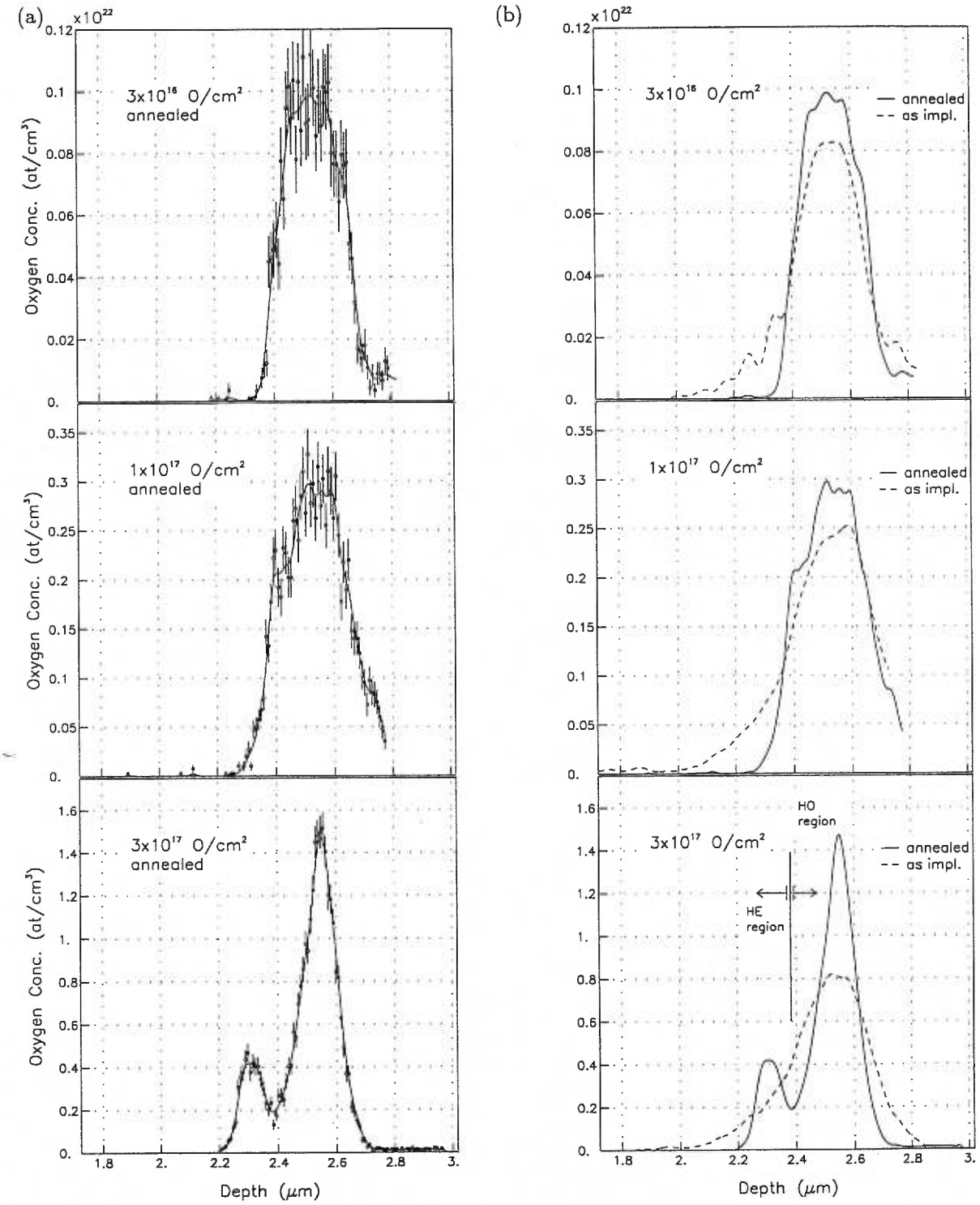

Figure 4-22. Oxygen concentration profiles of as-implanted and annealed $\phi = 0.3$, 1.0 and 3.0×10^{17} O/cm^2 samples. The dots are calculated from ERD data, and the solid and dashed lines are the ERD results after smoothing.

The oxygen is located in a well defined depth range of 2.4 to 2.75 μm. The peak concentration of oxygen has increased from 0.8 to 1×10^{21} O/cm^3 during the anneal. There is a small, but noticeable, kink in the profile between the EOR and the substrate located at 2.65 μm, with an oxygen concentration of $\sim 0.7 \times 10^{21}$ O/cm^3.

The $\phi = 1.0 \times 10^{17}$ O/cm^2 sample also has a broad region of maximum oxygen concentration (3.0×10^{21} O/cm^3) in the same depth region as the low dose sample, as well as a kink in the deeper interface, only now this kink is at a depth of 2.75 μm, again with an oxygen concentration of 0.7×10^{21} O/cm^3. In addition to this, there is another region, approximately 0.1 μm wide, with an oxygen concentration of 2.0×10^{21} O/cm^3, extending into the silicon film. Again, the oxygen that was in the silicon film before annealing is no longer there, having diffused to the EOR region.

The $\phi = 3.0 \times 10^{17}$ O/cm^2 sample has a completely different oxygen profile than the other two samples. There is no longer a broad region of evenly distributed oxygen. Instead, there are two very sharp and distinct peaks, separated by 0.2 μm. The first peak is at d_O (the depth in the as-implanted samples where there is a sudden increase in the damage concentration) and has a maximum oxygen concentration of 4×10^{21} O/cm^3. The second peak, centered at 2.55 μm (R_p), has a maximum concentration of 15×10^{21} O/cm^3, an increase of 90% from the peak as-implanted concentration.

In addition to the ERD analysis, the oxygen concentration of the 3.0×10^{17} O/cm^2 sample was analyzed with SIMS, again using the ^{16}O signal and the $^{62}(SiO_2)$ signal. The results are shown in figure 4-23. The ^{16}O profile was normalized to the total dose and the $^{62}(SiO_2)$ profile was scaled so that the peak concentration was the same as the ^{16}O peak concentration. Although the noise signal for the ^{16}O ion is significantly larger than the noise signal for the $^{62}(SiO_2)$ molecule, two of the three $^{62}(SiO_2)$ peaks in the silicon film can still be seen, to a lesser degree, in the ^{16}O profile. Within this limitation, the $^{62}(SiO_2)$ profile has the same shape as the ^{16}O profile indicating that all the oxygen in the sample is now in the form of SiO_2 precipitates.

In the silicon film, the oxygen concentration is not evenly distributed. There are three distinct bumps located at depths of 0.55, 1.4 and 1.85 μm. The first two are broad ($\sim$0.4 μm wide) while the third oxygen bump is a very narrow peak approximately 0.1 μm wide. To insure that these bumps were not just a local phenomenon, the sample was probed six times and identical results were obtained. These bumps have concentrations less than 10^{19} O/cm^3, three orders of magnitude lower than the peak

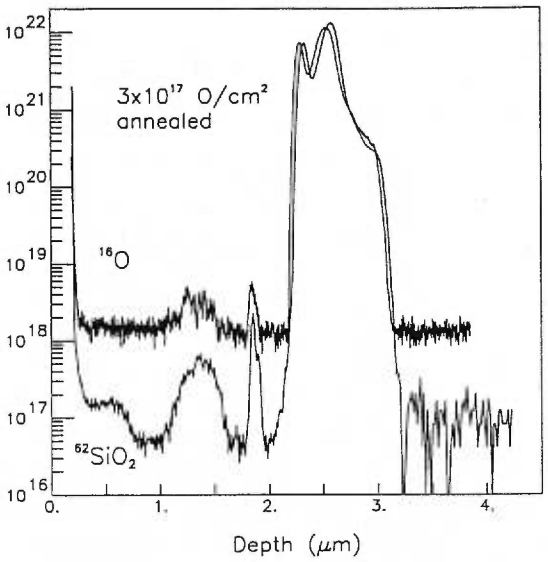

Figure 4-23. Oxygen concentration profile of annealed $\phi = 3.0 \times 10^{17}$ O/cm^2 sample using SIMS analysis of ^{16}O and $^{62}(SiO_2)$. The ^{16}O spectrum has been normalized to the total dose. The ordinate axis represents the oxygen concentration per cm^3. The $^{62}(SiO_2)$ spectrum has been scaled so that the peak concentration matches the ^{16}O peak concentration.

concentration at the EOR. At the EOR, the oxygen concentration rises sharply to form two distinct peaks of oxygen at 2.3 μm and at 2.6 μm, with the same general shape as the ERD results. The peak concentrations are 0.7×10^{22} and 1.2×10^{22} O/cm^3, respectively. As the oxygen concentration falls, there is a kink in the spectrum at 3 μm, with an oxygen concentration of 0.4×10^{21} O/cm^3. This kink is at the same depth as the kink in the as-implanted sample.

The annealed profiles of $^{62}(SiO_2)$ and ^{16}O are overlaid on their respective as-implanted profiles and shown in figure 4-24a and 4-24b. The shape of the $^{62}(SiO_2)$ profile in the interface region between the EOR and substrate did not change significantly during the anneal, suggesting that in this region the total volume of the oxide precipitates did not increase. In the silicon film, the concentration of $^{62}(SiO_2)$ decreased, indicating that the precipitates in this region dissolved and the oxygen then diffused to the EOR and the surface, with the exception of the 'bumps' in the profile. Looking at the ^{16}O profile, it can be seen that the oxygen concentration is reduced everywhere, excluding the EOR, indicating a net diffusion of oxygen, regardless of phase, towards the EOR.

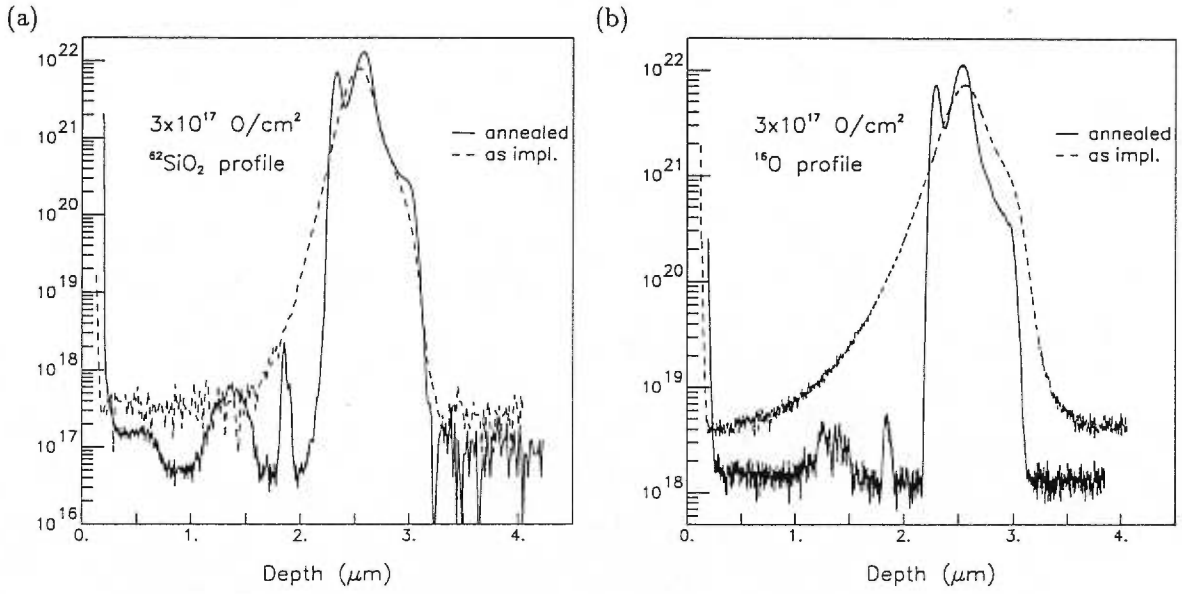

Figure 4-24. The annealed and as-implanted (a) $^{62}(SiO_2)$ and (b) ^{16}O oxygen concentration profiles for a $\phi = 3.0 \times 10^{17}$ O/cm^2 sample.

4-3-3-3 Discussion

For oxygen implantation with doses between 3×10^{16} and 3×10^{17} O/cm^2, the as-implanted oxygen concentration profiles are similar in shape, in spite of the fact that the oxygen doses vary by a factor of ten. In contrast, the oxygen concentration profiles of the annealed samples are remarkably different (see figure 4-22). The oxygen profile of the 3×10^{16} O/cm^2 sample is boxlike in shape, the profile for the 1×10^{17} O/cm^2 sample is broader with a distinctive 'step' in the concentration. And finally, the profile for the 3×10^{17} O/cm^2 sample, although extending over a broader region, has separated into two very distinct sharp peaks at depths R_p and d_O, which are the depths of the peak as-implanted oxygen concentration and peak damage region respectively.

There are two possible explanations for the differences in the annealed oxygen concentration profiles. The first is that the profiles of the oxygen concentration is just a direct manifestation of the Ostwald ripening process. Even in the simplest of systems, the redistribution of oxygen during the anneal can result in very complex concentration profiles. For example, a homogeneous distribution of oxides of equal size can result in a multi-band oxygen distribution after annealing [73,74]. The number of bands is a function of the original density of precipitates where an increase in the density of precipitates increases the number of bands (§2-5-3). Since the higher-dose sample has a larger

concentration of oxygen, it is not hard to imagine that the initial density of precipitates is also larger, and thus the final oxygen distribution is composed of two bands. The lower-dose sample has a lower density of precipitates and thus does not form a multi-band structure. The concentration profile of the intermediate-dose sample could be a transition from the lower-dose to the higher-dose profiles.

Although Ostwald ripening alone could account for the oxygen distributions, there are reasons to believe that this is not so. The first reason is the fact that the smaller of the two oxygen peaks shown in figure 4-22 is at the same depth as the onset of damage in the as-implanted sample. It has been well established that oxygen will getter on crystalline damage sites [61], and this effect should not be ignored. The diffusion and annihilation of the silicon interstitials also plays a significant role in the final structure of the annealed sample since the silicon interstitials that are released into the matrix during the growth of oxides precipitates inhibit the growth rate of those same precipitates [70]. The distribution of silicon interstitials is also mediated by the original distribution of damage. Consequently, any explanation describing the reasons for the shapes of the oxygen profiles should include HE precipitation, which is the preferential precipitation of oxygen on damage sites resulting in larger, but fewer, precipitates.

It has been hypothesized [88] that if the oxygen current density during the implant is low, and if the temperature of the sample is high, then HE precipitation, occurring at d_O, prevails over HO precipitation, occurring at R_p, at low oxygen doses, and that at very low doses, HO precipitation is impossible (§2-5-1). Given our experimental conditions of T_i=570°C, $J \approx 1\ \mu A/cm^2$, and $\phi < 3.0 \times 10^{17}\ O/cm^2$ we would expect that this effect would be observable in at least some of our results. However, careful analysis of the depths of oxide precipitation after annealing clearly indicates that HE precipitation is not the predominate factor, even at the lowest dose of $3 \times 10^{16}\ O/cm^2$.

Taking this into account, the differences in the oxygen profiles of the annealed samples can be explained if we make the following assertions; (1) HO precipitation does occur, (2) HE precipitation also occurs, and is a function of the quantity of the radiation induced damage, (3) although ET precipitation may or may not occur, it does not affect the oxygen profiles in the neighbourhood of d_O, (4) there are at least two local maxima of precipitate sizes, located at d_O and R_p and (5) the number and size of the precipitates increases with increasing dose.

Figure 4-25 is a schematic of the general distribution of the precipitates in the samples, assuming that the size of the precipitates are proportional to $\sqrt[3]{C(x)}$, except in the region of damage, and $C(x)$ is the concentration of oxygen at depth x. The preferential precipitation at d_O produces larger and more stable precipitates, and has been accounted for by artificially increasing the radius of the precipitates, and subsequently decreasing their density. This figure is only used to illustrate the problem, and the reader should take note that the size of the precipitates shown in the figure is not indicative of the actual size. In this simple representation, it is assumed that the ramp-up time of the anneal is sufficiently fast so that very little dynamic annealing occurs before the sample reaches the maximum temperature of 1300°C. Thus all the precipitates with a radius less than the critical radius at 1300°C ($\sim$ 50 nm [12]) will dissolve, leaving a distribution of precipitates similar to what is shown in figure 4-25c. It is then *this* distribution of precipitates that affects the Ostwald ripening process, rather than the as-implanted distribution (figure 4-25b).

For the 3×10^{16} O/cm^2 sample, the majority of the precipitates are below the critical radius, including the precipitates at d_O, and consequently they dissolve during the initial stages of annealing. During this time the residual radiation damage is also annealed and hence the preferential oxidation sites are removed. New precipitates will form, all else being equal, in the region of highest oxygen concentration. These new precipitates will now act as gettering centers for the remaining solute oxygen which diffuses inwards from the 'wings' of the original oxygen distribution. This is readily observed by comparing the annealed and as-implanted profiles for this dose (figure 4-22). Some structure is observed in the region of maximum oxygen concentration, and could be related to the natural segregation of oxides into separate bands via the Ostwald process.

For the 1×10^{17} O/cm^2 sample, the precipitates at d_O dissolve, but unlike the lower dose, there is a broad region centered around R_p with stable precipitates (figure 4-25). The solute oxygen which migrates inward from the silicon film not only encounters stable precipitates, but also the damage that is trapped between these precipitates. This region now getters the oxygen *before* it can finish diffusing towards d_O. Hence the 'step' in the concentration profile, and the reduced gettering efficiency at R_p (figure 4-22).

For the highest dose sample (3×10^{17} O/cm^2), the stable precipitates form two bands centered at R_p and d_O (figure 4-25c). These precipitates grow by the normal Ostwald process. It is interesting to note that there is no net diffusion of oxygen during the anneal between the HO and HE regions

(a) depth distribution of precipitate sizes

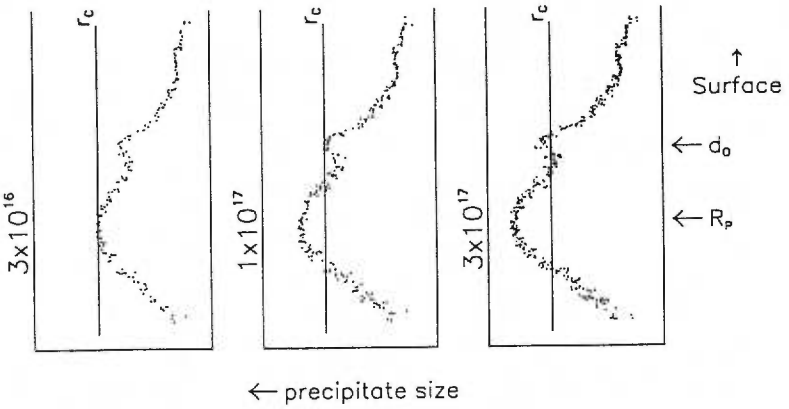

(b) distribution of precipitates at 600°C, (as-implanted)

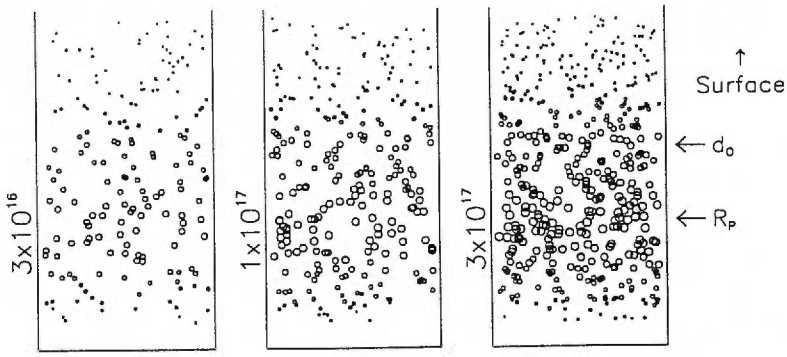

(c) distribution of precipitates at 1300°C, (before Ostwald ripening)

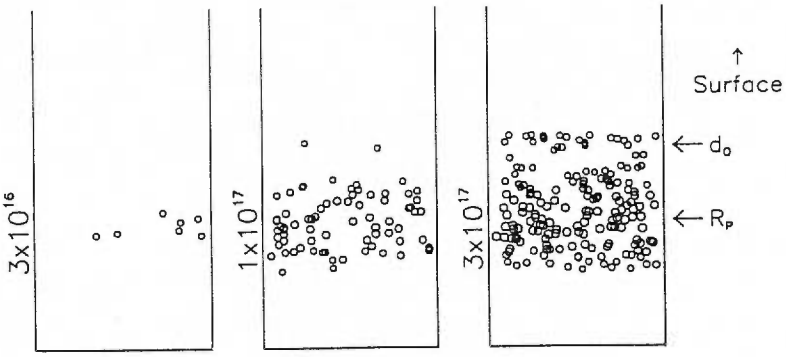

Figure 4-25. A schematic diagram illustrating the relationship between precipitate sizes and the initial stages of annealing. (a) A possible depth distribution of precipitate sizes assuming a constant density of precipitates in all regions except d_O. r_c represents the critical radius at 1300°C. (b) The corresponding cross-sectional distributions of precipitates. (c) The same distributions as shown in (b), but with all the precipitates smaller than r_c dissolved.

(figure 4-22). Thus the first peak, located at 2.3 μm, is formed predominantly by the diffusion of oxygen from the silicon film and can be considered to be independent of the growth of the peak at R_p.

Thus the gross features of the oxygen profiles, before and after annealing, can be explained if the following two points are assumed. First, there is preferential oxidation in regions of high crystalline damage, and secondly, that a significant portion of the precipitates dissolve (at least at the doses used in this experiment) in the very early stages of annealing. Once these initial conditions are satisfied, the oxygen profiles after annealing for 12 h can be explained by the standard Ostwald ripening process.

Because the precipitates at d_O act as a diffusion barrier between the silicon film and the EOR, any oxide layer made with doses of $\phi = 3.0 \times 10^{17}$ O/cm^2 or higher must be at least as thick as the distance separating d_O and R_p. If the density of the silicon dioxide is 2.32 g/cm^2 and the minimum width of the layer is between 0.2 and 0.4 μm, the minimum dose needed to form an oxide layer would be $\phi \sim 1-2 \times 10^{18}$ O/cm^2.

The lower oxygen concentrations in the film and substrate of the samples could not be probed by ERD, but some information is available from the XTEM analysis of the samples, and the SIMS analysis of the 3×10^{17} O/cm^2 sample. Let us first discuss the oxygen concentration which extends beyond R_p. The XTEM photos of the as-implanted samples (figures 4-10, to 4-12) clearly show that there is some damage and/or oxides well past the peak concentration depth, extending as far as 3 μm into the sample. Comparing the XTEM photo and the SIMS analysis (figure 4-24) for the highest dose sample, we see that the 'spots' in the photo corresponds to the presence of oxygen in that depth region. After annealing it can be seen that (figure 4-21) there is no visible damage or precipitates in the lowest dose sample between 2.7-3.0 μm. In the intermediate dose sample there are a few precipitates in this region, and in the highest dose sample there is a large number of small precipitates. The results of the XTEM photos would suggest that the oxide precipitation in the deeper regions of the substrate is a function of dose. But this, as will be shown in later sections, is not always reproducible.

In addition to the non-reproducibility, another factor should also be discussed. The SIMS data was obtained from the same target as the one used for the XTEM photos, but the ERD data was obtained from a different target, although the history of the targets were nominally the same. The SIMS results show a larger concentration of oxygen in the substrate, before and after annealing, than

the ERD results. Two possible explanations for this could be: (1) there was unintentional channeling in the target analyzed by SIMS or, (2) the Cs^+ ions used to sputter the target for the SIMS analysis knocked the oxygen atoms further into the target during the sputtering process, causing the oxygen profile, as obtained by SIMS, to be incorrect.

Finally, the three peaks of oxygen concentration in the silicon film of the 3×10^{17} O/cm^2 sample (figure 4-24) will be discussed. As the reader will recall, there is evidence of damage and/or oxide precipitates in the silicon film before annealing (figure 4-12), although there are no peaks in the as-implanted profiles. In spite of the fact that the damage distribution could not be ascertained to any great accuracy†, it is presumed that the oxygen profile in the annealed sample is a result of the oxygen interacting with the damage that was already present in the as-implanted sample. Tamura *et al.* [61] have also noted oxygen concentration peaks in the film of ion-implanted silicon ($\sim$ $^1/_2 R_p$) after annealing, even when the implanted ion was not oxygen. They attribute this to vacancy rich regions within the silicon film acting as gettering centers for oxygen. Since the defects seen in the as-implanted sample is a result of strain release via the condensation of vacancies, the oxygen is no longer bound to the vacancies. The oxygen is now free to form oxide precipitates [20].

To recap the results and conclusions of this section, we have: (1) HO and HE precipitation occurs in the as-implanted samples, (2) the final oxygen concentration profile is dependent on the distribution of oxide precipitates that remain *after* the furnace temperature has reached its maximum, (3) ET precipitation (precipitation that occurs well past R_p) can neither be confirmed nor denied since there is a question of reproducibility and possible accidental channeling in the 3×10^{17} O/cm^2 sample, (4) the three oxygen peaks in the silicon film of the 3×10^{17} O/cm^2 sample can be attributed to the as-implanted damage profile, but the reason for the shape of the peaks, their location, and even their number, is not clear and (5) it is not possible to form a SiO_2 layer using only a mono-energetic oxygen beam with doses less than $\phi = 1 \times 10^{18}$ O/cm^2.

† The distribution of damage in this sample can only be hypothesized since the XTEM photos were not sufficient to give a profile of the damage, and the RBS/C spectrum was not sensitive enough to probe the damage in this region.

4-4 OXYGEN IN PRE-DAMAGED SILICON

The next step in understanding the interaction between damage and the behaviour of oxygen in silicon is to study oxygen implanted into pre-damaged samples. By pre-damaged samples we refer to silicon that has been implanted with silicon, at the specified energy and dose, and subsequently annealed for 1 h at 900°C. The silicon doses used were $\phi = 5 \times 10^{14}$ and 1×10^{15} Si/cm^2. The energy of the silicon implants ranged between 2.00 and 2.75 MeV. The energy of the oxygen implants were fixed at 2.5 MeV, and the doses ranged between $\phi = 0.3 \times 10^{17}$ and 3.0×10^{17} O/cm^2. The oxygen implants were carried out with a sample temperature of 570°C. The specific experimental conditions (dose rate, temperature of implant, *etc.*) of the silicon and oxygen implants are given in §4-1.

There is one exception to the above description of pre-damaged samples. In one instance, while implanting oxygen into a virgin silicon sample, the heater for the sample holder malfunctioned and stopped heating right at the start of the implantation procedure. However, the malfunction was not noted until approximately 10 minutes later. At this time the total implanted dose was $\sim 2 \times 10^{15}$ O/cm^2. The temperature at the start of the implant was 570°C, and based on earlier tests on the heating system itself, I estimate that the final temperature, after 10 minutes, was less than 200°C. The sample was left within the implantation chamber for more than 2 days while the heater was being repaired. After this, oxygen was again implanted at 570°C to give a final dose of 1.0×10^{17} O/cm^2. Hereafter, this particular sample is described as having a pre-damage of 2×10^{15} O/cm^2, with T_i=300°C. This is the only sample that was not annealed before the final oxygen implantation. It should also be noted that the temperature, of this particular pre-damaged implant, is only an approximation.

In all cases, the pre-damaged depth of the silicon implant, d_{Si}, is less than the range, R_p, of oxygen in silicon.

The oxygen concentration profiles and the damage profiles are studied as a function of (1) oxygen dose, (2) distance separating the pre-damage region from the oxygen implant and (3) pre-damage type. A summary of the these relationships is shown in Table 4-V. The distribution of the oxide precipitates in the as-implanted samples are inferred from the status of the annealed samples.

TABLE 4-V

A summary of the experimental parameters and results. (a) The experimental results and interpretation of pre-damaged samples. (b) The experimental results and interpretations of oxygen implanted into pre-damaged samples, as a function of pre-damage conditions and oxygen dose. Double arrows indicate trends. The silicon pre-damage depth is denoted by d_{Si}. The depth of the maximum damage production during the oxygen implant is defined as d_o.

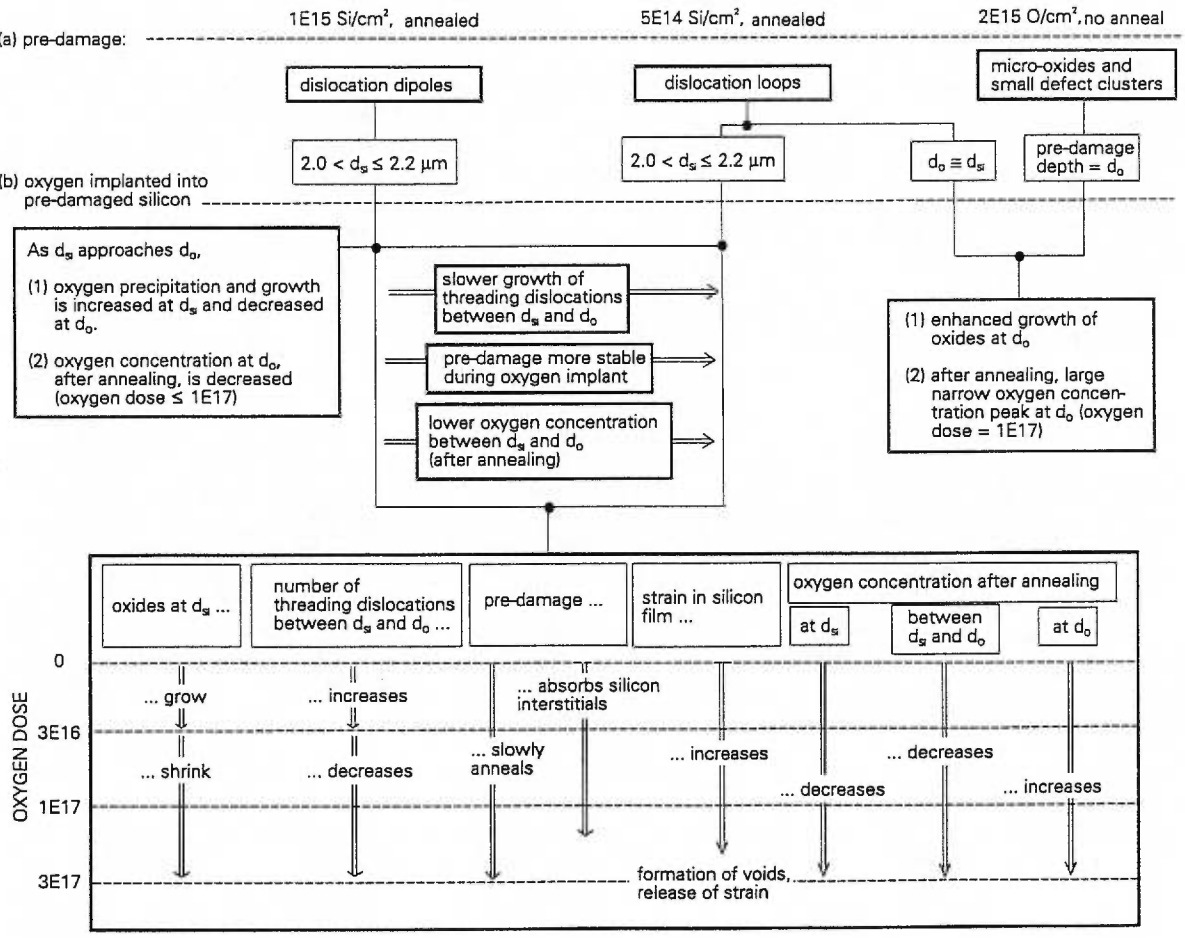

4-4-1 Damage

The damage in the samples was analyzed using RBS/C with a 3 MeV He probing beam, and a total detector angle of 67.5°, unless otherwise stated. The aligned direction was <110>. Besides RBS/C, XTEM was also used to characterize the damage. However, given the large investment in time necessary to prepare XTEM samples, only samples pre-damaged with 2.00 MeV Si were analyzed with this technique.

4-4-1-1 As-implanted

The as-implanted damage profiles as a function of oxygen dose, as well as a function of the pre-damage conditions, was measured using RBS/C analysis and the results are shown in figures 4-26 to 4-28. On the left side of the figures, the aligned yield (χ), normalized to the random yield, is shown in each individual graph for samples with equivalent oxygen doses, but with different pre-damage conditions. The pre-damaged conditions are listed on the figure itself, and the individual spectra have been vertically offset in order to make the comparison between spectra easier. For the sake of comparison, the RBS/C spectra and the damage profiles for the standard (no pre-damage) samples are also shown.

The damage profiles, shown adjacent to the χ curves, were calculated based on the following assumptions: 1) the energy loss of He in the aligned direction is 60% of the energy loss in a random direction, and 2) the predominant cause of de-channeling in the samples is due to point-like defects. Using the same arguments as discussed in §4-3-2-1, we surmise that the resulting damage profiles give a reasonable approximation of the damage distribution within the sample, although the depth scale is only an approximation.

When comparing the pre-damaged samples to the standard samples, it is immediately obvious that the general distribution and concentration of the large damage peak at ~2.5 μm is not affected by the presence of the pre-damage. Since the pre-damage depth d_{Si} is less than the range of the implanted oxygen, R_p, one would expect that any differences in the damage profiles would occur at a depth shallower than R_p. In all cases where the pre-damage was 5×10^{14} Si/cm^2 at 2.00 MeV there is a very small, but noticeable, region of damage in the vicinity of 2 μm (indicated by arrows in the figures), which is the depth of the pre-damage for this Si implant energy. At higher Si implant

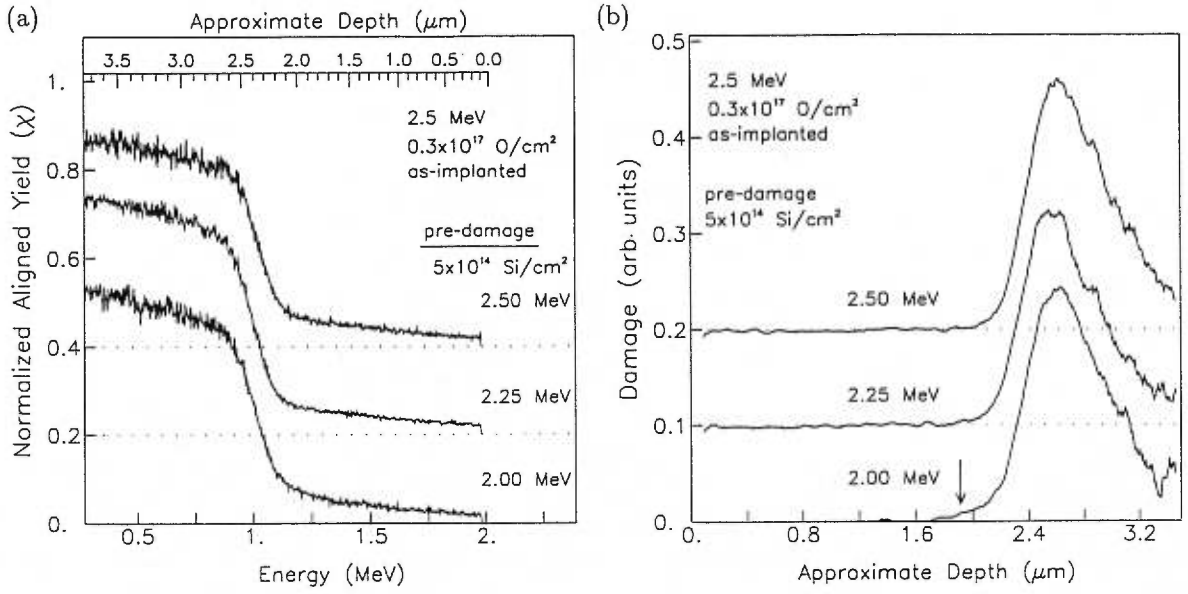

Figure 4-26. (a) The normalized aligned yield (χ) for as-implanted $\phi = 0.3 \times 10^{17}$ O/cm^2 (5×10^{14} Si/cm^2 pre-damaged) samples. (b) The calculated damage profiles assuming only point defects. The depth scales were calculated assuming that the stopping power in the aligned direction was 0.6 that of a random direction.

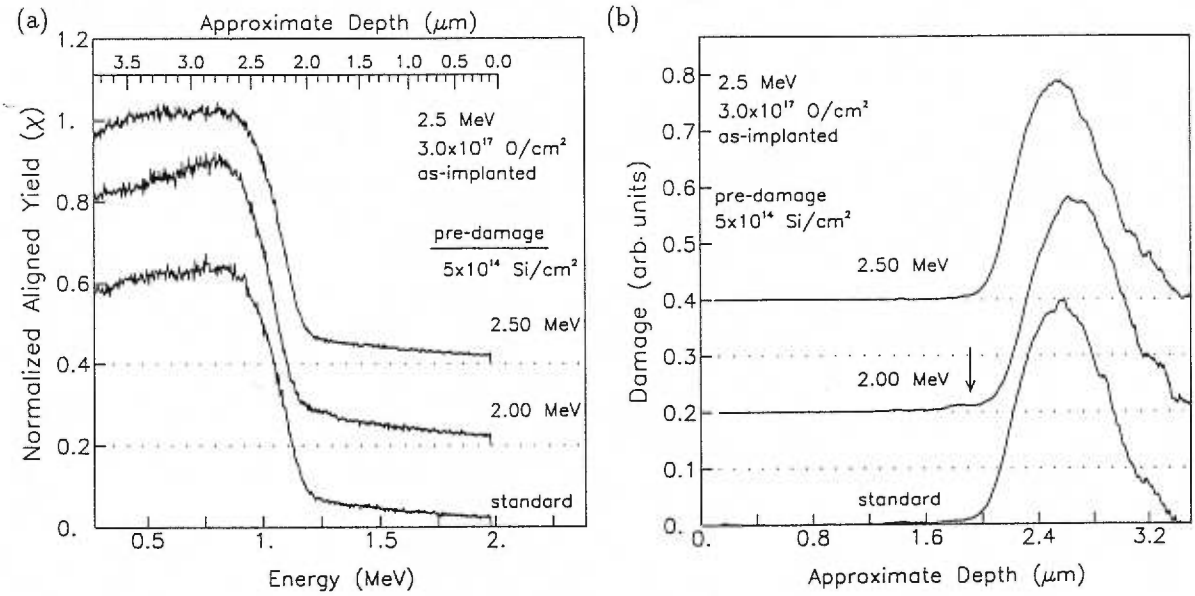

Figure 4-27. (a) The normalized aligned yield (χ) for as-implanted $\phi = 3.0 \times 10^{17}$ O/cm^2 (5×10^{14} Si/cm^2 pre-damaged) samples. (b) The calculated damage profiles assuming only point defects. The depth scales were calculated assuming that the stopping power in the aligned direction was 0.6 that of a random direction. (*standard* refers to no pre-damage)

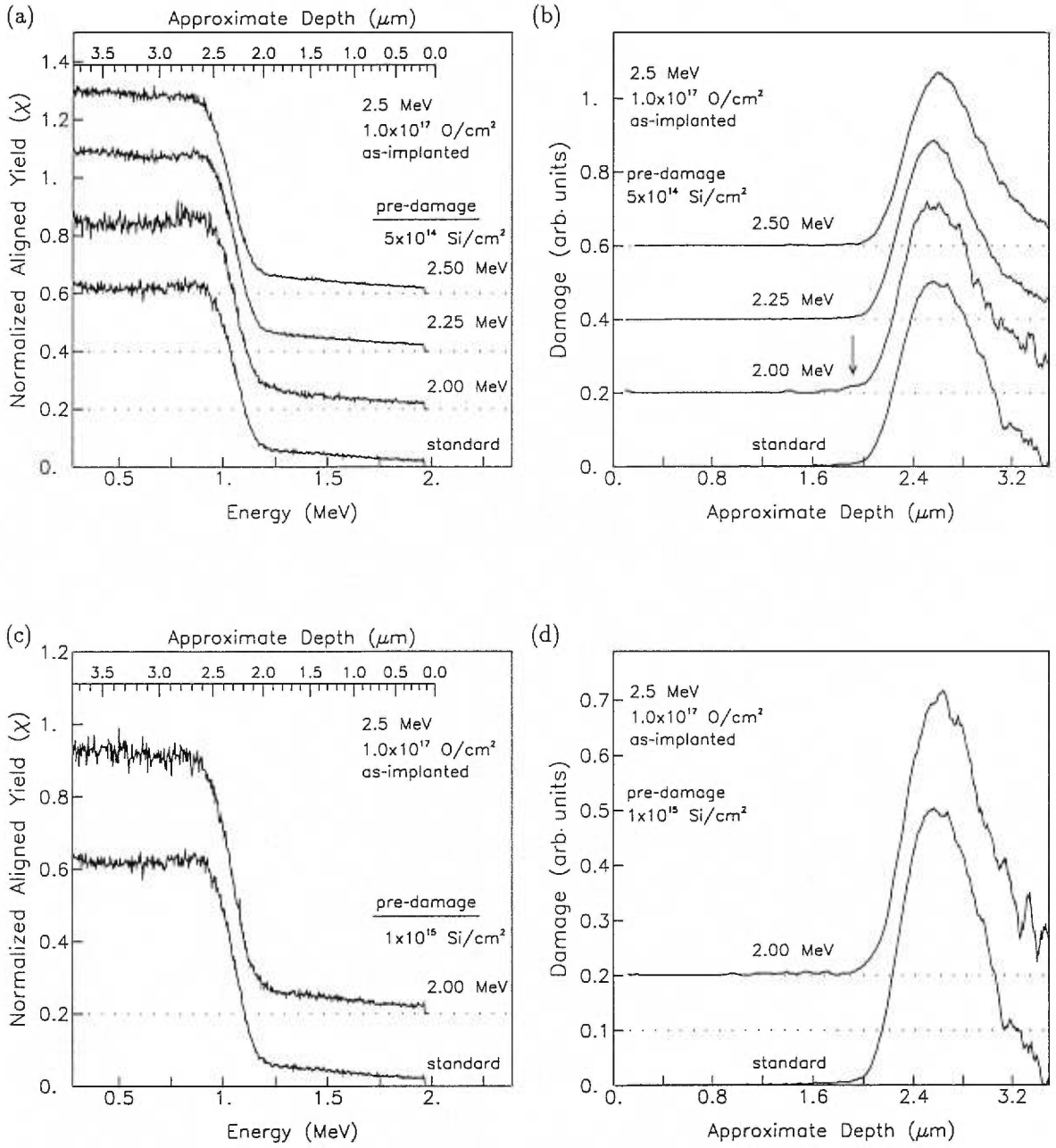

Figure 4-28. (a) The normalized aligned yield (χ) for as-implanted $\phi = 1.0 \times 10^{17}$ O/cm^2 ((a) 5×10^{14} Si/cm^2 and (c) 1×10^{15} Si/cm^2 pre-damaged) samples. The calculated damage profiles ((b) 5×10^{14} Si/cm^2 and (d) 1×10^{15} Si/cm^{2}pre-damaged) assuming only point defects. The depth scales were calculated assuming that the stopping power in the aligned direction was 0.6 that of a random direction. (*standard* refers to no pre-damage)

energies, the pre-damaged region is deeper, and hence closer to the damage caused by the oxygen implant, and thus it is not possible to separate these two damage regions.

To better understand the nature of the defects in our samples, the samples pre-damaged with 2.00 MeV silicon were analyzed via XTEM. To illustrate the similarities and differences between samples with different oxygen doses, XTEM photos of pre-damaged samples implanted with $\phi = 0.3 \times 10^{17}$, 1.0×10^{17} and 3.0×10^{17} O/cm^2 are shown in figure 4-29. The pre-damage was $\phi = 5 \times 10^{14}$ Si/cm^2. In these samples there are, at minimum, two very distinct defect regions, as was noted in the channeling spectra. One of these defect regions is located at the same depth ($\sim$2 μm) as the original pre-damage. The defect characteristics in this region are different for each oxygen dose. The other major defect region, in the depth range of 2.5 μm, has the same characteristics and depth as in the standard samples, and thus we conclude that it is a result of the oxygen implantation itself. For the highest dose sample, $\phi = 3.0 \times 10^{17}$ O/cm^2, (figure 4-29c) there is a third defect region $\sim$0.5 μm wide located around 1.3 μm, and is characterized by small black spots. This is not seen in the lower dose samples, even at higher magnifications. The silicon substrate is not completely defect-free, as can be seen by the 1 μm dislocation extending into the substrate along the <111> direction (labelled 'A' in figure 4-29c). This has been seen before in other samples. In the following paragraphs, each defect region will be presented separately.

The defect characteristics of the defect band at the EOR are similar to the standard samples (see figures 4-10 to 4-12) insofar as (a) the damage starts abruptly at 2.3 μm, (b) the interface between the damage layer and the substrate is not sharp. Instead, the quantity of damage slowly decreases as it extends into the substrate to a maximum depth of 3 μm, and finally (c) the defects closer to the surface are characterized by small dark lines (dislocations or stacking faults), and the defects deeper in the sample are characterized by small dark spots (oxide precipitates or small amorphous pockets). The highest dose sample ($\phi = 3.0 \times 10^{17}$ O/cm^2) has the largest visible strain, which is to be expected. Since this damage region has been thoroughly discussed in §4-3-2 we will not go into it in any further detail. For simplicity's sake, this defect region will henceforth be referred to as the 'main defect band'.

Next, let us consider the defect region centered around 2 μm. This is the depth at which the original pre-damage was located (d_{Si}). The damage in this region for samples pre-damaged with 5×10^{14} Si/cm^2 is significantly different than the original damage structure (*cf.* figure 4-5) as the

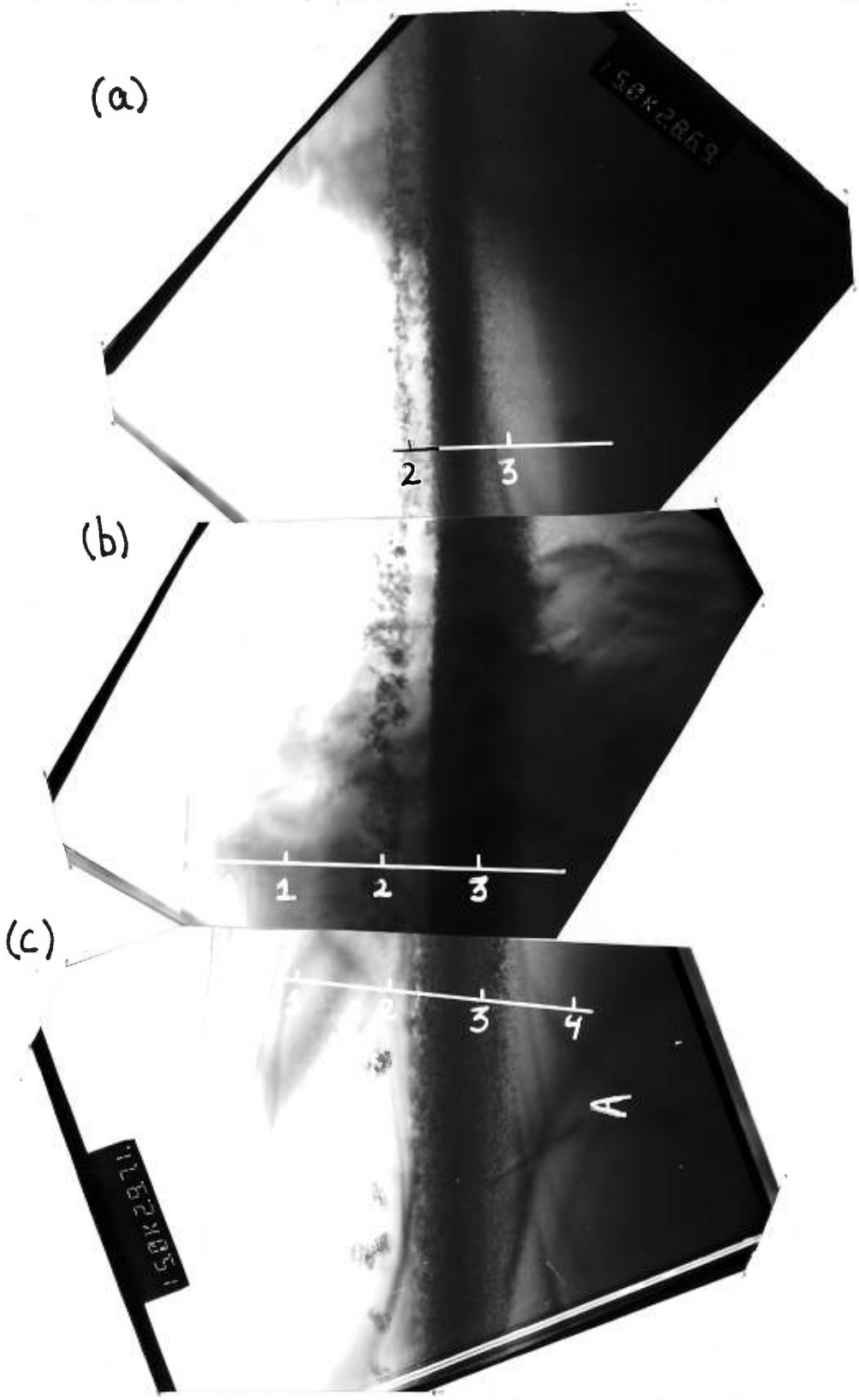

Figure 4-29. XTEM photos of as-implanted ϕ = (a) 0.3, (b) 1.0 and (c) 3.0×10^{17} O/cm^2 (2.00 MeV, 5×10^{14} Si/cm^2 pre-damaged) samples. M=15,000x, $\vec{B}$ = [110], $\vec{g}$ = <111>. The scale units are given in μm .

dislocation loops are no longer present, as can be seen in figure 4-29. Because the amount of damage in this region decreases with increasing oxygen dose, we conclude that the original pre-damage is being annealed during the implantation. For the lowest oxygen dose, $\phi = 0.3 \times 10^{17}$ O/cm^2 (figure 4-29a), the defects form a continuous network of dislocations parallel to the surface, with an occasional defect which extends from the pre-damaged region to the main defect band along the <111> direction. At a dose of 1.0×10^{17} O/cm^2 (figure 4-29b) the defect range is now broader, but the defects no longer form a continuous network. Again, there are defects that extend between the two damaged regions. At the highest oxygen dose, $\phi = 3.0 \times 10^{17}$ O/cm^2 (figure 4-29c), this defect region consists only of isolated pockets of damage, surrounded by strain fields.

In an effort to further characterize this defect region, higher magnification XTEM photos were taken of the same samples described above and are shown in figure 4-30. In the lowest dose sample (figure 4-30a) there is evidence of dislocations (straight lines), predominantly along the <100> and <113> directions, as well as oxide precipitates (small dark polygons). In the medium dose sample (figure 4-30b) there is no longer any evidence of simple dislocations, although the oxide precipitates are still evident. The darker undulating lines in the photo are a result of an imperfect thinning of the sample rather than defect contrast. For the highest dose sample (figure 4-30c), it is difficult to determine anything about the remaining defects, except that there is a large strain field surrounding the individual defect clusters.

As was seen in figures 4-5 and 4-6, the original pre-damage is significantly different when the silicon dose is increased from 5.0×10^{14} to 1.0×10^{15} Si/cm^2. One would then also expect that the sample will be different after implanting it with oxygen. Figure 4-31 shows XTEM photos of just such a sample, with an oxygen dose of $\phi = 1.0 \times 10^{17}$ O/cm^2 and a pre-damage of 2.00 MeV, $\phi = 1.0 \times 10^{15}$ Si/cm^2. In the as-implanted sample, the damage cannot be described as having two distinct bands. Unlike the damage profiles with equivalent oxygen doses (figures 4-11 and 4-29), the transition between the silicon film and the main damage region (at 2.3 μm) is not abrupt. Instead, at 2 μm there are a few small dark spots (which could be oxide precipitates, point-defect clusters, or small amorphous pockets) whose density rapidly increases as one goes deeper into the sample. At 2.3 μm, the defect contrast has gradually changed from small dark spots to a mixture of spots and thin dark lines. At this depth, the defect contrast is similar to the previously studied samples. As was also seen in the other samples of equivalent oxygen dose, the defect contrast in the deeper layers of

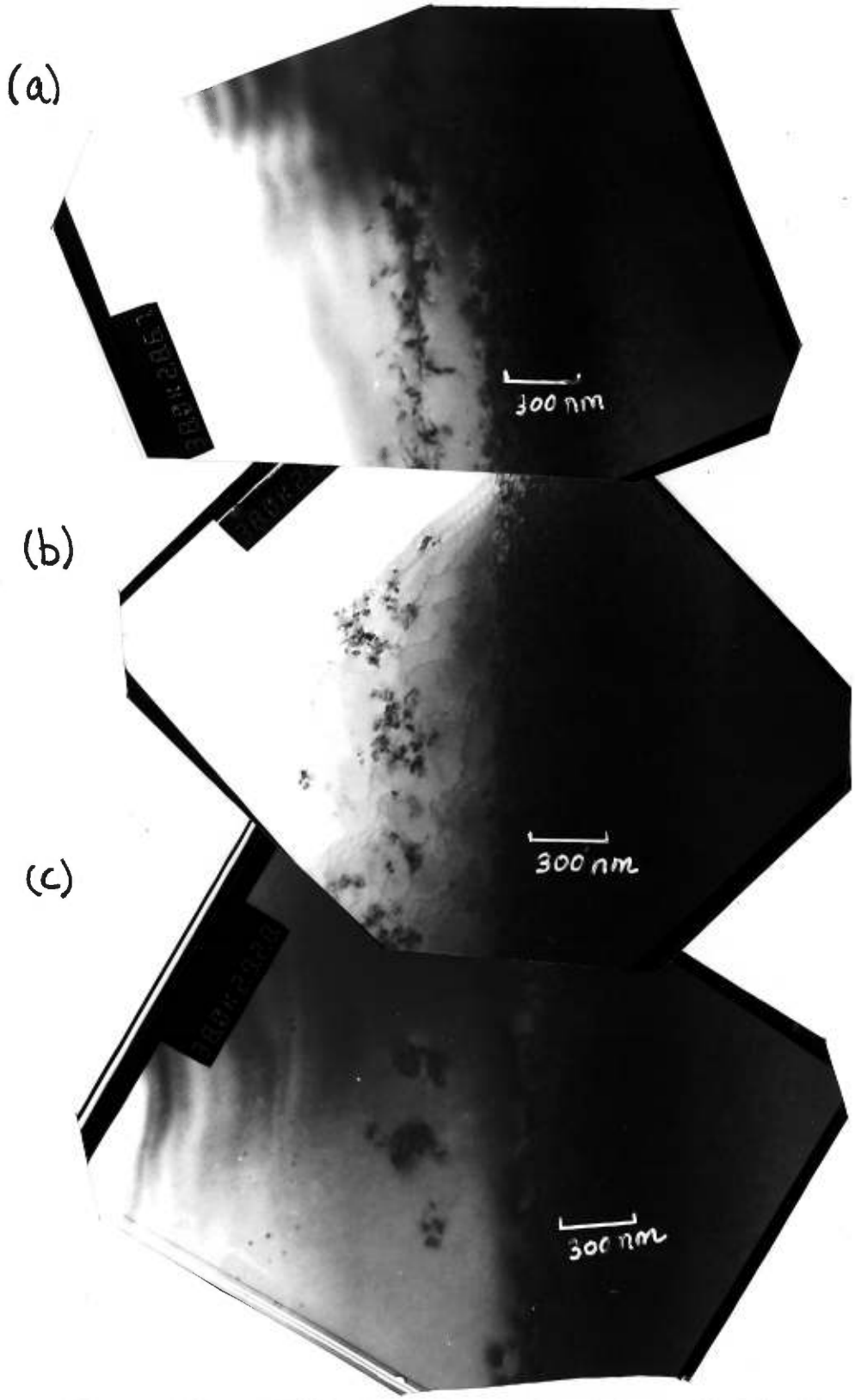

Figure 4-30. XTEM photos of as-implanted ϕ = (a) 0.3, (b) 1.0 and (c) 3.0×10^{17} O/cm^2 (2.00 MeV, 5×10^{14} Si/cm^2 pre-damaged) samples. M=38,000x, $\vec{B}$ = [110], $\vec{g}$ = <111>.

the sample are again characterized by small dark spots. Including all the visible signs of damage, the defect region extends from 2.0 to 3.2 μm. What is not evident is any distinct layer of damage which corresponds to the original pre-damage depth.

The last defect region to be presented is the one located around 1.3 μm, which is only visible in the high dose ($\phi = 3.0 \times 10^{17}$ O/cm^2) sample (figure 4-30c). Figure 4-32 is a magnified view of these defects, giving a clearer picture of their size and spatial distribution. Their size varies about a mean of ~20 nm and the width of the defect band is ~0.5 μm. Without knowing the exact thickness of the sample foil it is impossible to calculate the density of these defects. However, if we assume a thickness of 100 Å, the density is $\sim 10^{16}$ /cm^3. The defects were analyzed again at a higher magnification, and the results are shown in figure 4-33. These photos were taken with no strongly diffracted beam. The microscope was adjusted so that the photo in figure 4-33a was 420 nm under-focused, the photo in figure 4-33b was in focus, and the photo in figure 4-33c was 1.2 μm over-focused. The relative intensity of the defects compared to the background changes as one goes from under-focused to over-focused, where the defects in the under-focused photo are lighter than the background, and have dark rims, and the defects in the over-focused photo are darker than the background with light rims. These image contrasts, as a function of the focus, are considered to be characteristic of cavities [132], and hence we conclude that these defects are indeed cavities. This is not unusual since other researchers have observed cavities in keV oxygen [13,20,81,101,102] and in keV nitrogen [137] implanted samples. The walls of the cavities are predominantly bounded by the {111} planes, with a small rounding of the tips along the {100} and {110} planes, in a manner similar to the oxide precipitates.

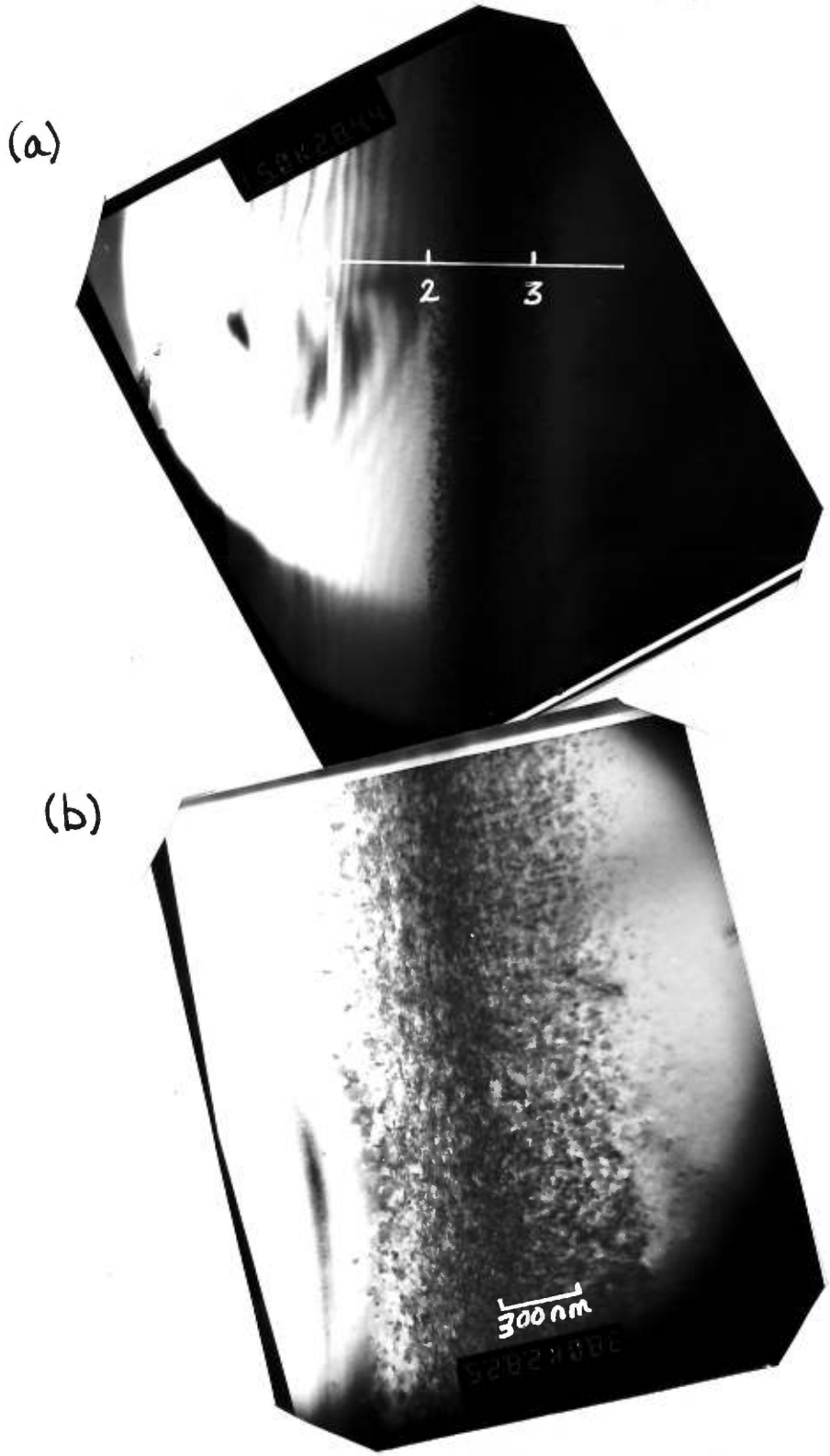

Figure 4-31. XTEM photos of as-implanted $\phi = 1.0 \times 10^{17}$ O/cm^2 (2.00 MeV, 1×10^{15} Si/cm^2 pre-damaged) sample. (a) M=15,000x, $\vec{g}$ = <111>. (b) M=38,000x, $\vec{g}$ = <011>. $\vec{B}$ = [110]. The scale units are given in μm .

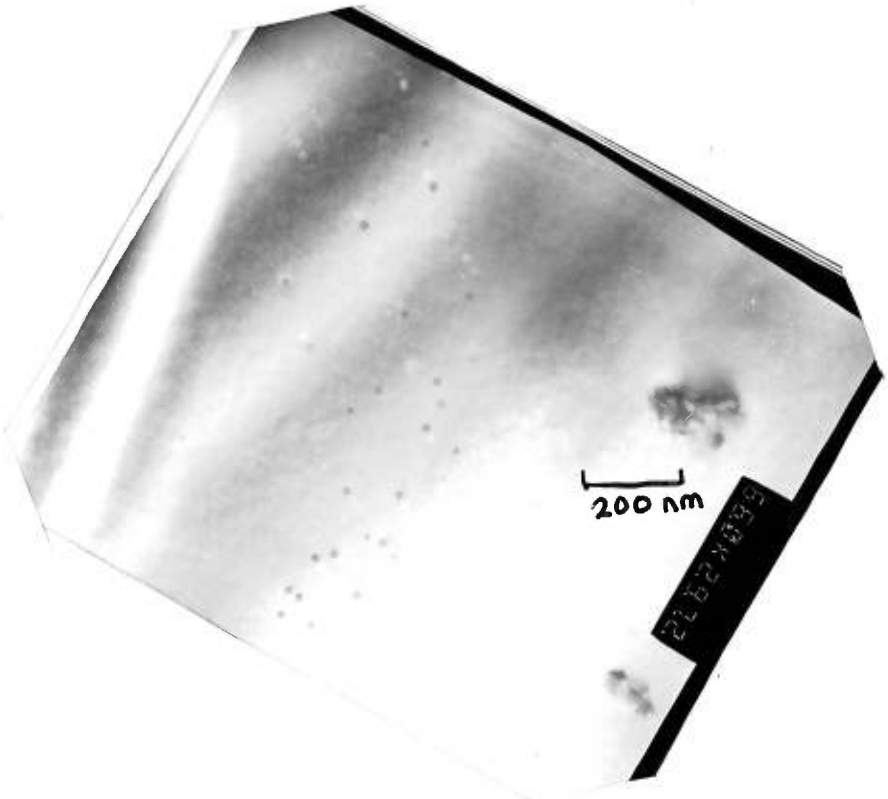

Figure 4-32. XTEM photo of as-implanted $\phi = 3.0 \times 10^{17}$ O/cm^2 (2.00 MeV, 5×10^{14} Si/cm^2 pre-damaged) sample. M=66,000x, $\vec{B}$ = [110], $\vec{g}$ = <111>.

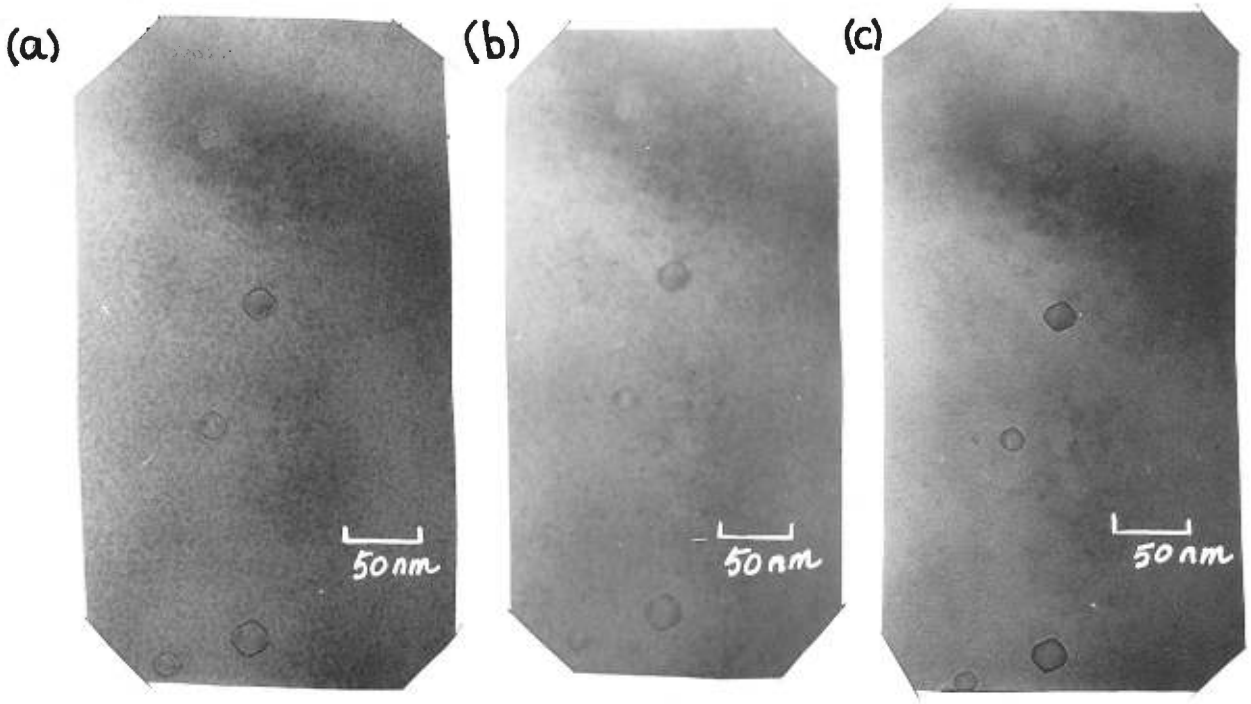

Figure 4-33. XTEM photos of defects in the film of the ϕ =3.0 $\times$ 10^{17} O/cm^2 (2.00 MeV, 5×10^{14} Si/cm^2 pre-damaged) sample. (a) 420 nm under-focused. (b) In focus. (c) 1.2 μm over-focused. M=200,000x, $\vec{B}$ = [110], $\vec{g}$ = multi-beam.

4-4-1-2 Annealed

After the samples were annealed for 12 h at 1300°C, they were analyzed by RBS/C and XTEM. The analyzing conditions for RBS/C, regarding the analyzing beam and detector angles *etc.*, are the same as the previous section, unless otherwise stated.

The annealed RBS/C profiles as a function of oxygen dose as well as a function of the pre-damage conditions are shown in figures 4-34 to 4-36. It should be noted that prior to the RBS/C analysis, each sample was dipped in HF to remove the surface oxide which grew on the samples during the anneal. Some samples had more oxide than others depending on whether N_2 or Ar/O_2 was used as the ambient gas during the anneal. Consequently, the relative depth scales between spectra may be off by as much as 0.15 μm. The aligned yield (χ), normalized to the random yield, is shown in each individual graph for samples with equivalent oxygen doses, but with different pre-damage conditions. For the sake of comparison, RBS/C spectra from standard samples are also shown. As can be seen in these figures, the amount of de-channeling is reduced considerably after the anneal, which indicates the reduction of the number of point defects within the sample.

When comparing the RBS/C results of the annealed samples as a function of the pre-damage condition, there is little difference between spectra which have equivalent oxygen doses, with the exception of the sample pre-damaged with oxygen (figure 4-36c). For this sample, there are two distinct slopes in χ as one goes from the non-damaged region to the damaged region. Extended defects are typically related to the derivative of the aligned yield, and hence these two changes in slope are indicative of two damage regions. Figure 4-37 shows the damage profiles, which were calculated assuming only the presence of extended defects, for this sample as well as the standard sample[†]. The two peaks in the sample pre-damaged with oxygen are well separated (0.22 μm) and very distinct. This is not the case for the standard sample, which has a 'step' in the damage profile approximately 0.15 μm from the main damage peak. These damage profiles are similar in shape to their respective oxygen concentration profiles, although the relative heights of the peaks for sample pre-damaged with oxygen are reversed. This means that, although the maximum de-channeling occurs in the same regions as the maximum oxygen concentration, it is not a direct one-to-one correlation. Since the

[†] Because of the better depth resolution, the damage profile of the standard sample was calculated using the RBS/C spectrum taken after the sample had been etched (figure 4-13d).

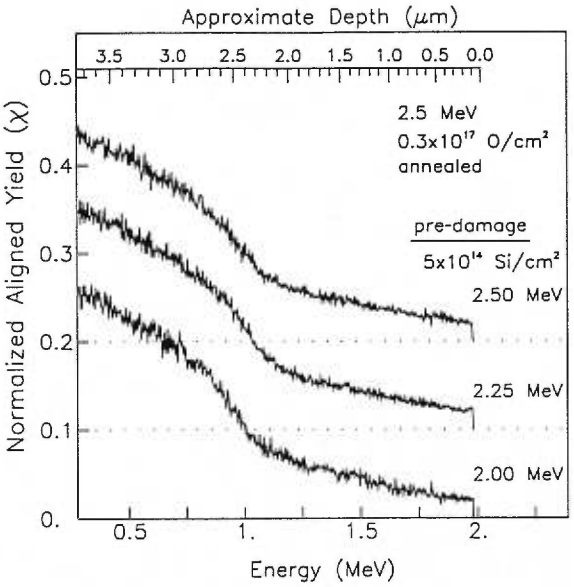

Figure 4-34. The normalized aligned yield (χ) for annealed $\phi = 0.3 \times 10^{17}$ O/cm^2 (5×10^{14} Si/cm^2 pre-damaged) samples. The depth scales were calculated assuming that the stopping power in the aligned direction was 0.6 that of a random direction.

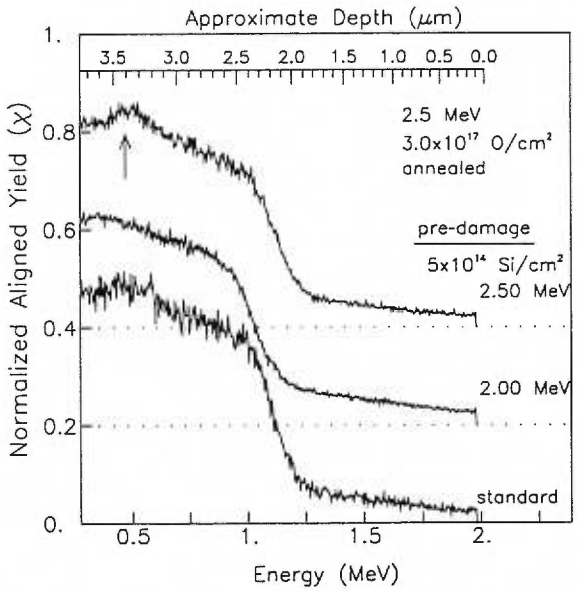

Figure 4-35. The normalized aligned yield (χ) for annealed $\phi = 3.0 \times 10^{17}$ O/cm^2 (5×10^{14} Si/cm^2 pre-damaged) samples. The arrow indicates direct backscatter from oxygen atoms in the sample. The depth scales were calculated assuming that the stopping power in the aligned direction was 0.6 that of a random direction. (*standard* refers to no pre-damage)

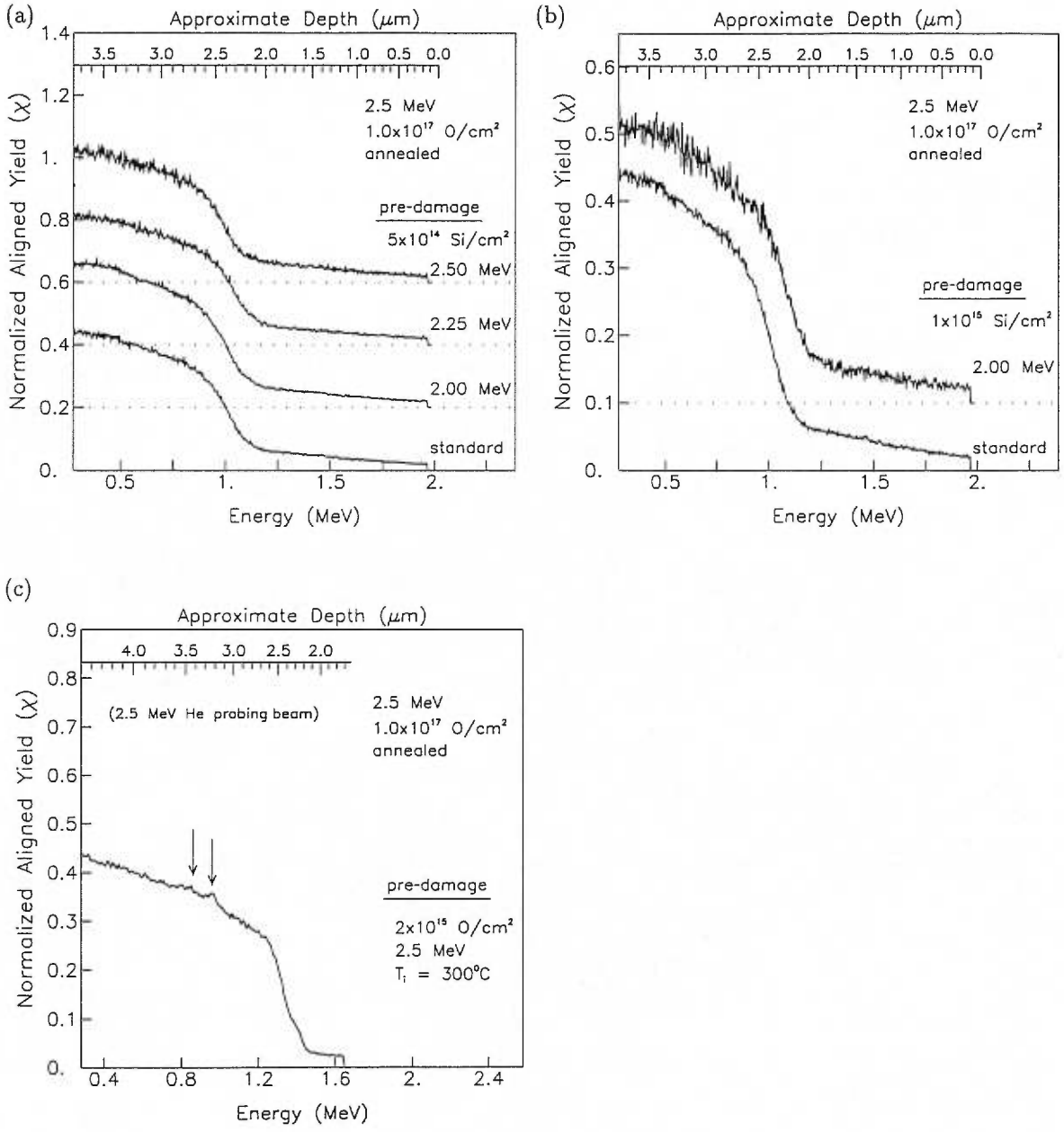

Figure 4-36. The normalized aligned yield (χ) for annealed $\phi = 1.0 \times 10^{17}$ O/cm^2 ((a) 5×10^{14} Si/cm^2, (b) 1×10^{15} Si/cm^2 and (c) 2×10^{15} O/cm^2, T_i=300°C, pre-damaged) samples. The sample analyzed in *(c)* was etched 1.62 μm prior to the analysis. The arrows indicate direct backscatter from oxygen atoms in the sample. The depth scales were calculated assuming that the stopping power in the aligned direction was 0.6 that of a random direction. (*standard* refers to no pre-damage)

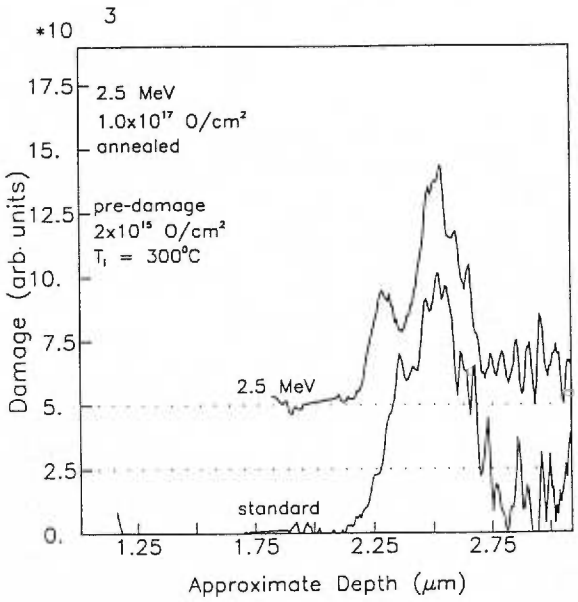

Figure 4-37. The calculated damage profiles assuming only extended defects for $\phi = 1.0 \times 10^{17}$ O/cm^2 (2×10^{15} O/cm^2 pre-damaged and standard) samples. The depth scales were calculated assuming that the stopping power in the aligned direction was 0.6 that of a random direction. (*standard* refers to no pre-damage)

above analysis was based on the assumption that only dislocations were present, we conclude that the number of dislocations is not a direct, linear function of the concentration of oxygen.

Aside from the above specific case, not much information is available through RBS/C analysis about the changes in the damage profiles as a function of the pre-damage condition, in either the annealed or as-implanted samples. So, again, XTEM was used to study samples pre-damaged with 2.00 MeV silicon.

Figure 4-38 shows the XTEM results for the annealed $\phi = 0.3 \times 10^{17}$ O/cm^2 sample pre-damaged with 5.0×10^{14} Si/cm^2. In these photos, the 'wave-like' images which occur in the thinner regions of the sample foil are related to the preparation of the sample, rather than any inherent defects. The 0.33 μm thick surface oxide ('A' in figure 4-38a) which grows during the anneal can be readily seen. All measurements of the depth have been adjusted to account for the volume of Si used in the growth of the oxide cap. The dark region immediately under the surface oxide is a thin layer of strained silicon. Deeper in the sample, at about 2 μm, there is a band of oxide precipitates which corresponds exactly to the damaged region seen in the as-implanted sample (*cf.* figure 4-29a). However, very few of the original defect structures, other than oxide precipitates, remain. In figure 4-38a one can see

three dislocations extending between this initially damaged region and the main defect band. An expanded view of one of these defects is shown in figure 4-38b. In this photo it can be clearly seen that the dislocations are pinned by the oxide precipitates. The slightly darker contrast surrounding the dislocations are caused by residual stress in the silicon. The majority of the defects in the main band are located in the region 2.3 – 2.7 μm. There is at least one defect ('B' in figure 4-38a) which extends 3 μm into the substrate.

XTEM photos of the annealed $\phi = 1.0 \times 10^{17}$ O/cm^2 sample, pre-damaged with 5.0×10^{14} Si/cm^2, are shown in figure 4-39. At d_{Si} (2 μm) a band of oxide precipitates remains. Unlike the lower-dose sample, these photos do not show any dislocations stretching from the main band all the way to the pre-damaged region, nor are there any dislocations within the pre-damage region itself. There are no visible signs of stress in this region (see figure 4-39b) either. However, there are dislocations which span the region from the main band to precipitates located at ~2.2 μm, halfway to d_{Si}. The main defect band, which extends from 2.4 – 3.0 μm (figure 4-39a), is composed mostly of dislocations, each being pinned at both ends by oxide precipitates. In figure 4-39b, the strain in the main defect band is evident, to such an extent that it is difficult to see the individual oxide precipitates.

Finally, in figure 4-40, XTEM photos of the annealed $\phi = 3.0 \times 10^{17}$ O/cm^2 sample, pre-damaged with 5.0×10^{14} Si/cm^2, are shown. In both photos, the silicon film has two distinct contrasts, the shallower region being lighter. This is due to the relative thickness of the sample foil. Looking at the region around 1.3 μm, it can be seen that the voids that were in the as-implanted sample have decreased in density, but have increased in size (*cf.* figure 4-30). They are now ~50 nm, as compared to 20 nm before the anneal. At a depth of 2 μm there are a few remaining oxide precipitates. However, there are no visible dislocations extending between this region and the main defect band. As was the case for the 1.0×10^{17} O/cm^2 sample, there are precipitates located at a depth only slightly more shallow than the main band, and they are connected via dislocations. An expanded view of one of these defects (located at the bottom of the photo in figure 4-40a) is shown in figure 4-40b. The silicon substrate is not defect free, which can be seen by the two long dislocations, labelled 'A' and 'B' (figure 4-40a), which extend to depths >4 μm. The alternating contrast of defect 'A' is an indication that the defect is steeply inclined to the beam direction of [110]. Although it is not absolutely certain, it appears that defect 'B' starts at the site of an oxide precipitate which is located at a depth of 3 μm.

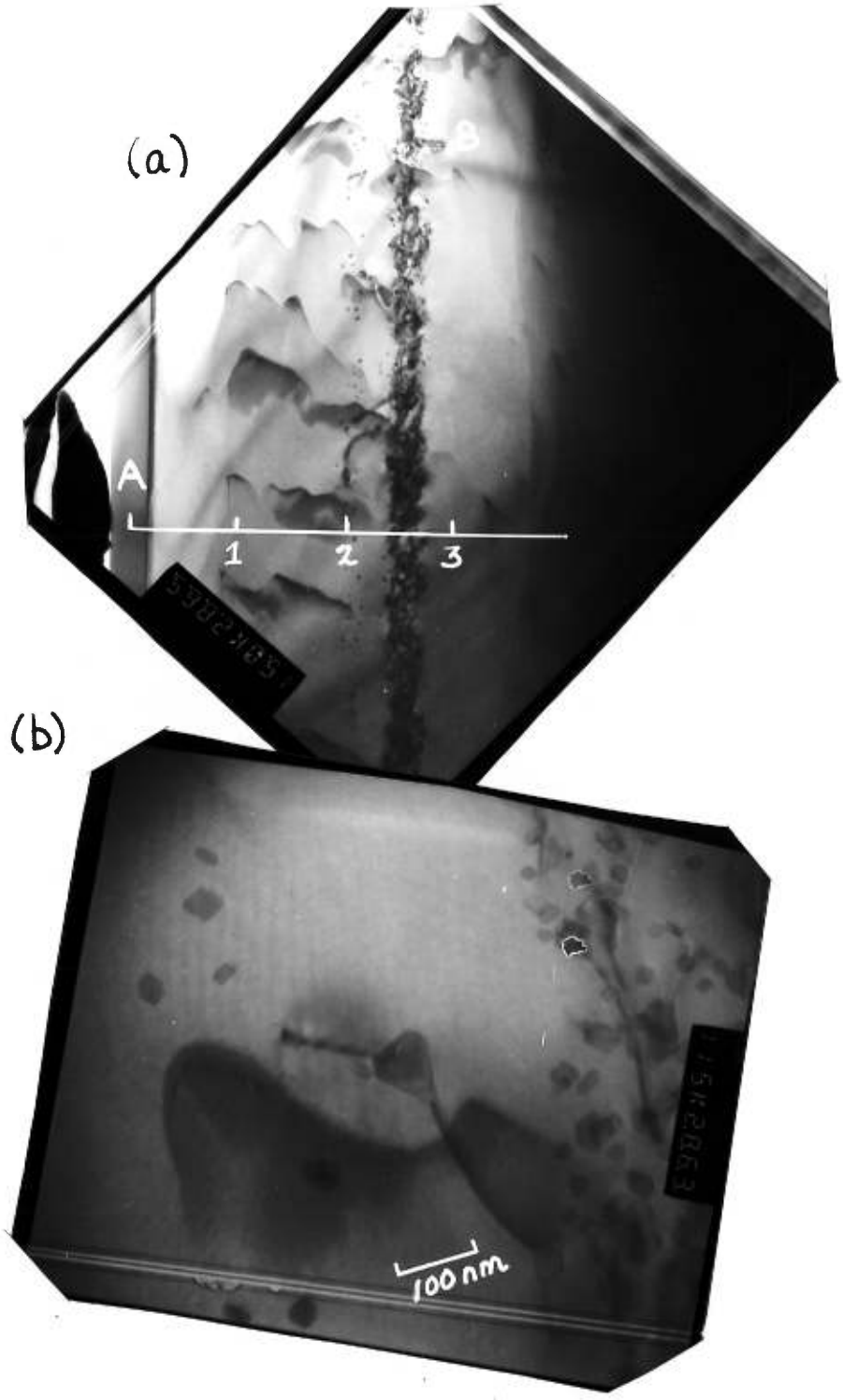

Figure 4-38. XTEM photos of annealed $\phi = 0.3 \times 10^{17}$ O/cm^2 (2.00 MeV, 5×10^{14} Si/cm^2 pre-damaged) sample. (a) M=15,000x and (b) M=115,000x. $\vec{B}$ = [110], $\vec{g}$ = <111>.

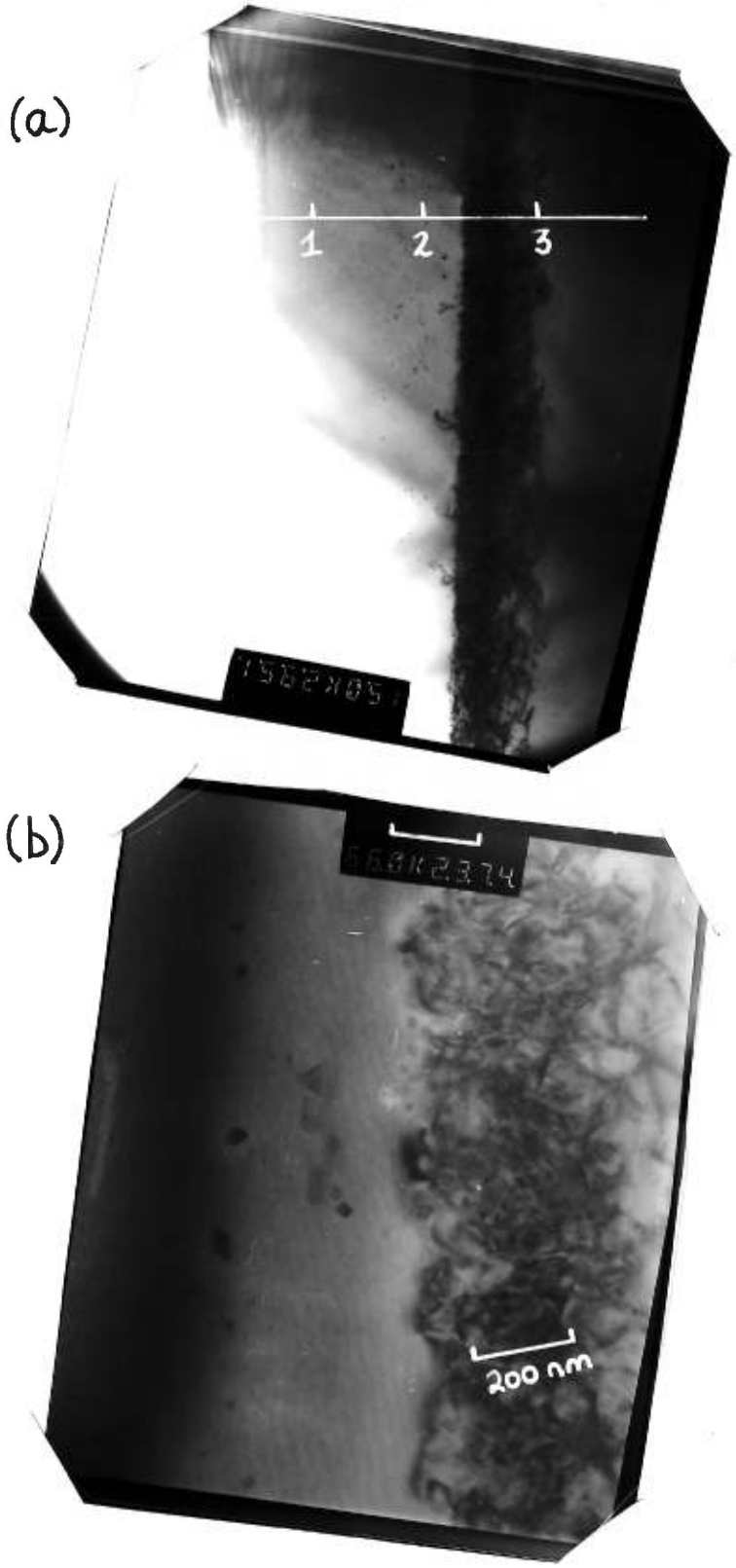

Figure 4-39. XTEM photos of annealed $\phi = 1.0 \times 10^{17}$ O/cm^2 (2.00 MeV, 5×10^{14} Si/cm^2 pre-damaged) sample. (a) M=15,000x, $\vec{g}$ = <115> and (b) M=66,000x, $\vec{g}$ = <400>. $\vec{B}$ = [110]. $\vec{g}$ = <111>. The scale units are given in μm .

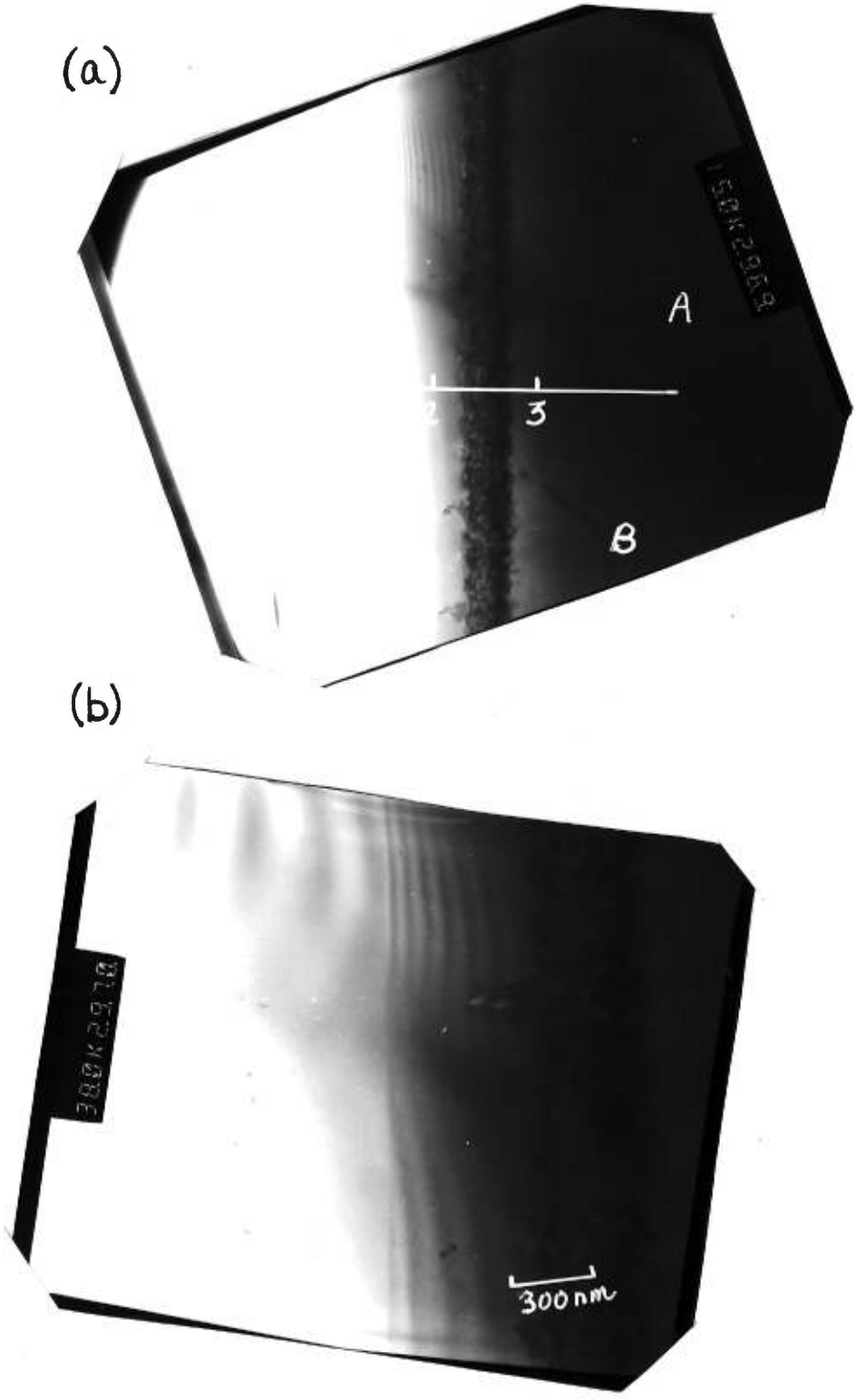

Figure 4-40. XTEM photos of annealed $\phi = 3.0 \times 10^{17}$ O/cm^2 (2.00 MeV, 5×10^{14} Si/cm^2 pre-damaged) sample. (a) M=15,000x, and (b) M=38,000x. $\vec{B} = [110]$, $\vec{g} = <111>$. The scale units are given in μm .

The annealed $\phi = 1.0 \times 10^{17}$ O/cm^2 sample, pre-damaged with 1.0×10^{15} Si/cm^2, was also analyzed by XTEM. The results are shown in figure 4-41. The photo in figure 4-41 was taken with no strongly diffracted beam. There are no visible signs of damage in the silicon film. The dislocations between oxides are clearly evident, and are present over a depth range of 2.2 - 3.0 μm. In most respects, the damage seen in this photo is no different from the damage seen in other samples with equivalent dose.

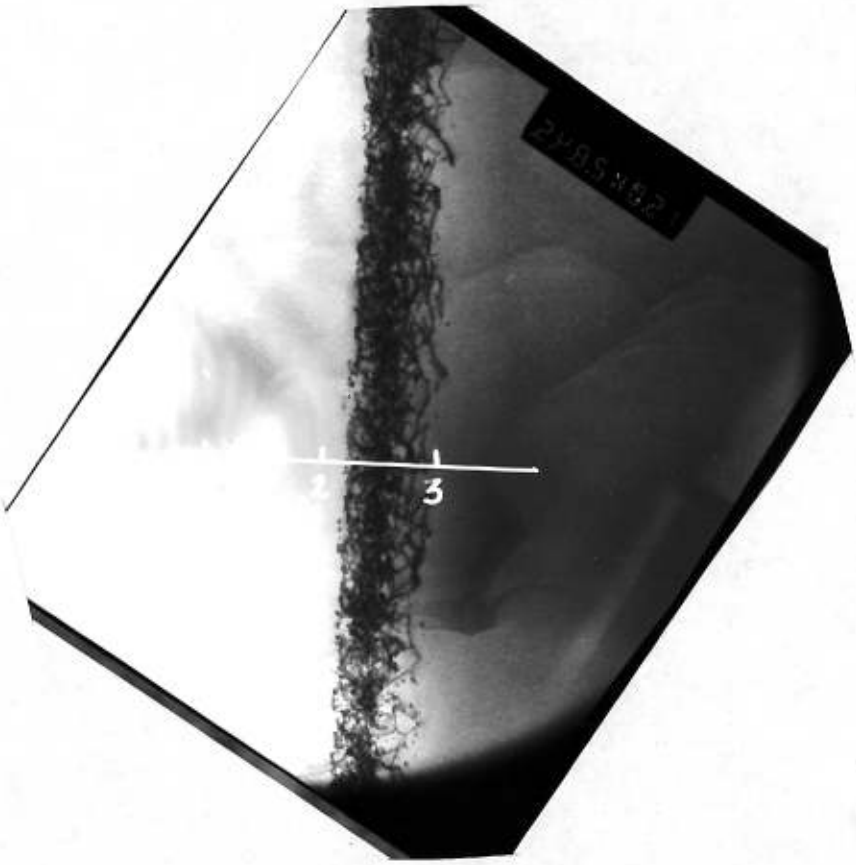

Figure 4-41. XTEM photo of annealed $\phi = 1.0 \times 10^{17}$ O/cm^2 (2.00 MeV, 1×10^{15} Si/cm^2 pre-damaged) sample. M=15,000x. $\vec{B}$ = [110], $\vec{g}$ = multi-beam. The scale units are given in μm .

4-4-1-3 Discussion

To help clarify the nature of the defects found in the pre-damaged samples implanted with oxygen, the defect contrast from all the XTEM photos have been summarized for the as-implanted samples (Table 4-VI) and the annealed samples (Table 4-VII). Each depth region in the sample will be discussed separately, starting with the silicon film.

It was only in the samples implanted with $\phi = 3.0 \times 10^{17}$ O/cm^2 that there was any observable damage in the silicon film. However, the nature of the damage depends on whether or not the sample was damaged with silicon prior to the oxygen implant. In the as-implanted samples, the damage in the standard sample appeared to be a mixture of oxide precipitates and very small ($\leq$10 nm) dislocations (figure 4-12b). In the pre-damaged sample the defects were voids, with diameters in the range of 20 nm.

To explain this difference, we must first refer to the work done by Venables and Zhou regarding the interaction of oxygen, vacancies and strain, in oxygen implanted silicon [14,20]. It was shown that in low dose ($\leq 10^{17}$) as-implanted samples, the silicon is positively strained in the region of peak damage (d_O), and negatively strained in the surface region. The negative strain, whose magnitude is dependent on the oxygen dose, is directly related to an excess of vacancies in the silicon film. The oxygen in this region is bound in vacancy complexes and cannot form precipitates. If the strain exceeds the elastic limit of silicon (0.33 – 0.65% [15]) dislocations form at the boundary between the negatively and positively strained silicon† with a subsequent reduction in the strain and number of vacancies. The released oxygen is now able to form precipitates. Looking at the damage in the surface film in the standard, $\phi = 3.0 \times 10^{17}$ O/cm^2, as-implanted sample, it is evident that the strain in the silicon film exceeded the elastic limit, resulting in the formation of small dislocations ('B' in figure 4-12b) and oxide precipitates ('A' in figure 4-12b).

Another observed mechanism for the release of strain in the the silicon film is the formation of O_2 gas filled cavities [20]. As the vacancies agglomerate to form voids, the oxygen atoms that are bound to the vacancies form gaseous oxygen which then fills the void, keeping it stable. Hence the oxygen is not free to form precipitates. This mechanism of strain relief is consistent with the

† For keV implants, this occurs near the surface. For MeV implants this depth is $\sim 1/2\, R_p$.

TABLE 4-VI

Damage (as seen in XTEM photos) in as-implanted samples as a function of depth and implant-conditions. The pre-damage was 2.00 MeV silicon implant followed by a 1 h, 900°C, anneal. The oxygen was implanted with an energy of 2.5 MeV.

	Silicon Film	Pre-Damage Region	Peak Damage Region	Substrate
No Pre-Damage			Predominantly dislocations. Damage starts at ~2.3 μm.	Small dark spots are seen...
0.3×10^{17} O/cm^2	No visible damage.	No visible damage.	Film/damage interface is relatively sharp, extends to 2.7 μm.	$\sim 10^9$/cm^2, maximum depth 3.0 μm.
1.0×10^{17} O/cm^2	No visible damage	No visible damage.	Film/damage interface is sharp, extends to 3.0 μm.	$> 10^{10}$/cm^2, maximum depth 3.4 μm.
3.0×10^{17} O/cm^2	Very small black spots plus a few larger spots with strain are seen centered around 1.3 μm($10^7 - 10^8$).	No visible damage.	Film/damage interface is sharp, extends to 3.2 μm.	$> 10^{10}$/cms, maximum depth 3.4 μm.
5.0×10^{14} Si/cm^2			Predominantly dislocations. Damage starts at ~2.3 μm.	Small dark spots are seen...
0.3×10^{17} O/cm^2	No visible damage.	Continuous network of dislocations, 0.2 μm wide, interspersed with oxide precipitates. Dislocations extend from this region to next damage region.	Un-damaged/damaged interface is not sharp, extends to 2.7 μm.	$\sim 10^9$/cm^2, maximum depth 3.3 μm.
1.0×10^{17} O/cm^2	No visible damage.	Dislocations and highly strained regions. Width of layer ~0.3 μm. Dislocations extend from this region along <111> direction to next damage region.	Un-damaged/damaged interface is not sharp, extends to 3.2 μm.	$> 10^{10}$/cm^2, maximum depth 3.4 μm.
3.0×10^{17} O/cm^2	Many voids (~20 nm) ($\sim 10^9$/cm^2) centered around 1.3 μm. No sign of stress.	Isolated regions of defects surrounded by highly strained silicon. Dislocations extending between this region and the next are not seen.	Un-damaged/damaged interface is not sharp, extends to 3.2 μm.	$> 10^{10}$/cm^2, maximum depth 3.4 μm. One long dislocation along <111> direction ($\sim 10^7$/cm^2) extends to a final depth of 4 μm.
1.0×10^{15} Si/cm^2				
1.0×10^{17} O/cm^2	No visible damage.	No dislocations, but many small black spots, probably oxide precipitates. Density increases with depth, until this region merges into next.	No clear delineation between previous damage region and this one. Damage is predominantly dislocations, extends to 3.2 μm.	Small dark spots are seen, $\sim 10^{10}$/cm^2, up to a depth of 3.4 μm. One long dislocation ($\sim 10^7$/cm^2) along <111> direction extends to a final depth of 3.8 μm.

TABLE 4-VII

Damage (as seen in XTEM photos) in annealed samples as a function of depth and implant-conditions. The pre-damage was 2.00 MeV silicon implant followed by a 1 h, 900°C, anneal. The oxygen was implanted with an energy of 2.5 MeV, and subsequently annealed for 12 h at 1300°C.

	Silicon Film	Pre-Damage Region	Peak Damage Region	Substrate
No Pre-Damage			Predominantly oxides and dislocations. Damage starts at ~2.3 μm.	Small precipitates are seen...
0.3×10^{17} O/cm^2	No visible damage.	No visible damage.	Film/damage interface is relatively sharp, extends to 2.7 μm.	$\sim 10^8$/cm^2 between 2.5 – 2.7 μm.
1.0×10^{17} O/cm^2	No visible damage.	No visible damage.	Film/damage interface is sharp, extends to 2.7 μm.	$\sim 10^8$/cm^2, maximum depth 3.2 μm.
3.0×10^{17} O/cm^2	Very small black spots are seen at depths greater than 1 μm. One large ($^1/_2$ μm long) unknown defect at 1.3 μm.	No visible damage.	Film/damage interface is relatively sharp, extends to 3.0 μm.	10^{10}/cm^2 (2.7-3.2μm) spots with dislocations, maximum depth 3.2 μm.
5.0×10^{14} Si/cm^2			Predominantly oxides and dislocations. Damage starts at ~2.3 μm.	Small precipitates are seen...
0.3×10^{17} O/cm^2	No visible damage.	Many oxides and a few dislocations. Dislocations extend from this region to next damage region.	Un-damaged/damaged interface is sharp, extends to 2.7 μm.	10^7/cm^2, with dislocation, at 3.2 μm. Otherwise no precipitates past 2.8 μm.
1.0×10^{17} O/cm^2	No visible damage.	Lots of precipitates, larger precipitates halfway between this region and next. Dislocations extend from oxides in middle region to next damage region.	Un-damaged/damaged interface is relatively sharp, extends to 3.0 μm.	10^{10}/cm^2 (2.7-3.2μm) spots with dislocations, maximum depth 3.2 μm.
3.0×10^{17} O/cm^2	Voids (~50 nm) (~ 10^9/cm^2) centered around 1.3 μm. No sign of stress.	Isolated regions of precipitates. Dislocations extending between this region and the next are not seen.	Un-damaged/damaged interface is relatively sharp, extends to 2.7 μm.	$\sim 10^8$/cm^2 deeper than 2.8 μm. Long dislocations very deep in substrate.
1.0×10^{15} Si/cm^2				
1.0×10^{17} O/cm^2	No visible damage.	No dislocations, or precipitates.	Density of precipitates and dislocations increases slowly with depth, starting at 2.2 μm.	10^9/cm^2 precipitates, and dislocations, are seen up to a depth of 3.1 μm.

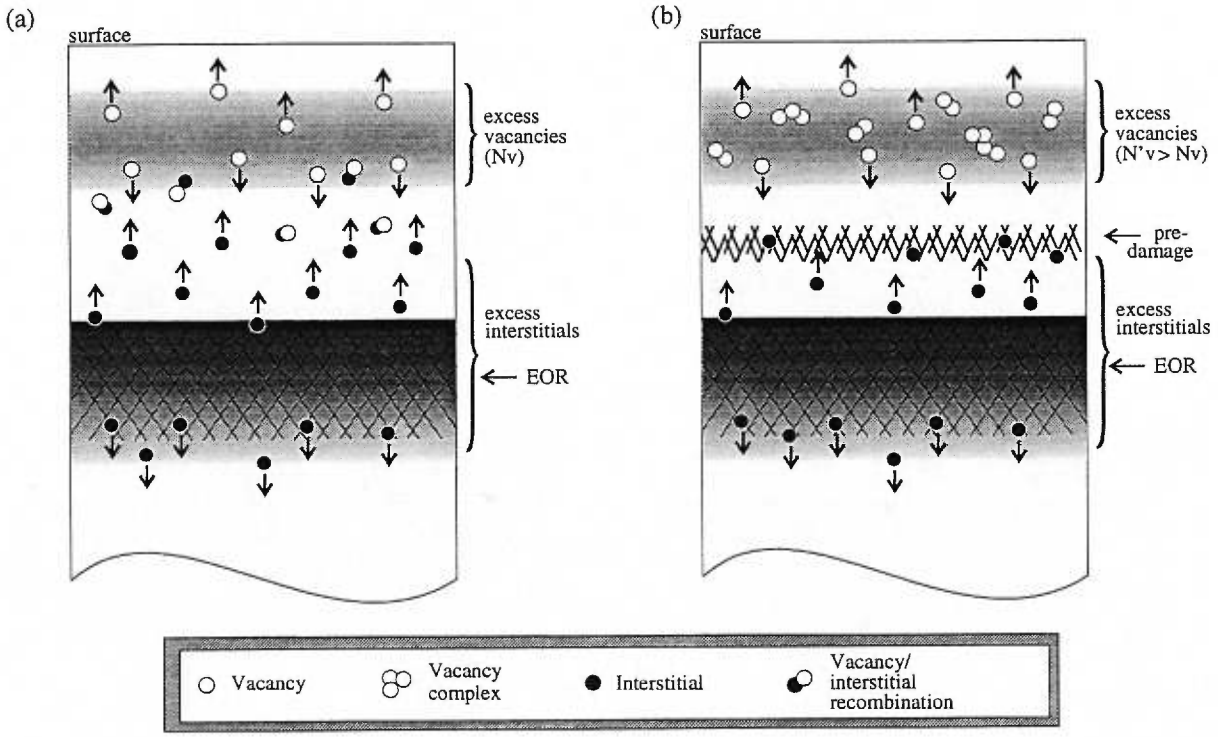

Figure 4-42. Schematic of the interaction of silicon interstitials and vacancies in the early stages of oxygen implantation into (a) virgin and (b) pre-damaged silicon sample.

observed results of the pre-damaged 3.0×10^{17} O/cm^2 sample, which had voids and no observable oxide precipitates in the silicon film.

The question now becomes, why, in the pre-damaged sample, was the strain released by the formation of voids, rather than dislocations and precipitates? The first and foremost effect of the pre-damage is its ability to act as a sink for excess interstitials generated near the EOR [21]. Thus, it is an effective barrier preventing the silicon interstitials from the EOR migrating to the near-surface region. This ability to act as a sink for the interstitials is not constant with time, since the damage at d_{Si} changes as a function of dose. However, up to a dose of 1.0×10^{17} O/cm^2 there is an almost continuous layer of damage. So, at least in the early stages of the implantation, the silicon film is more vacancy-rich than its standard counterpart. With a larger density of vacancies, the probability is higher that the vacancies will interact to form larger and more stable vacancy complexes, or void-like defects. A schematic illustrating this process is shown in figure 4-42. As the dose increases,

the damage at d_{Si} no longer forms a complete barrier to the silicon interstitials. However, once the micro-voids have formed, they continue to grow.

The damage in the silicon film in these samples ($\phi = 3.0 \times 10^{17}$ O/cm^2) behaved in predictable ways during the anneal. In the annealed, standard sample, the damage in the film was difficult to analyze. However, it appears that the tiny dislocations have annealed, whereas the oxide precipitates remain. In the pre-damaged sample, the size of the voids grew larger, with a subsequent decrease in density. It is clearly the as-implanted damage characteristics which determines the nature of the post-anneal damage in this region.

The next region to be discussed is the pre-damage region, located at a depth d_{Si}. As was mentioned earlier, the pre-damage acts as a sink for the silicon interstitials which are generated during the oxygen implantation and precipitation. Essentially, the silicon interstitial atom binds to the edge of the dislocation, becoming part of the extra atomic plane which comprises extrinsic dislocations. This causes the dislocations to grow. The implanted oxygen also interacts with the pre-damage, where the edge of the dislocation is an attractive site for the nucleation of oxide precipitates. These precipitates then impede the absorption of the silicon interstitials onto the existing dislocation. It is by this mechanism that they prevent the dislocations from growing, effectively 'pinning' the dislocation. In addition to these processes, there is dynamic annealing of the pre-damage which also occurs during the implantation. The oxygen ion loses energy via elastic collisions (binary collisions, formation of phonons, *etc.*) which heats the sample locally. Coupled with the fact that the sample is kept at a global temperature of 570°C, the local temperature is sufficient to cause some of the existing damage to anneal during the implantation.

Thus, we can now explain the defect characteristics of the pre-damaged samples (2.00 MeV, 5.0×10^{14} Si/cm^2) as a function of oxygen dose. At the lowest oxygen dose ($\phi = 0.3 \times 10^{17}$ O/cm^2), the defect structure has changed from the original extrinsic dislocation loops to a continuous network of small dislocations, with evidence that there are oxide precipitates decorating these dislocations. Similarly, other dislocations originating from the peak of the oxygen damaged region (d_O) have been pinned by the pre-damage layer. As the dose increases to $\phi = 1.0 \times 10^{17}$ O/cm^2 the dynamic annealing effect becomes noticeable, insofar as the dislocation network in the pre-damage layer is no longer continuous. The defect structure has continued to evolve, due to the interaction of the oxygen and silicon interstitials, where there appear to be fewer dislocations and more oxide precipitates. And

finally at the highest dose of $\phi = 3.0 \times 10^{17}$ O/cm^2, there are only isolated pockets of damaged regions left, which also appear to be oxide precipitates surrounded by highly strained crystalline silicon. At this stage, no dislocations spanning the region between d_O and d_{Si} are seen in the XTEM photos. Upon annealing, for all the samples, the majority of the dislocations disappear, with only oxide precipitates to mark the original location of the pre-damage. The few remaining dislocations extend between the oxides.

For the sample pre-damaged with 2.00 MeV, 1.0×10^{15} Si/cm^2, the processes involved are the same, but the results are remarkably different. In this case, the original pre-damage did not consist of a band of dislocation loops, but rather long dislocation dipoles along the (001) and {111} planes (figure 4-6). There were also regions near d_{Si} where there were no visible dislocations. With an oxygen dose of only 1.0×10^{17} O/cm^2, all of the dislocation dipoles have annealed and there was no evidence of any other dislocations.

The differences between this sample and the standard sample can lead one to hypothesize about the evolution of the damage in the sample, as a function of oxygen dose. Unlike the standard case, the damage in the as-implanted sample does not start abruptly at 2.3 μm. Instead there is a gradual increase of small defect clusters starting at 2.0 μm, which eventually merge with the main defect band. It appears as if the damage between 2.0 μm and 2.3 μm could not be effectively annealed during the implant. It is hypothesized that in the earlier stages of the implant, before the pre-damage was annealed, there were dislocations extending between the two damage regions. These provided the nucleation sites for oxide precipitation. As the oxygen dose increased, the dislocations were annealed and the oxide precipitates, or oxygen/point defect clusters, remained. With very few, if any, dislocations remaining at d_{Si}, there are no preferential nucleation sites for oxide formation at this depth. When the sample is annealed, the oxygen migrates towards the main oxide band via the Ostwald ripening process. As a result, the silicon film has no observable defects up to a depth of 2.2 μm.

The main defect region (2.3 – 3.2 μm) appears to be unaffected by the presence of pre-damage. In all the as-implanted samples, the damage appears to be comprised mostly of dislocations in the shallower region of the main defect band, and small defect clusters and/or precipitates in the deeper regions. Again, in all the samples, the damage extends into the substrate to depths greater than 3 μm. However, after the samples are annealed the quantity of damage past R_p is different for each sample

(see Table 4-VII under 'Substrate'). The damage in this region is predominantly oxide precipitates with dislocations stretching between them, and all the samples have at least one or two precipitates at depths greater than 3 μm. The $\phi = 0.3 \times 10^{17}$ O/cm^2 sample has only a very few of these defects, independent of the pre-damage. At $\phi = 1.0 \times 10^{17}$ O/cm^2 however, the samples pre-damaged with either 5.0×10^{14} or 1.0×10^{15} Si/cm^2 have many such defects, while the standard sample has very few. To add to the confusion, the reverse is true for the $\phi = 3.0 \times 10^{17}$ O/cm^2 samples. If there was accidental channeling of the oxygen beam during the implantation, it is not evident in the XTEM analysis of the as-implanted samples, although it is not obvious that it would be noticeable, even if it had occurred. Cerofolini's hypothesis about ET precipitation (§2-5-1-2) cannot be used to explain the differences in the relative intensities of the precipitates as a function of pre-damage, since ET precipitation is directly related to the number of hot collisional cascades at the EOR, and the cascade development in this region is not affected by damage located 1 μm prior to the EOR. Thus, we can conclude either one of two things, (1) there was accidental channeling in some of the samples, and that this is not evident in the as-implanted XTEM photos, or (2) the residual damage and precipitates in the silicon substrate is an extremely sensitive function of one of the implantation or annealing parameters. However, which parameter that might be is not evident.

4-4-2 Oxygen Distribution

The distribution of oxygen ions and oxide precipitates were characterized by ERD, SIMS and XTEM, before and after annealing. No distinction is made between samples that have been annealed in an Ar/O_2 flow or N_2 flow as the oxygen profiles remain the same. This is discussed in Appendix A. The reader should be reminded that the ERD spectra have been shifted so that the depth range is consistent with the RBS/C results, as described in §4-3-1. The depth of the pre-damage was estimated using TRIM.

4-4-2-1 As-Implanted

The as-implanted oxygen concentration profiles, as a function of the pre-damage conditions, were measured using ERD analysis and the results are shown in figure 4-43 ($\phi = 3.0 \times 10^{17}$ O/cm^2), and figure 4-44 ($\phi = 1.0 \times 10^{17}$ O/cm^2). The dots are the original data points and the error bars indicate the statistical uncertainty in the data. The solid line is the same data after being smoothed using a

FFT algorithm. The pre-damage depths are indicated by arrows. As can be seen in these figures, there are only slight variations in the oxygen profiles as a function of the pre-damage conditions. The oxygen profiles near d_{Si}, for either dose, do not show any excess oxygen peaks which are larger than the statistical fluctuations. For the case of $\phi = 3.0 \times 10^{17}$ O/cm^2 the differences in the oxygen profiles seem to be a result of the statistical fluctuations of the data itself. However, for the $\phi = 1.0 \times 10^{17}$ O/cm^2 samples, the oxygen concentration profile is broader at the peak concentration for the standard and 2.00 MeV pre-damaged samples than it is for the samples pre-damaged with higher energies of silicon.

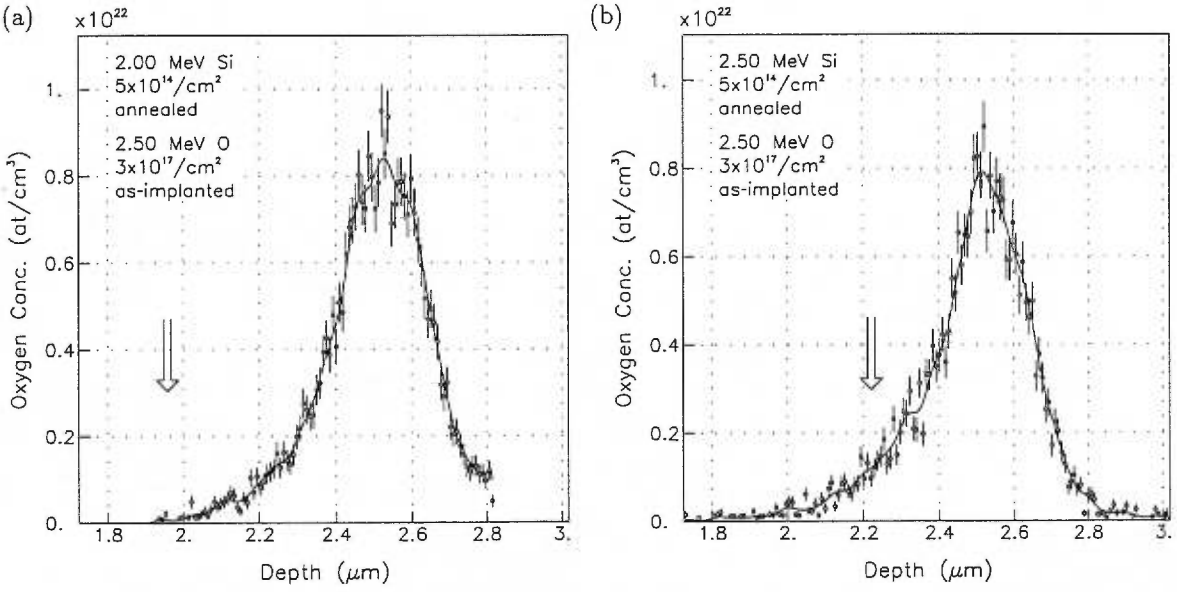

Figure 4-43. Oxygen concentration profiles for as-implanted $\phi = 3.0 \times 10^{17}$ O/cm^2 ((a) 2.00 MeV and (b) 2.50 MeV, 5×10^{14} Si/cm^2 pre-damaged) samples. The arrows indicate the depth of the silicon pre-damage. The dots are calculated from ERD data, and the solid lines are the results after smoothing.

Another sample (ϕ =1.0×10^{17} O/cm^2) pre-damaged with 2.00 MeV, 5×10^{14} Si/cm^2 was studied by SIMS and the results are shown in figure 4-45. The oxygen content was profiled by using the ^{16}O and $^{62}(SiO_2)$ signal. The ^{16}O spectrum has been normalized to the implanted dose. The $^{62}(SiO_2)$ has not been normalized, although the scale was chosen so that the peak concentration of the $^{62}(SiO_2)$ signal is the same as the peak concentration of the ^{16}O signal. The $^{62}(SiO_2)$ profile shows a marked difference from the ^{16}O profile, which indicates that not all of the oxygen has precipitated into SiO_2. The SiO_2 signal increases above background after the ^{16}O concentration signal

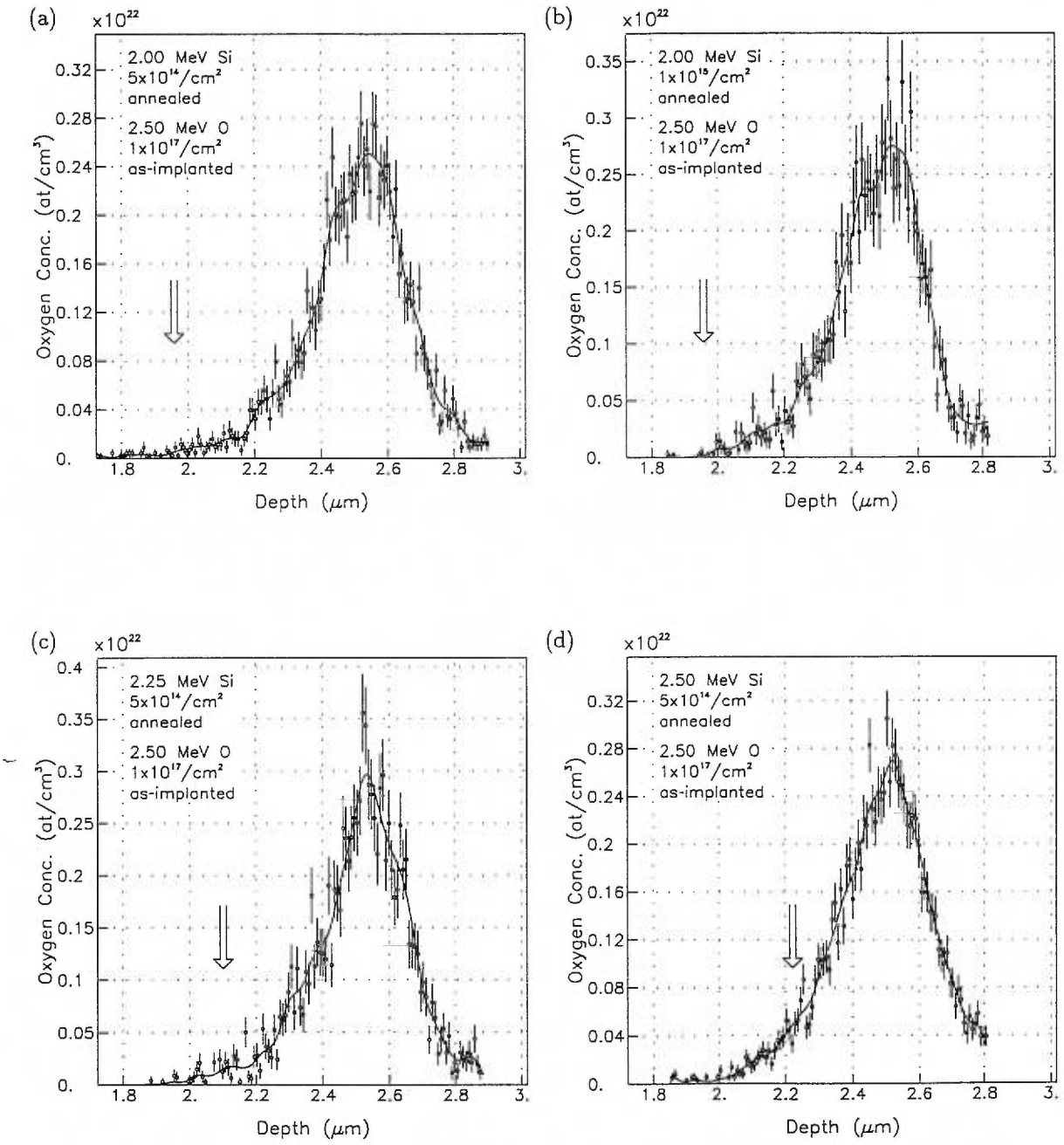

Figure 4-44. Oxygen concentration profiles for as-implanted $\phi = 1.0 \times 10^{17}$ O/cm^2 ((a) 2.00 MeV, (b) 2.00 MeV, (c) 2.25 MeV and (d) 2.50 MeV, 5×10^{14} Si/cm^2 pre-damaged) samples. The arrows indicate the depth of the silicon pre-damage. The dots are calculated from ERD data, and the solid lines are the results after smoothing.

exceeds 5×10^{19} O/cm^3, which indicates that the surface region, at least, is supersaturated with non-precipitated oxygen†.

The total oxygen concentration rises smoothly, starting from 3×10^{18} O/cm^3 at the surface, and gradually increasing in concentration until it reaches 1.95 μm. At this depth, indicated by the arrow, there is a slight bump in the oxygen concentration, starting at 1.8 μm and ending at 2.1 μm. This is consistent with the XTEM photos shown in §4-4-1-2 which indicate the presence of precipitates at this depth. The integral concentration of excess oxygen in this peak, shown in greater detail in figure 4-45b, is $\sim 5 \times 10^{14}$ O/cm^2. This excess concentration clearly indicates that the pre-damage site preferentially attracts oxygen. After the bump, the concentration of oxygen continues to increase smoothly to a peak concentration of 2.4×10^{21} O/cm^3, at $R_p = 2.55$ μm. Past this point, the concentration of oxygen falls smoothly as one goes deeper into the substrate. The SiO_2 concentration falls below the detection limit of the apparatus after 3 μm, and again, at this point the total oxygen concentration is $\sim 5 \times 10^{19}$ O/cm^3. After 3.5 μm, there is no detectable evidence of oxygen.

4-4-2-2 $\phi = 0.3 \times 10^{17}$ O/cm^2, Annealed

When the samples are annealed, the predominant factors in the final concentration profile are (a) the total oxygen concentration profile, (b) the initial distribution and sizes of the oxide precipitates, and (c) the location of the damage sites which act as preferential oxidation centers. From the previous sections it is known that the remaining pre-damage is a function of the oxygen dose, and consequently the effects of the pre-damage on the oxygen concentration profiles are different for each dose. The results will be presented accordingly.

Figure 4-46 is an XTEM photo of an annealed $\phi = 0.3 \times 10^{17}$ O/cm^2 sample pre-damaged with 2.00 MeV 5×10^{14} Si/cm^2. Although an ERD spectrum is not available for this target, it is possible to obtain a general idea of the oxygen concentration profile from the photo. Assuming that the majority of the oxygen is in the form of precipitates, there is an oxygen concentration peak at 2 μm, which is comprised of small (40 nm) precipitates. There is also another peak at 2.2–2.3 μm consisting of the larger (100 nm) precipitates (only one precipitate is seen in this photo) located between d_{Si} and the main oxygen band. And finally, the bulk of the oxygen is located around 2.55 μm. These three oxygen peaks are also seen in the sample pre-damaged with 2.25 MeV silicon.

† This was also the case for the standard ϕ=3.0×10^{17} O/cm^2 sample (see figure 4-18).

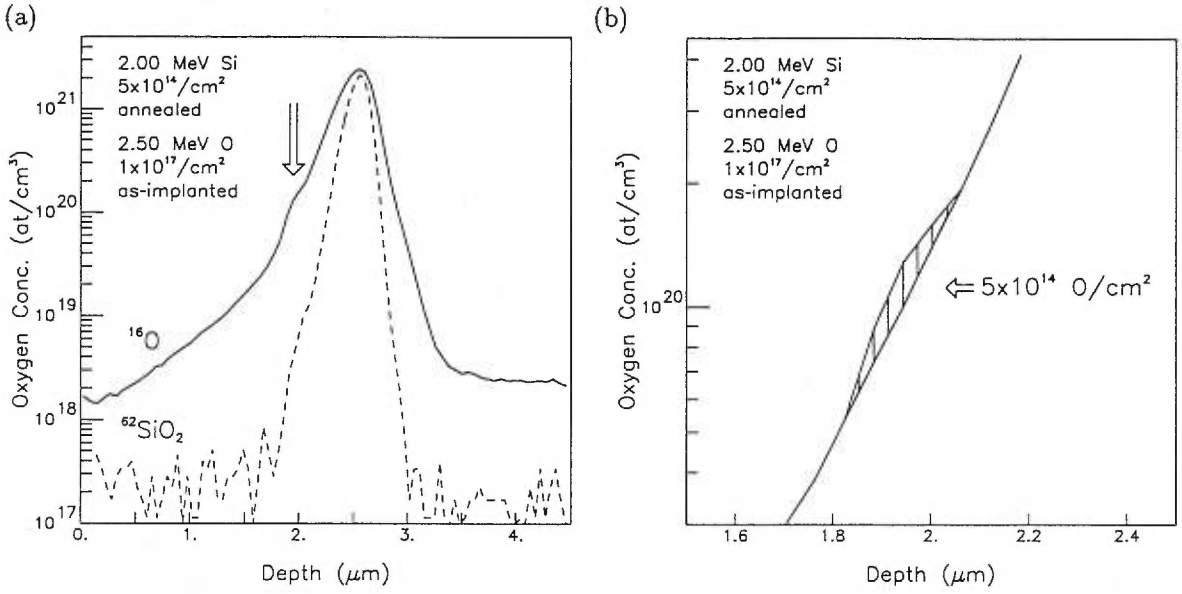

Figure 4-45. (a) Oxygen concentration profile of as-implanted $\phi = 3.0 \times 10^{17}$ O/cm^2 (2.00 MeV, 5×10^{14} Si/cm^2 pre-damaged) sample using SIMS analysis of ^{16}O and $^{62}(SiO_2)$ signal. The ^{16}O spectrum has been normalized to the total dose. The $^{62}(SiO_2)$ spectrum has been scaled so that the peak concentration matches the ^{16}O peak concentration. The arrow indicates the depth of the silicon pre-damage. (b) Same as (a), but expanded to show the bump in the oxygen profile at a depth of 2 μm. The integral oxygen concentration under the bump, indicated by dashed lines, is 5×10^{14} O/cm^2.

The oxygen concentration profile for the annealed sample pre-damaged with 2.25 MeV, 5×10^{14} Si/cm^2 and implanted with $\phi = 0.3 \times 10^{17}$ O/cm^2 is significantly different from the standard sample. The ERD spectrum of the pre-damaged sample is shown in figure 4-47. The fluctuations in the smoothed curve indicate a complex structure. There is a small oxygen concentration peak at ~2.15 μm which roughly corresponds to d_{Si}, the depth of the pre-damage. A larger peak follows at 2.25 μm, which is approximately halfway between d_{Si} and d_O, and finally, the oxygen concentration reaches its maximum of 1.2×10^{21} O/cm^3 at 2.55 μm. Although the oxygen concentration falls rapidly beyond this depth, there is a significant level of oxygen (~2×10^{20} O/cm^3) up to a depth of 2.8 μm.

4-4-2-3 $\phi = 1.0 \times 10^{17}$ O/cm^2, Annealed

Figure 4-48 shows the oxygen concentration profiles of the annealed $\phi = 1.0 \times 10^{17}$ O/cm^2 samples pre-damaged with 5×10^{14} Si/cm^2, at 2.00, 2.25, 2.50 and 2.75 MeV. The depths of the pre-damage are indicated by arrows in each graph. The first thing to note is that there is not any significant

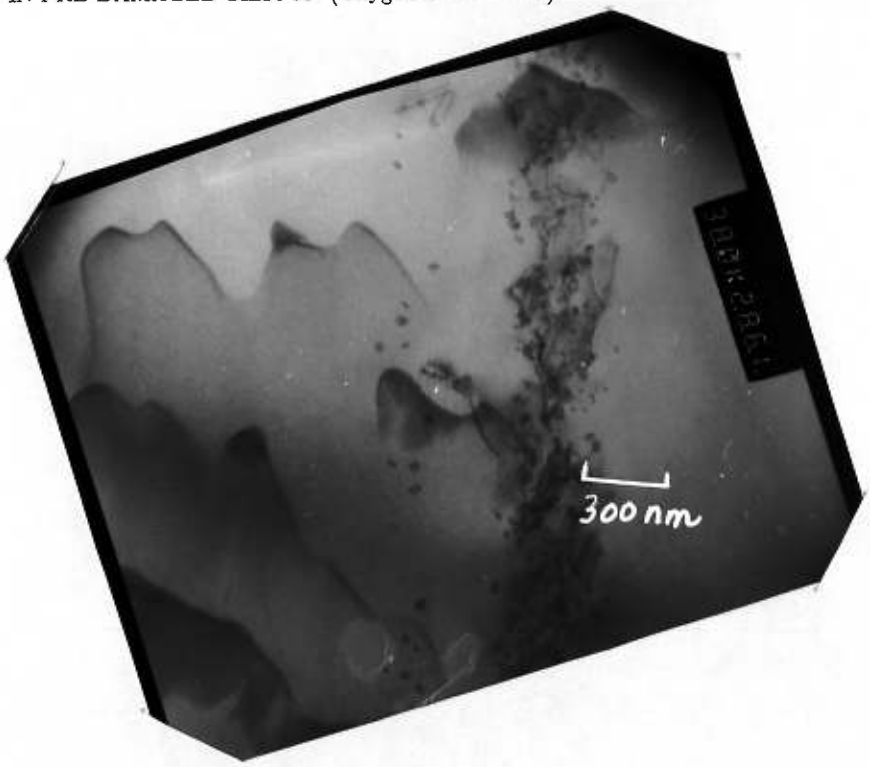

Figure 4-46. XTEM photo of annealed $\phi = 0.3 \times 10^{17}$ O/cm^2 (2.00 MeV, 5×10^{14} Si/cm^2 pre-damaged) sample. M=38,000x, $\vec{B} = [110]$, $\vec{g} = <111>$.

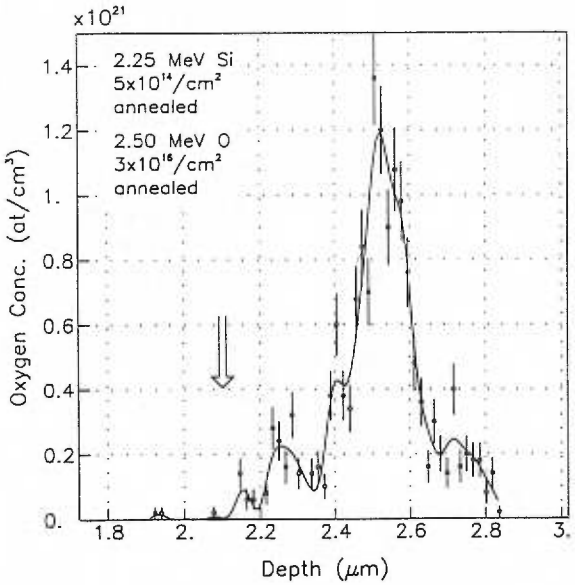

Figure 4-47. Oxygen concentration profile of annealed $\phi = 0.3 \times 10^{17}$ O/cm^2 (2.25 MeV, 5×10^{14} Si/cm^2 pre-damaged) sample. The arrow indicates the depth of the silicon pre-damage. The dots are calculated from ERD data, and the solid lines are the results after smoothing.

increase, or peak, in the oxygen concentration profiles at d_{Si} for the samples implanted with 2.00, 2.25 and 2.50 MeV silicon. However, for the sample pre-damaged with 2.75 MeV silicon, d_{Si} (=2.3 μm) is almost the same depth as d_O (=2.33 μm), and it is only in this sample that there is a large oxygen concentration peak at d_{Si}.

With the exception of the sample pre-damaged with 2.50 MeV silicon, the concentration of oxygen around d_O changes rapidly, going from more than 0.2×10^{21} to more than 1.5×10^{21} O/cm^3 over a distance of 70 nm. This distance is larger than the depth resolution of the ERD system (35 nm [123]), which indicates that the interface between the silicon film and the oxygen-damaged region is not sharp. This is consistent with the XTEM photos. For the sample pre-damaged with 2.50 MeV silicon, the oxygen concentration increases gradually from less than 0.1×10^{21} to 3.1×10^{21} O/cm^3 over a much larger distance of 300 nm.

In spite of the lack of an obvious oxygen concentration peak at d_{Si} (with the exception of the 2.75 MeV pre-damaged sample) the annealed oxygen concentration profiles are very much a function of the pre-damage location, where the major difference in concentration occurs at 2.33 μm. In the standard sample, the oxygen concentration at 2.38 μm was 2.1×10^{21} O/cm^3 and at R_p it was 3.0×10^{21} O/cm^3. In the pre-damaged samples, the oxygen concentration at d_O varies dramatically as a function of d_{Si}, decreasing as d_{Si} approaches, but is not equivalent to, d_O. For these samples there is very little change in the concentration of oxygen at R_p. But, when d_{Si} increases from 2.2 μm to 2.3 μm ($d_O \approx 2.33$ μm), the oxygen concentration at d_O increases from less than 0.5×10^{21} to 3.1×10^{21} O/cm^3. As a consequence, there is a decrease in the oxygen concentration at R_p. This is illustrated in figure 4-49.

The oxygen concentration in the silicon film is difficult to measure with ERD because the concentration of oxygen is so low. However, it can be seen that there are small oxygen peaks at 2.2 μm in the annealed $\phi = 1.0 \times 10^{17}$ O/cm^2 samples pre-damaged with 2.00, 2.25 and 2.75 MeV Si, but not in the sample pre-damaged with 2.50 MeV Si. In all the samples where this peak was seen, it did not correspond to d_{Si}.

One of the annealed $\phi = 1 \times 10^{17}$ O/cm^2 samples (2.00 MeV, 5×10^{14} Si/cm^2 pre-damage) was also analyzed with SIMS and the results are shown in figure 4-50. The sample had been etched before the analysis so the oxygen concentration in the near-surface region was not profiled. The

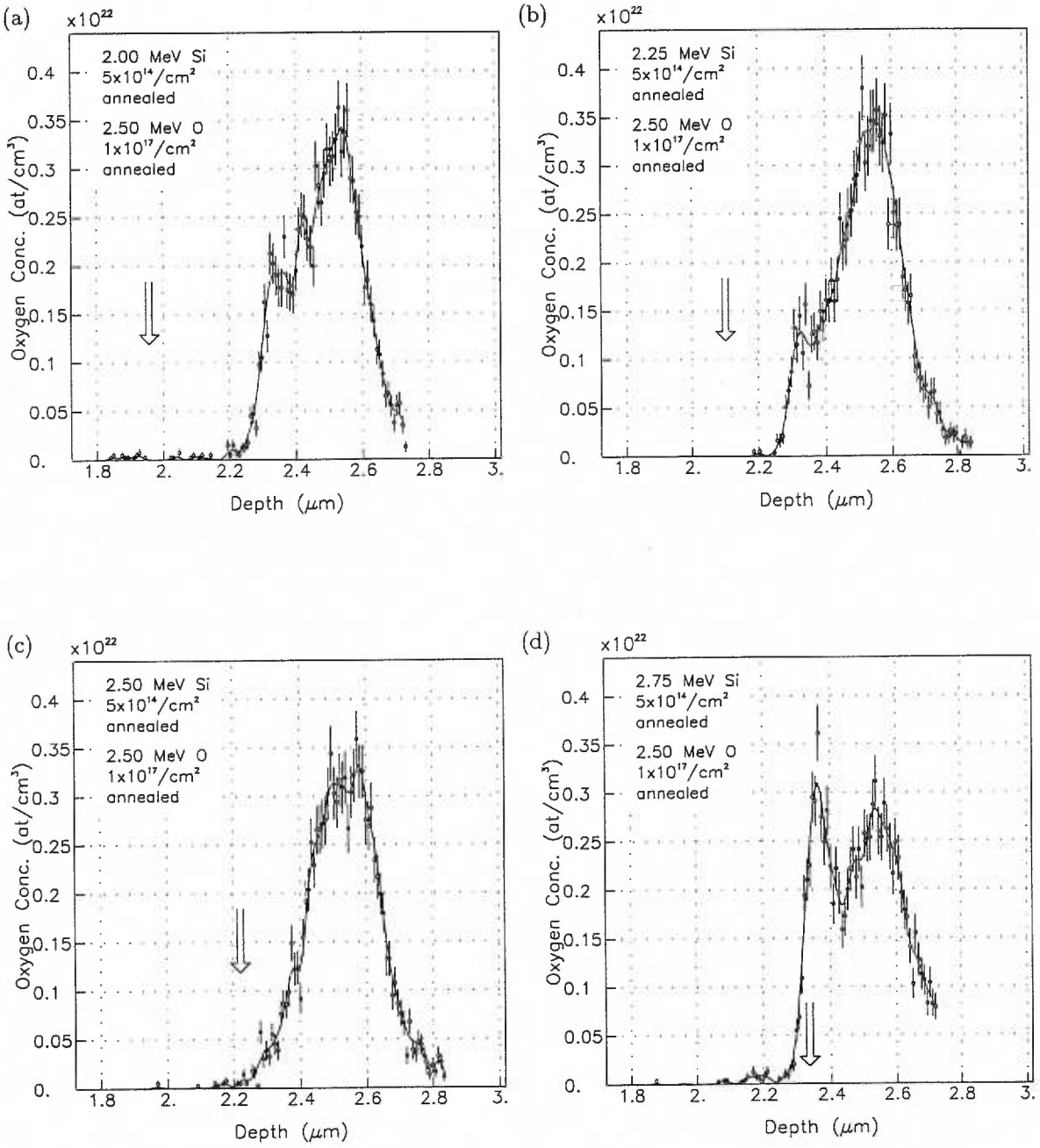

Figure 4-48. Oxygen concentration profiles of annealed $\phi = 1.0 \times 10^{17}$ O/cm^2 ((a) 2.00, (b) 2.25, (c) 2.50 and (d) 2.75 MeV, 5×10^{14} Si/cm^2 pre-damaged) samples. The arrows indicate the depth of the silicon pre-damage. The dots are calculated from ERD data, and the solid lines are the results after smoothing.

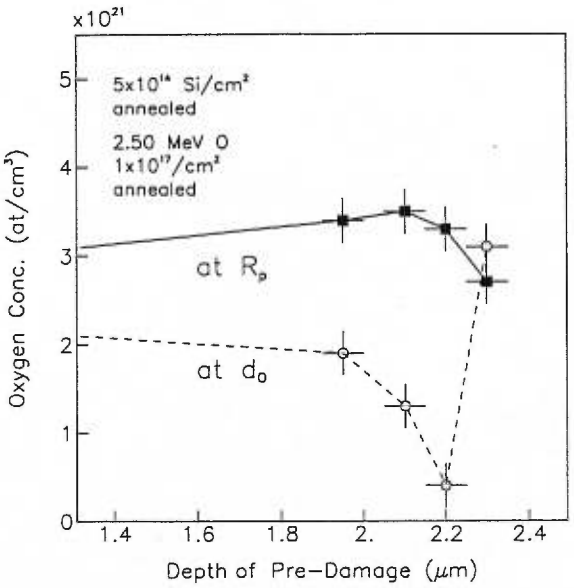

Figure 4-49. Oxygen concentration at the oxygen-damaged depth d_O, and at the maximum range of oxygen in silicon, R_p, as a function of the pre-damage depth.

oxygen concentration is presented on a log scale so that the low levels of oxygen can be seen. Between 1.8 and 2.0 μm (the approximate region of pre-damage) there is a constant oxygen concentration of 2×10^{19} O/cm^3. The total integrated oxygen under this curve is 2.5×10^{14} O/cm^2. At 2.2 μm there is a another peak in the oxygen concentration with a maximum of 1×10^{20} O/cm^3, with a total integrated concentration of 1.2×10^{15} O/cm^2. The concentration profile past this depth is consistent with the ERD analysis, within the statistical limits. An XTEM photo of a similar sample is shown in figure 4-51. The oxygen concentration peaks in the SIMS spectrum are consistent with the oxides seen in the XTEM photo. The peak around 1.9 μm is composed of small (~25 nm) precipitates randomly scattered within a 0.2 μm depth region. The larger peak at 2.2 μm is composed of fewer, but much larger (100 nm), precipitates. These precipitates are not randomly scattered, but rather they appear in groups which are immediately adjacent to the main oxygen band. Because of the high density of precipitates, it is not possible to measure the size of the precipitates in the main oxygen band, or to visually differentiate the shape of the oxygen profile in this region. After the main oxygen band one sees many ~50 nm precipitates in the silicon substrate up to a depth of 3 μm.

The oxygen concentration profiles for the annealed $\phi = 1 \times 10^{17}$ O/cm^2 samples pre-damaged with 1×10^{15} Si/cm^2 at 2.00 and 2.25 MeV are shown in figure 4-52. The results are rather surprising

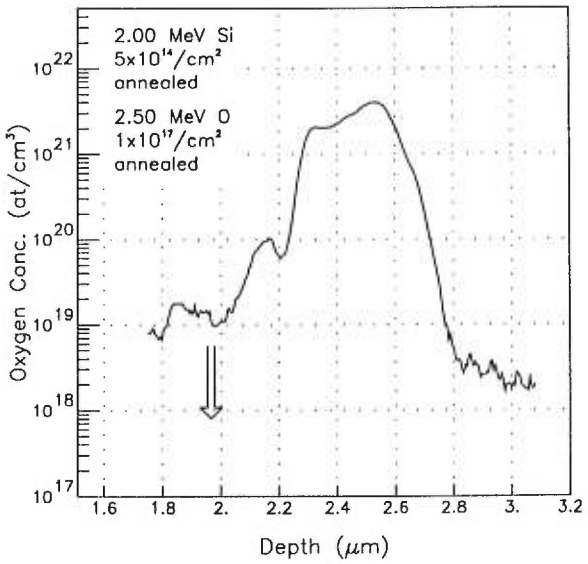

Figure 4-50. Oxygen concentration profile of annealed $\phi = 1.0 \times 10^{17}$ O/cm^2 (2.00 MeV, 5×10^{14} Si/cm^2 pre-damaged) sample using SIMS analysis of ^{16}O. The spectrum has been normalized to the total dose. The arrow indicates the depth of the silicon pre-damage.

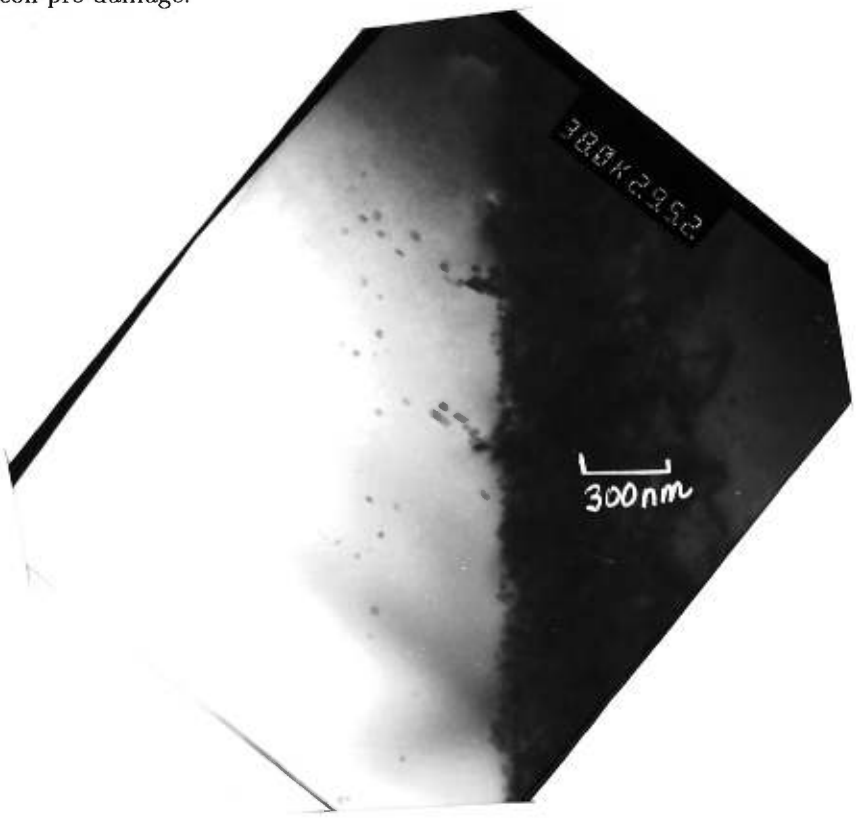

Figure 4-51. XTEM photo of annealed $\phi = 1.0 \times 10^{17}$ O/cm^2 (2.00 MeV, 5×10^{14} Si/cm^2 pre-damaged) sample. M=38,000x, $\vec{B}$ = [110], $\vec{g}$ = <111>.

for the sample pre-damaged at 1.95 μm (2.00 MeV Si). There is a significant oxygen concentration peak at 2.2 μm, with a concentration of 0.7×10^{21} O/cm^3. This peak is not at the same depth as d_{Si}. In the XTEM photo of this sample (figure 4-53) there is also no evidence of any oxide precipitates at d_{Si}. The two oxygen concentration peaks cannot be individually distinguished in the XTEM photo. The oxygen concentration at R_p is 3.3×10^{21} O/cm^3, which is the same as the previously discussed samples. The sample pre-damaged at 2.1 μm (2.25 MeV Si) has a similar structure to the sample pre-damaged with 5×10^{14} Si/cm^2 (shown in figure 4-51b), except for two things; (1) there is no evidence of an oxygen concentration peak at 2.2 μm and (2) there is a higher oxygen concentration at d_O.

Finally, figure 4-54 shows the oxygen concentration profile for an annealed $\phi = 1.0 \times 10^{17}$ O/cm^2 sample pre-damaged with 2.5 MeV, 2×10^{15} O/cm^2 with a substrate temperature of 300°C. In this sample there is an extremely sharp peak centered at 2.33 μm, with a maximum concentration of 3.7×10^{21} O/cm^3. This is the highest concentration of oxygen seen in any of the $\phi = 1.0 \times 10^{17}$ O/cm^2 samples studied in this thesis. The FWHM of this peak is 70 nm, which is only slightly larger than the depth resolution of the ERD system at this depth (35 nm). The second peak, at R_p (2.55 μm), has a maximum concentration of 3.0×10^{21} O/cm^3. Although it is not a distinct peak, there is a low level of oxygen at 2.2 μm.

4-4-2-4 $\phi = 3.0 \times 10^{17}$ O/cm^2, Annealed

The ERD oxygen concentration profiles for annealed $\phi = 3.0 \times 10^{17}$ O/cm^2 samples, pre-damaged with 5×10^{14} Si/cm^2, at 2.00 and 2.50 MeV are shown in figure 4-55. The depths of the pre-damage are indicated by arrows in each graph. The characteristics of these profiles are defined by two separate regions of oxygen, the first being at d_O (2.33 μm), and the second at R_p (2.55 μm). These profiles have the same general shape as the oxygen concentration profile of the standard sample with the same oxygen dose. The oxygen concentration peaks in the sample pre-damaged with 2.00 MeV silicon are broader than the other samples. However, this could be a result of the sample preparation prior to the ERD analysis. This particular sample was etched many times in KOH, and as a result, the surface of the sample was no longer smooth. Any irregularities in the sample surface decrease the ERD depth resolution, so the broadening of the peak at 2.33 μm may be an artifact of the analysis rather than a physical reality. However, this would not affect the detection of a low level of oxygen at 2.2 μm,

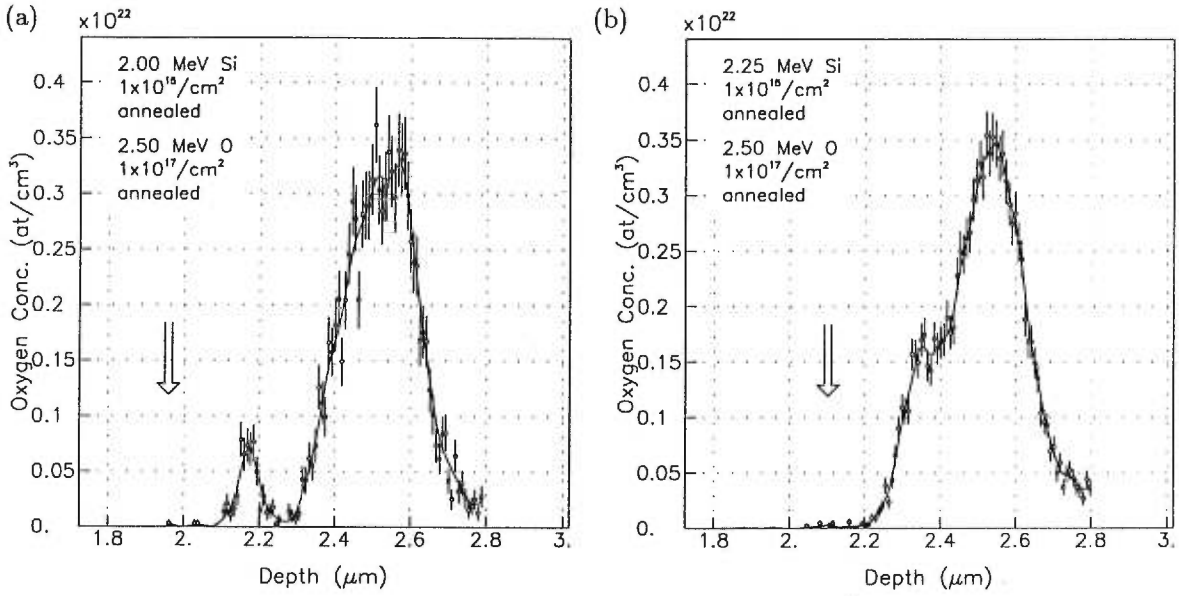

Figure 4-52. Oxygen concentration profiles of annealed $\phi = 1.0 \times 10^{17}$ O/cm^2 ((a) 2.00 MeV and (b) 2.25 MeV, 1×10^{15} Si/cm^2 pre-damaged) samples. The arrows indicate the depth of the silicon pre-damage. The dots are the calculated ERD data, and the solid lines are the results after smoothing.

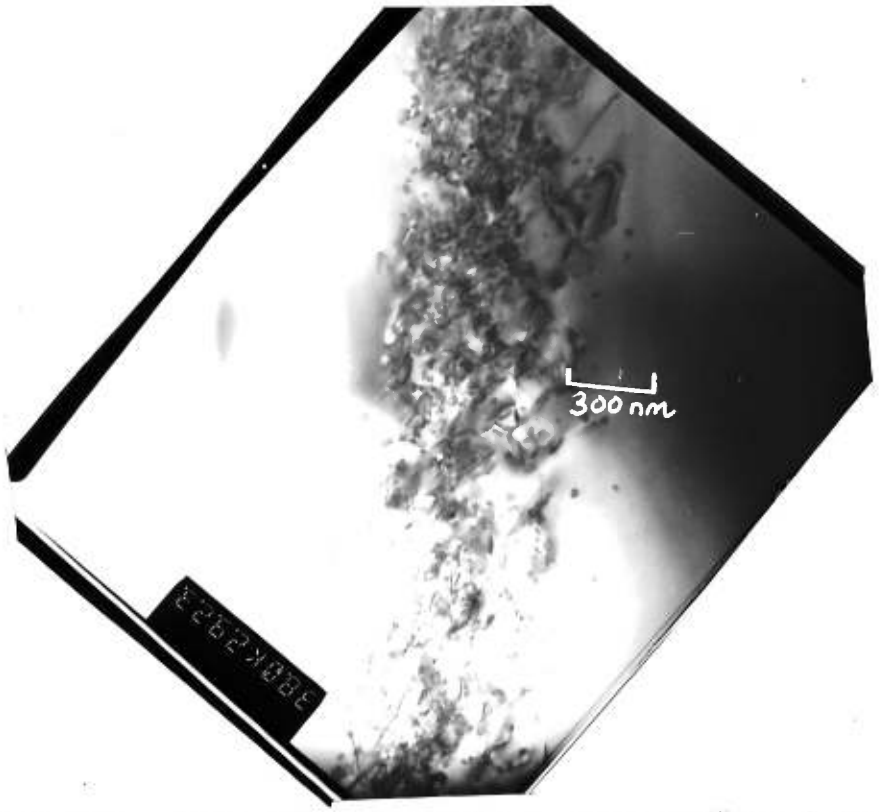

Figure 4-53. XTEM photo of annealed $\phi = 1.0 \times 10^{17}$ O/cm^2 (2.00 MeV, 1×10^{15} Si/cm^2 pre-damaged) samples. M=38,000x, $\vec{B} = [110]$, $\vec{g} = <111>$.

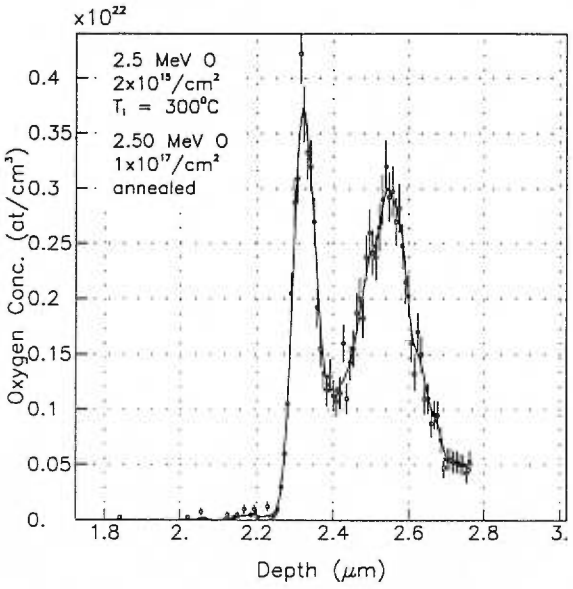

Figure 4-54. Oxygen concentration profile of annealed $\phi = 1.0 \times 10^{17}$ O/cm^2 (2.50 MeV, T_i=300°C, 2×10^{15} O/cm^2 pre-damaged) sample. The dots are calculated from ERD data, and the solid lines are the results after smoothing.

which is seen in the sample pre-damaged with 2.00 MeV silicon, but not in the sample pre-damaged with 2.50 MeV silicon.

An XTEM photo of an annealed $\phi = 3.0 \times 10^{17}$ O/cm^2 sample, pre-damaged with 2.00 MeV silicon is shown in figure 4-56. In this photo it is possible to see the difference in oxygen density in the main oxygen band. The precipitates size range from 50 – 100 nm, and very few precipitates are seen past 2.8 μm. There are some precipitates remaining at 2 μm. However, since these are not seen in the ERD results, we can conclude that the oxygen concentration is lower than the detection limit of the ERD analysis (1×10^{20} O/cm^3). There are no precipitates at 2.2 μm in this photo. However they have been observed in other XTEM results (figure 4-40). These precipitates are typically grouped together (rather than randomly spaced) and are located adjacent to the main oxygen band.

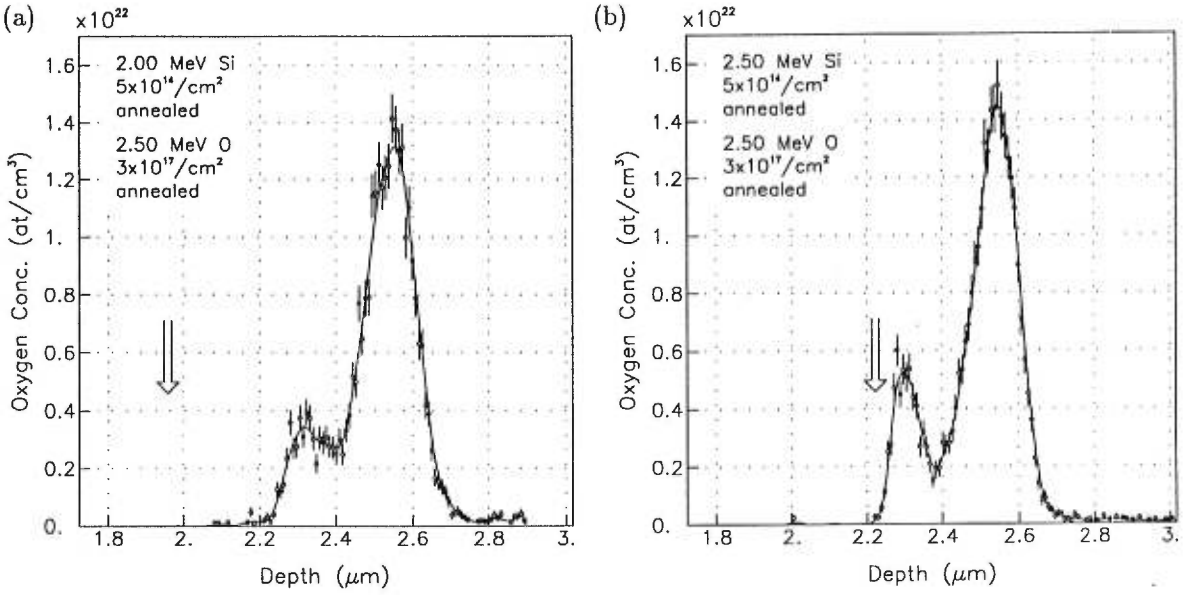

Figure 4-55. Oxygen concentration profiles of annealed $\phi = 3.0 \times 10^{17}$ O/cm^2 ((a) 2.00 MeV and (b) 2.50 MeV, 5×10^{14} Si/cm^2 pre-damaged) samples. The arrows indicate the depth of the silicon pre-damage. The dots are the calculated ERD data, and the solid lines are the results after smoothing.

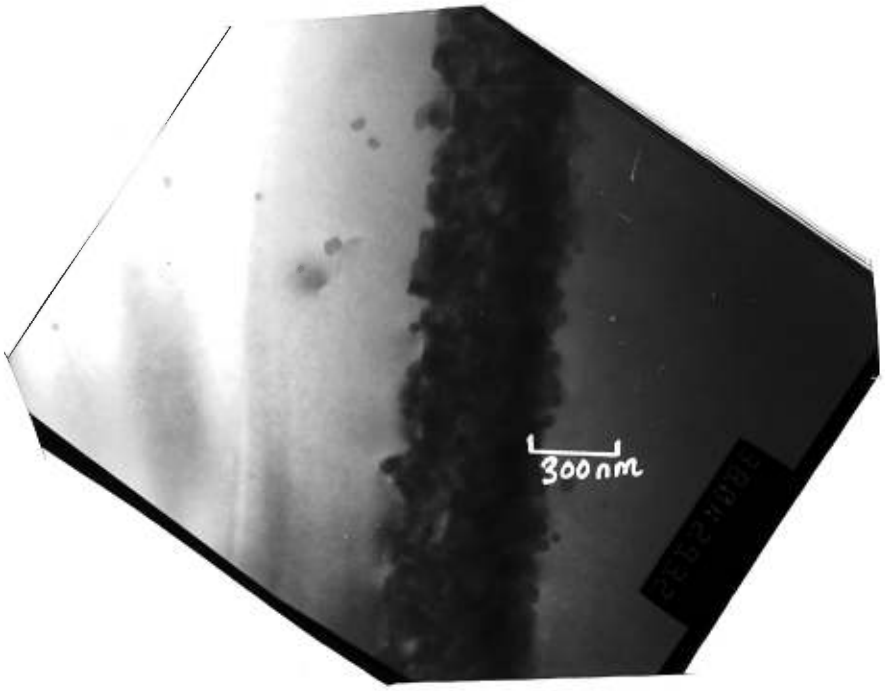

Figure 4-56. XTEM photo of annealed $\phi = 3.0 \times 10^{17}$ O/cm^2 (2.00 MeV, 5×10^{14} Si/cm^2 pre-damaged) sample. M=38,000x, $\vec{B}$ = [110], $\vec{g}$ = <111>.

4-4-3 Discussion

It has been well established elsewhere (§2-5 and §4-3-3) that the oxygen profiles after annealing are very much a function of the conditions of the sample in the as-implanted state, with regards to the damage profile and the distribution and size of the oxide precipitates. First, to facilitate the understanding of the experimental results, a list containing the relevant information about the as-implanted samples, or the oxygen-in-silicon properties in general, is given below:

(1) If the sample temperature is high (> 400°C) and the current density is low, then, during the early stages of oxygen implantation, HE (heterogeneous) precipitation† dominates. The oxygen ions then diffuse from R_p to the damaged regions. As the dose increases the supersaturation of oxygen at R_p is sufficient for HO (homogeneous) precipitation to occur. Thereafter there is a competition between these two precipitation processes (§2-5-1-2).

(2) Ostwald ripening occurs even during the implant. Ostwald ripening is a very complex process, which sometimes results in multi-peak oxygen concentration profiles, even in the simplest of systems (§2-4). However, in most cases larger precipitates will grow at the expense of smaller precipitates.

(3) Aside from the pre-damage region d_{Si}, there are two very distinct regions of dynamic annealing within the sample. In the shallower region (less than 2.3 μm) the majority of the damage produced during the oxygen implant is able to recover, *in situ*, whereas in the deeper region (greater than 2.3 μm) the damage produced is not able to recover efficiently, with the result that a dense network of small dislocations remains (§4-3-2 and §4-4-1).

(4) For all the samples studied by RBS/C, the results do not show any significant differences in the damage profiles at depths greater than 2.3 μm (figures 4-26 to 4-28).

(5) The pre-damage consists primarily of (a) dislocation loops or (b) dislocation dipoles (figures 4-5 and 4-6). Since dislocations and extended defects are good sinks for interstitials [21], the pre-damage region acts as a diffusion barrier and as a sink for the excess interstitials (§4-4-1-3).

† preferential precipitation on damage sites

(6) Because the diffusion rate, in silicon, of silicon interstitials is higher than the diffusion rate of oxygen, it is typically the oxygen diffusion which limits the growth rate of the precipitate, not the silicon interstitial diffusion [72].

(7) There is an excess of oxygen (greater than background) at d_{Si} (figure 4-45) and it has precipitated (figure 4-30).

(8) There are threading dislocations spanning the region between d_{Si} and d_O. XTEM photos suggest that there is preferential precipitation along these defects (figure 4-30). The RBS/C analysis confirms that there is more damage in this region than in the standard samples (figures 4-26 to 4-28).

(9) The presence of extended defects slows down the dissolution of precipitates during high temperature annealing [75].

Using the above information, the following description is surmised (and illustrated in figure 4-57): In the early stages of implantation, there are three depth regions in which there is precipitation. These three regions are (1) the pre-damaged region d_{Si}, (2) the oxygen-damaged region d_O and (3) the depth range of oxygen in silicon R_p. In the VERY early stages of the implant, the majority of the nucleation sites for oxidation are at d_{Si}. Hence, this is the first region where oxides form. At this stage the quantity of point defects at d_O, generated by the incoming oxygen ions, is low enough that the defects self-anneal rather than form stable defect complexes. However, as the oxygen dose increases, the density of defects increases to a point where self-annealing is no longer complete, and stable defect complexes form. These, in turn, provide nucleation sites for oxide precipitation in the vicinity of d_O. In this region there are more oxygen ions deposited per unit time than there are around d_{Si}, and consequently the precipitates here grow faster than their counterparts at d_{Si}. As the precipitates grow at d_O, they absorb the oxygen ions that otherwise might have diffused to d_{Si}, which means that the rate of growth of precipitates at d_{Si} is reduced. We define a critical dose ϕ_{HE} such that, when $\phi = \phi_{HE}$, the average size of the precipitates at d_{Si} is the same as the average size of the precipitates at d_O. It is important to note that ϕ_{HE} is dependent upon the number of stable damage sites at d_O. Damage from the incoming oxygen ions continues to be created during the entire implantation procedure, and so there will always be new nucleation sites for precipitation at d_O. The excess silicon interstitials within this region are not free to migrate to the surface, but instead they interact with the

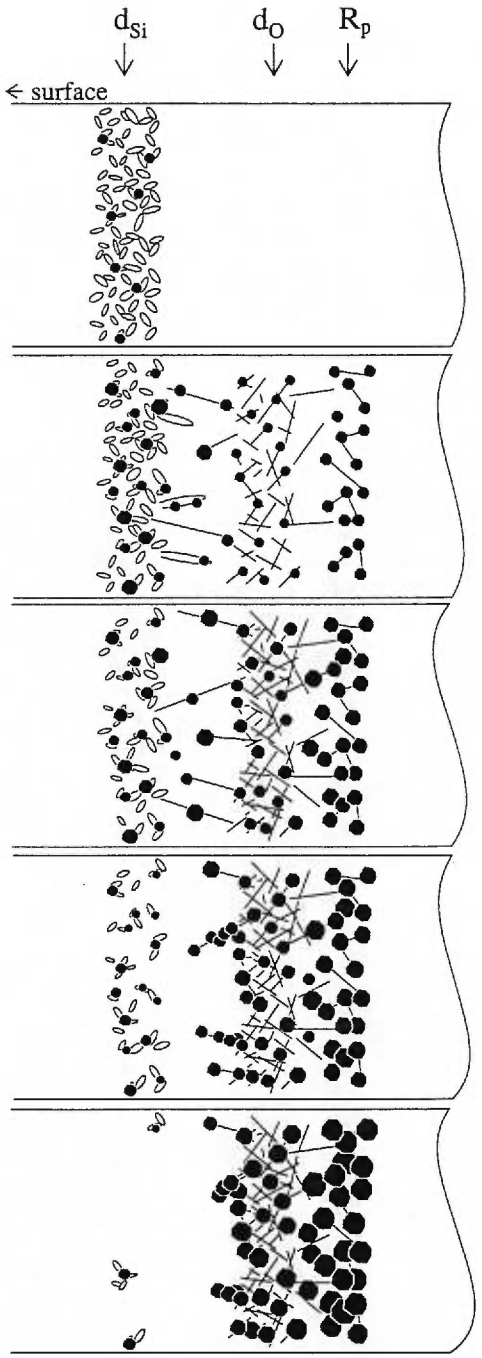

$\phi << \phi_{HE}$

-very early stage of implantation
-oxide precipitation primarily at d_{Si}
-oxygen diffuses from R_p to d_{Si}

$\phi < \phi_{HE}$

- growth of existing oxides at d_{Si}
- still forming new precipitates at d_{Si}
- level of damage at d_{Si} is decreasing
- damage begins to accumulate at d_O
- heterogeneous precipitation at d_O
- growth of threading dislocations

$\phi \cong \phi_{HE}$

- no new growth of oxides at d_{Si}
- level of damage at d_{Si} is decreasing
- continuing HE precipitation at d_O
- continued growth of threading dislocations
- HO precipitation at R_P

$\phi > \phi_{HE}$

- oxides at d_{Si} are dissolving
- level of damage at d_{Si} is decreasing
- precipitates at d_O continue to grow
- threading dislocations are annealing
- precipitates at R_P continue to grow

$\phi >> \phi_{HE}$

- oxides at d_{Si} are almost completely dissolved
- damage at d_{Si} almost completely dissolved
- precipitates at d_O continue to grow
- threading dislocations are annealing
- precipitates at R_P continue to grow

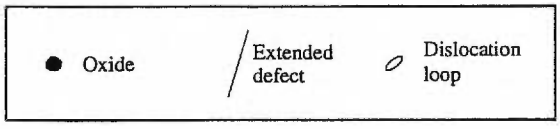

Figure 4-57. A schematic illustration of the evolution of the damage and precipitates during an oxygen implantation into pre-damaged silicon. ϕ_{HE} is defined as the oxygen dose (ϕ) when the average size of the precipitates at d_O is the same as the average size of the precipitates at d_{Si}.

pre-damage or with the oxygen-damage, causing the growth of threading dislocations between these two layers. Thus a new region of preferential oxidation is formed, which spans the region between d_{Si} and d_O.

Homogeneous precipitation occurs at R_p when the concentration of oxygen exceeds the solubility limit ($\sim 10^{18}$ O/cm^3). Once the precipitates have formed at R_p, they grow faster than the precipitates at d_O because there is more oxygen deposited in this region, per unit time, than there is at d_O. We define another critical dose ϕ_{HO} such that, when $\phi = \phi_{HO}$, the average size of the precipitates at d_O is the same as the average size of the precipitates at R_p.

During the course of the implantation, the growth and dissolution of the precipitates is a function of not only the sizes of the oxide precipitates, but also of the local oxygen solute concentrations, the diffusion coefficients and the production of new nucleation sites for precipitation.

4-4-3-1 Effect of Oxygen Dose

Continuing with the above description, consider what happens as the oxygen dose increases from $\phi = 0.3$ to 3.0×10^{17} O/cm^2. In the specific case of 5×10^{14} Si/cm^2 pre-damage at 2.00 MeV, we have observed that as the oxygen dose increases, there is a decrease of damage at d_{Si} (figure 4-29), as well as a reduction in the number of oxide precipitates and threading dislocations. This suggests that, at these doses, precipitates at d_O and R_p are growing at the expense of the precipitates at d_{Si} and hence $\phi > \phi_{HE}$ and $\phi > \phi_{HO}$.

Given that the remaining quantity of damage and precipitates at d_{Si} is an inverse function of the oxygen dose, one would expect that the pre-damage effects would, after annealing, be less noticeable for the higher-dose samples. This is consistent with our results. The general effects of the pre-damage on the final annealed oxygen distribution, for the specific case of 5×10^{14} Si/cm^2 pre-damage at 2.00 MeV, can now be explained as follows.

$\phi = 0.3 \times 10^{17}$ O/cm^2

The difference between the $\phi = 0.3 \times 10^{17}$ O/cm^2 standard sample and the sample pre-damaged with 2.25 MeV[†], 5×10^{14} Si/cm^2 is strikingly apparent, especially at depths less than 2.3 μm, as compared to the samples implanted at higher oxygen doses. The most obvious difference is the

[†] An oxygen concentration profile of a sample pre-damaged with 2.00 MeV Si was not available.

presence of an oxygen peak at 2.25 μm. This peak is located halfway between d_{Si} (2.1 μm) and d_O (2.35 μm). It is associated with the precipitates that decorated the threading dislocations between d_{Si} and d_O in the as-implanted sample. The small oxygen peak at 2.15 μm is a result of the stable oxide precipitates which originally formed on the pre-damage, which implies that $\phi \sim \phi_{HE}$. The precipitates at d_O were not sufficiently large compared to the precipitates at R_p ($\phi > \phi_{HO}$), or to the precipitates decorating the threading dislocations. Consequently they dissolved and the oxygen was absorbed into the precipitates either at 2.15 μm or at R_p. The final result is an oxygen concentration profile with three distinct peaks at d_{Si}, $^1/_2(d_{Si} + d_O)$ and R_p.

$\phi = 1.0 \times 10^{17}$ O/cm^2

As the oxygen dose increases from 0.3 to 1.0×10^{17} O/cm^2, the precipitates at d_O and at R_p continue to grow, while the number and the size of the precipitates at d_{Si} diminishes. There is also a decrease in the number of threading dislocations between these two regions (figure 4-29). As a result, the difference in the annealed oxygen profiles between the pre-damaged and standard samples is less noticeable at this dose. The differences are a slight broadening of the oxygen concentration distribution, a lowering of the oxygen concentration in this region, and the presence of very small oxygen peaks at 1.9 and 2.1 μm (figure 4-50). The first oxygen peak at 1.9 μm is at the same depth as d_{Si}. The precipitates are, on the average, smaller than the precipitates at d_O ($\phi > \phi_{HE}$), and so only a small fraction (10%) of the oxygen remains in this region after annealing. The oxygen peak at 2.1 μm, which is a little more than halfway between the d_{Si} (1.95 μm) and d_O (2.35 μm), is a result of the precipitates which decorated the threading dislocations that connected the damage at d_{Si} and d_O. The most obvious change in the annealed oxygen profile, compared to the standard, is the broadening of the oxygen peak. This can be attributed to the presence of the threading dislocations previously mentioned. These dislocations retard the dissolution rate of the oxides that are located at the border of the 'hardly damaged'/'highly damaged' regions. This reduction in the rate of dissolution is sufficient to stabilize some of the precipitates long enough so that they will grow during the anneal, rather than dissolving. The lower oxygen concentration at d_O, compared to the standard sample, will be discussed in the next section.

$\phi = 3.0 \times 10^{17}$ O/cm^2

The difference in the oxygen profiles between the $\phi = 3.0 \times 10^{17}$ O/cm^2 pre-damaged and the standard samples is almost not detectable via ERD analysis[‡], which implies that $\phi \gg \phi_{HE}$. However, a very low oxygen concentration just in front of d_O is seen in the pre-damaged sample. Using the results of the XTEM analysis, it is concluded that this residual oxygen concentration is yet again a remnant of precipitates decorating the threading dislocations in the as-implanted sample.

These results indicate that the precipitates on the threading dislocations appear not to dissolve completely, even with doses much higher than ϕ_{HE}.

4-4-3-2 Effect of Silicon Pre-damage Depth

It is safe to assume that the rate of stable damage production at d_O (~2.3 μm) in the pre-damaged silicon is less than that in the standard samples, as many of the interstitials generated in this region migrate to, and are trapped or annihilated by, the pre-damage. Because this process is limited by the diffusion of the silicon interstitials, it is also safe to assume that the rate of absorption of the interstitials is a function of the distance between the two regions ($d_O - d_{Si}$). Thus the growth rate of stable damage at d_O is a decreasing function of d_{Si}, and it then follows that the critical dose ϕ_{HE} is an increasing function of d_{Si}.

Since the precipitates at d_{Si} grow relatively unhindered while $\phi < \phi_{HE}$, and since the growth rate of these precipitates is a function of the quantity of oxygen deposited near d_{Si} (which is also a positive function of d_{Si}), it is clear that the size of the precipitates at d_{Si}, when $\phi = \phi_{HE}$, is a positive function of d_{Si}. As a consequence, the size of the precipitates remaining at d_{Si}, at the end of the implantation is also a positive function of d_{Si}. It is also hypothesized, although not verified with XTEM, that as the precipitates at d_{Si} grow larger, the precipitates more effectively impede the migration of the interstitials, which in turn creates more threading dislocations between d_{Si} and d_O. Thus, the final state of the as-implanted sample, as a function of d_{Si} ($d_{Si} \neq d_O$) is that, as d_{Si} increases (1) the size of the precipitates at d_{Si} increase, (2) the size of the precipitates at d_O decrease,

‡ Note that the surface of the 3.0×10^{17} O/cm^2 pre-damaged sample after etching was not smooth, and hence the depth resolution of the ERD analysis, for this sample only, is greatly deteriorated.

(3) the quantity of damage at d_O decreases, (4) there are more threading dislocations between d_{Si} and d_O and (5) the precipitates at R_p are not significantly affected.

In the oxygen concentration profiles for the as-implanted $\phi = 1.0 \times 10^{17}$ O/cm^2 samples (shown in figure 4-44), there is a small (possibly insignificant) difference in the profiles, as a function of d_{Si}. In the samples pre-damaged with 2.00 MeV silicon ($d_{Si} = 1.95$ μm), the oxygen profiles are broad, and could be composed of two peaks, one at 2.55 μm, and the other at 2.4 μm. The oxygen profiles of samples pre-damaged with silicon energies higher than 2.00 MeV ($d_{Si} = 2.1$ and 2.2 μm) do not have any indication of a secondary peak at 2.4 μm, possibly indicating that some of the oxygen from d_O has diffused towards d_{Si} or R_p. Unfortunately, the statistical fluctuations within the data itself prevents a definitive interpretation of the data.

Fortunately, the oxygen concentration profiles for annealed $\phi = 1.0 \times 10^{17}$ O/cm^2 samples, pre-damaged with 5×10^{14} Si/cm^2 (figures 4-48 and 4-49), can be understood quite simply within the framework of the model described above. The difference in the oxygen concentration at d_O between the standard sample and the sample pre-damaged with 2.00 MeV silicon can be attributed to a slower growth in size and number of precipitates at d_O, due to the annihilation of the excess interstitials by the pre-damage. Similarly, as d_{Si} approaches d_O, the size of the precipitates at d_O are even further reduced in number and size, and consequently, during the anneal, the Ostwald ripening process favours the larger precipitates in the R_p region, until, as in the 2.50 MeV pre-damaged sample ($d_{Si} = 2.2$ μm), there is no longer any oxygen concentration peak at d_O at all! However, this region is not completely devoid of oxygen, the reason being that the defects at d_O retard the dissolution of oxides, and so, although the oxides did not grow, they took too long to dissolve. The precipitates at d_{Si}, in the as-implanted samples, are never sufficiently large to be able to grow during the anneal. However, they are large enough not to be completely dissolved during the anneal, as one can see in the XTEM photos and SIMS analysis, if not in the ERD analysis.

For the specific case of 2.75 MeV silicon pre-damage ($d_{Si} \approx d_O$), the growth of the oxide precipitates during the implantation is different than previously described. In this case, the preferential precipitation at the pre-damaged and oxygen-damaged regions are in the same place, and consequently the growth rate of the precipitates are enhanced. This results in larger precipitates whose radii are larger than the critical radius at the anneal temperature. The result, after annealing, is two distinct and well separated bands of oxygen precipitates.

4-4-3-3 Effect of Pre-damage Type

The experiments discussed and included in this thesis include three different types of pre-damage. The first two types are produced by a silicon implant at room temperature, followed by a 1 h, 900°C anneal. When $\phi(Si) = 5 \times 10^{14}$ Si/cm^2, the resulting pre-damage is composed almost entirely of dislocation loops (figure 4-5), and when $\phi(Si) = 1 \times 10^{15}$ Si/cm^2, it is composed almost entirely of dislocation dipoles (figure 4-6). The third defect type is created by a 2.5 MeV oxygen implant (2×10^{15} O/cm^2) at $\approx 300°C$, *not* followed by an anneal. The defects comprising this pre-damage have not been analyzed. However, their nature can be reasonably postulated using the known properties of the behaviour of oxygen in silicon and the damage produced by ion beam implantations.

Let us first discuss the differences between the $\phi = 1.0 \times 10^{17}$ O/cm^2 samples pre-damaged with 5×10^{14} Si/cm^2 and 1×10^{15} Si/cm^2. The pre-damage is different for the two samples, so the initial conditions are not the same. One of the biggest differences between these samples is that the total length of dislocation line available as a sink for silicon interstitials is much smaller for the sample with dislocation dipoles than it is for the samples with numerous small dislocation loops. This reduces the rate at which silicon interstitials can be absorbed into the pre-damage for the 1×10^{15} Si/cm^2 samples, and it also reduces the number of nucleation sites for oxide precipitation. In simplistic terms, if all the parameters of the sample (oxygen dose, pre-damage depth, *etc.*) are equivalent, except for the silicon pre-damage dose, then $\phi_{HE}(1 \times 10^{15}\ \text{Si/cm}^2) < \phi_{HE}(5 \times 10^{14}\ \text{Si/cm}^2)$.

The damage profile, as seen in the XTEM photo (figure 4-31), for the as-implanted $\phi = 1 \times 10^{17}$ O/cm^2 sample, pre-damaged with 1×10^{15} Si/cm^2, is significantly different from that of an equivalent sample with 5×10^{14} Si/cm^2 pre-damage (figure 4-30). For the 5×10^{14} Si/cm^2 pre-damaged sample, there are defects and oxide precipitates at d_{Si}, as well as the remains of threading dislocations located at depths just shallower than d_O. Other than the threading dislocations, the visible damage at d_O starts abruptly. For the 1×10^{15} Si/cm^2 pre-damaged sample, there is no damage at d_{Si}, and although there are no signs of threading dislocations, there are many oxygen/defect complexes in the region joining d_O and d_{Si}. There is no sharp delineation of the onset at damage at d_O, instead it is a gradual increase of damage as one goes from d_{Si} to d_O.

To explain these differences, we hypothesize the following scenario for the 1×10^{15} Si/cm^2 pre-damaged sample: During the early stages of the implantation, there is a rapid growth of threading

dislocations between d_{Si} and d_O, faster than in the 5×10^{14} Si/cm^2 pre-damaged sample, and consequently there is a much broader region of nucleation sites for oxide precipitation. Thus the damage at d_{Si} is not the only immediate source of oxide growth, and so, instead of a few large precipitates at d_{Si}, there are oxide precipitates located throughout the region from d_{Si} to d_O. These precipitates grow rapidly during the early stages of the implantation. The point defects which are continuously produced during the implantation are blocked by the oxide precipitates, and consequently they aggregate to form even more defects in this region, which results in the damage profile seen in the XTEM photos. In this sample, it is the damage that forms between the pre-damage and the oxygen-damage depths that is more pronounced than the damage at d_{Si}.

And so, after annealing, there is a difference in the oxygen concentration profiles for the two $\phi = 1.0 \times 10^{17}$ O/cm^2, 2.00 MeV silicon (d_{Si}=1.95 μm) pre-damaged samples. The oxygen concentration profile of the 5×10^{14} Si/cm^2 pre-damaged sample has two large oxygen concentration peaks, 2×10^{21} O/cm^3 at d_O (2.33 μm) and 3.5×10^{21} O/cm^3 at R_p (2.55 μm). In addition, there are two very small oxygen concentration peaks, 2×10^{19} O/cm^3 at d_{Si} (1.95 μm) and 1×10^{20} O/cm^3 at $1/2\,(d_{Si} + d_O)$ (2.2 μm), (figures 4-48 and 4-51). In the 1×10^{15} Si/cm^2 pre-damaged sample the peak at 2.2 μm is almost a factor of ten larger than in the previously described sample, and there is no oxygen concentration peak at d_O. We hypothesize that the oxygen concentration peak at 2.2 μm is not a result of larger precipitates existing at this depth in the as-implanted sample, but that it is a result of the Ostwald ripening of a uniform distribution of oxides, of equal size, throughout the region spanning d_{Si} and d_O. If the density of precipitates is low, only one oxygen concentration peak will form (§2-4-3). There is no oxygen concentration peak at d_O because the oxygen in this region diffused either to R_p or to the growing precipitates at 2.2 μm.

For the sample pre-damaged with 2.25 MeV, 1×10^{15} Si/cm^2, (d_{Si}=2.1 μm), d_{Si} is closer to d_O and thus the dynamic annealing during the implantation is more effective than for the above described sample. By the time the implanted oxygen has reached the final dose of $\phi = 1.0 \times 10^{17}$ O/cm^2, the pre-damage has been completely annealed. Thus the dislocations between d_O and d_{Si} also have time to anneal, releasing the oxygen to diffuse towards R_p and d_O. After the sample is annealed, the shape is similar to the standard sample, with only a slight reduction in the oxygen concentration at d_O.

Next let us discuss the differences between samples pre-damaged with 5×10^{14} Si/cm^2 (T_i=room temperature, annealed) and samples pre-damaged with 2×10^{15} O/cm^2 (2.5 MeV,

T_i=300°C, no anneal). There was no analysis of the oxygen pre-damage. However, according to the theories presented by Cerofolini *et al.* [88], at this low dose, low flux, and elevated temperature, the majority of the implanted oxygen form precipitates at d_O (see §2-5-1), where the oxygen from R_p diffuses to d_O. The sample was not annealed, and so we expect that the damage in this region consists of small defect clusters. Since the depth of the pre-damage in an oxygen pre-damaged sample is, by definition, equivalent to d_O, we will compare the $\phi = 1 \times 10^{17}$ O/cm^2 sample, pre-damaged with oxygen (figure 4-54), with an equivalent sample, pre-damaged with 2.75 MeV 5×10^{14} Si/cm^2, such that $d_{Si} \approx d_O$ (figure 4-48). In both of these samples, there is a higher concentration of oxygen, after annealing, at d_O than there is at R_p. In the sample pre-damaged with silicon, this affect was attributed to a preferential growth of precipitates at d_{Si} in the VERY early stages of the implantation. In the oxygen pre-damaged sample the oxide precipitates at d_O already exist. Thus both samples have an enhanced growth of precipitates at d_O, which results in similar profiles after annealing. The oxygen concentration peak at d_O is sharper for the oxygen pre-damaged sample, and this could indicate many things, (a) the oxygen pre-damage was more effective at gettering oxygen into a smaller depth region during the implantation than the silicon pre-damage, (b) the precipitates at d_O were slightly larger at the end of the implantation or (c) there were fewer dislocations between d_O and R_p and thus the precipitates in this region dissolved quicker and more effectively during the anneal. Both samples have a small oxygen concentration peak at 2.2 μm. The exact mechanism which is responsible for this peak is not known, but because it is present in both samples at the same location, it does not appear to be related to the type of pre-damage.

It has been clearly demonstrated that the final oxygen concentration profile is dependent on the type of pre-damage. The number of threading dislocations between d_{Si} and d_O is related to the stability of the pre-damage during the oxygen implantation itself, which in turn changes the quantity of precipitates in the region $1/2\,(d_O + d_{Si})$. Thus the relevant properties of the pre-damage are (1) the rate that interstitials can be absorbed by the pre-damage, (2) the number of nucleation sites for oxide precipitation and (3) the relative stability of the pre-damage during the oxygen implantation.

Chapter 5
Summary

In this work we studied silicon samples that were implanted with high energy oxygen and silicon ions. The purpose was to determine the interactions between oxygen ions, oxide precipitates, silicon self-interstitials, vacancies and extended defects. Using the results of the analysis (chapter 4), we have formulated simple models which describe the behaviour of the oxygen and the defects in the sample during the implantation. These models can then predict the subsequent oxygen profile after the sample has been annealed at a high temperature. A relationship has been found between the quality of the silicon film and the number of self-interstitials diffusing from the end-of-range to the sample surface. We have not, however, been successful in modelling the behaviour of the precipitation of oxygen in the silicon substrate.

5-1 RANGE AND STRAGGLING

The most probable projected range, R_p, of 2.5 MeV oxygen in silicon was found to be 2.55 ± 0.10 μm, with a straggle of $\sim$0.15 μm. The range is a little larger than the value predicted by TRIM (2.38 μm), however this discrepancy is not unusual for high energy oxygen implantations, since no diffusion or crystalline effects are considered in the TRIM calculations.

5-2 QUALITY OF THE SILICON FILM

5-2-1 Function of Dose

We have seen that the depth d_O, up to which the silicon film retains a high crystalline quality, is not a function of oxygen dose when the doses are in the range 0.3×10^{17} to 3.0×10^{17} O/cm^2. We have concluded that the depth d_O is a function of the rate of recombination of defects in the film, independent of the oxygen concentration. With an implant temperature of 570°C, and a dose rate of $\phi/s < 6 \times 10^{12}$ O/cm^2·s, the silicon film maintains a high level of crystallinity up to a depth of 2.33 μm.

5-2-2 Release of Strain

The low level of crystalline damage in the silicon film does not preclude the presence of strain resulting from an uneven distribution of vacancies and interstitials. It has been hypothesized by Holland [15] and Zhou [14] that when the strain in the silicon film exceeds a critical value, it is released by the formation of extended defects and oxide precipitates. This hypothesis has been partially verified by our work insofar as we have found small defect clusters at a depth of 1–1.3 μm ($\sim$ $^1/_2\, R_p$) in samples implanted with an oxygen dose of 3×10^{17} O/cm^2. The presence of oxide precipitates at this depth has been inferred from the resulting oxygen concentration peak after a high temperature anneal. Extended defects, seen in similar work by Holland [15], Zhou [14] and Ellingboe [13], are found when the oxygen dose is slightly higher ($\phi > 7 \times 10^{17}$ O/cm^2). It is therefore concluded that the defect clusters and precipitates seen in our samples are the precursors to the extended defects mentioned above.

In this work we have also shown that the defect clusters in the silicon film in the as-implanted and annealed samples can be modified by the presence of a band of extended defects (pre-damage) located at $d_{Si} > 0.9R_p$. Instead of small defect clusters and precipitates at 1.3 μm, there are voids filled with gaseous oxygen. This phenomenon is explained by the theories proposed by Venables [20] regarding vacancies, oxygen and strain relief, in silicon. There are excess vacancies in the film which are decorated with oxygen. We have concluded that since the interstitials produced by the oxidation of the silicon at R_p are prevented by the pre-damage layer from diffusing to the silicon film, there is a reduction of interstitial/vacancy pair recombination. As the vacancies agglomerate to form voids, the oxygen atoms that are bound to the vacancies form gaseous oxygen which then fills the void, keeping it stable.

With regards to the defects in the silicon film there are many unanswered questions. Since no strain measurements were taken, it is not possible to verify the relationship between strain release and the formation of defect clusters or voids in the silicon film. Nor is it understood why the defect clusters and the vacancies form in a well defined depth region around 1.3 μm. By studying strain, using the XRD technique, as a function of oxygen dose in standard and pre-damaged samples, some of these questions could be answered.

5-3 OXIDE PRECIPITATION

5-3-1 Standard Sample

For the standard (not pre-damaged) samples we have developed a realistic model, based on our experimental results, to describe the interplay between the homogeneous and heterogeneous precipitation. In our model there is no net diffusion of oxygen to the highly damaged areas in the samples. The model is simplistic and assumes that everywhere, except in the region near d_O, the mean size of the precipitates is proportional to the cubed root of the concentration, where α is the constant of proportionality. The preferential oxidation at d_O is represented by a Gaussian distribution of larger, but fewer, precipitates. Any precipitate smaller than $r_c(T)$ at the anneal temperature (T) is dissolved in the very early stages of the anneal. Only the precipitates that remain contribute to the normal Ostwald ripening process. It is not necessary to know the absolute value of r_c and α because their relative size, with respect to each other, has been estimated from our experimental results (see figure 4-50). The only significant unknown parameter in this model is the relative increase in size of the precipitates in the d_O region. When this increase is 30%, the model can be used quite effectively to describe the post-anneal oxygen concentration for the samples, implanted with doses between 0.3×10^{17} and 3.0×10^{17} O/cm^2, studied in this work.

Based on this model, we conclude that at high implant energies (2.5 MeV) it is not possible to form BOX (buried oxide) structures with low oxygen doses ($< 10^{18}$ O/cm^2). At low oxygen doses the precipitates at d_O and R_p dissolve and thus, the annealing process does not favour one precipitation region over another. At intermediate doses there are a few precipitates at R_p that survive the initial stages of annealing. However there is still sufficient damage at d_O to retard the diffusion of oxygen from the silicon film to R_p. At higher doses the precipitates at d_O remain as do the precipitates at R_p. The precipitates at d_O act as a diffusion barrier for the oxygen from the silicon film. Consequently, any stoichiometric oxide layer must be at least as thick as the distance separating d_O and R_p. Thus the minimum dose for SIMOX production is $\phi \sim 1\text{–}2 \times 10^{18}$ O/cm^2.

5-3-2 Pre-damaged Sample

We have also developed a model to explain the interplay we have observed between different damage regions and oxide precipitation. The concentration and size of oxide precipitates at R_p is not grossly affected by the presence of pre-damage when the pre-damage depth is less than d_O. The majority of the differences occur in the depth region encompassing the oxygen-induced damage region at d_O and the pre-damage region d_{Si}. It was shown that, during the early stages of the implanting, oxide precipitates preferentially form at d_{Si}. These precipitates getter oxygen more efficiently than the smaller precipitates at d_O, which results in an initial rapid growth of the precipitates at d_{Si}. The stability of the damage and/or oxides at d_O is reduced, and the result is that the precipitates in this region are smaller than in the equivalent standard samples. However, the precipitates at d_O still grow faster than the precipitates at d_{Si}, due mostly to the larger concentration of oxygen being deposited per unit time at d_O. We have defined a dose ϕ_{HE} to be the dose at which the precipitates at d_O are the same size as those at d_{Si}. The dose ϕ_{HE} increases as the distance between d_O and d_{Si} decreases. For $d_O - d_{Si} = 0.40$ μm, $\phi_{HE} \simeq 0.3 \times 10^{17}$ O/cm^2. We have also seen that the concentration of oxygen at d_O, in the annealed samples, is reduced as d_{Si} approaches d_O. When d_{Si} and d_O are sufficiently close (0.1 μm) the pre-damage region getters oxygen and interstitials so effectively that the oxygen concentration at d_O in the annealed sample is 75% lower than that in an equivalent standard sample.

In addition to providing a sink for oxygen and silicon interstitials, the pre-damage also acts as a diffusion barrier between the end-of-range and the silicon film. Thus many interstitials are trapped on the R_p side of the pre-damage, and so they either aid in the growth and annihilation of the pre-damage or they combine to form threading dislocations between the two damage regions. These dislocations then getter oxygen, which can lead to the additional oxygen peaks observed in some of our annealed samples.

Due to the dynamic annealing of the pre-damage and the precipitates at d_{Si}, the above described effects are more pronounced at lower oxygen doses, ($< \phi_{HE}$). We predict that at higher doses of oxygen ($> 3.0 \times 10^{17}$ O/cm^2), most of the effects of the presence of pre-damage at d_{Si}, when $d_{Si} < d_O$, will diminish. What will remain is a small number of stable precipitates at d_{Si} in addition to an oxygen concentration profile that is similar to the oxygen concentration profile of an equivalent standard sample. Unfortunately this leads us to the next conclusion that it is still not possible to form a

BOX structure by high temperature oxygen implantation into pre-damaged silicon samples when the pre-damage depth is less than d_O.

Our results have shown that for samples pre-damaged at depths equivalent to d_O, the final oxygen concentration after annealing is substantially different than the concentration profiles previously discussed. The preferential precipitation and growth of oxides on the pre-damage at d_{Si} does not compete with the precipitation and growth of oxides at d_O. Since both processes occur at the same depth, oxide precipitation is enhanced in this region. For samples implanted with $\phi = 1.0 \times 10^{17}$ O/cm^2 and then annealed, there is a large (3.5×10^{21} at/cm^3) narrow (70 nm) oxygen concentration peak at d_O. This peak contains about 40% of the total oxygen, as compared to the 25% in the standard sample. The concentration of oxygen is 75% higher than the normal concentration at this depth, and slightly higher than its typical peak concentration. The ERD analysis indicates that there may be a residual concentration of oxygen just shallower than d_O. However these samples have not been analyzed by either SIMS or XTEM, which would yield a better analysis.

5-4 SILICON SUBSTRATE

At this stage, we do not have an explanation as to why oxide precipitates remain in the silicon substrate in some annealed samples and not others. There does not appear to be a pattern regarding these precipitates, and so it is necessary to determine a causal relationship between the parameters used in making the samples and the precipitates in the substrate. The first step in such an investigation is to determine the reproducibility of the results, and in doing so, narrow down the most probable cause. Although it has not been verified, we believe that there is planar channeling which occurs during the implantation, which in turn changes the oxygen distribution within the sample, especially at depths greater than R_p.

5-5 FURTHER WORK

Although we have not succeeded in forming a BOX structure at high implant energies, we believe that enough knowledge has been gained regarding the effects of pre-damage in the silicon sample to show that further research is warranted. The next logical step in this series of investigations would be to increase the depth of the pre-damage so that it is deeper than d_O, but less than R_p. The pre-damage should be made with a low temperature oxygen implantation. The advantages of using oxygen

pre-damage are two-fold. Firstly, the gettering efficiency of the oxygen pre-damage is slightly more effective than silicon pre-damage, and secondly, the sample need not be removed from the implantation chamber between the pre-damage implantation and the regular implantation. Another variation of the experiments could include a shift in oxygen energy at some point during the regular implantation so that the precipitates at the pre-damage depth continue to grow faster than the precipitates at either d_O or R_p. ERD could be used as an method of rejecting sets of parameters that don't work. In the more promising samples, low levels of oxygen in the silicon film and substrate would be investigated with analysis techniques that are more sensitive than ERD, such as SIMS and XTEM. If it were possible to adjust the pre-damage and implant energy parameters such that all the oxygen would be concentrated at d_O within a 0.1 μm layer, the minimum oxygen dose would be only 4.5×10^{17} O/cm^2! As this would allow one to produce an oxide layer in less time and with less damage in the silicon film, the results of such further investigation would definitely be worthwhile.

Chapter 6
Conclusion

In this thesis we have studied the oxidation process of oxygen implanted into pre-damaged silicon as a function of the type of pre-damage, the depth of pre-damage and the oxygen dose. The conclusions are based on the observations of damage, oxide precipation and the oxygen concentration profiles of the post-anneal samples.

Two types of pre-damage were studied, and it was concluded that the relevant properties of the pre-damage are: the rate that interstitials can be absorbed by the pre-damage, the number of nucleation sites for oxide precipitation and the relative stability of the pre-damage during the oxygen implantation.

The relationship between the oxide precipitation process during the oxygen implantation and the pre-damage is described by the following. The pre-damage region does not adversely change the nature of the oxidation process at the depth of maximum oxygen concentration. During the early stages of implantation there is preferential oxidation and more efficient gettering of oxygen in the pre-damage region (d_{Si}) than in the implantation induced damage region (d_O). This has the effect of reducing the oxygen concentration at d_O in the annealed samples. The affect of the pre-damage in the sample is more pronounced as the distance between d_{Si} and d_O is decreased. As the oxygen dose increases, the pre-damage begins to anneal which reduces the oxidation and gettering efficiency at d_{Si}. This in turn reduces the effects of pre-damaging the sample, especially in the region of d_O. Unfortunately this leads us to the conclusion that it is not possible to form a BOX structure by high temperature, high energy oxygen implantation into pre-damaged silicon samples when the pre-damage depth is less than d_O. For samples pre-damaged at depths equivalent to d_O, the preferential precipitation and growth of oxides on the pre-damage at d_{Si} does not compete with the precipitation and growth of oxides in the region of d_O. The result, after annealing, is a high narrow peak in the oxygen concentration in the region of d_O.

Although we have not succeeded in forming a BOX structure at high implant energies, we believe that it may be possible if the energy of the oxygen is modified during the implantation itself. Further work is required to investigate this possibility.

References

[1] A. Auberton-Herve, A. Wittkower, B. Aspar, *Nucl. Instr. Meth.*, **B96** (1995) 420-424.

[2] A. Ionescu and Cristoloveanu, *Nucl. Instr. Meth.*, **B84** (1994) 265.

[3] W. Ensinger, *Nucl. Instr. Meth.*, **B84** (1994) 181.

[4] C.J. Griffin, J.A. Kilner, R.J. Chater, A. Staton-Bevan, K.J. Reeson, P.L.F. Hemment, and J.R. Davis, *Nucl. Instr. Meth.*, **B39** (1989) 215-219.

[5] T.P. Sjoreen, O.W. Holland, D. Fathy, K. More, and R.F. Davis, *Nucl. Instr. Meth.*, **B10/11** (1985) 564-579.

[6] A.H. van Ommen, *Nucl. Instr. Meth.*, **B39** (1989) 194-202.

[7] G.K. Celler, P.L.F. Hemment, K.W. West, and J.M. Gibson, *Appl. Phys. Lett.*, **48** (1986) 532.

[8] K.J. Reeson, *Nucl. Instr. Meth.*, **B19/20** (1987) 269-278.

[9] A. Yoshino, K. Kasama, and M. Sakamoto, *Nucl. Instr. Meth.*, **B39** (1989) 203-206.

[10] A. Golanski, A. Perio, J.J. Grob, R. Stuck, S. Maillet, and E. Clavelier, *Appl. Phys. Lett.*, **49** (1986) 1423.

[11] S. Maillet, R. Stuck, J.J. Grob, A. Golanski, R. Pantel, and A. Perio, *Nucl. Instr. Meth.*, **B19/20** (1987) 294-298.

[12] C.W. Nieh, F. Xiong, C.C. Ahn, Z. Zhou, D.N. Jamieson, T. Vreeland Jr., B. Fultz, and T.A. Tombrello, in: *Silicon-On-Insulator and Buried Metals in Semiconductors*, eds. J.C. Sturm, C.K. Chen, L. Pfeiffer, and P.L.F. Hemment, *Mat. Res. Soc. Symp. Proc.*, **vol 107** (1988) 73.

[13] S. Ellingboe, M.C. Ridgway, and P.J. Schultz, *J. Appl. Phys.*, **73** (1993) 1133.

[14] D.S. Zhou, O.W. Holland, and J.D. Budai, *Appl. Phys. Lett.*, **63** (1993) 3580.

[15] O.W. Holland, D.S. Zhou, and D.K. Thomas, *Appl. Phys. Lett.*, **63** (1993) 896.

[16] S. Nakashima and K. Izumi, *J. Mater. Res.*, **Vol 8** (1993) 523-534.

[17] G.F. Cerofolini, S. Bertoni, P. Fumagalli, L. Meda, and C. Spaggiari, *Phys. Rev. B*, **47 (16)** (1993) 10174.

[18] L. Meda, S. Bertoni, G.F. Cerofolini and C. Spaggiari, *Nucl. Instr. Meth.*, **B80/81** (1993) 813-817.

[19] K.S. Jones, H.G. Robinson, J. Listebarer, J. Chen, J. Liu, B. Herner, H. Park, M.E. Law, D. Sieloff, J.A. Slinkman, *Nucl. Instr. Meth.*, **B96** (1995) 196-203.

[20] D. Venables and K.S. Jones, *Nucl. Instr. Meth.*, **B74** (1993) 65-69.

[21] F.R.N. Nabarro, Theory of Crystal Dislocations, Oxford University Press (1967)

[22] M. Lannoo and J. Bourgoin, Point Defects in Semiconductors I and II, Springer-Verlag, Heidelberg (1981)

[23] J.W. Corbett, J.P. Karins, T.Y. Tan, *Nucl. Instr. Meth.*, **182/183** (1981) 457-476.

[24] J.F. Ziegler, J.P. Biersack, U. Littmark, *Pergamon Press, New York*, **Vol 1** (1985) ed. J.F. Ziegler.

[25] J.J. Grob, A. Grob, P. Thevenin, P. Siffert, C. D'Anterroches and A. Golanski, *J. Mater. Res.*, **4** (1989) 1227.

[26] J.J.. Grob, A. Grob, P. Thevenin, and P. Siffert, *Nucl. Instr. Meth.*, **B30** (1988) 34-37.

[27] H.F. Kappert, K.F. Heidemann, D. Eichholz, E. te Kaat, and W. Rothenmund, *Appl. Phys.*, **21** (1980) 151-158.

[28] W.R. Fahrner, K. Heidemann, and P. Schöttle, *Phys. Stat. Sol.*, **70** (1982) 463.

[29] K. Touhouche, J. Jackman and A. Yelon, *Nucl. Instr. Meth.*, **B80/81** (1993) 857.

[30] G. Carter and W.A. Grant, *Nucl. Instr. Meth.*, **199** (1982) 17-35.

[31] J.W. Williams, *Rep. Prog. Phys.*, **49** (1986) 491-587.

[32] L.C. Feldman, J.W. Mayer, S.T. Picraux, Materials Analysis by Ion Channeling, Submicron Crystallography, Academic Press, New York, (1982)

[33] S. Mader, *Ion Implantation Damage in Silicon*, Ion Implantation, Science & Technology, Academic Press, Orlando (1984), ed. J.F. Ziegler, pg 109

[34] D.A. Thompson and R.W. Walker, *Nucl. Instr. Meth.*, **132** (1976) 281-284.

[35] C. Cellini, A. Carnera, M. Berti, A. Gasparotto, D. Steer, M. Servidori, S. Milita, *Nucl. Instr. Meth.*, **B96** (1995) 227-231.

[36] K. Laaziri, S. Roorda, L. Cliche, *Nucl. Instr. Meth.*, **B90** (1994) 438-441.

[37] O.W. Holland and C.W. White, *Nucl. Instr. Meth.*, **B59/60** (1991) 353-363.

[38] A. Golanski, A. Grob, J.J. Grob, O.W. Holland, S.J. Pennycook, and C.W. White, *Nucl. Instr. Meth.*, **B62** (1992) 365-371.

[39] T.A. Belykh, A.L. Gorodishchensky, L.A. Kazak, V.E. Semyannikov, and A.R. Urmanov, *Nucl. Instr. Meth.*, **B51** (1990) 242-246.

[40] S.M. Hu, *Appl. Phys. Lett.*, **48** (1986) 115.

[41] Qing-tai Zhao, Zhong-lie Wang, Tian-bing Xu, Pei-ran Zhu, Jun-si Zhou, Xiang-dong Liu, Ji-tian Liu and Ke-ming Wang, *Nucl. Instr. Meth.*, **B82** (1993) 575.

[42] R.G. Elliman, J.S. Williams, S.T. Johnson and A.P. Pogany, *Nucl. Instr. Meth.*, **B15** (1986) 439.

[43] N. Hecking, K.F. Heidemann and E. Te Kaat, *Nucl. Instr. Meth.*, **B15** (1986) 760.

[44] J.F. Ziegler, *Nucl. Instr. Meth.*, **B6** (1985) 270-282.

[45] J.K.N. Lindner, R. Domres, and E.H. Te Kaat, *Nucl. Instr. Meth.*, **B39** (1989) 306-310.

[46] P.J. Schultz, C. Jagadish, M.C. Ridgway, R.G. Elliman and J.S. Williams, *Phys. Rev. B.*, **44** (1992) 9118.

[47] A.E. Michel, *Nucl. Instr. Meth.*, **B37/38** (1989) 379-383.

[48] L. Sealy, R.C. Barklie, K.J. Reeson, W.L. Brown and D.C. Jacobson, *Nucl. Instr. Meth.*, **B62** (1992) 384-387.

[49] A. Battaglia, F. Priolo, and E. Rimini, *Nucl. Instr. Meth.*, **B59/60** (1991) 382-385.

[50] N.W. Ashcroft, N.D. Mermin, Solid State Physics, Saunders College: Holt, Rinehart and Winston, Philadelphia (1976)

[51] J. Washburn, *Defects in Semiconductors*, eds. J. Narayan and T.Y. Tan, *Mat. Res. Soc. Symp. Proc.*, **vol 2** (1980) .

[52] L. Calcagno, S. Coffa, C. Spinella and E. Rimini, *Nucl. Instr. Meth.*, **B45** (1990) 442.

[53] T.Y. Tan, *Defects in Semiconductors*, eds. J. Narayan and T.Y. Tan, *Mat. Res. Soc. Symp. Proc.*, **vol 2** (1980) .

[54] U. Gosele, W. Frank, *Defects in Semiconductors*, eds. J. Narayan and T.Y. Tan, *Mat. Res. Soc. Symp. Proc.*, **vol 2** (1980) .

[55] K.S. Jones, S. Prussin, and E.R. Weber, *Appl. Phys. A*, **45** (1988) 1.

[56] I.F. Bubb, D.J. Chivers, J.R. Liu, A.P. Pogany, K.T. Short, H.K. Wagenfeld, and J.S. Williams, *Nucl. Instr. Meth.*, **B2** (1984) 761.

[57] A. Claverie, L. Laanab, C. Bergaud, A. Martinex, and D. Mathiot, *Nucl. Instr. Meth.*, **B96** (1995) 202-209.

[58] J. Gyulai, *Damage Annealing in Silicon and Electrical Activity*, Ion Implantation, Science & Technology, Academic Press, Orlando (1984), ed. J.F. Ziegler, pg 139

[59] Y. Yatsurugi, N. Akiyama, Y. Endo, and T. Nazaki, *J. Electrochem. Soc.*, **120** (1973) 975.

[60] D.K. Sadana, N.R. Wu, J. Washburn, M. Current, A. Morgan, D. Reed, and M. Maenpaa, *Nucl. Instr. Meth.*, **209/210** (1983) 743-750.

[61] M. Tamura, T. Ando, and K. Ohyu, *Nucl. Instr. Meth.*, **B59/60** (1991) 572-583.

[62] M. Tamura, and T. Suzuki, *Nucl. Instr. Meth.*, **B39** (1989) 318-329.

[63] J. Stoemenos, K.J. Reeson, A.K. Robinson, and P.L.F. Hemment, *J. Appl. Phys*, **69** (1991) 793.

[64] C. Jaussaud, J. Margail, J. Stoemenos, and M. Bruel, in: *Silicon-On-Insulator and Buried Metals in Semiconductors*, eds. J.C. Sturm, C.K. Chen, L. Pfeiffer, and P.L.F. Hemment, *Mat. Res. Soc. Symp. Proc.*, **vol 107** (1988) 17.

[65] S. Maeyama, and K. Kajiyama, *Jap. J. Appl. Phys.*, **21** (1982) 774-751.

[66] K.J. Reeson, K.G. Stephens, and P.L.F. Hemment, *Nucl. Instr. Meth.*, **B39** (1989) 290-295.

[67] J. Margail, J. Stoemenos, C. Jaussaud, and M. Bruel, *Appl. Phys. Lett.*, **54** (1989) 526.

[68] K.G. Stephens, K.J. Reeson, B.J. Sealy, R.M Gwilliam and P.L.F. Hemment, *Nucl. Instr. Meth.*, **B50** (1990) 368-378.

[69] J.C. Mikkelsen Jr., in *Oxygen, Carbon, Hydrogen and Nitrogen in Crystalline Silicon*, eds. J.C. Mikkelsen Jr. *et al.*, *Mat. Res. Soc. Symp. Proc.* **59** (1986) 369.

[70] W.J. Taylor, T.Y. Tan, and U.M. Gosele, *Appl. Phys. Lett.*, **59** (1991) 2007.

[71] M.J. Binns, W.P. Brown, J.G. Wilkes, R.C. Newman, F.M. Livingston, S. Messoloras, and R.J. Stewart, *Appl. Phys. Lett.*, **42** (1983) 525.

[72] U. Gösele, T.Y. Tan, *Appl. Phys.*, **A28** (1982) 79-92.

[73] S. Reiss and K.H. Heinig, *Nucl. Instr. Meth.*, **B84** (1994) 229.

[74] S. Reiss, R. Weber, K.-H Heinig, W. Skorupa, *Nucl. Instr. Meth.*, **B89** (1994) 337-341.

[75] F. Shimura, *Appl. Phys. Lett.*, **39** (1981) 987.

[76] A. Nejim, Y. Li, C.D. Marsh, P.L.F. Hemment, R.J. Chater, J.A. Kilner, L.F. Giles, *Nucl. Instr. Meth.*, **B74** (1993) 170-174.

[77] L.F. Giles, F. Cristiano, A. Nejim, G. Curello, and P.L.F. Hemment, *Ion Implantation Technology - 94*, eds. S. Coffa, G. Ferla, F.Priolo, E. Rimini, (1995) 771.

[78] S.J. Krause, C.W. Jung, T.S. Ravi, S.R. Wilson and D.E. Burke, in: *Silicon-On-Insulator and Buried Metals in Semiconductors*, eds. J.C. Sturm, C.K. Chen, L. Pfeiffer, and P.L.F. Hemment, *Mat. Res. Soc. Symp. Proc.*, **vol 107** (1988) 93.

[79] D.M. Maher, A. Staudinger, and J.R. Patel, *J. Appl. Phys.*, **47** (1976) 3813.

[80] A. Nejim, C.D. Marsh, L.F. Giles, P.L.F. Hemment, Y. Li, R.J. Chater, J.A. Kilner, and G.R. Booker, *Nucl. Instr. Meth.*, **B84** (1994) 248.

[81] M.K. El-Ghor, S.J. Pennycook, T.P. Sjoreen, C.W. White, and J. Narayan, in: *Silicon-On-Insulator and Buried Metals in Semiconductors*, eds. J.C. Sturm, C.K. Chen, L. Pfeiffer, and P.L.F. Hemment, *Mat. Res. Soc. Symp. Proc.*, **vol 107** (1988) 79.

[82] J.A. Kilner, R.J. Chater, P.L.F. Hemment, R.F. Peart, E.A. Maydell-Ondrusz, M.R. Taylor, and R.P. Arrowsmith, *Nucl. Instr. Meth.*, **B7/8** (1985) 293-298.

[83] P.L.F. Hemment, K.J. Reeson, A.K. Robinson, J. Stoemenos, J.A. Kilner, R.J. Chater, G.K. Celler and J.R. Davis, *Nucl. Instr. Meth.*, **B39** (1989) 210-214.

[84] R.J. Chater, J.A. Kilner, P.L.F. Hemment, K.J. Reeson, and J.R. Davis, *Nucl. Instr. Meth.*, **B19/20** (1987) 290-293.

[85] J. Narayan, S.Y. Kim, K.Vedam, R. Manukonda, *Appl. Phys. Lett.*, **51** (1987) 343.

[86] C.G. Tuppen, M.R. Taylor, P.L.F. Hemment, and R.P. Arrowsmith, *Appl. Phys. Lett.*, **45** (1984) 57.

[87] I.H. Wilson, *Nucl. Instr. Meth.*, **B1** (1984) 331-343.

[88] G.F. Cerofolini, S. Bertoni, L. Meda and C. Spaggiari, *Nucl. Instr. Meth.*, **B84** (1994) 234.

[89] R. Weber, R. Müller and W. Skorupa, *Nucl. Instr. Meth.*, **B84** (1994) 286.

[90] S.M. Hu, *Appl. Phys. Lett.*, **36** (1980) 1.

[91] J.A. Kilner, S.D. Littlewood, P.L.F. Hemment, E. Maydell-Ondrusz, and K.G. Stephens, *Nucl. Instr. Meth.*, **218** (1983) 573-578.

[92] J.D. Larson, *Nucl. Instr. Meth.*, **189** (1981) 71-91.

[93] O.W. Holland, T.P. Sjoreen, D. Fathy, J. Narayan, *Appl. Phys. Lett.*, **45** (1984) 1081.

[94] J.R. Davis, M.R. Taylor, G.D.T. Spiller, P.J. Skevington, and P.L.F. Hemment, *Appl. Phys. Lett.*, **48** (1986) 1279.

[95] A.E. White, K.T. Short, J.L. Batstone, D.C. Jacobson, J.M. Poate, and K.W. West, *Appl. Phys. Lett.*, **50** (1987) 19.

[96] K. Touhouche, Y. Tao, A. Yelon, G. Kajrys, Y. Trudeau, K. Oxorn, S. Bultena, and G. Gagnon, *Nucl. Instr. Meth.*, **B59/60** (1991) 676-679.

[97] K. Touhouche, Y. Tao, and A. Yelon, *Can. J. Phys.*, **69** (1991) 307.

[98] G. Harbeke, E.F. Steigmeier, P.L.F. Hemment, K.J. Reeson, and L. Jastrzebski, in: *Silicon-On-Insulator and Buried Metals in Semiconductors*, eds. J.C. Sturm, C.K. Chen, L. Pfeiffer, and P.L.F. Hemment, *Mat. Res. Soc. Symp. Proc.*, **vol 107** (1988) 133.

[99] A. Pérez-Rodríguez, A. Romano-Rodríguex, J. Macía and J.R. Morante, E. Martin and J. Jiménez, *Nucl. Instr. Meth.*, **B84** (1994) 275.

[100] E.F. Steigmeier, G. Harbeke, K.J. Reeson, P.L.F. Hemment, and A.K. Robinson, *Nucl. Instr. Meth.*, **B37/38** (1989) 304-307.

[101] S. Visitserngtrakul, B.F. Cordts, and S. Krause, *Mat. Res. Soc. Symp. Proc.*, **vol 157** (1990) 161.

[102] Bent Nielsen, K.G. Lynn, and T.C. Leung, B.F. Cordts, S. Seraphin, *Phys. Rev. B*, **vol 44 No. 4** (1991) 1812.

[103] A.H. van Ommen, B.H. Koek, and M.P.A. Viegers, *Appl. Phys. Lett.*, **49** (1986) 1062.

[104] A.H. Van Ommen, in: *Silicon-On-Insulator and Buried Metals in Semiconductors*, eds. J.C. Sturm, C.K. Chen, L. Pfeiffer, and P.L.F. Hemment, *Mat. Res. Soc. Symp. Proc.*, **vol 107** (1988) 43.

[105] C. Jaussaud, J. Stoemenos, J. Margail, M. Dupuy, B. Blanchard, and M. Bruel, *Appl. Phys. Lett.*, **46** (1985) 1064.

[106] H. Koyama and T. Kashiwaki, *Appl. Phys. Lett.*, **38** (1981) 791.

[107] A.H. Hamdi, F.D. McDaniel, R.F. Pinizzotto, M.S. Matteson, H.W. Lam, and S.D.S. Malhi, *Appl. Phys. Lett.*, **41** (1982) 1143.

[108] A. Stolmeijer, *IEEE Trans. Elec. Dev.*, **ED-33** (1986) 450.

[109] B.Y. Mao, P.H. Chang, H.W. Lam, B.W. Shen, and J.A. Keenan, *Appl. Phys. Lett.*, **48** (1986) 794.

[110] T.F. Cheek Jr. and Daniel Chen, in: *Silicon-On-Insulator and Buried Metals in Semiconductors*, eds. J.C. Sturm, C.K. Chen, L. Pfeiffer, and P.L.F. Hemment, *Mat. Res. Soc. Symp. Proc.*, **vol 107** (1988) 53.

[111] J.Blake, J.C. Gelpey, D.M. Lee, L. Rowland, and G.A. Rozgonyi, in: *Silicon-On-Insulator and Buried Metals in Semiconductors*, eds. J.C. Sturm, C.K. Chen, L. Pfeiffer, and P.L.F. Hemment, *Mat. Res. Soc. Symp. Proc.*, **vol 107** (1988) 61.

[112] P. Sioshansi and F. Namayar, in: *Silicon-On-Insulator and Buried Metals in Semiconductors*, eds. J.C. Sturm, C.K. Chen, L. Pfeiffer, and P.L.F. Hemment, *Mat. Res. Soc. Symp. Proc.*, **vol 107** (1988) 67.

[113] S.L. Ellingboe and M.C. Ridgway, in *Beam Solid Interactions: Fundamentals and Applications Symposium*, eds. Nastasi, M., Herrilt, L.R., Herbots, N. Averback, R.S., *Mat. Res. Soc. Symp. Proc.*, (1995) 147.

[114] A.E. White, K.T. Short, R.C. Dynes, J.M Gibson, and R. Hull, in: *Silicon-On-Insulator and Buried Metals in Semiconductors*, eds. J.C. Sturm, C.K. Chen, L. Pfeiffer, and P.L.F. Hemment, *Mat. Res. Soc. Symp. Proc.*, **vol 107** (1988) 3.

[115] A. Nejim, Y. Li, C.D. Marsh, P.L.F. Hemment, R.J. Chater, J.A. Kilner and G.R. Booker, *Nucl. Instr. Meth.*, **B80/81** (1993) 822-826.

[116] L.D. Dyer, G.J. Grant, C.M. Tipton, and A.E. Stephens, *J. Electrochem. Soc.*, **136/10** (1989) 3016.

[117] S.C. Gujrathi, P. Aubry, L. Lemay, and J.-P. Martin, *Can. J. Phys.*, **65** (1987) 950-955.

[118] K. Oxorn, S.C. Gujrathi, S. Bultena, L. Cliche, and J. Miskin, *Nucl. Instr. Meth.*, **B45** (1990) 166-170.

[119] S.C. Gujrathi and S. Bultena, *Nucl. Instr. Meth.*, **B64** (1992) 789-795.

[120] D. Hinrichsen, D. Hetherington, S.C. Gujrathi, and L. Cliche, *Nucl. Instr. Meth.*, **B45** (1990) 275-280.

[121] F. Pászti, E. Szilágyi and E. Kótai, *Nucl. Instr. Meth.*, **B54** (1991) 507-512.

[122] E. Szilágyi, F. Pászti, G. Amsel, *Nucl. Instr. Meth.*, **B100** (1995) 103-121.

[123] S.C. Gujrathi, D. Poitras, J.E. Klemberg-Sapicha and L. Martinu, *12th Int. Conf. on Ion Beam Analysis*, (1995) accepted for publication.

[124] Wei-Kan Chu, James W. Mayer, Marc-A Nicolet Backscattering Spectrometry Academic Press, Orlando, (1978)

[125] L.C. Feldman, J.W. Mayer, Fundamentals of Surface and Thin Film Analysis North Holland, New York, (1986)

[126] D.V. Morgan (ed.), Channeling - Theory, Observation and Applications, John Wiley & Sons, London, (1973)

[127] H-J Gossmann and L.C. Feldman, *MRS Bulletin*, **August/Sept** (1987) 30.

[128] R. Simonton and D. Kamenitsa, *Nucl. Instr. Meth.*, **B37/38** (1989) 344-347.

[129] F.H. Eisen, G.J. Clark, J. Bottiger and J.M Poate, *Radiat. Eff.*, **13** (1972) 93.

[130] D.W. Hetherington, *Nucl. Instr. Meth.*, **B90** (1994) 84-87.

[131] Z. Sroubek, *Nucl. Instr. Meth.*, **194** (1982) 533.

[132] Edington, J.W., Practical Electron Microscopy in Materials Science, Van Nostrand Reinhold Co, New York (1976)

[133] Glauert, Audrey M. (ed.), Practical Methods in Electron Microscopy, North Holland Publishing Co., London (1972)

[134] CM20 Electron Microscope User's Manual, Philips Export B.V., Eindhoven, The Netherlands (1989)

[135] J.C. Bravman and R. Sinclair, *J. Elec. Microscopy Tech.*, **1** (1984) 53-61.

[136] K. Touhouche, *Implantation ionique d'oxygène à haute énergie dans le silicium*, PhD Thesis, École Polytechnique (Montreal) 1992.

[137] R. Schork and H. Ryssel, *Ion Implantation Technology - 94*, eds. S. Coffa, G. Ferla, F.Priolo, E. Rimini, (1995) 885.

Appendix A

Nitrogen in-diffusion and accumulation in oxygen-implanted silicon during thermal annealing

Reprinted from ION IMPLANTATION TECHNOLOGY-94

North Holland Publishing (1995) 791-796

ION IMPLANTATION TECHNOLOGY – 94
S. Coffa, G. Ferla, F. Priolo, E. Rimini (eds.)

Nitrogen in-diffusion and accumulation in oxygen-implanted silicon during thermal annealing

S. BULTENA[1], S.C. GUJRATHI[1], J.L. BREBNER[1], A. YELON[2], S. ROORDA[1]
Groupe de recherche en physique et technologie des Couches Minces.

[1]Département de Physique, Université de Montréal,
C.P. 6128, Succ. Centre-Ville, Montréal, Québec, H3C 3J7 CANADA

[2]Département de Genie Physique, École de Polytechnique,
C.P. 6079, Succ. Centre-Ville, Montréal, Québec, H3C 3A7 CANADA

Silicon wafers implanted with 2.5 MeV O^+ have been studied by the Elastic Recoil Detection / Time-of-Flight (ERD/TOF) technique to determine the depth profile of light element impurities before and after a 12 h, 1300°C furnace anneal. The oxygen doses were not sufficient to produce a continous buried SiO_2 layer. Significant levels of nitrogen (~ 10^{19} - 10^{20} at/cm^3) were found in all samples that had been annealed in a N_2 atmosphere, including a sample that had a 1000 Å oxide cap deposited before the anneal. As-implanted samples, as well as those annealed in an Ar/O_2 atmosphere, have nitrogen concentrations lower than our detection limit of 10^{18} at/cm^3. The nitrogen concentration was found to be consistently ~6% of the oxygen concentration, even though the oxygen doses varied by a factor of 10. The depth profiles of the nitrogen were similar to the depth profiles of the oxygen. From this we surmise that the nitrogen is preferentially accumulating in the region of the oxide precipitates.

1. INTRODUCTION

For the fabrication of SIMOX (Separation by IMplanted OXygen), silicon is implanted with oxygen and then annealed at high temperatures (1200° - 1425°C) for long periods of time (~6–24 h). The quality of the final oxide layer and the silicon overlayer improves with longer annealing times, and with higher annealing temperatures [1 ,2 ,3 ,4]. The anneal is typically performed in either an Ar (with ~1% O_2) atmosphere, or in a N_2 atmosphere on samples previously covered with an oxide cap. However, it should be noted that the gas ambient used during annealing can significantly affect the formation of oxide precipitates in silicon [5].

It is known [6] that implanted nitrogen accumulates both at the interface of surface oxide and bulk silicon, and at damaged regions within the sample. The final concentration of nitrogen in the SiO_2/Si interface region was shown to be independent of the implanted dose, but longer anneal times resulted in larger concentrations of nitrogen in this region. The behaviour of implanted oxygen and implanted nitrogen in silicon has been studied by Borun *et al.* [7], who found that SiO_2 precipitates act as gettering sites for nitrogen, which then form stable $Si_xO_yN_z$ phases upon annealing. There is a non-linear nitrogen dose dependence on the formation of the $Si_xO_yN_z$ phase due to the precipitation of an Si_3N_4 phase outside of the oxide gettering centers. These Si_3N_4 precipitates can then act as gettering centers for the free oxygen atoms.

Hamdi and McDaniel [8] reported that annealing in a N_2 ambient rather than in an Ar ambient resulted in a decrease of the surface crystallinity of SIMOX samples. Nejim *et al,* [9] did not find evidence that the atmosphere during the annealing had any effect on the dislocation density in the annealed structure. However, they found that the buried oxide layer, in samples annealed in an Ar/O_2 atmosphere, always had a planar top, whereas this was not always the case for samples annealed in a N_2 atmosphere.

The SIMS (Secondary Ion Mass Spectrometry) data of Davis *et al.* [10] showed a significant amount of nitrogen, ~5×10^{20} at/cm^3, in their low energy, high dose (~10^{18} at/cm^2) SIMOX samples. They attributed this to the un-intentional implantation of nitrogen hydride during the oxygen implantation itself, although they also noted an increase in the total nitrogen concentration if the samples were annealed in N_2 rather than an Ar/O_2 atmosphere. Kilner *et al.* [11] also analyzed low energy, high

Table 1.
Nitrogen to oxygen concentration ratios in implanted silicon after annealing in N_2 at 1300°C for 12 hours.

	silicon implant	O Implant dose (/cm^2)	N/O ± 10%	N areal density /cm^2
1-2	no	1×10^{17}	0.066	6.6×10^{15}
1-3	yes	1×10^{17}	0.066	6.6×10^{15}
2-3	yes	3×10^{16}	0.058	1.74×10^{15}
2-4	yes	1×10^{17}	0.089	8.9×10^{15}
2-8	yes	1×10^{17}	0.083	8.3×10^{15}
2-10	yes	3×10^{17}	0.044	13.2×10^{15}
3-11‡	yes	1×10^{17}	0.050	5.0×10^{15}
3-19	no	1×10^{17}	0.048	4.8×10^{15}

‡1000 Å SiO_2 cap deposited before annealing.

dose SIMOX samples using SIMS, and found that the nitrogen concentration was consistently below 1×10^{17} at/cm^3, even after annealing in a N_2 atmosphere at 1300°C for 4 h.

Clearly, if there is nitrogen contamination within the sample, the formation kinetics of SIMOX structures during the anneal becomes more complex. With nitrogen accumulating on oxides and on damaged regions, the oxide growth rate will be reduced as a function of the nitrogen concentration [12 ,13], and, if the concentration of nitrogen is significant, oxygen will getter on Si_3N_4 precipitates.

A recent approach to SIMOX production is to reduce the total dose needed to form a continuous buried oxide layer [14] and to go to higher energies, which typically results in a better crystalline surface layer [15]. With this in mind, we decided to investigate the nitrogen contamination in low dose (3×10^{16} - 3×10^{17}) high energy (2.5 MeV) oxygen implanted silicon.

2. EXPERIMENT

Czochralski grown n-type [100] silicon wafers were used as targets. At various stages, both silicon and oxygen were implanted using a 6 MV TANDEM. The vacuum in the chamber was kept below 5×10^{-8} torr during the implantation.

Prior to the oxygen implant, six of the eight samples discussed in this paper were implanted with 5.0×10^{14} to 1.0×10^{15} at/cm^2, 2.0 – 2.5 MeV Si^+ and subsequently annealed at 900 °C for 1 h in a N_2 atmosphere. During the silicon implantation, the samples were held at room temperature via a massive copper heat sink. The purpose of this was to investigate what effect extended defects have on the oxygen during implantation and annealing, and will be discussed in a subsequent paper.

Oxygen was implanted at an energy of 2.5 MeV with doses ranging from 3×10^{16} to 3×10^{17} at/cm^2. The sample temperature was maintained at 570°C by a feedback system connected to a thermocouple, which was clamped to the front surface of the wafer. Consequently, the fluctuations in temperature were consistently below 3°C. The oxygen doses were insufficient to produce a continuous SiO_2 buried layer. Eight samples were implanted, and after being cut in two, one of the two halves of each sample was annealed in a conventional furnace for 12 h at 1300°C in a dry N_2 atmosphere. Of the remaining eight halves, 3 were also annealed for 12 h at 1300°C with an atmosphere composed of 95% Ar and 5% O_2. The rest were left in the as-implanted state. A summary of the implant conditions and subsequent anneals is listed in Table 1.

All samples were analyzed using ERD/TOF (Elastic Recoil Detection / Time-Of-Flight) technique, which is described in detail by Gujrathi *et al.* [16]. The time-of-flight measurement in coincidence with the energy of the scattered or recoiled particle leads directly to a measurement of its mass, with a resolution better than 1 amu for masses below 24 amu. By selecting only those events within a certain mass window, an independent energy spectrum for each target element is obtained. This permits the detection of low concentrations of all light elements, simultaneously. The energy spectrum of each element detected is then de-convoluted to produce a depth profile of its relative concentration [17].

Typically, the incident ion used to bombard the target is 30 MeV ^{35}Cl and the scattering angle is set to 30° in the forward direction. A probing depth of ~1 μm of light elements in silicon is obtained. When used on standard quartz or silicon nitride samples, this beam consistently gives expected oxygen and nitrogen concentrations, within 5%. There is a small percentage of tailing in the energy signal of the surface barrier detector (SBD) causing signals from a heavier recoil atom to appear to be of

a lower mass, which subsequently affects the detection limit. To reduce this noise from the probing beam we used a 40 MeV ^{63}Cu beam, which kinematically cannot recoil from silicon at a 30° angle, to analyze samples 1-2 and 1-3. However, this approach reduced the probing depth to 0.8 μm, and also decreased the depth resolution significantly in the region of interest, due to multiple scattering within the target. Consequently, all other samples were analyzed with the Cl beam.

The detection limits of ERD/TOF also depend upon the beam current and irradiation time. In the present experiment, the beam current was typically 5 nA and the irradiation time was ~2 h. With 11 counts in the integrated peak giving a statistical uncertainty of 30%, we calculate the detection limit of nitrogen to be ~3×10^{14} at/cm^2 (~10^{18} at/cm^3 peak concentration). The depth resolution of oxygen and nitrogen in silicon at the surface is 90 Å and better than 150 Å at a depth of 0.5 μm.

Because ERD/TOF has a probing depth of ~1 μm, which is less than the range of 2.5 MeV O^+ (2.5 μm), it was necessary to remove the surface layer between subsequent ERD analyses. This was done either with a reactive ion etch (RIE) or with a wet chemical etch of KOH (where the etch rates were known [18]). The etch depth was measured with a profilometer, and the ERD depth scale was calculated using standard dE/dx measurements assuming a silicon density of 2.32 g/cm^3. To avoid any possible influence of the prior Cu or Cl beam, each ERD analysis was done on a different spot on the wafer.

3. RESULTS

Fig. 1 shows the number of detected events versus the calculated mass, in the mass range of 10-18 amu, from sample 1-2 (2.5 MeV, 1×10^{17} O^+/cm^2) before and after annealing in a N_2 atmosphere. Each spectrum corresponds to a different depth region of the sample, obtained by etching the sample in KOH between measurements. Each peak corresponds to a specific element, (carbon C, oxygen O, and nitrogen N) where the area under the peak is a function of the relative concentrations of the elements with respect to the silicon peak (not shown and normalized to 1). No nitrogen was detected in the as-implanted sample (nor was it detected in a *virgin* sample). However, it can be

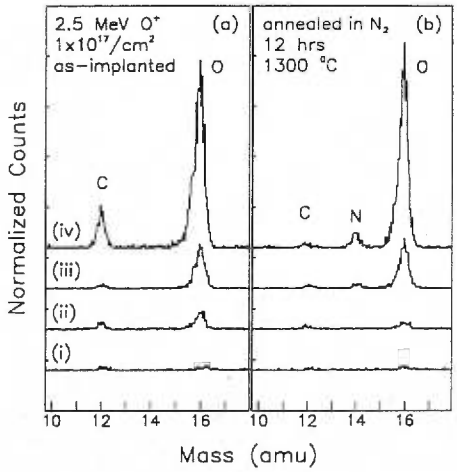

Figure 1. ERD/TOF mass spectra sample 1-2, (a) as-implanted and (b) annealed. Each individual spectrum corresponds to a different region of depth in the samples, (i) 0.9-1.8 μm, (ii) 1.3-2.2 μm, (iii) 1.5-2.5 μm, (iv) 1.8-2.7 μm. The ordinate scale represents the counts, normalized to the total number of integrated counts in the silicon mass peak (not shown).

clearly seen that nitrogen is detected in the annealed half of the sample, and only in that depth region of the sample that has a significant oxygen concentration. Note that the apparent increase in the carbon concentration is due to carbon impurities within the target chamber itself, which are deposited on the sample during the ERD analysis.

The absolute concentration of nitrogen can be approximated by using the following equation [19] and the concentration of oxygen, which is known to within 5%.

$$\frac{\Delta C_N}{\Delta C_O} = \frac{\sigma_N \eta_N}{\sigma_O \eta_O} \frac{\Delta E_N}{\Delta E_O} \frac{F_O}{F_N} \qquad (1)$$

where ΔC = the number of integrated counts in the mass peak, σ = Rutherford cross section, η = absolute concentrations (at/cm^2), ΔE = energy window corresponding to the mass peak, F = depth factor (relative stopping power), and the subscripts N and O refer to nitrogen and oxygen respectively.

The results of this calculation are listed in Table 1. It should be noted that all the as-implanted samples, as well as those samples that had been annealed in Ar with 5% O_2 atmosphere, contained less than our detectable limit of nitrogen. However, all oxygen implanted samples that had been annealed in a N_2 atmosphere, including a sample

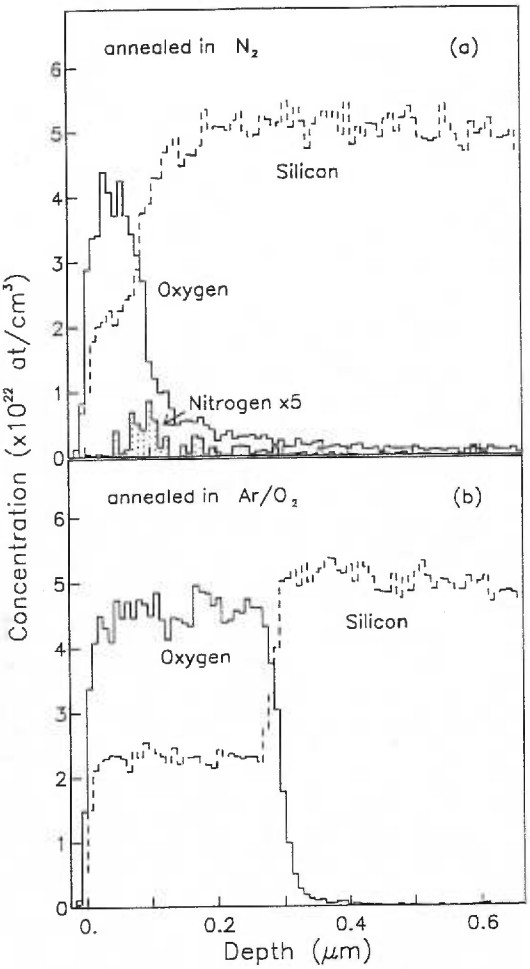

Figure 2. Oxygen and nitrogen depth profiles in the surface region after annealing for 1300°C for 12 h in (a) N_2 and (b) 95% Ar and 5% O_2 atmosphere. The nitrogen concentration has been increased by a factor of 5, for ease of viewing.

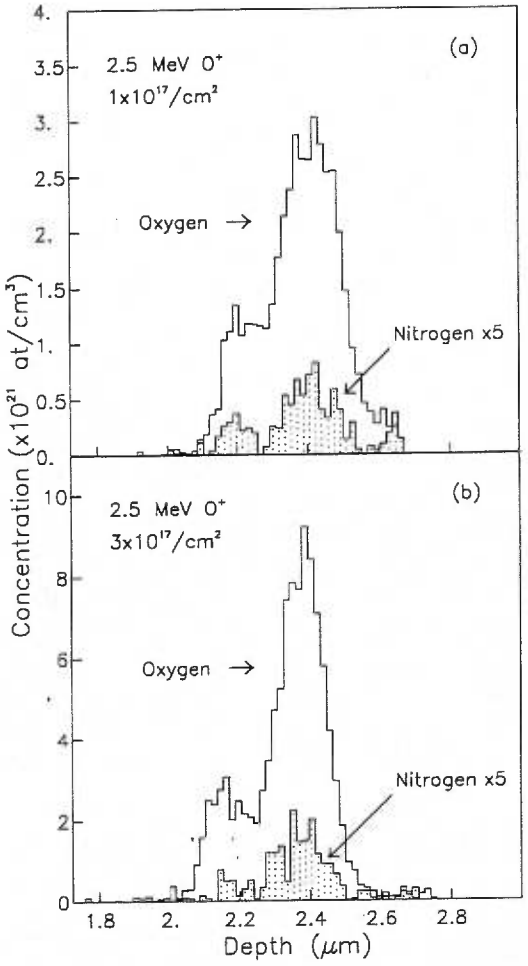

Figure 3. Oxygen and nitrogen depth profiles, in the vicinity of the implanted region, of samples (a) 3-11 and (b) 2-10 after annealing. The nitrogen concentration has been increased by a factor of 5, for ease of viewing.

that had a 1000 Å SiO_2 cap deposited by PECVD (Plasma Enhanced Chemical Vapour Deposition) before annealing, had integrated nitrogen doses between 1.7×10^{15} to 1.3×10^{16} at/cm^2. Although the concentration of implanted oxygen varied by a factor of 10 (3×10^{16} to 3×10^{17} at/cm^2), the relative concentration of nitrogen to oxygen was consistently found to be between 5 and 9%.

Fig. 2 shows the oxygen and nitrogen depth profiles for the surface region of an un-implanted sample, subjected to the same processing steps as all the other samples, annealed in N_2 (2a) and annealed in an Ar/O_2 mix (2b). The sample annealed in N_2 has a thin (70 nm) surface oxide layer which is most likely due to the residual oxygen present in the furnace during the anneal. The interface between the oxide and the substrate is not sharp, and there is a significant amount of oxygen extending into the substrate. The peak nitrogen concentration is situated in the interface between the bulk SiO_2 and the bulk silicon. The total concentration of nitrogen was 1.2×10^{16} at/cm^2. Our results inidicate a broad region (60 nm) of nitrogen contamination. However, if the SiO_2/Si interface is not smooth, our results are not inconsistent with having a thin layer

of Si_3N_4 formed at the interface, similar to the results reported by Josquin and Tamminga [6]. The sample annealed in Ar/O_2, shown in figure 2b, has an oxide layer ~300 nm thick, and the interface between the oxide and the bulk silicon is considerably sharper. There were no detectable traces of nitrogen in this sample.

Fig. 3 shows a part of the oxygen and nitrogen concentration profiles of samples 3-11 and 2-10 (oxygen doses of 1×10^{17} and 3×10^{17} at/cm^2, respectively). Both oxygen profiles consist of two peaks, the first corresponding to the end-of-range (EOR) damage caused by the oxygen implant itself, and the second corresponding to the maximum range of the oxygen ions. It can be seen that, within the limits of statistical error, the depth profiles of the nitrogen have the same shape as the oxygen profiles, where the nitrogen to oxygen ratio remains fixed at approximately 5%. Cross-sectional Transmission Electron Microscopy (XTEM) pictures (not shown), with equivalent doses of oxygen, clearly indicate that the oxide is in the form of hexagonal and spherical precipitates, with radii of ~20-50 nm. The region of maximum oxygen concentration is composed of many small oxide precipitates rather than a continuous buried layer.

The oxygen concentration profiles did not appear to be affected by the inclusion of nitrogen in the sample, as shown in Fig. 4. One half of sample 2-8 was annealed in Ar/O_2 and the other half was annealed in N_2. These samples were etched independently and subsequently profiled with ERD. The depth scale was corrected for the respective removal of the surface layer, and as a result, the probing limit is slightly smaller for the sample annealed in the Ar/O_2 atmosphere. Within the limits of resolution, the profiles are indistinguishable.

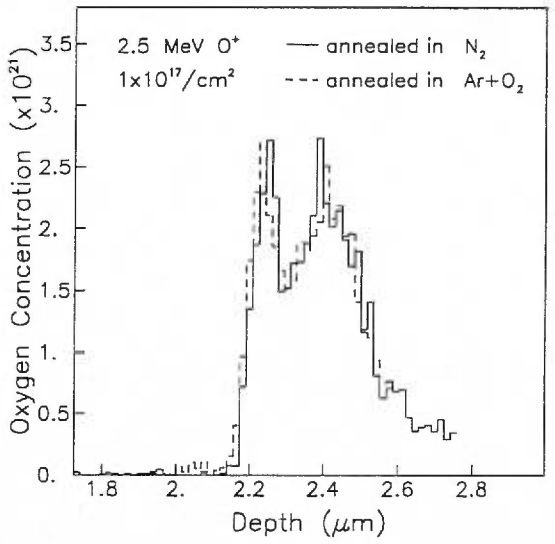

Figure 4. Oxygen concentration profiles of sample 2-8, with one half of the target annealed in N_2 (solid line) and the other half annealed in Ar/O_2 (dashed line), at 1300°C for 12 h.

4. DISCUSSION

We found more than 10^{19} at/cm^3 of nitrogen in the area of the oxygen implant, in all the samples that had been annealed in a N_2 atmosphere (12 h at 1300°C), and found no nitrogen in any of the other samples. The intrinsic nitrogen impurity in commercially grown silicon is less than 10^{15} N/cm^3 [20], therefore the total integrated nitrogen concentration (in a 0.3mm sample) is less than 3×10^{13} N/cm^2, a factor of almost 500 times less than the measured nitrogen in sample 2-10. Therefore, it is not likely that this is the source of our nitrogen contamination. We use a TANDEM accelerator for our oxygen implantations, and hence accidently implanting nitrogen in the form of nitrogen hydride, as might have been the case in Davis *et al.* [10], is not possible. The only process that is different between those samples that have detectable amounts of nitrogen versus those that do not, is the anneal in a N_2 atmosphere. This leads us to the conclusion that it is this N_2 atmosphere which is the source of the nitrogen contamination within our samples.

Nitrogen was also found in a sample that had a 1000 Å oxide cap deposited prior to annealing in a N_2 atmosphere. This is not suprising, since it has been demonstrated that SiO_2 is not a barrier to nitrogen diffusion [6,10].

The two striking features of the nitrogen profiles are that (1) the final nitrogen concentration is a function of the oxygen concentration within the sample, and (2) the nitrogen depth profile has the same shape as the oxygen profile. If the nitrogen is forming Si_3N_4 at the Si/SiO_2 boundaries, where the thickness is dependent only on the anneal temperature and time [6], then one would expect that the nitrogen concentration would be a function of the surface area of the oxide precipitates. Assuming

that the number of precipitates is constant, the nitrogen concentration would go as $(\text{dose})^{2/3}$. However, as the dose increases, not only does the size of the precipitates increase, but they merge together to form even larger precipitates, thus further decreasing the surface area of the Si/SiO_2 interface. In this case the exponent in the nitrogen concentration dose dependency would be less than 2/3, which is considerably less than the one experimentally observed. A higher oxygen dose increases the crystalline damage in the silicon, which provides additional gettering centres for the nitrogen, and it is also likely that the damage will affect the diffusivity of nitrogen in silicon. In-diffusion seen in our studies may be due to nitrogen being gettered by damage regions and oxygen precipitates.

The above discussion assumes that the oxide precipitates are stable. However in the as-implanted samples, the implanted region is highly damaged with small oxide precipitates, and the larger precipitates only form *during* the anneal. Fritzsche and Rothmund determined that the growing oxide film on a N_2 implanted silicon sample is actually an oxynitride polymer [21]. Similarly Borun *et al.* [7] found that implanted nitrogen and oxygen form a $Si_xO_yN_z$ dielectric phase during the anneal. It is known that Si_2N_2O, SiO_2, and Si_3N_4 are all stable in contact with silicon at temperatures between 700-1000°C [22]. From the Gibb's free energy [22], SiO_2 is the most favoured compound to be formed. From this, and from our experimental results showing that the nitrogen to oxygen ratio was constant throughout the depth, independent of the damage profile, we hypothesize that the nitrogen in our samples is reacting with the oxygen and silicon to form an oxynitride phase, in addition to the SiO_2 phase, during the anneal. However, further research is required to determine the exact chemical nature of the respective elements in the sample.

5. CONCLUSION

We have found that nitrogen diffuses into oxygen implanted silicon samples during a high temperature anneal (1300°C for 12 h) in N_2 atmosphere and preferentially accumulates in the region of the oxide precipitates, keeping the nitrogen-to-oxygen ratio ~6%. This in-diffusion is not impeded by the presence of a SiO_2 surface layer.

1. A. Yoshino, K. Kasama and M. Sakamoto, Nucl. Instr. Meth., B39 (1989) 203.
2. K.G. Stephens, K.J. Reeson, B.J. Sealy, R.M. Gwilliam and P.L.F. Hemment, Nucl. Instr. Meth., B50 (1990) 368.
3. K.J. Reeson, Nucl. Instr. Meth., B19/20 (1987) 269.
4. C.K. Celler, P.L.F. Hemment, K.W. West and J.M. Gibson, Appl. Phys. Lett., 48 (1986) 532.
5. S.M. Hu, Appl. Phys. Lett. 36 (1980) 561.
6. W.J.M. Josquin and Y. Tamminga, J. Electrochem. Soc., vol 129, No. 8 (1982) 1803.
7. A.F. Borun, A.B. Danilin, V.N. Mordkovich and E.M. Temper, Rad. Eff., 107 (1988) 9.
8. A.H. Hamdi and F.D. McDaniel, Appl. Phys. Lett. 41 (1982) 1143.
9. A. Nejim, Y. Li, C.D. Marsh, P.L.F. Hemment, R.J. Chater, J.A. Kilner, L.F. Giles, and G.R. Booker, Nucl. Instr. Meth., B74 (1993) 170.
10. G.E. Davis, K.S. Jones, S. Prussin, Mater. Res. Soc, vol 107 (1988) 111.
11. J.A. Kilner, R.J. Chater, S. Biswas, P.L.F. Hemment, and K.J. Reeson, Mater. Res. Soc vol 107 (1988) 151.
12. J. Wada and M. Ashikawa, J. Appl. Phys., 15 (1978) 389.
13. M. Ramin, H. Ryssel, and H. Kranz, Appl. Phys., 22 (1980) 393.
14. G.F. Cerofolini, S. Bertoni, L. Meda and C. Spaggiari, Nucl. Instr. Meth. B84 (1994) 234.
15. A.E. White, K.T. Short, J.L. Batstone, D.C. Jacobson, J.M. Poate, and K.W. West, Appl. Phys. Lett., 50 (1987) 19.
16. S.C. Gujrathi, P. Aubry, L. Lemay, and J.-P. Martin, Can. J. Phys., Vol 65 (1987) 950.
17. K. Oxorn, S.C. Gujrathi, S. Bultena, L. Cliche and J. Miskin, Nucl. Instr. Meth., B45 (1990) 166.
18. H. Seidel, L. Csepregi, A. Heuberger, H. Baumgartel, J. Electrochem. Soc., 137 (1990) 3612.
19. S.C. Gujrathi, ASC Symp., Series no. 440, Metallization in Polymers, eds. E. Sacher, J. Pireaux and S.T. Kowalczyk (1990) chap. 6, p 88.
20. Y. Yatsurugi, N. Akiyama, Y. Endo, and T. Nozaki, J. Electrochem. Soc., 120 (1973) 975.
21. C.R. Fritzsche and W. Rothmund, J. Electrochem. Soc., 120 (1973) 1603.
22. A.S. Bhansali, R. Sinclair and A.E. Morgan, J. Appl. Phys., 68 (1990) 1043.